



TÉCNICO
LISBOA

**UNIVERSIDADE DE LISBOA
INSTITUTO SUPERIOR TÉCNICO**

**Design and commissioning of the magnetic
diagnostics system for COMPASS-U**

André Gonçalves Torres

Supervisor: Doctor Horácio João Matos Fernandes

Co-Supervisors: Doctor Bernardo Brotas de Carvalho
Doctor Aleš Havránek

Thesis approved in public session to obtain the PhD Degree in
Technological Physics Engineering

Jury final classification: **Pass With Distinction and Honour**

2023

UNIVERSIDADE DE LISBOA
INSTITUTO SUPERIOR TÉCNICO

**Design and commissioning of the magnetic diagnostics system
for COMPASS-U**

André Gonçalves Torres

Supervisor: Doctor Horácio João Matos Fernandes

Co-Supervisors: Doctor Bernardo Brotas de Carvalho
Doctor Aleš Havránek

Thesis approved in public session to obtain the PhD Degree in
Technological Physics Engineering

Jury final classification: **Pass With Distinction and Honour**

Jury

Chairperson:

Doctor Luís Paulo da Mota Capitão Lemos Alves, Instituto Superior Técnico, Universidade de Lisboa;

Members of the Committee:

Doctor Horácio João Matos Fernandes, Instituto Superior Técnico, Universidade de Lisboa;

Doctor Manuel Garcia-Muñoz, Department of Atomic Molecular and Nuclear Physics, Universidad de Sevilla, Espanha;

Doctor Martin Hron, Institute of Plasma Physics of the Czech Academy of Sciences, República Checa;

Doctor Pedro Jorge dos Santos de Assis, Instituto Superior Técnico, Universidade de Lisboa.

Funding Institution

Fundação para a Ciência e a Tecnologia

Abstract

The magnetic diagnostic system delivers fundamental data to the operation and physics exploitation of magnetic confinement nuclear fusion devices. Whilst under continuous improvement since the first devices, the construction of new reactors poses an opportunity for advancements in magnetic diagnostics, tailored to their specific challenges and opportunities.

The COMPASS-U tokamak, being developed in Prague, Czech Republic will have a unique set of parameters, featuring a 5 T toroidal magnetic field and metallic first wall heated to high temperatures. Enabled by an extensive set of diagnostics, this device will be able to support ITER operation and address DEMO and power plant relevant challenges.

In this thesis, the challenges of magnetic diagnostic development for such a unique machine are addressed, and the design and development of key subsystems is shown – from sensors to cabling and electronics. Methods for precise calibration and measurement of magnetic sensor are developed; mitigation of the influence of metallic structures in sensors are studied; conclusions towards the choice of long data-transmission cables are drawn; and the implementation of a real-time numerical integration methods are qualified and new hardware developed.

While these development steps have the ultimate goal of adequacy to the COMPASS-U operation and scientific program, the systematic approaches carried out and described can be applied future devices.

Keywords

Nuclear fusion, tokamak, magnetic diagnostic, magnetic sensors, data-acquisition.

Resumo

O sistema de diagnóstico magnético fornece dados fundamentais para a operação e exploração científica de dispositivos de fusão nuclear por confinamento magnético. Embora esteja em constante aperfeiçoamento desde os primeiros dispositivos, a construção de novos reatores representa uma oportunidade para avanços em diagnósticos magnéticos, adaptados aos desafios e oportunidades específicos.

O tokamak COMPASS-U, desenvolvido em Praga, na República Checa, terá um conjunto único de parâmetros, dos quais se destaca o campo magnético toroidal de 5 T e a parede interna metálica aquecida a altas temperaturas. Graças a uma ampla coleção de sistemas de diagnóstico, este dispositivo estará numa posição de suportar a operação do ITER e abordar problemas relevantes tanto para o DEMO como futuras centrais elétricas.

Nesta tese, os desafios relativos ao desenvolvimento de um sistema de diagnóstico magnético para uma máquina tão única são discutidos e é exposto o projeto e desenvolvimento dos principais subsistemas: desde os sensores ao cabeamento e eletrônica. São desenvolvidos métodos para calibração e medição precisas de sensores magnéticos; estuda-se a mitigação da influência de estruturas metálicas em sensores; são tiradas conclusões sobre a escolha de cabos de transmissão de dados para longas distâncias; é qualificada a implementação de métodos de integração numérica em tempo real e novo hardware é desenvolvido.

Embora estas etapas de desenvolvimento tenham como objetivo último a adequação à operação e ao programa científico do COMPASS-U, as abordagens sistemáticas descritas e levadas a cabo podem ser aplicadas a dispositivos futuros.

Palavras Chave

Fusão nuclear, tokamak, diagnóstico magnético, sensores magnéticos, aquisição de dados.

Acknowledgments

First and foremost I would like to express my gratitude towards my supervision team. Specifically, to Dr. Horácio Fernandes for the academic and scientific guidance, the pragmatism and vision. To Dr. Bernardo Carvalho for the direct help and for the extensive work that served both as a foundation to build my own and as a learning tool. And to Dr. Aleš Havránek for the insightful and critical feedback, observations and discussions throughout the work.

I would like to thank the COMPASS-U administration and team. In particular, the magnetic diagnostic group. A special thanks to Dr. Tomáš Markovič, whose thoroughness was an example and inspiration, to Dr. Vladimír Weinzettl for the full support and to Dr. Karel Kovařík for all the help and MIC terminations.

I would also like to thank Dr. António Batista for all the help on electronics design, analysis and testing. A special thanks also to Eng. Mykyta Varavin for the time and skill granted and to Dr. Pedro Lourenço for the help and discussions.

On a personal level, I would like to thank my family, APPLAuSE colleagues and my friends Bernardo Gonçalves, Miguel Levy and Ricardo Ferreira for the continuous support. Most of all, to my wife, Agata, I am grateful for the patience over these years and for the motivation for writing the thesis.

Finally, I acknowledge and thank the *Fundação para a Ciência e a Tecnologia* for funding this work, under the APPLAuSE PhD Program.

Contents

Acronyms	xi
1 Introduction	1
1.1 Nuclear Fusion	2
1.2 The tokamak	4
1.3 Motivation	5
1.4 Thesis Outline	6
2 Magnetic diagnostic	7
2.1 Principles of magnetic diagnostic	8
2.1.1 'The' key diagnostic in tokamaks	8
2.1.2 Physical principle	8
2.1.3 Types of magnetic sensors	9
2.1.3.A Flux loops	9
2.1.3.B Diamagnetic loops	10
2.1.3.C Rogowski coils	13
2.1.3.D Magnetic probes	13
2.1.3.E Saddle loops	14
2.1.3.F Hall probes	15
2.1.3.G Fiber Optic Current Sensors	16
2.1.3.H Motional Stark effect sensor	17
2.2 Applications of magnetic diagnostic	18
2.2.1 Equilibrium reconstruction	18
2.2.2 Real-time control	19
2.2.3 MHD modes	24
2.3 Data acquisition	27
2.3.1 Key concepts of data acquisition	27
2.3.1.A Filtering	27
2.3.1.B Dynamic range and oversampling	29
2.3.1.C Aliasing	30
2.3.1.D Transmission lines and input impedance	32
2.3.2 Signal integration	33
2.3.3 Analogue and Digital Integration	34
2.4 Development of modern magnetic diagnostic systems	36
2.4.1 Sensor design and construction	36
2.4.2 Equilibrium reconstruction	38
2.4.3 Real-time control	39
2.4.4 Signal integration	40
3 Development of sensors for COMPASS Upgrade	45
3.1 COMPASS Upgrade	46
3.2 Challenges and implications to the development of the magnetic diagnostic	48
3.3 Architecture of the magnetic diagnostic	50
3.4 Testbench for calibration of magnetic sensors	52
3.4.1 Preliminary setup	52
3.4.2 Frequency response measurements using Helmholtz coil	53
3.4.2.A Helmholtz coil construction	54

3.4.2.B	Frequency response measurement	57
3.4.2.C	Alignment	59
3.4.2.D	Automation	60
3.4.3	Effective area measurements	63
3.4.3.A	Accuracy and external calibration	63
3.4.4	Rogowski coil measurements	67
3.5	Sensor prototyping and development	68
3.5.1	Mineral Insulated Cables	68
3.5.2	Flux loop measurements on COMPASS	71
3.5.3	MHD probes calibration	74
3.5.4	Development of MIC probe prototypes	79
3.5.4.A	Application of MIC probes response to COMPASS data	83
4	Ex-vessel cabling	87
4.1	Signal path from sensor data acquisition system	88
4.2	Ex-vessel cabling options	89
4.3	Testing of externally induced noise	89
4.3.1	Experimental setup	90
4.3.2	Results and analysis	92
4.4	Test of cross-talk	96
4.4.1	Experimental setup	96
4.4.2	Results and analysis	97
4.5	Cable selection	98
5	Digital integrator development	103
5.1	Conceptual qualification of digital integration as a solution for COMPASS-U	104
5.1.1	Architecture of a digital integrator with phase switched modulation	104
5.1.2	Assessment of requirements for COMPASS-U magnetics	106
5.1.2.A	Resolution	106
5.1.2.B	Signal during disruption	109
5.1.2.C	Drift requirement	111
5.2	Testing of digital integration on COMPASS	112
5.2.1	Integration of COMPASS pulses	112
5.2.2	High frequency recovery	114
5.3	COMPASS-U modular DAS concept	116
5.3.1	Two-channel architecture and operation modes	116
5.3.2	Input Output Processor	117
5.4	Electronics design and development	118
5.4.1	Key components market research	118
5.4.2	Insulated power supply	119
5.4.3	Input Stage	122
5.4.4	Anti-aliasing filtering and ADC driving	123
5.4.5	ADC communication and digital signals	125
5.5	Prototype testing and qualification	128
5.5.1	Testing software	129
5.5.2	Benchtop tests	130
5.5.3	Implementation of extended dynamic range	132
5.5.4	Acquisition of ISTTOK discharges	134
5.5.5	Demodulation error minimization	136
5.5.5.A	Systematic approach for demodulation error minimization	137
5.5.5.B	MFB filter adjustments	138
5.5.5.C	Input filter contribution	142
5.5.6	Drift and temperature dependence	144
5.6	Implementation for COMPASS-U	146
6	Conclusions and Future Work	147
6.1	Summary and achievements	148
6.2	Outlook and future work	151

Bibliography	153
Appendix A Helmholtz coil structure technical drawing	A-1
Appendix B Calculation of the field homogeneity integrals	B-1
B.1 1D	B-2
B.2 2D	B-2
B.2.1 Circular	B-2
B.2.2 Rectangular	B-2
B.2.3 Racetrack	B-3
B.3 Computed corrections	B-4
Appendix C Module configurations	C-1
Appendix D Determination of MFB filter components	D-1

Acronyms

$\Sigma\Delta$ Sigma-Delta. 118
AA Anti-Aliasing. 138, 146, 150
ADC Analog-to-Digital Converter. 34, 35, 41, 104–106, 112, 114, 116–119, 123–127, 129, 130, 132, 134, 136–139, 142, 146
API Application Programming Interface. 60
ATCA Advanced Telecommunications Computing Architecture. 42, 43, 104, 112, 113, 116–118, 129, 144, 145, 151
AWG Arbitrary Waveform Generator. 60, 63
CMI Czech Metrology Institute. 64–67, 148
CMOS Complementary Metal-Oxide-Semiconductor. 104
CMRR Common Mode Rejection Ratio. 38, 41, 96
CODAC Control Data Access and Communication. 39, 43, 116
COTS Commercial Off-The-Shelf. 88, 150
CUDb COMPASS-U Database. 106, 108
DAC Digital to Analog Converter. 41, 112, 117
DAQ Data AcQuisition. 27, 33, 35, 74, 84, 88, 91, 99, 112, 148
DAS Data Acquisition System. 25, 30, 33, 40, 48, 52, 71, 74, 77, 78, 88, 91, 93, 96–99, 101, 104, 105, 108, 112, 116, 118, 137, 142
DMA Direct Memory Access. 112, 117, 129
DSP Digital Signal Processing. 30, 35
DTFT Discrete-Time Fourier Transform. 31
ECRH Electron Cyclotron Resonance Heating. 37, 48
EFDA European Fusion Development Agreement. 47
EFIT Equilibrium FITting. 18, 38, 39
EFPS Equilibrium Field Power Supply. 22
ELM Edge Localized Mode. 50, 85, 113, 114
EMF ElectroMotive Force. 8–10, 109
EMI ElectroMagnetic Interference. 119, 120
EO Electronics Offset. 104, 105, 118, 122, 129, 132, 136
EPR External Partial Rogowski. 13, 83
ET EMF-Time. 120
FEM Finite Element Method. 149
FEXT Far End cross Talk. 96–98, 100
FFT Fast Fourier Transform. 71
FIFO first In, First Out. 117
FIR Finite Impulse Response. 27
FOCS Fiber Optic Current Sensor. 16
FPGA Field-Programmable Gate Array. 35, 104, 112, 117, 118, 127, 129, 132, 136, 140
FPSC Fast Plant System Controller. 117
FWHM Full Width at Half maximum. 29
HDI Human Development Index. 2
HFS High-Field Side. 4, 15, 22, 85, 109, 134
HP High-Pass. 27
IC Integrated Circuit. 104, 118–120, 139, 146
ICRH Ion-Cyclotron Resonance Heating. 26
IIR Infinite Impulse Response. 27
INL Integrated Non-Linearity. 118

IO Input/Output. 118, 127
IOP Input-Output Processor. 116–118, 129, 134, 146, 150
IPP Institute of Plasma Physics of the Czech Academy of Sciences. 46, 65
IPR Inner Partial Rogowski. 13
IRQ Interrupt ReQuest. 129
ISOL ISOLated. 112
ITPA International Tokamak Physics Activity. 24
LCFS Last Closed Field Surface. 23, 39, 40
LDO Low-Dropout Regulator. 118, 121, 128
LFS Low-Field Side. 15, 22, 134
LMD Liquid Metal Divertor. 48
LP Low-Pass. 27, 28, 41, 106, 112, 120, 122, 124
LSB Least Significant Bit. 128, 136
LTCC Low-Temperature Co-fired Ceramic. 14, 38
LTI Linear Time Invariant. 27, 84, 149
LVDS Low-Voltage Differential Signaling. 118, 119, 127
LVTTL Low-Voltage Transistor–Transistor Logic. 126, 127
MARTE Multithreaded Application Real-Time executor. 134
MFB Multiple FeedBack. 124, 128, 138
MFPS Magnetizing Field Power Supply. 22
MHD MagnetoHydroDynamic. 8, 11, 15, 18, 21, 24–27, 34, 35, 50, 52, 74, 75, 83, 84, 105, 106, 114–116, 132, 148–150
MIC Mineral Insulated Cable. 36, 49–54, 64, 68, 69, 71, 73, 79, 81, 83, 85, 88, 94, 109, 148, 149, 151
MIMO Multiple Input Multiple Output. 112
MISO Master Input Slave Output. 127
ML Machine Learning. 40
MLCC Multi-Layer Ceramic Capacitor. 122
MSB Most Significant Bit. 126
MSE Motional Stark Effect. 17, 19
NBI Neutral Beam Injector. 48
NEXT Near End cross Talk. 96, 97
NTM Neoclassical Tearing Mode. 26
OD Outer Diameter. 53, 56, 57, 69, 75, 81, 93, 148
OPAMP Operational AMPlifier. 34, 35, 40, 41, 104–106, 116, 119, 123, 125
P-EFIT Parallel EFIT. 18
PC Personal Computer. 55, 60, 91, 148
PCB Printed Circuit Board. 14, 38, 43, 118–120, 131, 146, 150
PCIe Peripheral Component Interconnect Express. 117
PFC Plasma Facing Component. 37, 46, 48
PID Proportional-Integral-Differential. 22
PSP Passive Stabilizing Plate. 19, 39, 106, 109
RAM Random-Access Memory. 129
RIC Radiation Induced Conductivity. 38
RICE Research and Innovation Centre for Electrical engineering. 51
RIED Radiation Induced Electrical Degradation. 38
RIEMF Radiation Induced EMF. 38
RMS Root Mean Square. 97
RT-EFIT Real-Time EFIT. 18
RWM Resistive Wall Modes. 15, 25
S/H Sample and Hold. 40, 41
SAR Successive Approximation Register. 118
SC Shape Controller. 39
SDK Software Development Kit. 60
SFPS Shaping Field Power Supply. 22
SNR Signal to Noise Ratio. 15, 30, 106, 116, 118, 130, 146
SPI Serial Peripheral Interface. 118, 119, 126, 127
SPICE Simulation Program with Integrated Circuit Emphasis. 75, 125, 139

STP Shielded Twisted Pair. [89](#), [93](#), [94](#), [96–99](#)
SVD Singular Value Decomposition. [26](#)
SXR Soft-X-Ray. [19](#)
TAE Toroidal Alfvén Eigenmode. [25](#)
TF Toroidal Field. [12](#), [150](#)
TP Twisted Pair. [88–90](#), [93](#), [96](#), [98](#), [100](#)
TPC Thick Printed Copper. [14](#), [16](#), [50–52](#), [74](#), [77](#), [148](#)
VDE Vertical Displacement Event. [39](#), [109](#)
VS Vertical Stability. [39](#)
VV Vacuum Vessel. [10](#), [13–15](#), [21](#), [24](#), [25](#), [39](#), [46](#), [47](#), [49](#), [69](#), [81](#), [88](#), [106](#), [109](#), [151](#)
WO Wiring Offset. [105](#), [106](#), [118](#), [122](#), [129](#), [136](#), [152](#)
XSC eXtreme Shape Controller. [39](#)

1

Introduction

Contents

1.1 Nuclear Fusion	2
1.2 The tokamak	4
1.3 Motivation	5
1.4 Thesis Outline	6

This work is part of an ambitious project: to develop a cutting-edge magnetic diagnostic system for COMPASS Upgrade. This endeavor requires an understanding of the current status among experimental nuclear fusion reactors in order to draw best practices from the previous developments and to identify and provide solutions for the problems that are unique to the device. Specifically, this effort includes the evaluation of the most adequate cabling choice for the manufacturing of sensors capable of operating up to 500°C ; the development and calibration to 0.2 % accuracy of local sensors that will be the basis for the plasma position and shape control; optimization of the frequency response of the sensors sensitive to fast perturbations of the plasma through laboratory measurements and modeling, taking into consideration the cables that connect the sensors to the data acquisition system.

The work culminates with the qualification, development and testing of the electronics front-end for a bespoke modular data acquisition system with real-time numerical integration. This system achieves and surpasses the accuracy requirements established for COMPASS Upgrade whilst removing the need for analog signal integrators.

1.1 Nuclear Fusion

The four figures in this section, almost by themselves, draw a clear picture of why energy production from nuclear fusion is such an important achievement for mankind, and an effort worth pursuing.

First, there is a clear correlation between development and energy consumption. In the plot in figure 1.1, development is represented by the Human Development Index (HDI) and the energy consumption is represented per capita. Without delving into the causation relation between the two, we

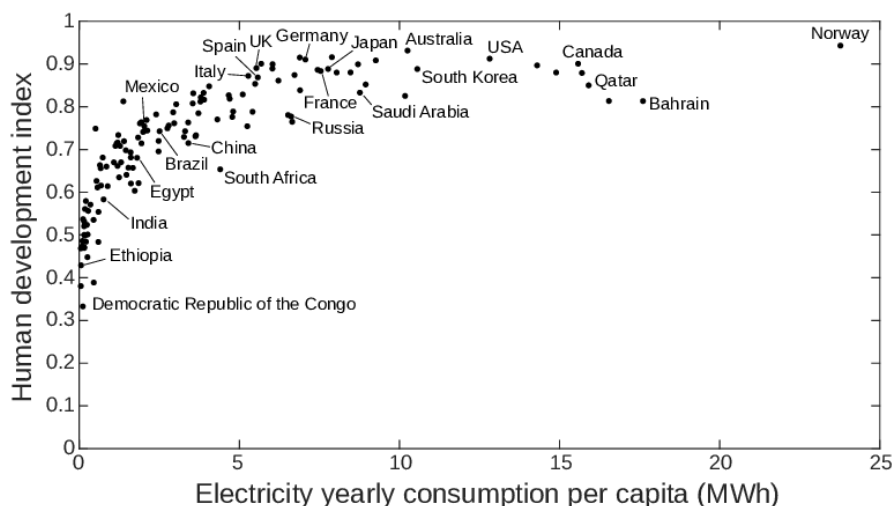


Figure 1.1: Human Development Index (HDI) versus per capita electricity consumption. Figure gathered from [1]. See original for references for the data sources.

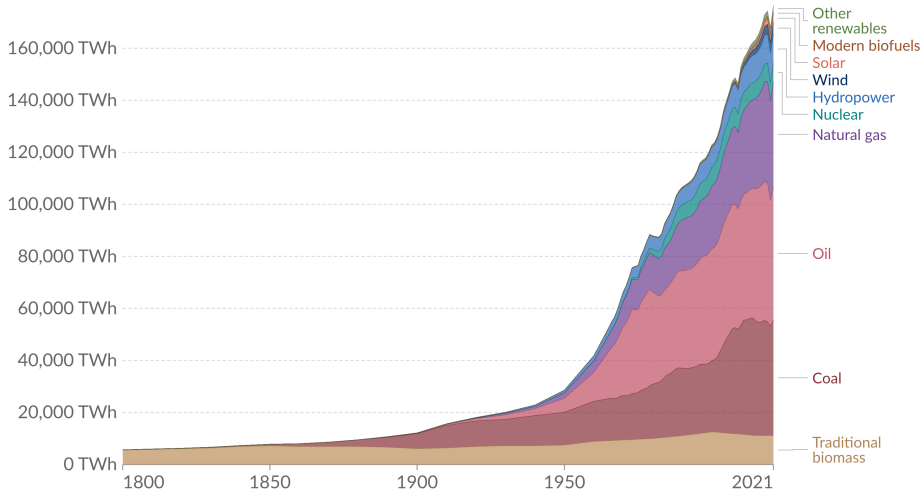
see that if we aim at moving the points up (*“make the world a better place”*), the energy consumption will be much higher.

A historical outlook, in figure 1.2, tells us that since the industrial revolution, that drastically improved the access to energy and conversion between energy types, the worldwide energy production has grown exponentially. This trend will continue in the foreseeable future, as population giants in rapid development will improve their quality of life using the same energy sources that spurred the development of the industrialized countries. However, it was found [3] that these sources of energy are not sustainable. The key problem being not their availability, but the emission of greenhouse gasses, in particular CO_2 , a byproduct of the burning of fossil fuel (wood, coal, oil, natural gas). Thankfully, new sources of energy were also discovered in the last century, photo-voltaic and, in particular, nuclear energy.

In order to harvest nuclear energy, one interacts with nuclei in order for them to assume a more stable configuration, in the process, releasing the difference in binding energy. For heavier atoms, this stability is achieved by decaying into lighter species (right-hand side of the plot in figure 1.3a). Nuclear fusion, on the other hand, is achieved by colliding light atoms that combine, resulting in a

Global primary energy consumption by source

Primary energy is calculated based on the 'substitution method' which takes account of the inefficiencies in fossil fuel production by converting non-fossil energy into the energy inputs required if they had the same conversion losses as fossil fuels.

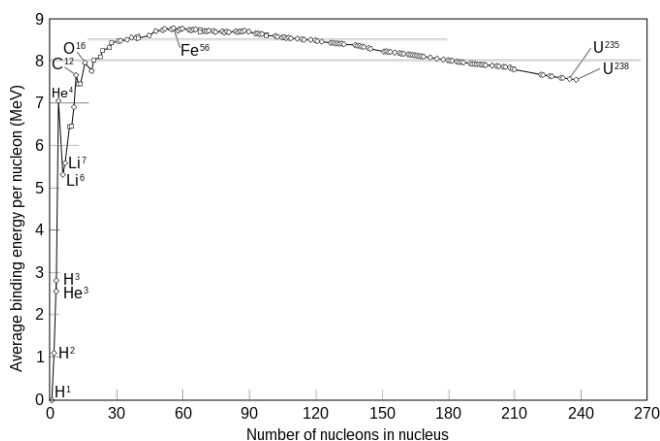


Source: Our World in Data based on Vaclav Smil (2017) and BP Statistical Review of World Energy. OurWorldInData.org/energy • CC BY

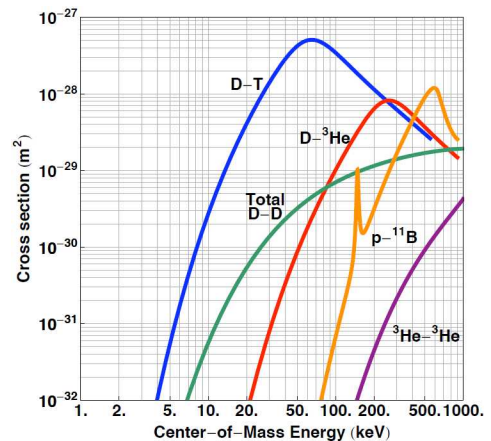
Figure 1.2: Global energy consumption since 1800, categorized by source. Attribution and data sources in figure, more details in [2].

more stable configuration. The energy gain in this case is much higher than in fission, as seen on the left-hand side of the same plot.

In order to fuse atoms, the strong nuclear force that binds neutrons and protons needs to overcome the Coulomb barrier, the repulsive electrical force between charged particles (protons). Moreover, not only the energy gain needs to be considered, but also the reactivity, how easy, or probable the reaction is. Specific reactions have different cross-sections, depending on the energy of the reagents. On the core of stars, reactions with H^1 are plentiful, but the low cross-sections make them unviable for a reactor on Earth. The reaction that is the current prime candidate for nuclear fusion on Earth is that of deuterium (D) and tritium (T), the hydrogen atoms with 1 and 2 neutrons, respectively:



(a)



(b)

Figure 1.3: (a): Nuclear binding energy versus atomic number. Attribution: Wikimedia Commons. (b): Reaction cross-section as function of energy for the most important candidates for nuclear fusion in reactor conditions. Figure gathered from [4].

It can be verified in figure 1.3a that this is one of the reactions that release more energy, 80 % of which in the neutron (n). Furthermore, in figure 1.3b we see that the D-T reaction not only has

one of the highest energetic outputs but also a high probability of collision at relatively low energies. Chargeless, the high energy neutron is not influenced by electric and magnetic fields and will interact with a blanket of material surrounding the reactor, transferring its energy into heat, that can eventually drive a turbine through a steam cycle.

On top of these reasons, what drives this reaction as the main path to achieving energy production from nuclear fusion, in the international, and in particular, European research communities, is the completeness of the fuel cycle solution. Deuterium is stable, harmless, and virtually unlimited, as it can be distilled from water, at a rate of 38 g per cubic meter of seawater [5]. Tritium on the other hand, is unstable and short-lived ($t_{1/2} \approx 12$ years) but can be created, or 'bred' from the interaction of a neutron with lithium. The concept of the future fusion power plant, regardless of magnetic or inertial confinement or any other technical architecture, will feature these 'breeding blankets', combining the heat-exchange process with the tritium breathing. Other ways of generating energy by fusion are possible, perhaps even economically viable, but it is the completeness of this solution – generating clean energy from abundant deuterium and lithium, that is in a position to address the global energy demand in the upcoming century.

1.2 The tokamak

Without access to the pressure ranges achieved in the cores of stars, on Earth, fusion is achieved at higher temperatures. Early attempts at confining a plasma using magnetic fields, proved flawed. Specifically, the z-pinch and θ -pinch concepts were plagued by instabilities and losses, respectively [6]. These early devices achieved only μ s discharges. A different topology, with a promising configuration for stable discharges was proposed by Lyman Spitzer in 1951: the stellarator. In these devices a 3-dimensional arrangement of external fields introduces rotation and creates closed magnetic field lines that confine the plasma. In parallel, in 1950, Andrei Sakharov and Igor Tamm proposed¹ the tokamak configuration, where the plasma is confined in a torus by an external toroidal magnetic field (B_{tor} , B_ϕ) and a poloidal field (B_{pol} , B_θ) created by a current (plasma current, I_p) induced in the ionized gas. This current is induced as the secondary of a transformer, see figure 1.4. With this configuration,

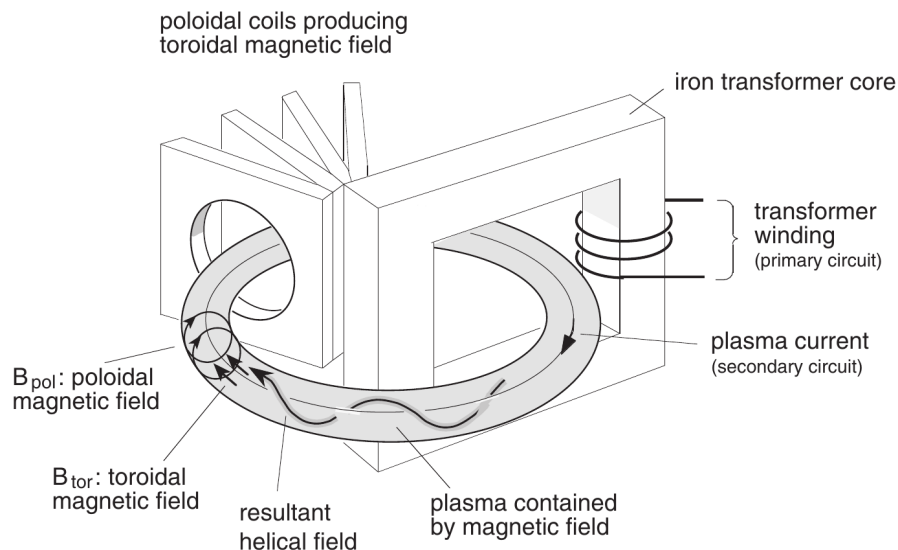


Figure 1.4: Schematic representation of magnetic confinement on a tokamak. Figure reproduced from [6].

the plasma can exist in equilibrium, that is, the kinetic pressure of the hot gas is compensated by the magnetic pressure. The toroidal magnetic field is much higher than the poloidal field, and due to the toroidal configuration, is also much higher on the inner part of the torus. The profile of B_{tor} follows roughly $1/R$, allowing us to refer to the inner part as the **High-Field Side (HFS)** and the outer the **HFS**.

¹The concept was secret at this point, with the configuration only being shared with the international community in the 2nd Geneva Conference on Peaceful Uses of Atomic Energy in 1958 [7].

This magnetic configuration, supported by the early results of Soviet machines, was very well received in the international community, and by the 1970s was perceived almost universally as the way for energy production from controlled nuclear fusion.

Despite the progress in the last few decades being perhaps underwhelming due to the extreme technological challenges in the implementation of this vision, the tokamak remains the most feasible reactor design. Particularly so in Europe, where the fusion effort is committed to the ITER and DEMO projects, both using the tokamak concept and aiming at sustained D-T fusion with local tritium breeding and net energy output. In parallel, stellarator research is also supported, motivated in part by the good results in the last decades. This can be seen on the official roadmap of the European fusion research [8], illustrated in figure 1.5.

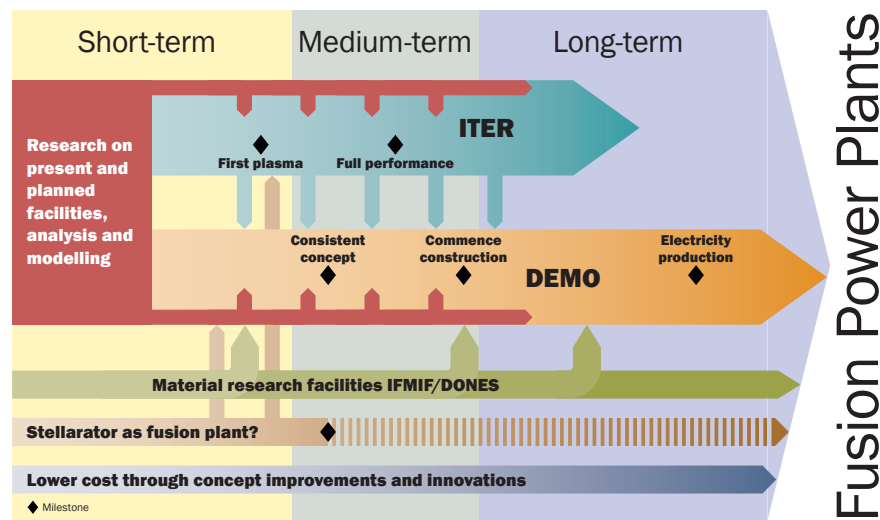


Figure 1.5: EUROfusion Roadmap phases and milestones. EUROfusion, figure reproduced from [9].

1.3 Motivation

“I venture to predict that a method will be found for liberating fusion energy in a controlled manner within the next two decades. When that happens the energy problems of the world will have been solved forever, for the fuel will be as plentiful as the heavy hydrogen in the oceans.” – Homi J. Bhabha, 1955, presiding the First International Conference on Peaceful Uses of Atomic Energy in Geneva

In the previous two sections, we saw how the concept of producing energy from nuclear fusion is known, and a clear path is established. Yet, fusion appears to be always 50 years away. This is partially due to the tremendous engineering challenges it entails.

Several scientific challenges were identified in the EUROfusion roadmap [8], of which we can highlight: (1) Demonstrate plasma regimes of operation that increase the success margin of ITER and satisfy the requirements of DEMO; (2) Demonstrate heat-exhaust systems capable of withstanding the large power loads in DEMO. These issues can only be addressed with complementary devices dedicated to pursuing these research goals. And in those, it is imperative to have good diagnostics, to ensure their operation at peak performance and gather clear and relevant measurements of the plasma parameters. Tokamak performance is an intricate optimization problem, formed by layers of systems that are inter-dependent and under continuous innovation.

This thesis concerns one of the innermost technical layers, the development of one of the most basic yet crucial diagnostic systems – magnetic diagnostic – on a new device that will support ITER operation and address DEMO (and power plant) physics and technological issues. In addition, by employing a technological solution – real-time numerical integration of magnetic signals – that is currently the state-of-the-art for devices with long discharges, the acquired knowledge and lessons

learned from the implementation on COMPASS-U will promote its development and adaptation to other devices.

While the magnetic diagnostic is just a small (yet important) piece of the overall device and its operation, this work approaches the topic in a lengthy and integral way: from the transduction to the data processing. For this reason, particular attention is given to the didactic component, making sure the lessons learned and, in particular, technical approaches and solutions can be used in the design of future systems.

1.4 Thesis Outline

This thesis is organized into 6 chapters, following a structured logic that closely parallels the magnetic diagnostic itself. That is, each chapter is dedicated to a specific component of the system, ascending from the physics and usage, the sensors themselves, the signal cabling and the data acquisition hardware.

Chapter 1 provides only the necessary introduction to nuclear fusion, and magnetic confinement in particular, aiming at contextualizing the work in the scientific field. This introduction purposefully omits technical detail or formulae, requiring no prior knowledge in the field of nuclear physics.

Chapter 2 introduces in length the magnetic diagnostic system. Due to its fundamental role for tokamak operation and plasma physics in general, key concepts are introduced as needed. This chapter should provide the necessary introduction and references for the understanding of the following chapters. Being organized in four sections, in the first, the physics and types of sensor are described; followed by the most common applications of the diagnostic system, the understanding of these is essential to properly design the diagnostic system. Section 2.3 provides an introduction to the data acquisition component, describing key concepts that are referenced in the work and discussing signal integration. Finally, section 2.4 provides the state of the art, on magnetic diagnostic system and its usages. With minimal specificity to the COMPASS-U, this chapter includes a review of the current status of magnetic diagnostic.

Chapter 3 delves with the sensor design and calibration. As sensor design is not universal, but rather constrained by the tokamak specifications and goals, COMPASS-U (3.1), the challenges for magnetic diagnostic design (3.2) and the architecture chosen (3.3) are introduced. The last two sections, both extensive, relate to the development and calibration of magnetic probes. In 3.4 the methods – two bespoke calibration setups – are described, that in 3.5 are used to optimize the development of the local sensors. Because this is an area of interest to all current and future devices equipped with magnetic sensors, the development of the calibration testbench is documented in length.

Chapter 4, is much shorter than the others. It explores the topic of sensor data transmission from sensors to data acquisition system (4.1), the cabling options available (4.2) and two tests performed in the laboratory. These are immunity to external magnetic noise and crosstalk, in section 4.3 and 4.4, respectively. Finally, conclusions are drawn towards cable selection (4.5).

Chapter 5 concerns the data acquisition system development. First as a concept (5.1) and preliminary qualification tests (5.2), then as a concept for COMPASS-U (5.3). Prototypes were developed (5.4) and tested (5.5). Finally, in 5.6, conclusions are drawn to the implementation and commissioning of the system for COMPASS-U.

Chapter 6 summarizes the achievements and conclusions towards the commissioning phase that now starts.

As the development of the diagnostic system is a complex undertaking, in the case of COMPASS-U tackled by a dedicated group of roughly five members. The thesis scope must be seen as only a part of that work, carried out by the author, and not a complete review of the design and commissioning of the system, as the title might otherwise suggest. For this reason, crucial design steps are only theoretically introduced, despite their development not being detailed in the document. These include, among others, the evaluation of the number of sensors needed and their positions, the integration of these sub-systems on the vacuum vessel and port distribution, the mechanical design of the sensors, and equilibrium reconstruction simulations.

2

Magnetic diagnostic

Contents

2.1 Principles of magnetic diagnostic	8
2.2 Applications of magnetic diagnostic	18
2.3 Data acquisition	27
2.4 Development of modern magnetic diagnostic systems	36

Due to being referred in the fusion community by many terms – magnetics, magnetic diagnostics, magnetics diagnostics, magnetic diagnostic, magnetics diagnostic – this dissertation will abide by the following rules in regards to the naming of the core subject of the thesis:

The magnetic diagnostic is a singular diagnostic the same way reflectrometry is a diagnostic regardless of how many positions, antennas, generators it possesses. In itself, it encompasses a set of magnetic sensors. The majority of which are inductive in nature, but not necessarily (Hall probes). Likewise, the ‘probe’ denomination is reserved those sensors which produce local measurements. Most are coils, provided the sensitive area is distributed over multiple turns, parallel across the axis of sensitivity. In the environment of a magnetic confinement device, special care has to be given to avoid confusion with coils that create and shape the magnetic fields and those which sense them. If dubious, the qualifiers diagnostic/sensing and power are used. When the context leaves no room for such confusion, the set of sensors (local or global, inductive or otherwise) can be referred as magnetics.

2.1 Principles of magnetic diagnostic

2.1.1 ‘The’ key diagnostic in tokamaks

It is common in tokamak experimental analysis, in particular those related to core plasma physics, to display prominently the plasma current. This measurement, by Rogowski coil, is simple, fast and reliable and gives a good proxy for the plasma performance and quality of the confinement. With this measurement one can evaluate how a certain process (intended or not) influences the plasma, resolved on a timescale much shorter than that of other diagnostics.

Beyond plasma current measurement, nuclear fusion devices rely on the magnetic diagnostic for some of the most essential measurements of the plasma – its shape, position, thermal energy and the strength and dynamics of the magnetic fields that confine the plasma. Beyond the global discharge parameters, magnetics can also probe into the local asymmetries and MagnetoHydroDynamic (MHD) instabilities as well as give us insight on the core and edge of the plasma alike.

With only a small number of diagnostics at its disposal, the first tokamaks made extensive use of magnetics to measure or estimate a number of plasma parameters [10]. Today, even with much more sophisticated and complete sets of diagnostics, the magnetic diagnostic is still one of the fundamental systems in tokamak research.

The magnetic diagnostic causes negligible perturbations on the plasma as it is external – only the fields outside the confined region are measured; and it is for the majority of cases (inductive sensors), passive, without energy input.

Magnetics are often classified as an ‘engineering diagnostic’ as beyond physics analysis, it is fundamental for the operation of the machine. Allied to a simple mechanical and electronic chain, the clear physical meaning of magnetics data makes it the go-to diagnostic for plasma position and shape control, as it provides latency-free data with near 100% availability and clear interpretation of the transduction process without requiring intensive signal processing.

The simplicity and accumulated experience [11, 12] in this diagnostic does not mean however that there are no open questions and active research on the topic. Beyond performance improvements, the main challenges on the development of magnetic diagnostics are: (i) long-pulse integration of signals, (ii) compatibility intense radiation environment; and (iii) high temperature compatibility.

2.1.2 Physical principle

Across all diagnostics one finds in fusion experiments, the magnetic diagnostic relies on the simplest physical working principle: electromagnetic induction. Faraday’s law of induction states that a conductive loop will gain an ElectroMotive Force (EMF) (ε) equal to the rate of change of the magnetic flux (Φ_B) it encloses. The flux represents the surface integral of a magnetic field (\mathbf{B}) crossing the enclosed area (S):

$$\Phi_B = \int_{\Sigma} \mathbf{B} \cdot d\mathbf{S} \quad , \quad (2.1)$$

and the sign is negative, as the direction of the current opposes that of the field that created it, in accordance to Lenz’s law:

$$\varepsilon = - \frac{d\Phi_B}{dt} \quad . \quad (2.2)$$

From this simple physical principle, three important considerations are immediately apparent: (i) the transduction part of magnetic sensors is trivial – the **EMF** at the ends of the conductive loop manifests itself as a difference of potential, measured as a voltage directly or as part of an electrical circuit; (ii) this voltage is proportional to the time derivative of the magnetic field, which can be obtained by integration of the signal; (iii) the spatial integral opens room for a wide range of applications and measurable quantities by simply defining the geometry of the sensor.

The majority of challenges in the design of magnetic diagnostics and, by extension, on this thesis can be traced back to one of these three points. The simplicity of the working principle leaves much hanging on the interpretation of the measurements. Adding one layer of complexity by introducing real-world assumptions to the previous equation, in a static sensor, where its shape does not change in time and has a defined effective area S_{eff} , Eq. (2.2) becomes:

$$V = -S_{eff} \frac{dB}{dt} . \quad (2.3)$$

The effective area will absorb in itself several linear parameters related to the geometry, such as number of turns and imprecision in manufacturing of the sensor. However, it does not include deviations or impressions in alignment or temperature related effects. That is, S_{eff} can be measured before installation of a sensor on its final location and at a given temperature. The magnetic field in (2.3) is also averaged over the entire S_{eff} .

2.1.3 Types of magnetic sensors

Numerous magnetic diagnostics can be devised by changing sensor shape and position. However, in the context of tokamak experiments, the well-defined plasma and experiment geometry that a key set of magnetics are usual (if not essential) across fusion experiments.

Figure 2.1 shows three of these sensors: Rogowski coil, diamagnetic loop, and magnetic probes (labeled as 'poloidal field coils' in the figure). To these, we must add 2 other that are not so easily represented in a poloidal cut of the plasma column: flux loops and saddle coils. Other more advanced or niche (non-inductive) magnetic sensors include: Hall probes, Faraday effect sensors and Motional Stark effect sensors.

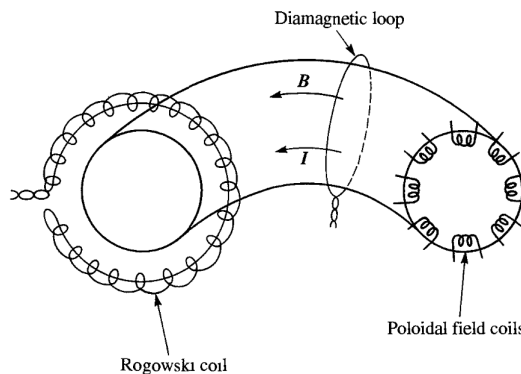


Figure 2.1: Illustration of three of the most widely used magnetic sensors in tokamaks [13].

The main functions of the different sensor types will be explained one by one. Table 2.1 summarizes in broad terms the main plasma parameters measured, as mentioned in the individual description. A more detailed view would have to be presented on a device level, as the exploitation of magnetics is machine dependent, beyond the broad strokes here presented. A similar table is presented in section 2.2, focusing on the applications rather than the measured quantities.

2.1.3.A Flux loops

If a single wire loop is run parallel to the plasma column in the toroidal direction, its effective area encompasses all the plasma, being sensitive to the poloidal flux (ψ) created by the current of the ring of plasma. The direct measurement of this loop is the toroidal **EMF** of the plasma, or the toroidal loop

Table 2.1: Types of magnetic sensors and main parameters obtained from the measurements, labeled as P if they are the primary method of measurement or S for supplementary. The supplementary category includes backup role, when a different sensor can more reliably provide that measurement or in case the measurements requires or provides data from or to complement other sensor.

	V_L	I_p	I_{VV}	B_P	B_{\perp}	B_T	β_{\perp}	l_i
Flux loop	P			P				
Rogowski		P	S					
Saddle loop				S	P			
Diamagnet						S	P	S
Probes		S	S	P	S	P		
IPR		S	S	S				
EPR			P					

voltage – for this reason, the sensor is sometimes called voltage loop. Having multiple voltage loops at different poloidal positions one can estimate not only the plasma EMF but also the voltage across passive structures, which is of importance in determining Vacuum Vessel (VV) eddy currents [14].

In terms of poloidal flux measurements, the measured flux corresponds to $\Phi = 2\pi\psi$, relative to the axis of symmetry. On tokamaks, this measurement will include the flux generated by the central solenoid or high permeability ($\mu_r \sim 2000 - 4000$) iron core for Ohmic heating of the plasma. This large contribution will be present on all flux loops and therefore can be removed by integrating the difference to a reference loop (typically midplane or enclosing the iron core), resulting in $\Phi = 2\pi(\psi - \psi_{ref})$ [12]. This is of particular interest when analogue integrators are used, as allows a better optimization of the input ranges of the electronics, which in turn allows an increase in the resolution.

Some devices can have dozens of flux loops, as the flux at different positions ($\phi(R, Z)$) is an important measurement for position control and equilibrium reconstruction (see section 2.2.1). Often ports or vessel-mounted auxiliary systems are in the way of the perfect full toroidal turns, and it is unavoidable to go around, bringing an extra complexity layer to the interpretation of the results or processing of the signals [15]. This challenge is particularly evident in figure 2.2, showing the path around the ports of some of the flux loops on TCV.

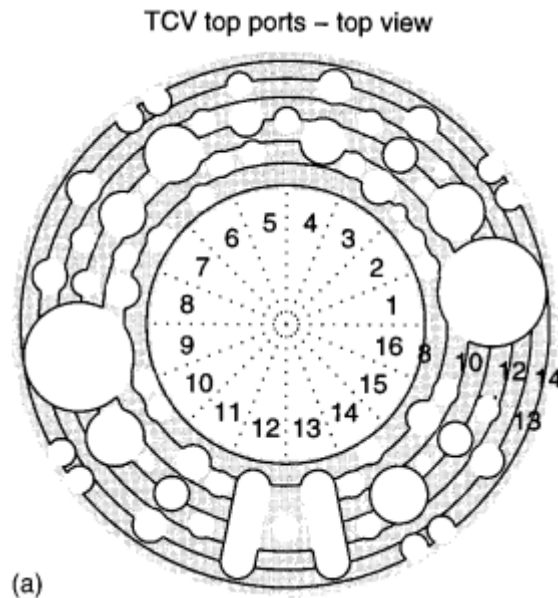


Figure 2.2: Arrangement of flux loops on TCV on a top view, navigating around the ports [15].

2.1.3.B Diamagnetic loops

Its geometry is one of the simplest – a loop around the plasma column, akin to the (poloidal) flux loop but on the poloidal plane, hence sometimes referred as toroidal flux loop. However, the transduction and interpretation of the measurements requires an understanding of the plasma equi-

librium. This loop can estimate of two important plasma parameters: its internal inductance (l_i , per unit length); and the plasma thermal energy (W) more often than not expressed by the poloidal beta (β_θ), the ratio of kinetic pressure to (poloidal) magnetic field pressure: $W = \frac{3}{8}\mu_0 R_0 \beta_\theta I^2$ [13].

Starting from the equilibrium equation:

$$\frac{(\nabla \times \mathbf{B}) \times \mathbf{B}}{\mu_0} = \nabla p \quad , \quad (2.4)$$

expanding and integrating both sides, we can obtain the following equations for an isotropic plasma, presented in an adimensional form:

$$3\beta_\theta + l_i - \mu_i = S_1 + S_2 \quad (2.5)$$

$$\beta_\theta + l_i + \mu_i = S_2 \frac{R_c}{R_0} \quad . \quad (2.6)$$

On the right-hand side of the equations, we find surface integrals of the field strength, the Shafranov integrals:

$$S_1 = \frac{1}{VB_a^2} \int B_P^2 \mathbf{r} \cdot d\mathbf{S} \quad (2.7)$$

$$S_2 = \frac{1}{VB_a^2} \int B_P^2 \mathbf{R}_0 \cdot d\mathbf{S} \quad , \quad (2.8)$$

S_1 and S_2 result from the decoupling in minor (\mathbf{r}) and major (\mathbf{R}_0) radii, respectively¹ [16]. The direction of the elementary surface $d\mathbf{S}$ normal is outwards. The equations are normalized to the plasma volume, V , and to the square of the edge poloidal field, B_a . This step entails a degree of arbitrariness and inconsistency among different sources, that can even be reflected in different values of β_θ [13].

Assuming a circular plasma, one can use $B_a^2 = \frac{\mu_0^2 I^2}{4\pi A}$ [13], however for elongated or D-shaped plasmas, the normalizations $B_a^2 = \frac{\mu_0^2 I^2}{l^2}$ [13, 17], that we shall follow, or $B_a^2 = \frac{\mu_0^2 I^2 R_0}{2V}$ [18] are common. These relate to the plasma poloidal area, A and its circumference, l . Furthermore, R_c is the current centroid:

$$R_c^2 = \frac{1}{\mu_0 I_p} \oint R^2 B_P ds \quad . \quad (2.9)$$

On the left-hand side of the equations (2.5) and (2.6), we find integrals over the plasma volume:

$$\beta_\theta = \frac{2\mu_0}{VB_a^2} \int p dV \quad (2.10)$$

$$l_i = \frac{1}{VB_a^2} \int B_P^2 dV \quad (2.11)$$

$$\mu_i = \frac{2\pi R_0}{V} \frac{2B_{T0}}{B_a^2} \Delta\phi \quad , \quad (2.12)$$

where μ_i is the plasma diamagnetic parameter, that depends on the toroidal field strength, B_{T0} in the absence of plasma and the diamagnetic flux, $\Delta\phi$, which is the difference between the poloidal flux with and without plasma:

$$\Delta\phi = - \int (B_T - B_{T0}) dS \quad . \quad (2.13)$$

Equations (2.5) and (2.6) can assume a more useful form if we consider their difference and sum, respectively:

$$\beta_\theta - \mu_i = \frac{1}{2}S_1 + \frac{1}{2}\left(1 - \frac{R_c}{R_0}\right)S_2 \quad (2.14)$$

$$\beta_\theta + \frac{l_i}{2} = \frac{1}{4}S_1 + \frac{1}{4}\left(1 + \frac{R_c}{R_0}\right)S_2 \quad . \quad (2.15)$$

In this form, these two equations decouple the inductance and diamagnetic flux information. These two betas are called the diamagnetic (β_{DIA}) and MHD (β_{MHD}) beta for equations (2.14) and (2.15),

¹A third integral S_3 , for the Z coordinate, that completes the set is omitted here.

respectively and are equal in an isotropic plasma. However, in anisotropic conditions, they are extended to [19, 20]:

$$\beta_{MHD} = \frac{1}{2}(\beta_{\theta\perp} + \beta_{\theta\parallel}) + \beta_{\phi} \quad (2.16)$$

$$\beta_{DIA} = \beta_{\theta\perp} \quad , \quad (2.17)$$

where $\beta_{\theta\perp}$, $\beta_{\theta\parallel}$ and β_{ϕ} are the components of poloidal beta associated with the perpendicular pressure, parallel pressure and toroidal flow.

Focusing on β_{DIA} , we can further introduce reasonable approximations for the specific case of tokamaks. In a stable plasma with position control and an optimized vessel, the centroid of the plasma will be close to the center of the chamber, therefore: $R_c/R_o \approx 1$. Also, assuming a torus, the Shafranov integral related to the minor radius will simplify to $S \approx 2$, with this factor coming from the integral ratio of r times the circumference by the area. Introducing the plasma shape as an ellipse (a, b), with area $A = \pi ab$ and circumference approximately given by $l \approx \pi(a + b)$, we can solve (2.14) for beta using (2.12) and the normalization $B_a^2 = \frac{\mu_0^2 I^2}{l^2}$ and the plasma elongation $\kappa = b/a$:

$$\beta_{DIA} = \beta_{\theta\perp} = 1 + \frac{(1 + \kappa)^2}{\kappa} \cdot \frac{2\pi B_{T0}}{(\mu_0 I)^2} \Delta\phi \quad . \quad (2.18)$$

This expression can be further simplified to its most common form, using $(1 + \kappa)^2 \approx 2(1 + \kappa^2)$ [12, 17, 19, 21]:

$$\beta_{DIA} = 1 + \frac{\kappa^2 + 1}{2\kappa} \cdot \frac{8\pi B_{T0}}{(\mu_0 I)^2} \Delta\phi \quad . \quad (2.19)$$

The elongation, plasma current and toroidal magnetic field can usually be assumed or measured by other diagnostics or as output of equilibrium reconstruction codes (that sometimes run in real-time). Therefore, to have a good estimate of the plasma poloidal beta and energy we just need to measure the diamagnetic flux, as in (2.13). The key challenge of this measurement is that the plasma toroidal flux is four orders of magnitude below that of the vacuum toroidal flux [22]. This means that one can not afford ‘percent’ errors in the processing. Two main coil configurations exist for this measurement – single and double loop (see figure 2.3). In this naming, we are considering the number of distinct loops encompassing the plasma, however, the single loop method still requires the subtraction of the vacuum component through other coils, referred as the compensation loop(s). The compensation loop can follow the diamagnetic loop, not encompassing the plasma [17, 23, 24] or rely on a combination of coils measuring the fields and currents on the Toroidal Field (TF) coils [22, 25].

On the other hand, in a two-loop configuration, as used in KSTAR [26], two parallel loops and homogeneously spaced in the radial direction fully encompass the plasma. Each will measure the diamagnetic flux plus a vacuum flux, dependent to their areas ($\Phi_{outer|inner}^0$). Therefore, being $k = \Phi_{outer}^0 / \Phi_{inner}^0$ the geometrical balance coefficient, the diamagnetic flux can be obtained as

$$\Delta\phi = \left(1 - \frac{1}{k}\right)^{-1} \left(\Phi_{inner} - \frac{\Phi_{outer}}{k}\right) \quad . \quad (2.20)$$

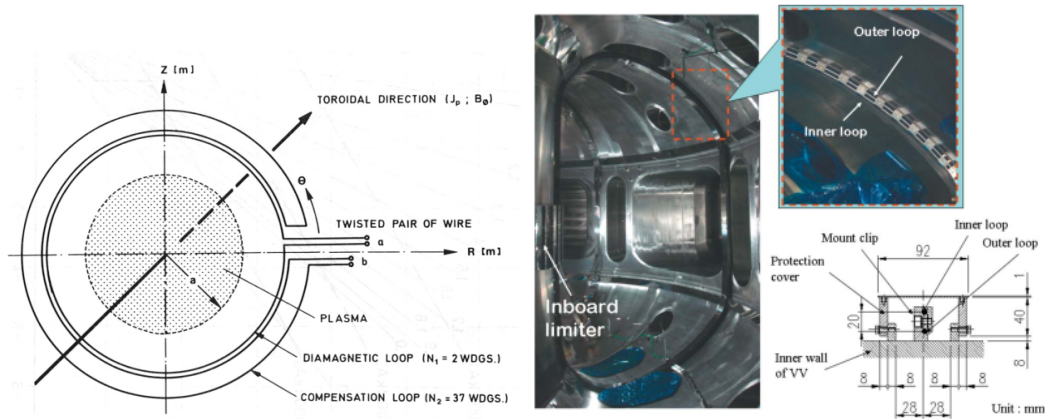


Figure 2.3: Two distinct diamagnetic flux measurements. Single loop, on the left-hand side, showing a single loop around the plasma column on ASDEX and a compensation loop [23]. Double loop, on the right-hand side, as installed on KSTAR, with two loops (inner and outer) encompassing the plasma [26].

2.1.3.C Rogowski coils

Plasma current is one of the most important plasma parameters, its precise measurement is achieved by a clever coil topology, see figure 2.4, named after the German physicist Walter Rogowski.

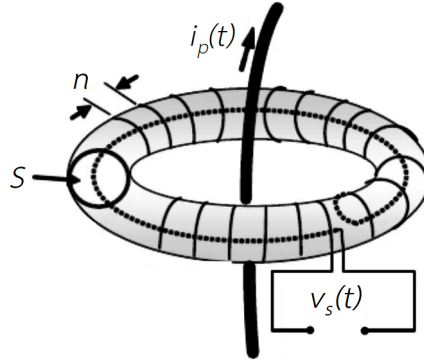


Figure 2.4: Topology of a Rogowski coil. Adapted from [27].

Ampère's law explains that the toroidal current will generate a magnetic field around, in the poloidal direction:

$$I = \frac{1}{\mu_0} \oint \mathbf{B} \cdot d\mathbf{l} \quad , \quad (2.21)$$

The projection of the helical structures (n revolutions per unit length) perpendicular to the poloidal direction (area S) seen in figure 2.1 will pick up this flux, i.e:

$$d\Phi = nS\mathbf{B} \cdot d\mathbf{l} \quad . \quad (2.22)$$

Likewise, the enclosed loop normal to the toroidal direction would pick up the toroidal magnetic field. To cancel this component, the wire that ends the helix structure is returned through the center of the helix. Having no contribution from the toroidal field, the current, given by Eq. (2.21), considering the integrated Eq. (2.22) and Eq. (2.3), is thus:

$$I = - \frac{\int V dt}{nS\mu_0} \quad . \quad (2.23)$$

It is important to note that the voltage does not depend on the length of the coil, only on the turn density, nor does it depend on the area of the main loop, only on the small helical loops. This is logical, as also Ampère's law is independent of the integral path, as long as it is closed and encompasses the current. This is the case for the complete (full poloidal coverage) as can be seen in Figure 2.1, however, due to space and assembly issues, some tokamaks implement, segmented (with small gaps not fully covered) or partial Rogowski coils (akin to poloidal magnetic probes). In these cases the plasma current is obtained by summation of the signal of the sensors and with interpolation to complete the full poloidal range [15]. An advantage of using partial Rogowski coils is that one can extract information about the current distribution on the \mathbf{VV} or other planar passive structures [12]. For a more accurate measurement of the \mathbf{VV} currents, it is possible to have a poloidal ring of Inner Partial Rogowski (IPR) and External Partial Rogowski (EPR), inside and outside the \mathbf{VV} , respectively, at the same toroidal position [21]. These coils can also be used as magnetic probes.

2.1.3.D Magnetic probes

"It is interesting to study the motion of a plasma column in a discharge vessel both to explain why it interacts with the wall and to determine the nature of its macroscopic state. If an electric current is flowing along a plasma column then one can obtain certain quantitative information about the motion of the column inside a discharge vessel by using magnetic probes to measure the field due to the current." – Sergei Mirnov [28].

Magnetic probes measure the change in local magnetic field close to the plasma boundary. These measurements were first proposed by Mirnov in their 1964 article², which the introduction is quoted

²Originally published in Russian in *Atomnaya Oievgrija* 17, 209 (1964)

in its entirety above. To say that the study of the motion of the plasma column is “interesting” is perhaps an understatement, in hindsight. Perhaps ironically, similar probes – often referred as Mirnov coils – would end up installed in abundance in each new tokamak and even included in the limited set of diagnostics envisioned for demonstrator reactor designs. Figure 2.5 shows as example the comparison of the two probe system installed by Mirnov on T-3 tokamak and an array of similar sensors on DIII-D tokamak.

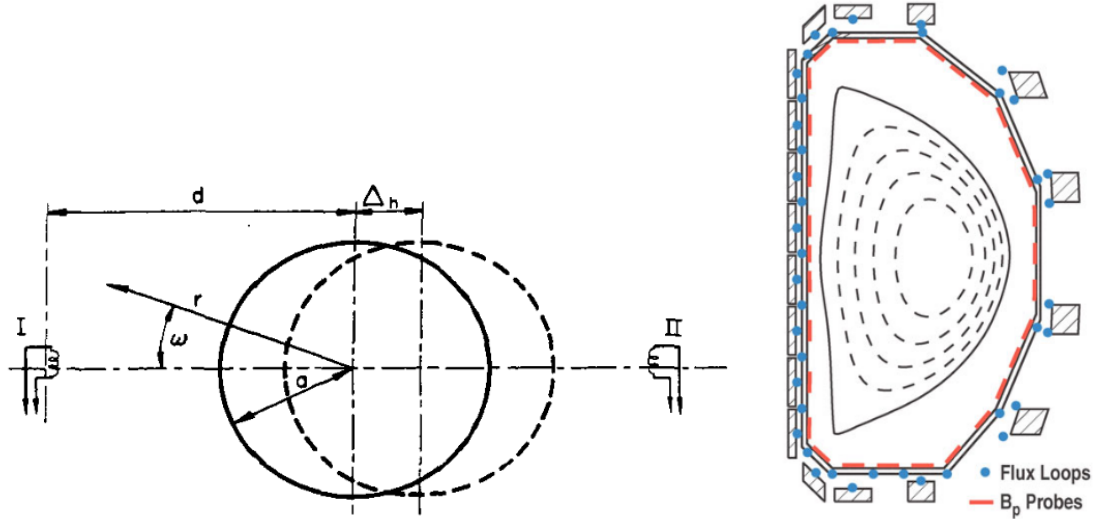


Figure 2.5: On the left-hand side, two poloidal field probes on T-3 tokamak [28]. On the right-hand side, poloidal array of similar probes (B_p , in red) on DIII-D tokamak [12]. Similar representations exist for the majority of tokamaks, as probes measuring poloidal field are part of the essential set of diagnostics.

Unlike previously mentioned magnetic sensors, the probes provide local measurements, as their dimensions are small compared to the plasma dimension. Typically, they are oriented to be sensitive to B_p , but depending on the orientation, they can be installed to provide local measurements of B_T or B_r or feature multiple windings in a single sensor, in which case referred as 2D or 3D.

The construction usually involves a wire wound around a mandrel, however there are several important factors to take into consideration. Often instead of circular, the sensor has a square, rectangular or a racetrack shape, making better use of the limited space available. One can increase the effective area of the sensor by increasing the number of turns and the area of each turn. A high number of turns will also increase quadratically its inductance, which can be problematic for measurements at higher frequencies. The parasitic and self capacitance of the sensor (C_p) will create a resonance with the self-inductance (L_p) at a frequency f_0 that can be estimated as

$$f_0 = \frac{1}{2\pi\sqrt{L_p C_p}} \quad (2.24)$$

This problem gets further complicated by the addition of cables that can have tens of meters or in some cases more than 100 m, adding capacitive components.

Depending on the harshness of each particular environment and space constraints, different materials are used. Instead of wound wire, as in Mirnov coils, it is also possible to use [Printed Circuit Board \(PCB\)](#)-like layered techniques, such as [Low-Temperature Co-fired Ceramic \(LTCC\)](#) [29, 30] or [Thick Printed Copper \(TPC\)](#) [31].

2.1.3.E Saddle loops

Saddle loops are usually mounted on the exterior of the **VV** on the outside, enclosing an area of its surface. They can also be installed on the surface of other structures, in or ex-vessel. Due to the curvature of the vessel, its 3D shape resembles a saddle, see figure 2.1, hence the name. On a ϕ, θ map (figure 2.6), these coils are rectangles, with sides along the toroidal and poloidal directions.

The measurement can have two interpretations, either as the average flux on the normal direction ($\Phi = S_{eff}(B_{\perp})$) or as a poloidal flux difference ($\Delta\psi$), between the positions of the two toroidal legs

of the rectangle: $\Phi = N\Delta\phi\Delta\psi$, where N is the number of turns and $\Delta\phi$ the toroidal span of the loop [12].

In some cases these sensors to cover the full surface of the VV , as in COMPASS (figure 2.6). This allows toroidal and poloidal mode number detection. Strategically placed saddle loops also allow the study of nonaxisymmetric fields caused by non-rotating MHD instabilities [32].

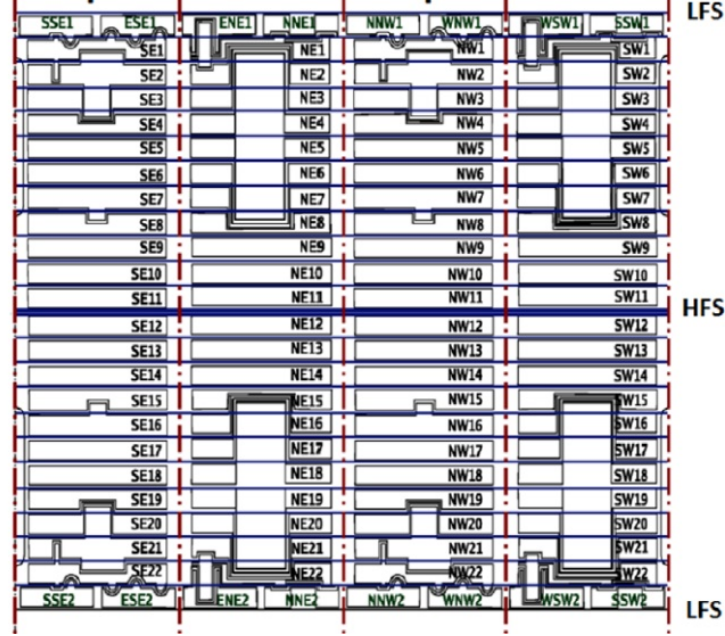


Figure 2.6: Map of compass saddle loops on COMPASS. Poloidal and toroidal directions on the vertical and horizontal axis, respectively. Labeling follows the cardinal directions. HFS and Low-Field Side (LFS) indicated for reference. It is visible how the saddle coils go around ports and other structures.

Apart from MHD activity, saddle loops are also a key source for equilibrium reconstruction and position (and shape) control algorithms. They can also be used in real-time feedback to control Resistive Wall Modes (RWM), as in RFX-mod [33].

2.1.3.F Hall probes

A non-inductive measurement of magnetic field can be obtained from the Hall effect. These sensors have two key differences to the other magnetic sensors: (i) its output is proportional to the field; (ii) they are active, requiring external energy.

When a current (I) flows in a conductor under a magnetic field (B), charged particles will be subject to an electromotive and Lorentz forces that cancel each other. A Hall voltage (V_H) appears perpendicular to the current and magnetic field directions, according to

$$V_H = \frac{IB}{ena} = R_H \frac{IB}{a} \quad , \quad (2.25)$$

where n is the charged particle density and a is the length of the material parallel to B . The material specific terms are absorbed in the Hall coefficient $R_B = (en)^{-1}$.

These sensors are usually very small (mm scale) and can be encapsulated in a 3D sensor providing a very localized measurement of all the field components. The key challenge with this sensor is the maximization of the Signal to Noise Ratio (SNR), since the measured voltages are very low. The Hall factor has a strong temperature dependence [34]. These factors make the measurement of MHD activity particularly challenging [35]. However, the fact that no integration is needed is of major relevance for devices which perform long pulses. The sensors were used for the real-time control of 2h discharges on TRIAM-1M [36] and will be installed on ITER (figure 2.7) [34].

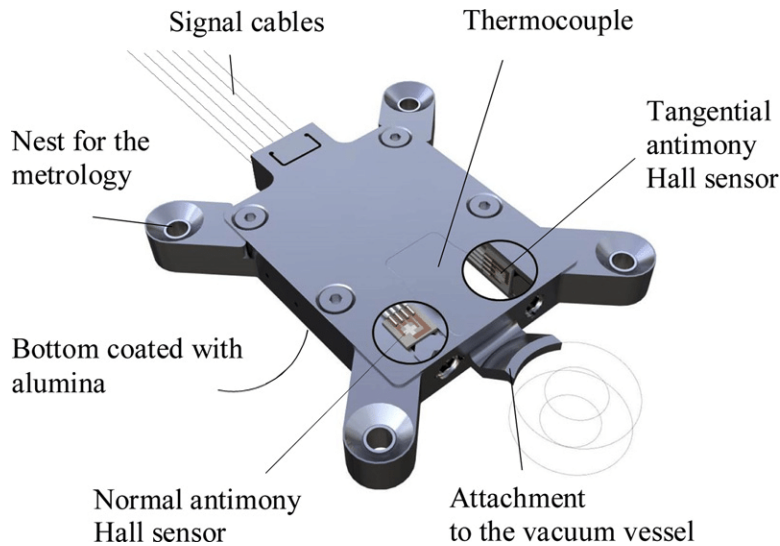


Figure 2.7: ITER-like Hall sensors unit, measuring two field components with integrated temperature measurement for Hall coefficient compensation [34].

A new sensor that combines Hall sensors and inductive TPC sensors is being explored as a diagnostic for long pulse measurements. The Hall sensor can be used to correct linear drift introduced by the integration of the TPC sensor signal. This would be able to provide steady-state local measurements with high bandwidth, ideal for reactor designs, where the number of individual diagnostics should be minimized.

2.1.3.G Fiber Optic Current Sensors

Perhaps in a gray zone regarding its classification as part of magnetic diagnostic, the **Fiber Optic Current Sensors (FOCSs)** are an alternative to Rogowski coils to measure plasma current, and therefore worth reference. The physical principle behind the FOCS is not induction but Faraday rotation. A linearly polarized light signal is run through an optical fiber encompassing a current. The magnetic field (B) along the light propagation path (l) will introduce a phase shift (ψ) given by

$$\psi = VBl \quad , \quad (2.26)$$

where V is the Verdet constant, that depends on the fiber and light properties. Integrating for the full fiber length of N turns, and introducing the Ampère theorem to relate to the current (I), we obtain

$$\psi = V \oint B dl = \mu_0 VNI \quad . \quad (2.27)$$

The technical implementation is beyond the scope of this thesis, but the main elements are visible in figure 2.8.

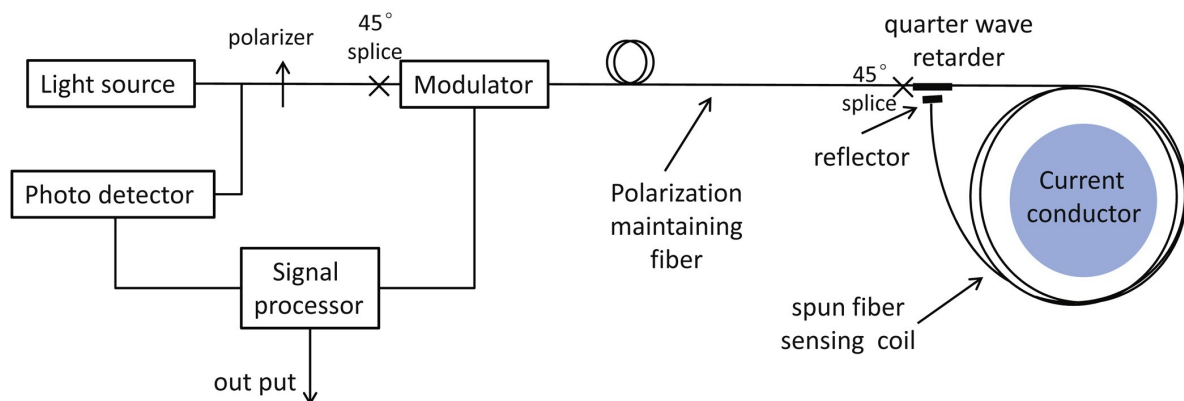


Figure 2.8: Scheme of a FOCS [37].

These sensors were implemented in Tore Supra Tokamak [38, 39] and more recently in EAST [37]. Once again, this solution is a promising way of overcoming the integrator drift problem for steady-state machines, providing slow plasma current measurements that might require more processing but, critically, no integration.

2.1.3.H Motional Stark effect sensor

Another diagnostic that is technically magnetic, whilst having completely different sensing principle is the **Motional Stark Effect (MSE)**. Unlike the inductive magnetics, that require minimal infrastructure and instrumentation, this diagnostic requires a neutral beam injected through the plasma (see figure 2.9).

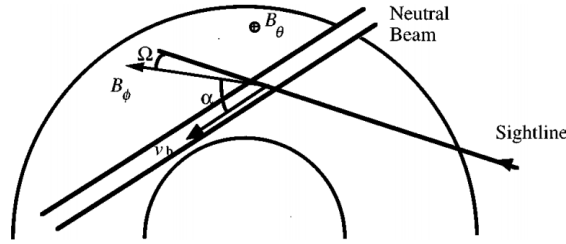


Figure 2.9: Scheme of the MSE diagnostic, showing the angles from the toroidal field to the neutral beam and to a sight line. [40].

The Lorentz electric field induced on atoms traveling in the magnetic field $E = v \times B$ will cause spectral line splitting and linear polarization of the light emitted [40]. The pitch angle

$$\gamma_p = \tan^{-1}(B_\theta/B_\phi) \quad , \quad (2.28)$$

that relates the local amplitudes of the poloidal and toroidal components of the field can be inferred from the relative amplitudes of the spectral lines [40, 41]. With this measurement, we obtain the profile of the safety factor

$$q(r) = \frac{r}{R \tan(\gamma_p)} \quad , \quad (2.29)$$

that is important in the theoretical modeling of plasma equilibrium, stability, and confinement [41].

This is something inductive magnetics can not provide – insight into the magnetic fields configuration inside the plasma. For this reason this diagnostic is complementary to the inductive magnetics, in particular for equilibrium reconstruction (see section 2.2.1).

2.2 Applications of magnetic diagnostic

The magnetic diagnostic is one of the more complete in tokamak exploitations. It is both an engineering and a physics diagnostic, as it provides crucial data for the safe operation of the device and at the same time sees extensive usage in plasma studies.

Understanding what is measured and how each sensor will be used is an important basis to the development of the hardware and electronics chain. The main usages can be roughly categorized as real-time control, plasma equilibrium reconstruction and MHD modes. The breakdown of which sensor are used for these categories is shown in table 2.2. These categories overlap, as some sensors are used for more than one of them. The adequacy of what sensor for each usage is an important part of development of magnetic diagnostic as a whole and sees continuous development during operation of the device.

Table 2.2: Summary of the usages of different magnetic sensors. For control, the control system is discriminated, for equilibrium reconstruction and MHD modes, Primary (P) or Supplementary (S) notation is used.

	Control	Eq. Reconstruction	MHD modes
Flux loop	Shape, position	P	
Rogowski	Plasma current	S	
Saddle loop		S	P
Diamagnet		S	
Probes	Shape, position	P	P
IPR	Position	S	S
EPR		S	

Beyond these three main topics, disruption studies is in itself a wide topic that extensively uses magnetic diagnostic. Specifically, the study of the currents and their propagation in the passive structures upon disruption [21, 42–44], the identification of disruption precursors in multi-diagnostic analysis [45–48], and the measurements of forces on the vessel and support structures in case of disruption [49].

These are examples of research topics that make extensive use of magnetic diagnostic and for which the magnetic diagnostic is critical. In the strictest definition, magnetic diagnostics application is even more spread due to providing some of the most elemental measurements, i.e. plasma current.

2.2.1 Equilibrium reconstruction

In a tokamak, the plasma can generally be considered to be in equilibrium. This equilibrium is ruled by the Grad-Shafranov equation, that generalizes the equilibrium equation,

$$\mathbf{j} \times \mathbf{B} = \nabla p \quad (2.30)$$

to an axisymmetric toroidal plasma, leaving two dimensions (R, Z) . By introducing generic functions of the poloidal flux (ψ) for the pressure $p(\psi)$ and toroidal field $F(\psi) = RB_T$, one can obtain the Grad-Shafranov equation,

$$\Delta^* \psi \equiv \frac{\partial^2 \psi}{\partial R^2} - \frac{1}{R} \frac{\partial \psi}{\partial R} + \frac{\partial^2 \psi}{\partial Z^2} = -\mu_0 R^2 \frac{dp}{d\psi} - F \frac{dF}{d\psi} \quad (2.31)$$

The deduction of this equation can be followed in [13] or as a guided exercise in [50]. We can see that this equation depends only on ψ and the knowledge of the $p(\psi)$ and $F(\psi)$ profiles (and derivatives). The magnetic measurements from poloidal field probes and flux loops (ψ) can be used to fit constrained polynomial expressions of the profiles [51].

When it comes to codes to execute this process, Equilibrium FITting (EFIT) [51] is the *defacto* standard in the tokamak community. Developed for operation in Doublet III tokamak (predecessor of DIII-D), over the course of the years EFIT was implemented in many other devices (see section 2.4.2) and was further developed into real-time (Real-Time EFIT (RT-EFIT) [52]) and parallel computing versions (Parallel EFIT (P-EFIT) [53]). In the majority of devices, however, equilibrium reconstruction codes are run in between discharges, as the information provided by the reconstruction helps operators and physicists alike have a clear picture of the discharge time evolution (see figure 2.10), and

eventually adjust parameters for the next discharges. Reconstructions with other parameters (higher order polynomials for instance) or constraints can be run for data analysis when execution time is not critical.

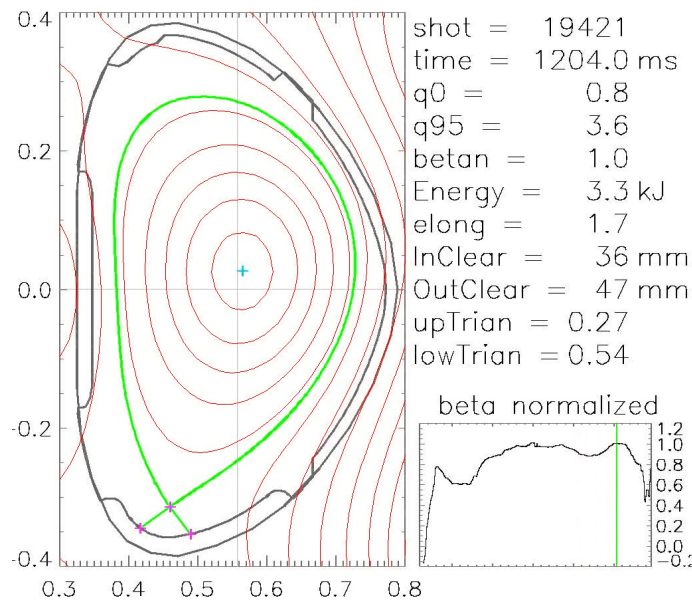


Figure 2.10: EFIT reconstruction on for the final discharge of COMPASS. Made available shortly after the discharge, it shows the temporal evolution of the magnetic equilibrium, though the isoflux lines (red), the current centroid (cyan) and the x- and strike-points (magenta). On the right-hand side, other parameters resultant from the reconstruction.

Beyond the flux loops that directly measure ψ , and probes that measure its spatial derivatives, additional magnetic sensors are or can be used. Saddle loops can provide differential ψ measurements, while plasma current and diamagnetic flux measurements can help constrain the profiles. The MSE diagnostic can provide additional constraints, by measuring the pitch angle of the magnetic field lines, the safety factor (q). This is an important measure to constrain $p(\psi)$ in devices equipped with such diagnostic [54–57]. Another important profile measurement source is the line integrated measurements from interferometry and polarimetry [54], Thomson scattering [58] or through Soft-X-Ray (SXR) tomography [59], among others.

Equilibrium reconstruction on magnetics does not demand a high bandwidth as reconstruction algorithms are run at ms cycles and require precisely the ‘equilibrium’ components of the signal, excluding all sorts of perturbations. However, as it depends on values of ψ it requires signal integration.

2.2.2 Real-time control

Why does a tokamak need control? In order to answer this question we need to understand how the plasma column behaves inside the vessel and what are the actuators we can use to interact with it.

Current is driven in the plasma as the secondary of transformer, the primary is usually called central solenoid as it sits on the inner part of the torus. The central solenoid drives the current while toroidal field coils around the poloidal cross-section generate the toroidal field. We now have a circular plasma in the center of the chamber. However, the surface area of the inside of the isobaric torus is smaller than the outside, which results in an outwards net force. The plasma will quickly drift towards the vessel. In early tokamaks this effect was counteracted by having a conductive vessel and/or outer shell. The eddy currents induced by the plasma on the passive structures will counteract the displacement, essentially balancing the outward force. On modern devices this effect is exploited by the metallic vessel and Passive Stabilizing Plate (PSP) but only slows down the diffusion of the plasma. In order to fully balance the outward force, a vertical magnetic field is imposed by ring coils above and below the plasma column, as can be seen in figure 2.11. The direction of the current must be opposite to that of the plasma current.

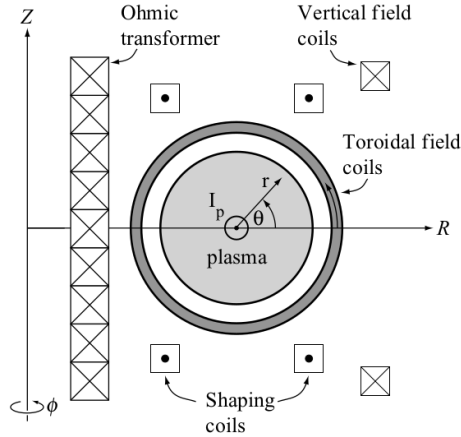


Figure 2.11: Cross-section of a generic tokamak with identification of the main active coils [50].

Figure 2.12 shows an example of these fields on a tokamak with circular cross-section – ISTTOK. We can see the magnetic field generated by the primary winding of the transformer, used to drive the current. In this aspect, ISTTOK is a peculiar circular device because the primary circuit sits on the outside. The implication is substantial and relevant for real-time control: we see that the vertical field lines are concave, i.e. the decay index [60]

$$n \equiv -\frac{R}{B_z} \frac{\partial B_z}{\partial R} \quad (2.32)$$

is marginally negative. In this configuration a small vertical displacement from the equilibrium position will be met with a force acting in the same direction, creating a positive feedback loop that needs to be controlled in real-time. As a result, on ISTTOK, the vertical field quadrupole and horizontal field dipole are controlled in real-time to balance the radial and vertical forces, respectively.

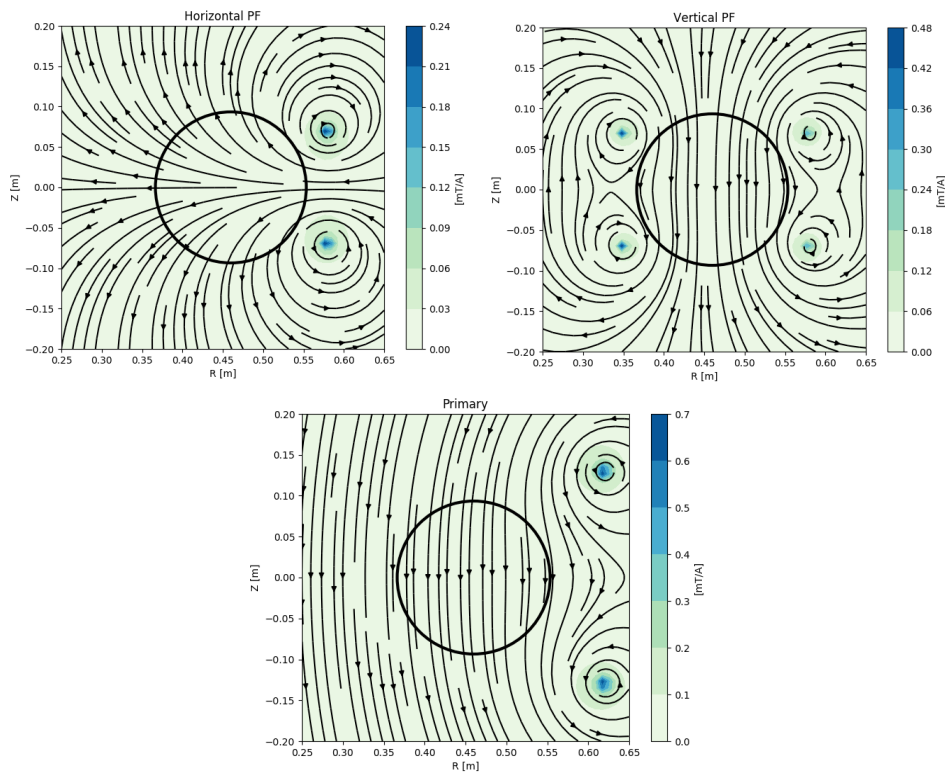


Figure 2.12: Illustration of the magnetic field generated by the three active coil circuits of ISTTOK labeled Horizontal and Vertical Poloidal Fields (PF) and Primary.

It was experimentally found that there is a limit on β for the plasma to be stable against MHD modes, both internal and external. This is the so called “Troyon limit” [50] and researchers quickly noticed that increasing the aspect ratio (a/R_0) or having non-circular plasmas will increase the critical β . In the majority of modern devices in the tokamak configuration, the plasma is D-shaped (see figure 2.13), with theory and experiment indicating enhanced stability at higher β for plasmas with some degree of elongation and outward pointing triangularity [50]. The D-shape is achieved with

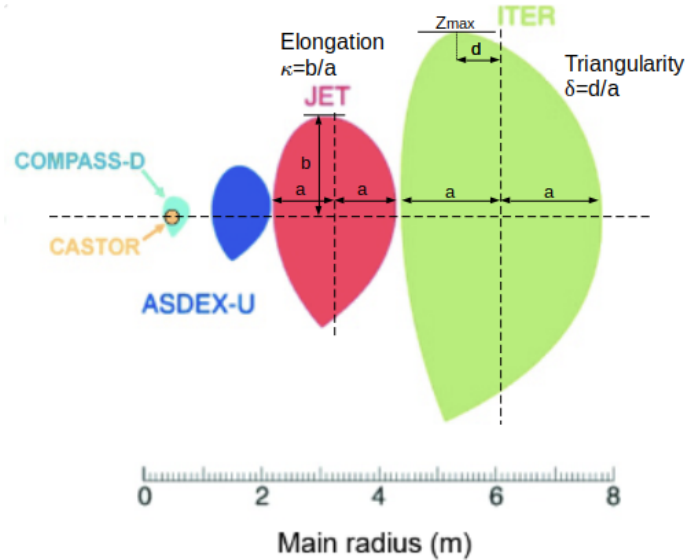


Figure 2.13: Cross-section of the plasma in tokamaks with different sizes. Illustration of the definition of elongation and triangularity.

so-called shaping coils (see figure 2.11). Unlike in the vertical field coils, the current on these coils has the same direction as the plasma current and therefore will “pull” the plasma column. This pull is larger the closer the plasma is. Likewise, the counteracting pull from the other coil is now smaller. This implies an elongated plasma is inherently vertically unstable and needs active control.

It is also important to realize that the procedure of a tokamak discharge, as beyond maintaining equilibrium, control is important to initiate and terminate the discharge. This process can be divided into four sequential stages:

1. *Breakdown.* The toroidal magnetic field is generated and the **VV** is filled with hydrogen gas. The gas is then ionized, forming the plasma.
2. *Ramp-up.* The plasma current is raised to the desired value. In order to prevent instabilities, the plasma is kept circular (limited) and the rise rate, linear or step-wise, is subject to methodical empirical experience for each device. It is also during this stage that the shaping of the plasma starts.
3. *Flat-top.* The core and typically the longest stage of the discharge. The plasma current is kept at the set-point and the scientific program for the pulse is carried out. The shaping of the plasma reaches its set-point and all macro-parameters of the plasma should remain constant, unless the objective of the pulse in particular states otherwise.
4. *Ramp-down.* Termination of the discharge, current and other major plasma parameters are safely driven to zero, preventing damage to the device. The opposite case is a disruption, whereby plasma confinement is uncontrollably lost (during any of the previous phases) and there is no ramp-down.

The boundaries between these stages are sometimes not clear. In particular, whether the plasma should be shaped before or after current is ramped-up to its set-point. Ramping the current too fast tends to cause mode-locking and lead to disruptions. Shaping the plasma while still ramping up the current prevents this [61].

Taking as example the D-shaped COMPASS tokamak discharge sequence, in figure 2.14 we can observe the effects of the current in the power coils on the plasma magnetic measurements – plasma

current, loop voltage and equilibrium. Breakdown is induced and current rises sharply due to the positive slope of the current produced by the [Magnetizing Field Power Supply \(MFPS\)](#). This can be observed by the sudden jump in loop voltage. The plasma is initially limited by the [LFS](#) limiter, but quickly the [Equilibrium Field Power Supply \(EFPS\)](#) current increases and pushes the plasma to the [HFS](#). With the action of the [Shaping Field Power Supply \(SFPS\)](#) the plasma is shaped from circular to elongated, still limited at the [LFS](#). The current has an overshoot as it was empirically found out that a short period ($\leq 5\text{ms}$) of stable current in [MFPS](#) helps prevent disruptions and consequently lowers the plasma current. At this stage the plasma starts being limited at the divertor and with additional shaping field the x-point is formed.

With the plasma shaped, during the flat-top, I_p is then kept constant by active feedback control. The plasma position is also kept at a set-point, through different power supplies with faster response for B_{radial} and $B_{vertical}$. The discharge is ideally terminated by reverting from diverted to limited circular plasma (soft-landing) while I_p is lowered gradually.

On COMPASS the described operation is mostly preset³, with the flat-top vertical and horizontal position being controlled through fast amplifiers, running [Proportional-Integral-Differential \(PID\)](#) controllers at $50\ \mu\text{s}$ cycles [62].

³The same applies to the omitted Toroidal Field Power Supply (TFPS), omitted.

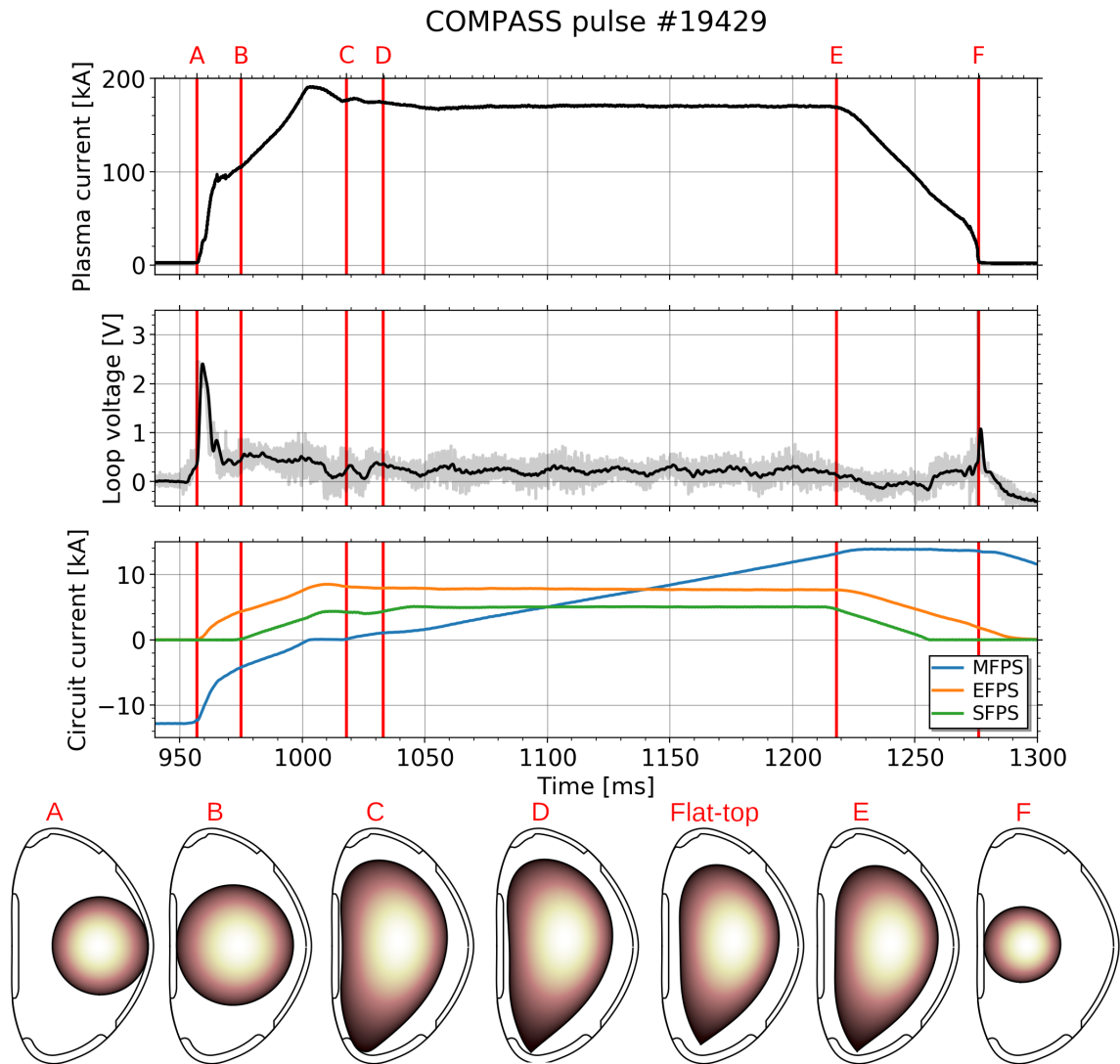


Figure 2.14: Identification of the discharge stages and key events on a compass diverted pulse (#19429). A: Breakdown; B: Shaping start; C: Limiter jump; D: X-point formation; Flat-top; E: Soft-landing; F: Plasma termination. From top to bottom, the first plot shows the measurement of plasma current through integrated Rogowski coil signal. The second shows the loop voltage, with a filtered trace, and the third the measurement of the currents on the main power supplies that control the active coils: Magnetizing, Equilibrium and Shaping Field Power Supplies, MFPS, EFPS, SFPS, respectively. Below, the EFIT equilibrium reconstruction showing the ψ distribution inside the Last Closed Field Surface (LCFS).

We are now in a position of assessing the main controllers present in tokamaks and their demands on the magnetic diagnostic. Figure 2.15 shows a schematic of a generic tokamak magnetic control system. In it, we can identify some key parameters to be controlled already discussed: vertical position, plasma current and shape.

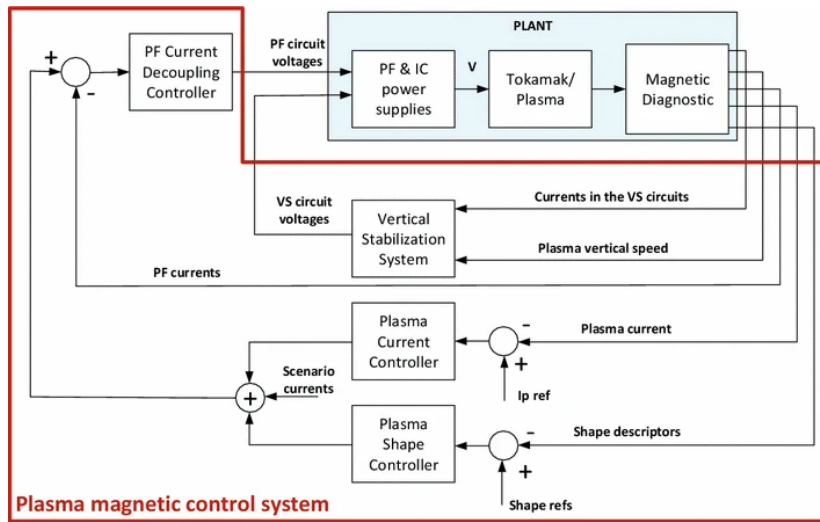


Figure 2.15: Diagram of the implementation of a generic control system for a tokamak. In the scheme the plant system is identified with actuators and sensors and the main control loops explicit. Figure gathered from [63].

For plasma current measurement, Rogowski coils are typically used – either full, partial, or segmented. Both probes and flux loops can detect the displacement of the plasma column for plasma position determination. The combination of the sensor used, regarding its position is very important, i.e. different combinations of sensors at key positions can be more sensitive to vertical or horizontal displacements.

For plasma shape, the sensor requirements are similar to equilibrium reconstruction (see section 2.2.1), albeit with the same consideration that instead of using all available signals, a combination of sensors in key positions is used.

On the vertical stability controller, the frequency response of the signal must also be taken into account, as delays introduced anywhere in the loop reduce the control parameter space. For this reason, a selection of sensors with faster response can be chosen, in detriment of a more accurate sensor combination. This is also the reason behind the usage of in-vessel power coils. Since the field does not need to penetrate the conductive VV a faster actuation is generated, while ex-vessel coils help reduce the current in the in-vessel circuit [63].

2.2.3 MHD modes

Various types of instabilities can disturb the equilibrium of a magnetically confined plasma. These can typically be described by perturbed MHD equations, hence referred as ‘MHD modes’. The uncontrolled growth of these perturbations is one of the main causes that leads to loss of confinement. Some limits can be theoretically established, but many of the disruption inducing instabilities are a result to minor error fields or magnetic field inhomogeneities. A detailed understanding of the physical phenomena behind each of the instabilities is provided in [13] and [50] and will not be reproduced here. Moreover, the progress in this area, has been summarized by the [International Tokamak Physics Activity \(ITPA\)](#) group on MHD stability, operational limits and disruptions [64].

Identification and study of the formation, growth and mitigation of these modes brings a greater understanding of the operational limits and is in some cases instrumental to the take full advantage of a devices capabilities.

Other diagnostics are also used for MHD mode studies. However, the simplicity, low cost, and high sensitivity to dynamic plasma features magnetics offers places it in an advantageous position for these studies. Despite being a diagnostic external to the plasma, the magnetic diagnostic can identify, determine the frequency and provide semi-quantitative information on the amplitude of the modes [12].

Most of the sensors described in section 2.1.3 offer some useful information towards MHD studies. Notwithstanding, ex-vessel mounted sensors will provide information only on the slowest modes, due to the shielding by the eddy currents on the conductive VV. Among the in-vessel sensors, probes (usually referred as Mirnov coils, see section 2.1.3.D) have key features that make them obvious choices – high frequency response, adequate effective area, and ability to form arrays due to their ‘point-like’ dimensions. Among magnetic probes, if only a limited set can be installed, those sensitive to poloidal magnetic field are the most useful. In general the perturbations are perpendicular to the equilibrium magnetic field, in the radial direction, compressing or expanding the poloidal field lines, and making the poloidal component of the flux the strongest.

Modes exhibit a periodic structure, with a given wavelength. In tokamaks, due to the axisymmetry in the toroidal direction, it is more usual to consider the toroidal mode number n , as the structure tends to be harmonic in this direction. Similarly, in the poloidal direction we can also consider the poloidal mode number m . This number is however more difficult to identify and interpret, as the wavelength can change over the poloidal angle θ due to the lack of symmetry with respect to θ .

The identification of the mode numbers is often done with arrays of magnetic probes in the respective direction. The separation between sensors determines the maximum mode number that can be resolved without aliasing. Follows from the Nyquist criterion that:

$$|n| < \frac{2\pi}{2 \cdot \Delta\phi}, \quad n \in \mathbb{Z} \quad . \quad (2.33)$$

This is equivalent for m and $\Delta\theta$, and the direction of the rotation (counter-clockwise or clockwise) dictates the sign of the mode.

The identification of the perturbations in the plasma according to their mode numbers is an important aspect of the operation of the device, as it leads to optimization of futures discharges. Likewise, the study of the propagation of these instabilities in the plasma also push our understanding of magnetically confined plasmas. This can be achieved by studying the natural plasma modes or by active MHD spectroscopy – inducing magnetic perturbations to excite some modes [65].

Physically, the perturbation can arise from very distinct processes (compression of magnetic field lines, differences in curvature and bending, etc. or kinetic effects). However, their detection with magnetic diagnostic usually comes down to a handful of techniques.

Slow perturbations, such as RWM, external kinks, tearing modes, can be detected with ex-vessel sensors or in-vessel sensors with low frequency response – either due to large area, and consequently large inductance or due to local shielding of the magnetic fields by conductive structures. In general, these perturbations tend to have low toroidal mode numbers ($n \leq 3$) [12] and are the most dangerous to the magnetic equilibrium.

On the other end of the spectrum are Alfvénic eigenmodes, that appear at hundreds of kHz range. Figure 2.16b shows a power spectrum of a magnetic probe at JET where Toroidal Alfvén Eigenmode (TAE) have been identified, as published in [66]. The detection of these modes requires fast sensors and Data Acquisition System (DAS). These also need to be well calibrated as the sensitivity must be the same (or at least know) across the full bandwidth of the measurements. It is not uncommon for devices to have dedicated sensors or even DAS to detect and study these high-frequency modes [67].

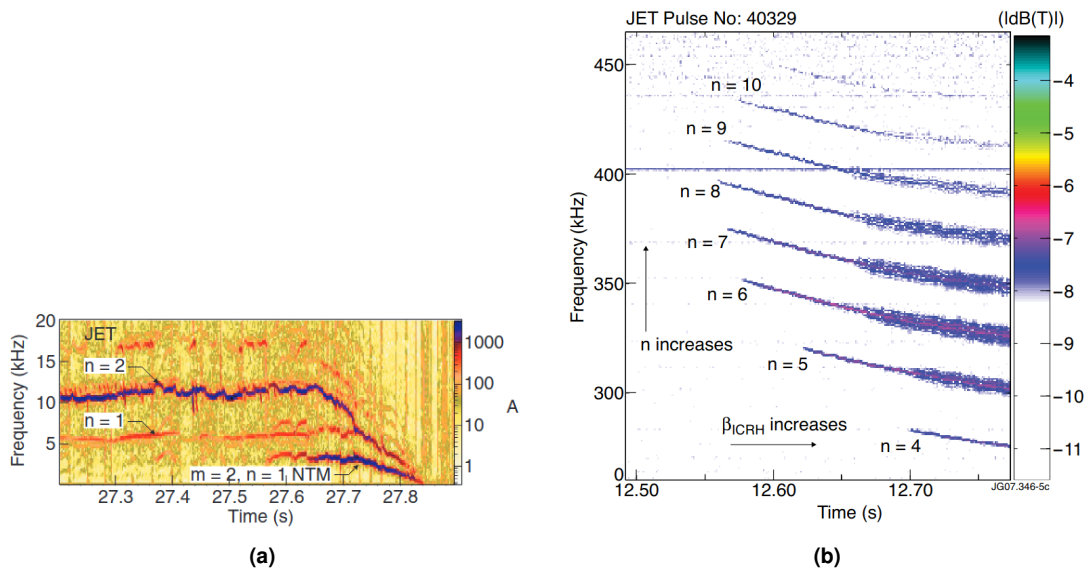


Figure 2.16: a) Spectrogram magnetic signal on JET pulse #50694. This experiment aimed at studying the Neoclassical Tearing Mode (NTM). Figure gathered in [68]. b) Spectrogram of a fast Mirnov coil for JET pulse #40329 showing the effect of increased Ion-Cyclotron Resonance Heating (ICRH) power on Alfvén instabilities. Figure gathered from [66].

A key distinction is whether a perturbation is rotating or not. Detection of rotating modes can rely on the analysis of sensor time traces and Fourier analysis of the signals. The rotation of these modes will be expressed by a characteristic frequency in the signal. This frequency is not always constant, but can chirp or slowly evolve.

For non-rotating modes, however, a sensors signal might not change substantially in time, but correlate strongly with nearby sensors. Correlation, coherence, space-domain Fourier analysis, Singular Value Decomposition (SVD) [69] or wavelet decomposition [70] are good tools to study these modes.

Figure 2.17 shows a simple example of the determination of the rotation speed and mode number ($m = 2$) on ISTTOK by correlation and coherence. Because it is a large aspect ratio circular tokamak, essential symmetric in θ , the mode is easily identifiable analytically. Beyond the analytical determinations, on the correlation plot it is also clearly visible that there are two maxima on a poloidal turn, hence $m = 2$.

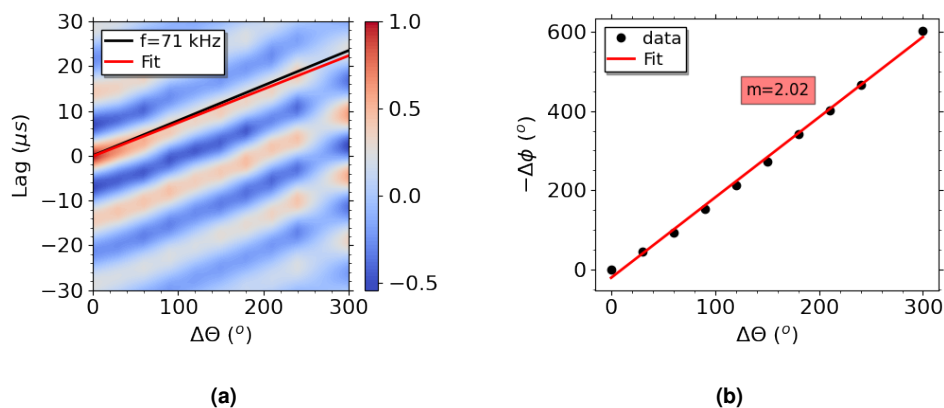


Figure 2.17: Study of a $m=2$ mode on ISTTOK discharge #36133. a) Poloidal mapping of the correlation of signals of a poloidal array of magnetic probes. Fit across the maxima in red ($13.7^\circ/\mu\text{s}$) and frequency determined by Welch method in black. b) Coherence phase for the same signals with a linear fit determining $m=2$.

Due to the large number of studies that can be conducted by measuring MHD modes with the magnetic diagnostic, the planning, development and installation of magnetic sensors must account this need. Poloidal and toroidal arrays of probes, at which positions and directions; what is the interest bandwidth and how sensitive should the sensors be are important issues to address.

2.3 Data acquisition

Data Acquisition (DAQ) is a key element of any diagnostic. Section 2.1 delved into the transduction part of magnetic diagnostic. On the opposite end, section 2.2 explained the need and usages of the data. This section will fill the gap in between, the stages the signal passes from transduction to usage by other systems: the limitations of sensors, the transmission of the signal, conditioning, digitization and processing. In short, data acquisition converts, signal into data.

In the particular case of the magnetic diagnostic, with a relatively simple and passive sensor, the key topic in **DAQ** is the integration of the signal. Not all magnetic signals need integration. As seen on previous sections, loop voltage, **MHD** mode detection, or controllers that are sensitive to the dynamics of the field are applications that directly use the signal proportional to dB/dt . Even a smaller number of applications needs the integration to be made in real-time. However, the ones that do are some of the most important measurements. Conversely, the signals that do not need integration have stricter requirements on the **DAQ** due to their high frequency components with proportionally higher amplitudes.

2.3.1 Key concepts of data acquisition

2.3.1.A Filtering

Filters are a complex and extensive topic with much published literature [71, 72]. However, as a recurrent topic in this work, the minimum necessary for the full understanding of the work carried out is introduced here.

The key concept of the filter is to limit the bandwidth of a signal. This can be advantageous when one wants to make evident or analyze only some frequency components of the signal's spectrum, reject noise on signal-free frequencies or isolate the signal from an intentionally modified spectrum (i.e. demodulating).

There are two elementary types of filter: **Low-Pass (LP)** – that keep the low frequencies and rejects high frequencies; and **High-Pass (HP)** that achieves the opposite. The first order combination of these two is also common: band-pass and band-stop. Some extremes are also noteworthy: a notch filter rejects just one specific frequency (extreme band-stop); an all-pass filter does not change the amplitude at any frequency but does modify the phase.

There are other planes by which filters can be categorized. They can be analog (electronic, mechanical) or digital depending on how they are implemented. Analog filters generally work in continuous time⁴ and can be active or passive if power is added to the system or not. Digital filters use a discrete time domain and can be **Infinite Impulse Response (IIR)** or **Finite Impulse Response (FIR)**. An example of the former is the digital implementation of an analog linear filter (e.g. Butterworth); and of the latter a running mean. Filters need not be linear, if the output is not a linear function of the input, such as in a running median or 'max-min' (digital) or an analog filter that clips high voltages with diodes. Filters made with passive components or linear amplifiers are generally linear. Another key characteristic of filters is its causality: in causal filters the output for a given time depends only on the current and past inputs. This is the case on analog filters as they represent physical systems and time only runs forward. Nevertheless, a digital filter need not be causal, as in the case of a running mean, taking the current, previous and subsequent samples. Likewise, in the digital domain we can revert the direction of time, applying a filter 'backwards', which is a technique to minimize phase distortion.

For continuous time, a **Linear Time Invariant (LTI)** filter is defined by a transfer function that is the ratio between the output and the input in Laplace space:

$$H(s) = \frac{Y(s)}{X(s)} = \frac{\mathcal{L}y(t)}{\mathcal{L}x(t)} \quad ,$$

being $s = j\omega$ the Laplace domain complex frequency⁵. The maximum order of the polynomials in s on the transfer function of a filter dictates its order ($m = 1, 2, \dots$). A first order **LP** filter has the transfer function:

$$H(s) = \frac{g_{DC}}{1 + s/\omega_c} \quad , \quad (2.34)$$

⁴Filters based on switched capacitors are discrete-time filters, as an exception.

⁵Generally, the Laplace frequency domain parameter is $s = \sigma + j\omega$, having a real component. Using $s = j\omega$ restricts the s-plane to the imaginary axis resulting in a formal agreement with Fourier transform

with a given DC gain (g_{DC}) and cutoff frequency ($\omega_c = 2\pi f_c$). Increasing the order to $m = 2$, a low pass filter can be re-written as:

$$H(s) = \frac{g_{DC}}{1 + p_1s + p_2s^2} = \frac{g_{DC}}{1 + s/(Q\omega_0) + s^2/\omega_0^2} \quad (2.35)$$

While the filter can be defined in a pure polynomial form (p_1, p_2), on the denominator for LP, it is convenient to evidence the natural frequency ω_0 and the quality factor Q as these have physical meaning.

As a complex function, the frequency response of a filter is commonly represented and measured in the form of plots of the magnitude (or gain) in dB and phase over the frequency (angular or not, in logarithmic scale). For the magnitude:

$$20\log_{10}|H| = 20\log_{10}\sqrt{H \cdot H^*} \quad ,$$

and for the phase:

$$\angle H = \arg(H) = \text{atan2}(\text{Im}(H), \text{Re}(H)) \quad ,$$

where atan2 is the two-argument arctangent function, that is equal to $\arctan\left(\frac{\text{Im}(H)}{\text{Re}(H)}\right)$ for positive real part and antipodal for negative real part. This representation is visible in figure 2.18 and is sometimes called *Bode plot*, but in a strict sense the Bode plot is only the straight-lines approximation of the transfer function. In this plot we can identify key features of filters. The first concerns the identification of the passing band. A natural point used is the ‘-3 dB’ frequency, that is extensively used in electronics. At this point, the power on the output is reduced to half, or in amplitude, to $\sqrt{\frac{1}{2}} \approx 0.707 \approx -3.01$ dB. For a first order filter this value corresponds to f_c and is dubbed the ‘corner’ or ‘cut-off’ frequency. However, some care must be taken, as this is not necessarily the ideal point for specification of bandwidth, being the output only 70% of the input, with the phase dropping considerably (see phase transfer functions in figure 2.18).

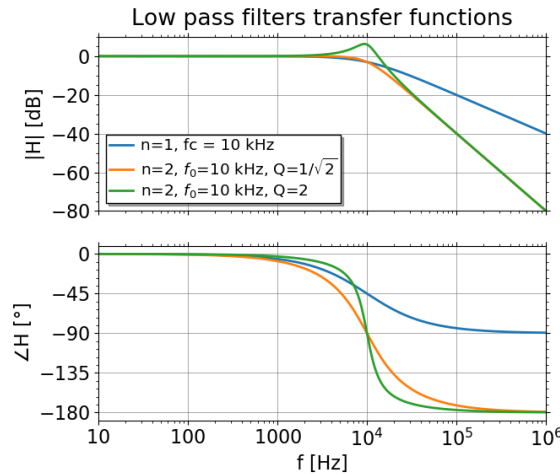


Figure 2.18: Transfer function of three low-pass filters corner frequency of 10 kHz.

This plot illustrates the constant roll-off of a filter that is dependent on its order: $-20 \times n$ dB per decade or $-6 \times n$ dB per octave. On the phase plot, we observe the $\pi/2$ and π phase shifts. One particularly relevant consequence is that for $f \gg f_c$ (deep in the reject band) the first order LP filter behaves like an integrator:

$$H(s) = \frac{1}{s} \quad , \quad (2.36)$$

with phase quadrature (90°) and exponentially decaying amplitude.

For filters of second order and above, the amplitude transfer function is not necessarily decrease monotonously, with resonances possible (see figure 2.18, in green). This is controlled by the dimensionless quality factor. This parameter, common to many oscillating or resonant physical systems, is

associated with the stored energy. On resonant systems as the filter is, Q can be understood as the frequency-to-bandwidth ratio:

$$Q = \frac{f_r}{\Delta f} \quad , \quad (2.37)$$

relating the resonant frequency and the resonance width, given by the **Full Width at Half maximum (FWHM)**. High Q means high, sharp resonances as Q is inversely proportional to the damping ratio $\zeta = (2Q)^{-1}$. The damping can be better observed not on the frequency domain but rather on the time domain, such as in the step response in figure 2.19. The step response is another useful visualization and measurement of filters, as it is easy to recreate – the response to a step transition – and provides useful time-domain measurements, such as the settling time, exponential τ and natural frequency.

Systems with $Q = 1/2$ are critically damped, while those with $Q > 1/2$ have a high quality factor and are underdamped. That is the case of the two-second order filters in figures 2.18 and 2.19. The orange trace is a second order Butterworth filter, that has the flattest passband possible for continuous time filters [73], achieved with $Q = 1/\sqrt{2}$.

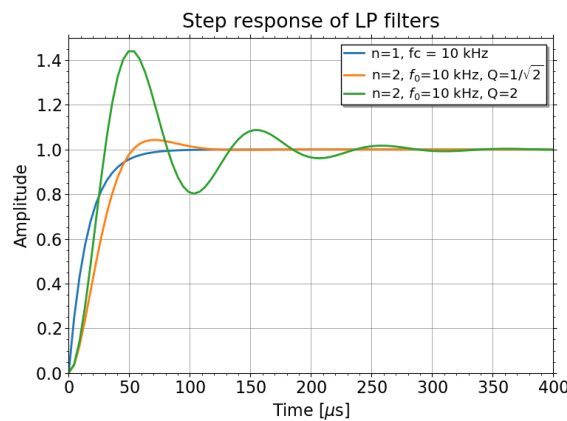


Figure 2.19: Step response of three low-pass filters corner frequency of 10 kHz.

2.3.1.B Dynamic range and oversampling

The dynamic range is the ratio between the highest and lowest possible values for a given system. For an ADC, the full-scale is given by the number of bits n , and the quantization error of 1 code usually marks the noise floor:

$$DR_{ADC} = 20 \log_{10} \left(\frac{2^n}{1} \right) = 6.02n \text{ dB} \quad . \quad (2.38)$$

The dynamic range can be increased by oversampling.

Often considered only on the realm of image processing, the dithering effect is also of importance in acquisition and processing of 1D data. Noise is generally an undesirable component, present in any real-life dataset or acquired signal. This undesirability is in fact the very definition used to distinguish it from signal. However, when a signal is sampled, either from an analogue source or due to re-sampling of a digital signal, noise can sometimes be beneficial. If we consider a constant signal, with a real value, say $s = 2.5$ which is sampled as an integer, the resulting sampling $x = S(s)$ will always output $x = 2$, independently of how many times it is measured. If a zero mean random noise e is added, and if the distribution is wide enough, the result of $y = S(x + e)$ is no longer necessarily 2, from sampling to sampling 1s or 3s, maybe 0s or 4s will appear, entirely depending on the distribution of e . But since $\langle e \rangle = 0$, $\langle y \rangle \rightarrow 2.5$, reaching a value that is beyond the sampling resolution. This is generally called oversampling, and is a useful technique if the timescale of the signal is much longer than the sampling time. In order to oversample a signal by a factor N , it should be sampled at N times the Nyquist rate which is twice the bandwidth of the signal, define by the highest frequency of interest,

$$f_s = NB \quad . \quad (2.39)$$

For each of the ADC codes, the oversampled signal can assume N values. Therefore, the dynamic range is increased by N , while the uncorrelated noise summation amounts to \sqrt{N} , resulting in a

net SNR increase by \sqrt{N} . With increasingly easy to implement **Digital Signal Processing (DSP)** and faster ADC and driving electronics, oversampling sees widespread implementation in **DAS**. Pushing the sampling (and Nyquist) frequencies to higher values, gives more room to design an analog anti-aliasing filter, while digitally the data can be easily filtered and downsampled back to the specified sampling rate.

But the applications of oversampling go beyond the application of expected value (mean), most relevantly, on integration this principle is also valid. Figure 2.20 shows how a signal below the nominal resolution of the ADC can be recovered after sampled and digitally integrated if there is sufficient dithering (incoherent) noise. If there are none or too little noise, not enough ADC codes are swept. However, the cumulative effect of noise integration leads also to significant distortion, even if the signal is indeed detected.

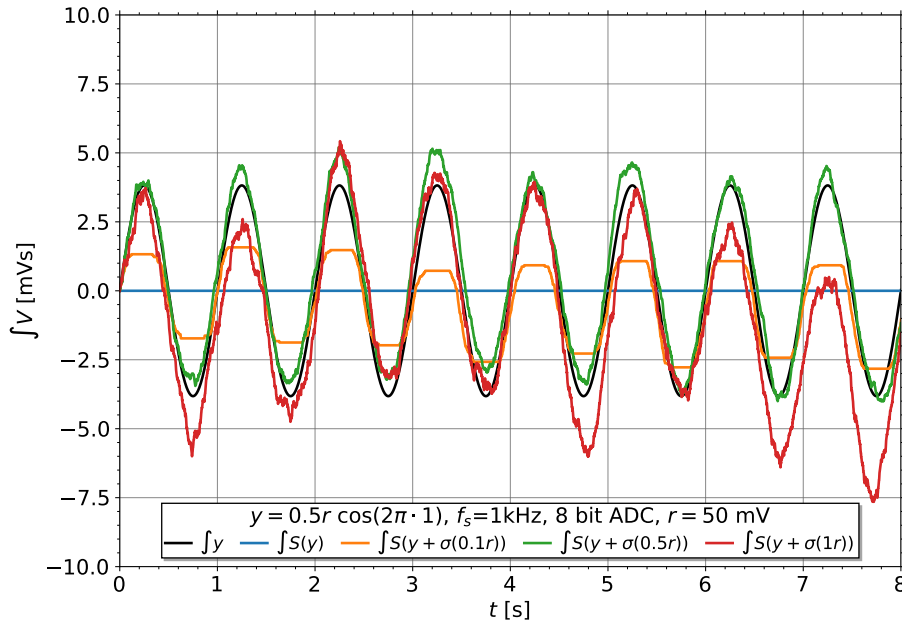


Figure 2.20: Demonstration of the dithering effect on a harmonic signal with amplitude below half a bit of the 8 bit ADC and a frequency 3 orders of magnitude below the sampling frequency. To the signal, an incoherent noise (with Gaussian distribution of $\sigma = \{0.2, 0.5, 1\}$ LSB).

2.3.1.C Aliasing

When a signal is sampled, with a constant sampling frequency f_s , care must be taken to avoid aliasing. If f_s is not sufficiently high, the aliases overlap (in frequency domain), so information is lost and perfect reconstruction is excluded. The minimum frequency a non-periodic signal with bandwidth B should be sampled is given by the Nyquist-Shannon criterion/theorem as:

$$f_s \geq 2B \quad . \quad (2.40)$$

Conversely, the maximum frequency that can be sampled without aliasing is $B \leq f_s/2 \equiv f_{Ny}$. This theorem is easy to visualize in time domain, and easy to understand in frequency domain. A signal composed of discrete harmonic components with frequencies above and below f_{Ny} , that is $B > f_s/2$, is exemplified in figure 2.21a. The sampled data (black circles) is indistinguishable from the signal with the components originally beyond f_{Ny} at $f' = f_s - f$. Without knowledge of the original signal, we can not fully reconstruct the data. We can see on the power spectrum in figure 2.21b that the aliases of the components beyond f_{Ny} fold into the reconstruction band. The only way to avoid this confusion is to ensure that the bandwidth of the sampled signal respects the Nyquist-Shannon criterion⁶. This

⁶C. E. Shannon proved the theorem in [74], pointing to a previous formulation (albeit in another form) by E. T. Whittaker [75]. In their 1949 article, Shannon also calls the $1/2W$ time interval corresponding to the band W the Nyquist interval. Nyquist is credited with pointing out the fundamental importance of this value in the field of telegraphy [74]. It is therefore possible to find mentions to the Whittaker-Shannon-Nyquist sampling theorem, any combination of these names or of the several others that independently deduced or proved it in the beginning of the XX century (Raabe, Kotel'nikov, Someya, Weston). The (*cardinal*) *theorem of sampling* is an alternative name that avoids any credit attribution.

is achieved by filtering the signal pre-acquisition, as exemplified in figure 2.22.

We can visualize a signal sampled at regular time intervals T in frequency domain by computing the **Discrete-Time Fourier Transform (DTFT)**, that is related to the Fourier transform X by:

$$X_{1/T}(f) = \sum_{k=-\infty}^{\infty} X(f - k/T) \quad . \quad (2.41)$$

The **DTFT** sums X repeated every $1/T=f_s$, on positive and negative ranges. The Fourier transform is recovered in the limit $T \rightarrow 0, f_s \rightarrow \infty$. We can now see in figure 2.21b the consequence of this summation for $f > f_{Ny}$ – the aliasing.

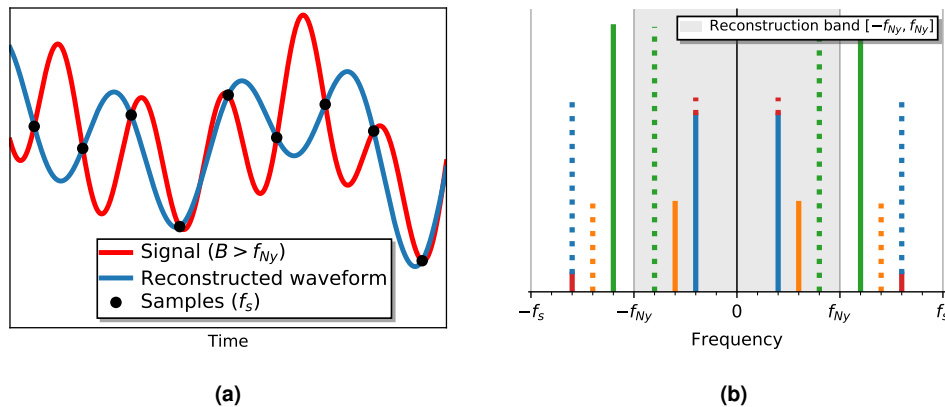


Figure 2.21: Illustration of aliasing of signal composed of four harmonic components, two below f_{Ny} and two above. The signal is represented in time domain **(a)**, and frequency domain **(b)** (power spectrum).

When designing a data acquisition system, an engineer must decide what degree of aliasing to accept, implementing (or not) an anti-aliasing filter (see figure 2.22). The key consideration is whether there are unwanted components above the expected signal bandwidth. If that is the case, one must take into consideration the roll-off of the filter as the cut-off frequency of the anti-aliasing filter, is typically placed at least on decade below the Nyquist frequency, in order to achieve a considerable attenuation at the high frequencies to be rejected.

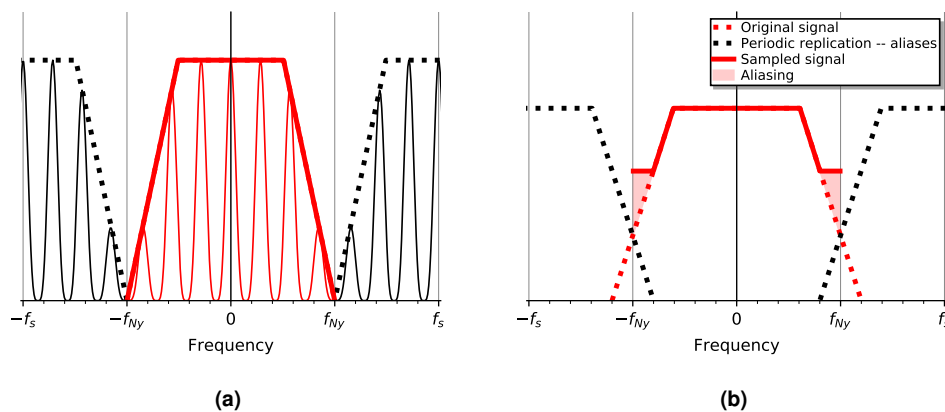


Figure 2.22: Implementation of an anti-aliasing filter in frequency domain (power spectra). In **(a)** thick lines represent the frequency response of the filter while thin lines are components of the signal (red, after filtering) and the aliases (black). In **(b)** the filtering is not well-adjusted and a part of the bandwidth folds into the sampling band, generating a shadowed area where there can be aliasing.

While in the majority of data acquisition tasks aliasing is a negative effect that engineers try to minimize, it can also be exploited, in order to sample high frequency regular signals with low sampling frequencies – under-sampling.

In section 2.2.3 it was mentioned that the same criterion can be used in space. Considering a perturbation that is stationary in space, the placement of sensors is essentially sampling its amplitude

and therefore the same thinking (and mathematical basis) to determine the maximum wave number (instead of frequency) that can be measured without aliasing.

2.3.1.D Transmission lines and input impedance

When considering a signal that is generated by a sensor that sits far away from the data acquisition, the propagation of the signal on the cables can not be neglected. This problem first appeared in the 19th century, when telegraphy introduced physical distances to the until then bench-top high frequency signals. For this reason, the equations, that are the basis of the transmission line model developed by O. Heaviside are often called the “telegrapher’s equations”. The key aspect of the transmission line model is that electromagnetic waves can be reflected on the wire and wave patterns emerge. This model is valid and crucial from low frequency power transmission, where minimizing power losses is key, to high (radio) frequency applications, where even small shifts in phase have great effect on the output.

As shown in figure 2.23a, this model characterizes the transmission line by its line impedance Z_0 , which interfaces with source and load impedances (Z_S and Z_L , respectively). Z_0 is commonly be represented by a distributed series resistance and inductance and parallel transmittance and capacitance (R, L, G, C)⁷ per unit length as illustrated in figure 2.23b.

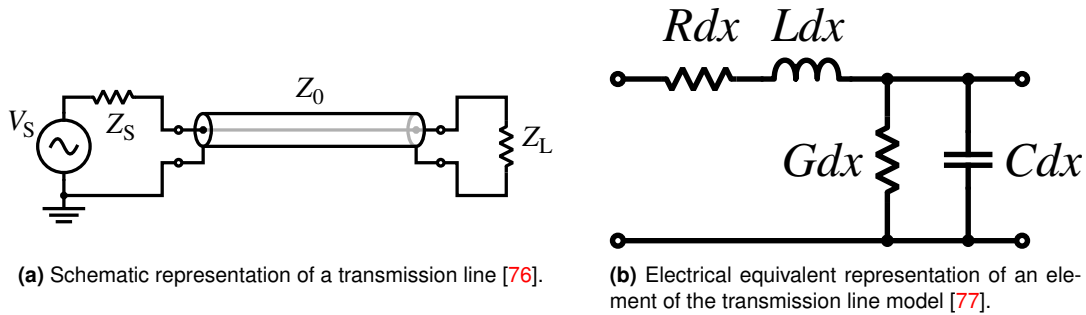


Figure 2.23: Schematic representation of a transmission line and one of its elementary building elements

This way, the telegrapher equation express the complex line voltage ($V(x)$) and current ($I(x)$) as:

$$\frac{\partial V(x, t)}{\partial x} = -(R + j\omega L)I(x, t) \quad (2.42)$$

$$\frac{\partial I(x, t)}{\partial x} = -(G + j\omega C)V(x, t) \quad (2.43)$$

These equations simplify into the wave equation. In the absence of losses ($R = G = 0$) the special case of plane waves appears:

$$\frac{\partial^2 V(x)}{\partial x^2} + \omega^2 LC V(x) = 0 \quad (2.44)$$

$$\frac{\partial^2 I(x)}{\partial x^2} + \omega^2 LC I(x) = 0 \quad (2.45)$$

The term $\omega^2 LC$ is the square of the wave number $k = \omega/u$, from where we get the phase velocity or propagation speed $u = 1/\sqrt{LC}$. The physical interpretation is that the power is transmitted as plane waves that are reflected and propagation speed of the return wave is the same as the forward wave. However, in general the dissipative terms will take energy away from the system and slow down the propagation, introducing both damping and dispersion. The telegrapher equations become:

$$\frac{\partial^2 V(x)}{\partial x^2} = \gamma^2 V(x) \quad (2.46)$$

$$\frac{\partial^2 I(x)}{\partial x^2} = \gamma^2 I(x) \quad (2.47)$$

⁷On the context of transmission lines it is common to use these symbols for the distributed parameters, a simplification that departs from convention. Often the ‘per unit length’ character is only noticeable in the units (e.g. $/m$). However, if in a given context, it leads to confusion, an alternate notation with a prime (e.g. R') will be used in this document.

where γ is the complex propagation constant:

$$\gamma \equiv \alpha + j\beta = \sqrt{(R + j\omega L)(G + j\omega C)} \quad , \quad (2.48)$$

and the characteristic impedance is:

$$Z_0 = \sqrt{\frac{R + j\omega L}{G + j\omega C}} \quad . \quad (2.49)$$

The characteristic impedance is generally not the impedance one would measure for a given cable. It represents only the amplitude ratio of a single voltage wave to the current wave. However, we need to account the reflected wave, that is also measured. The measurable (input) impedance Z_{in} at a distance l from the load is

$$Z_{in}(l) = \frac{V(l)}{I(l)} = Z_0 \frac{Z_L + jZ_0 \tanh(\gamma l)}{Z_0 + jZ_L \tanh(\gamma l)} \quad . \quad (2.50)$$

In the case of lossless transmission lines, neglecting the resistive terms simplifies these equations, while in many cases still providing a good approximation.

$$Z_0 \approx \sqrt{\frac{L}{C}} \quad . \quad (2.51)$$

In this case γ is purely imaginary

$$\gamma \equiv j\beta = j\omega\sqrt{LC} \quad (2.52)$$

and the input impedance can be expressed as

$$Z_{in}(l) \approx \frac{Z_L + jZ_0 \tan(\beta l)}{Z_0 + jZ_L \tan(\beta l)} \quad . \quad (2.53)$$

Special cases exist for when the length is a multiple of the wavelength ($\lambda = 2\pi/\beta$), half or quarter wavelength, short-circuited or open, but these cases are mostly relevant for power transmission lines and microwave engineering. For the realm of **DAQ**, the most relevant special case is the matched line (or matched load). This is the case when $Z_{in} = Z_0 = Z_L$, which prevents reflection.

Due to the importance of line matching for high frequency applications, data cables are developed in conformance to standards, usually with well specified characteristic impedance: Ethernet at 100 Ω , HDMI at 95 Ω , USB at 90 Ω and coaxial cables at 75 Ω or 50 Ω . It is not unusual for laboratory instrumentation to have output impedance in accordance with these values, in particular 50 Ω .

As a rule of thumb, in **DAQ** applications the input impedance should be much larger than that of the sensor. This is because the gain (and hence the accuracy of the acquisition) should be unitary. This gain (g) is the ratio between the input impedance of the **DAS** and total impedance of the **DAS**, analogous to a resistor divider

$$Z_{in} \gg Z_{out} \Rightarrow g = \frac{Z_{in}}{Z_{in} + Z_{out}} \rightarrow 1 \quad . \quad (2.54)$$

Notwithstanding, line-matching or tailoring of the input impedance for a specific sensor and cable is sometimes necessary, for high frequency measurements in which the resonant behavior of the reflected waver would be problematic to the measurement or the integrity of the sensor.

2.3.2 Signal integration

The integration of a magnetic sensor signal is usually performed with a separate electronic circuit that outputs a signal proportional to the time integral of its input – the integrator. Initially these were simple and passive RC filters [10, 11]. The transfer function of a RC filter is

$$H_{RC} = \frac{1}{1 + \tau s} \quad , \quad (2.55)$$

with $\tau = RC$ the time constant. For timescales much smaller than the time constant, i.e. $|\tau s| \gg 1$, the transfer function approximates that of the ideal integrator: $H_{int} = 1/s$.

The integration can be improved by building an integrator around an **OPerational AMPlifier (OPAMP)** with a capacitor on the feedback of the negative input, as in figure 2.24.

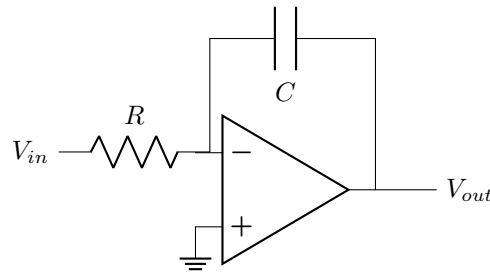


Figure 2.24: Schematic drawing of a simple active inverting integrator.

This is the basic inverting integrator, as the output of this circuit is given by

$$V_{out} = -\frac{1}{RC} \int V_{in} dt \quad . \quad (2.56)$$

Variations of this architecture are usually employed in magnetic diagnostic signal integrators. The gain is negative and inversely proportional to the time constant. It is usually expressed in milliseconds and used in place of the gain factor. A common improvement to this design is a resistor parallel to the feedback capacitor. This resistor makes the integrator less prone to saturation of the **OPAMP** to its positive or negative rail when the signal has a small DC component. We can see in the circuit in figure 2.24 that for a DC signal there is no feedback and the high gain of the **OPAMP** will eventually drive it to saturation. One has to mind that the resistor is parallel with the capacitor will form a RC filter, limiting the bandwidth of the integrator.

The key problem with signal integration is that of linear drift. Any parasitic DC component, such as **OPAMP** offset, added to the magnetic sensor signal will be integrated to a linear drift. Offline, this drift can be easily compensated as long as constant or slow varying. But this is not possible in real-time. Section 2.4.4 discusses several attempts to mitigate this problem.

2.3.3 Analogue and Digital Integration

As discussed in previous sections, many magnetic diagnostic signals need to be integrated in order to derive quantities such as magnetic field and current. Most importantly, control algorithms often need this data in real-time, and therefore electrical signal integrators are placed between the sensor and the data acquisition. Regardless of passive or active, these are considered analogue integrators, as they output a continuous electrical signal proportional to the integral of the input signal. However, one can instead sample the sensor signal directly and integrate it digitally – digital integration. With this method, processing can be immediately applied, before integration, an advantage highlighted as early as L. A. Artsimovich's 1972 review paper on "Tokamak devices" [10]: *An additional circuit can be used for preliminary integration of this signal, but in practice it is more convenient to obtain oscillograms of the derivative of δI_k ; it is then simpler to introduce the necessary corrections in the data (for example the correction for the effect of the conducting liner).*

While the technological improvements in the last half century completely changed data acquisition in scientific experiments, this conclusion still holds some merit today – it is simpler to process the signals before integration and leave that to the last step. However, this is not the most common practice in tokamak operation: digital integration is commonly used for offline processing of magnetics data, but real-time applications mostly relies on analog integrators. This is due to the following reasons:

1. The dynamic range of magnetic signals is very large – more than 5 orders of magnitude (100 dB), between the slow plasma movements in the flat-top, and high amplitude **MHD** oscillations or disruption signals. With an analogue integrator, one can adjust the RC constant or gain to ensure that the maximum expected signal fits in the **Analog-to-Digital Converter (ADC)** input range, while the resolution (noise floor) constraints will only interfere with high frequency oscillations.
2. Magnetic signals are fast, and incorrect sampling of the sensor signal can lead to losses that are propagated to the integral. This is not such a big problem in analogue integration because the integral 'history' is kept by the reactive components that perform the integration.

- Analogue signals are immediately available. They can have delays, even frequency dependent delays, depending on signal conditioning, but an analogue integrator will have no constant overhead delay. In digital systems, delays can be introduced, depending on processing and transmission steps in discrete time.

In the last decades, technological developments have mitigated these problems. Firstly, [ADCs](#) with more bits and fast and precise [OPAMPs](#) to drive them have become more widespread and cheap. [Table 2.3](#) shows the dynamic range (bipolar) for [ADCs](#) of different bits. We can observe that the jump from 16 (a convenient 2 byte size) to 18 bits brings an increase in dynamic range that makes it much more appropriate for magnetic signals.

Table 2.3: Bipolar dynamic range of ADCs with different number of bits.

n bits	Codes (\pm) $N = 2^{n-1}$	Dynamic range [dB] $20\log_{10}(N)$
12	2 048	66.2
16	32 768	90.3
18	131 072	102.4
22	2 097 152	126.4
24	8 388 608	138.5

Secondly, data acquisition is becoming faster. [ADCs](#) have an inherent trade-off between speed and accuracy and over time ($\sim 2-5$ years) new devices appear that can sample the same number of bits at faster rates. In [section 2.2](#) it was discussed that the equilibrium signal is limited to a 0-10 kHz band, while the majority of [MHD](#) activity manifest itself between 1-100 kHz with only the fastest Alfvénic modes above 100 kHz, this places a sampling frequency in the MHz range 2 decades above the bandwidth that needs integration. It was also shown in [section 2.3.1.B](#) how oversampling enables gains in dynamic range. Once again, [ADCs](#) at the MHz sampling rate are becoming more widespread and cheap, whilst respecting the bit number constraints discussed in the previous point.

Lastly, processing power increases and communication overheads reduce. With the advancements of real-time computing and cheap [Field-Programmable Gate Array \(FPGA\)](#) based processing, integrated [DAQ](#) and [DSP](#) systems are now possible with time delays that do not pose obstacles to the control systems.

But it was not any of these incremental advancements that motivated the implementation of the digital integrator in fusion research. This would be the integrator (linear) drift problem – the increased pulse lengths of tokamak devices made digital integration an able choice in magnetic diagnostic design for long-pulse operation due to the low integrator drift it can achieve. Specifically, digital integration with pulse modulation of the signal (periodic inversion). This technique requires digital integration and achieved good results in linear drift mitigation and is discussed in [section 2.4.4](#).

2.4 Development of modern magnetic diagnostic systems

2.4.1 Sensor design and construction

Sensor design is most often constrained by the particular challenges and particularities of the device than a straight evolution arrow, progressing to an ideal design. Newer sensor models are often not objectively better but rather more adequate to the new or upgraded device. Another aspect to take into consideration is that reliability is a key issue in design of magnetics. While many articles on the installation and commissioning of the magnetic diagnostic systems can be found, it is more challenging to find results on the decommissioning of these systems. This is in part because of survivorship bias – the systems mostly work as intended and allow the fulfillment of the scientific goals set for the device. A great amount of work is not put into the analysis of failures over time, which are accepted as a natural part of operating a scientific experiment for several years in very demanding environment, from an engineering point of view. The best resources to draw conclusions on this aspect are when overhauls to the magnetic diagnostic system are carried out and published [78–80], (magnetic) diagnostics overviews for new devices that go on this level of detail [81], and private communication with the operators of the diagnostic in established or decommissioned devices.

Due to its simplicity, many of the types of sensors reached design maturity with very little to point out, other than the material choices. This is the case for flux loops, saddle coils and diamagnetic loops. In the latter, notwithstanding the two design approaches described in section 2.1.3.B – single and double loop methods. Both methods see implementation in machines designed in the last two decades, with the driving motivation of one or the other lying mostly on machine-specific design constraints. That is, if there is space to pass two parallel windings separated by a gap large enough, or if it is preferable to measure error fields on the surrounding passive and active conductive structures.

In Rogowski coil construction, the situation is much the same. The available space and assembly constraints the diameter of the loops and whether a full enclosure of the poloidal cross-section of the plasma is possible. The most common construction for the coils consists of winding the turns on a rigid ceramic mandrel or flexible glass fiber rope. The latter was the approach recently followed on NSTX-U [78] and ITER [82, 83]. The research effort for ITER has shown that this method is advantageous over other methods such as a solid grooved mandrel (too rigid for tight bends) or a flexible solution without mandrel (robustness and pitch control issues) [83]. The selected design consists of a two winding configuration, insulated with glass fiber, with an external protective braiding and return wire through the center [82], as shown in figure 2.25. The same design is used in WEST [79]. The two layer approach allows an increase of the sensitivity without increasing the overall diameter.

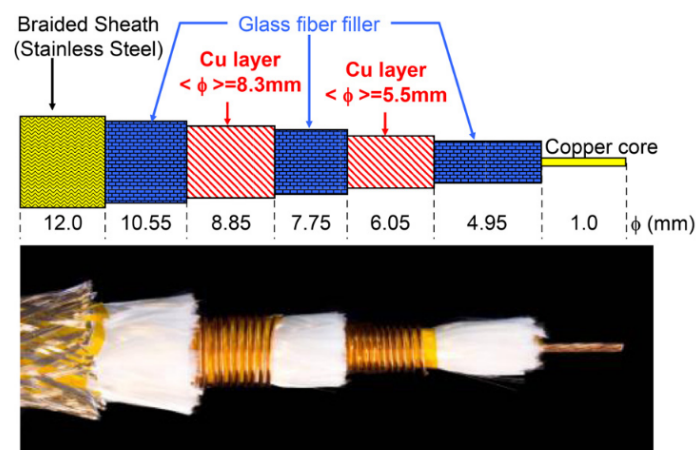


Figure 2.25: Design of the ITER and WEST continuous external Rogowski with layer-by-layer identification. Figure gathered from [82].

On KSTAR, a different approach was followed. The majority of magnetic sensors in this device is made out of Mineral Insulated Cable (MIC) due to its high-temperature compatibility, including the Rogowski coils [81]. MIC is a well established material for magnetic sensors on devices that operate at high temperatures.

In addition to the full Rogowski that encompasses the plasma and some conductive passive struc-

tures, the plasma current can also be reconstructed from a combination of partial Rogowski coils or local probes as demonstrated in TCV [15] and DIII-D [84]. While this is usually seen as a backup solution, recent research on KSTAR has shown that for the study of physics on the transients of the plasma current, this method is preferable. In this particular case, the disruption characteristic time was overestimated by an order of magnitude due to the eddy currents on the passive structures that are captured by the full Rogowski measurement [80].

The inductive sensor with more variability of designs are the magnetic probes. The conventional Mirnov coil consists of a wire wound around a core or mandrel. The materials for these two components are chosen according to the constraints of the device (allowed impurities, temperature resistance, expected forces). Bare copper is a common material for the conductor due to its high conductivity, with nickel being a common additive to the copper alloy to increase the melting point with minimal decrease in conductivity. For the mandrel, insulator ceramics such as alumina (Al_2O_3) or boron nitride (BN) are common for carbon free devices. Additional coatings of insulating material are common to protect the conductors and integrate the sensor into metallic Plasma Facing Component (PFC) tiles, supports, etc. These design features can be seen in the NSTX-U Mirnov coil design [78]. While this design is similar to the previous sensors in NSTX, a thin copper shielding was added to reject high-frequency noise from the Electron Cyclotron Resonance Heating (ECRH) antennas.

In designing a magnetic probe, there is often trade-off between effective area (dimension, number of turns of layers) and frequency response (see section 2.1.3.D). In the ITER tangential coils design a systematic approach was followed to determine key design parameters, constrained by the performance requirements. This approach is elaborated in [85] and graphically illustrated in figure 2.26, reproduced from the same source.

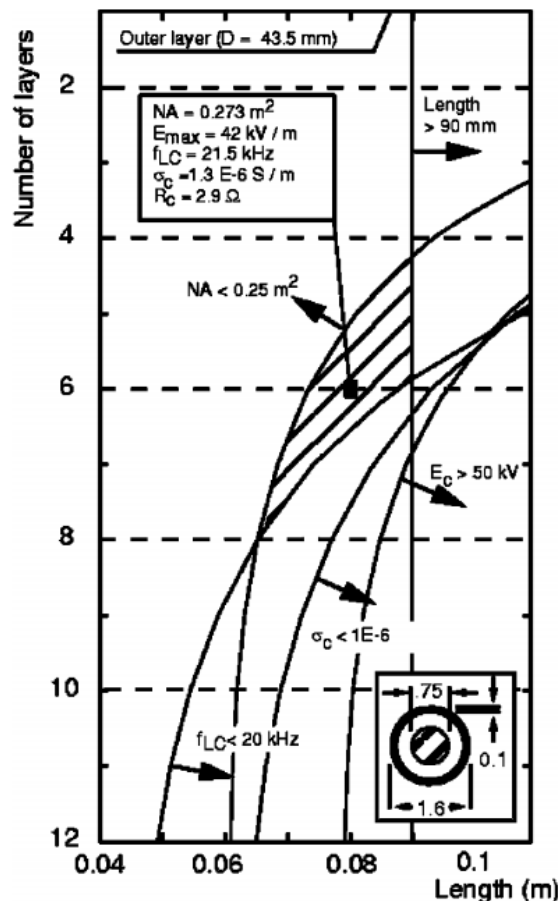


Figure 2.26: Constraints used in the design of the ITER tangential coils. The shadowed area represents the valid parameter space to design the coil as function of the number of turns and the length of the coil, with the constraints plotted as contours. The constraints used are: maximum effective area (NA), maximum length, radiation effects (E_c and σ_c), and resonance frequency (f_{LC} with 20 meters of leads included.). Figure gathered from [85].

For ITER, the high radiation environment of a burning plasma adds additional constraints for magnetic sensors' development. Specifically the minimization of [Radiation Induced EMF \(RIEMF\)](#), [Radiation Induced Conductivity \(RIC\)](#), and [Radiation Induced Electrical Degradation \(RIED\)](#) [85]. The main conclusions of this analysis was to establish adequate requirements on the insulator conductivity, accounting with [RIC](#), shielding due to the uncertain and permanent [RIED](#), and a high [Common Mode Rejection Ratio \(CMRR\)](#) on the integrators to mitigate the effect of [RIEMF](#). Crucially, a comprehensive hierarchy of redundancy plans was established for each key measurement/application. This substitution and replacement strategies, assumes loss of sensors from the primary set over the operation of the device and evaluates the eventual performance losses in such cases.

A key innovation on magnetic probe design was the employment of [PCB-like](#) sensors. By stacking layers of printed tracks connected by vias, one can achieve a high density of sensing planes. One of the key advantages of this method is that it allows the usage of industry-proven materials, resistant to high temperatures. The first development of such techniques in magnetic confinement fusion was carried out in PPPL for the LHD in the turn of the century [86]. This idea got a more recent implementation recently in TCV using the [LTCC](#) technology [29, 30]. The same technology saw further research and development for its implementation in ITER [87].

2.4.2 Equilibrium reconstruction

As discussed in section 2.2.1, equilibrium reconstruction is a very device dependent capability, as it depends on several diagnostics other than magnetic. However, accuracy is not the only metric for a good system. As processing power increased over time, real-time computation of the equilibrium became available and implemented in several devices. Table 2.4 shows which codes are routinely used in different relevant tokamaks (in operation or until recently). The first observation is that major devices either have a bespoke equilibrium reconstruction code or used [EFIT](#). Despite in general reaching the same goal, the implementation of these codes can be very different. In KSTAR, that initially run [EFIT](#), the unreliability of flux loop measurements (due to integrator saturation) motivated the development of a simpler algorithm, that led to improved results using only probe signals [88].

Table 2.4: Codes used for equilibrium reconstruction in modern tokamaks. Codes highlighted in **bold** are used in real-time.

Device	Equilibrium reconstruction codes	References
JET	EFIT++	[56]
DIII-D	EFIT, RT-EFIT	[19] [58] [52]
ASDEX-U	CLISTE, JANET++	[89] [90]
TCV	LIUQUE	[55]
WEST	EQUINOX, NICE	[91] [79]
EAST	P-EFIT	[53]
MAST-U	EFIT++	[92]
NSTX-U	EFIT01, RT-EFIT	[93] [52]
KSTAR	EFIT, IDK	[88]
Alcator C-mod	EFIT	[94]
COMPASS	EFIT	[95]
RFX-mod	V3FIT	[96]
ISTTOK	NICE	[97]

The trend towards real-time codes is also visible in the table. The computation of the profiles in real time has several advantages, as it can feed systems such as machine protection, diagnostics, and specially, advanced control [57, 93]. Even EQUINOX/NICE that are not currently used in real-time, were developed with that capability [79, 91].

In this introduction only a small overview of equilibrium reconstruction is given. However, in real implementations, these codes seldom work independently, and are fed (or feed) other algorithms that for instance calculate and impose constraints. We are seeing also an effort on the consolidation of complex code-bases such as the integration of [EFIT](#) into [OMFIT](#) [98, 99] and [EQUINOX](#) into [NICE](#) [54]. These two codes are also progressing towards implementation in ITER [100–102].

Machine learning techniques are also being considered for the equilibrium reconstruction problem, namely in an attempt to learn from the large sets of data from running tokamaks and predict/avoid

disruption events [103].

2.4.3 Real-time control

In modern tokamaks, the control algorithms are more complex than the introduction provided in section 2.2.2. Firstly, it is not obvious that the current centroid should be the controlled variable. In fact, in devices with large power dissipation, controlling the strike points or the gaps between the plasma and limiter is preferred.

Due to a larger elongation, spherical tokamaks have necessarily stronger vertical instability. **Vertical Stability (VS)** is therefore paramount to the operation of devices such as NSTX-U, where the **VS** controller uses only pairs of flux loops and Rogowski coils for current measurements [78]. The descriptor $I_P Z_P$ (where Z_P is the average vertical location of the plasma) is given by

$$I_P Z_P = \sum_i \alpha_i (\phi_{U,i} - \phi_{L,i}) \quad , \quad (2.57)$$

where α is a weight coefficient computed from **EFIT** reconstructions for each flux loop pair (Upper, Lower). For a constant plasma current, the difference in flux loop voltages is proportional to dZ_p/dt , which allows a very fast reaction to vertical movement.

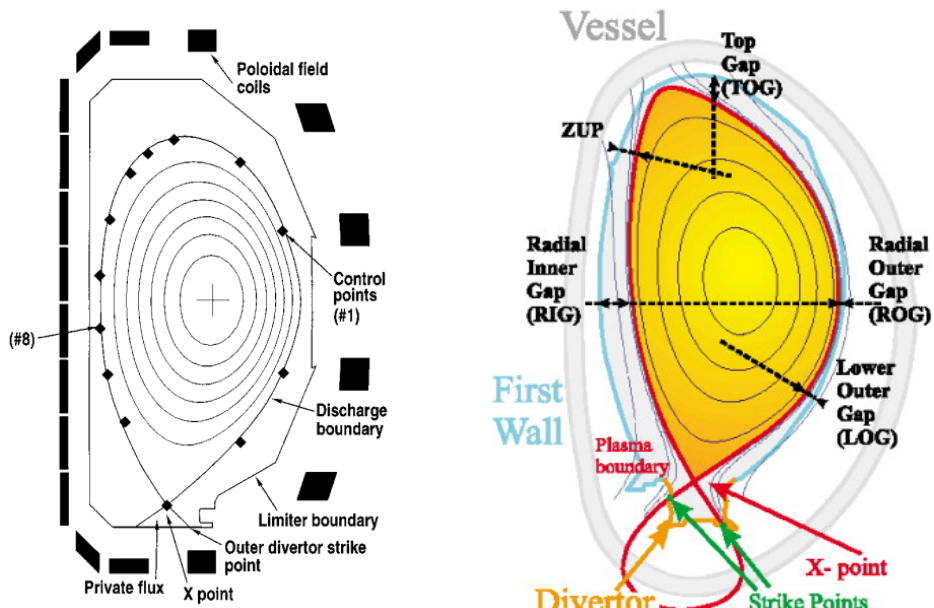
Control of the horizontal position by centroid computation, is typically used in circular plasma, with techniques similar to the **VS** system. For diverted plasmas on major devices, there are two approaches to shape control: gap and isoflux.

The isoflux method consists of defining a number of control points in the R,Z cross-section that define the **LCFS**. The current in the poloidal field coils is then adjusted in order for these points to have the same poloidal flux. Figure 2.27a shows an implementation of the method on a DIII-D diverted discharge. This method therefore requires real-time equilibrium reconstruction and therefore is used in devices with this capability, such as DIII-D [52] or EAST [104]. Full details of the implementation can be found in [52]. Generally, the method works by controlling the current in the active coils in a way that all other control points have the same ψ as a reference control point. The choice of the reference depends on the type of discharge, as this point is one that by definition must be on the **LCFS** – the x-point diverted plasmas or the limiter contact point for circular plasmas.

Shape control by gaps relies on the data from arrays of magnetic probes to determine $d\phi/dr$ along the segment, along with flux loops for ψ measurements. Figure 2.27b shows the plasma shape descriptors that can be controlled by the JET **Shape Controller (SC)**, some of them gaps. **SC** was upgraded to the **eXtreme Shape Controller (XSC)**, a particularly noteworthy system that controls more than 30 descriptors [105]. **XSC**-like solutions were also considered in other large experiments, such as EAST [106, 107] or JT60-SA [108]

A new challenge in control that future devices on the roadmap to reactor need to address is that of **Vertical Displacement Event (VDE)** prevention, or enhanced **VS** control. This is due to the absence of **PSP** or in-vessel active coils, in conjugation with a greater distance between the plasma and the **VV** imposed by the tritium breeding blanket [109].

A key takeaway from the state of the art of plasma control to magnetic diagnostic development is that in a modern diverted tokamak, several control systems are in play at different times, timescales, plant systems. This is well illustrated in figure 2.28, gathered from [93] where a description and explanation of the terms is provided. It shows that beyond having multiple controllers, for the same plant system, different algorithms can be used at different stages to better use the advantages of each method. Magnetic diagnostic for a new device must be abundant, redundant and well integrated in the **Control Data Access and Communication (CODAC)** architecture in order to provide a growing number of signals (integrated or proportional), at multiple locations and directions. Achieving this will allow a progressive expansion of the control capabilities as both operational experience and processing technology grows in the life-span of the device.



(a) Isoflux shape controller on a DIII-D diverted discharge. LCFS (Discharge boundary) and the control points shown. [52].
 (b) Plasma shape descriptors controlled by the JET standard shape controller [105].

Figure 2.27: Two different approaches to plasma shape control.

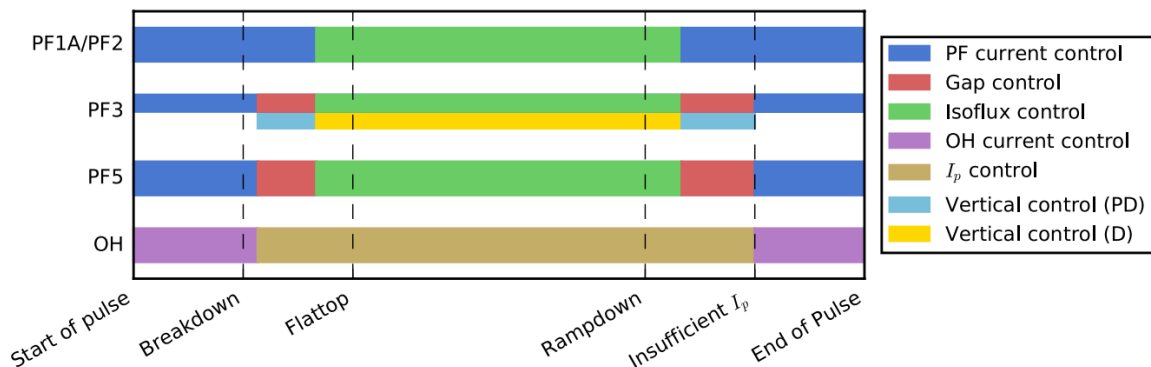


Figure 2.28: Illustration of the control algorithms employed at different stages of a typical NSTX-U discharge (horizontal axis) and for different active coils (vertical axis). Figure gathered from [93].

Finally, a recent advancement in the field of plasma control is the employment of [Machine Learning \(ML\)](#) techniques. A ML algorithm successfully controlled plasmas at TCV [110]. Its implementation on future devices is hindered by usual problems of ML, namely the requirement of training over large sets of data; and the hiding of the physical intuition behind abstract reward functions.

2.4.4 Signal integration

With plans for hour long pulses, upon planning for ITER magnetic diagnostic DAS, drift rejection and mitigation was the main concern. On the turn of the century, the long pulse tokamak Tore Supra possessed then the best performing low-drift integrators [85].

The Tore Supra integrators are described in detail in [111]. These make use of a highly symmetric design with strong attention paid to the quality of the components used (polypropylene capacitors with low leakage current, “zero drift” OPAMPs). The underlying principle are two integration cells, similar in concept to the simple inverting integrator shown in section 2.3.2 and represented in figure 2.29a. In figure 2.29b we can see two other important characteristics of this design, the auto-compensation mechanism through a [Sample and Hold \(S/H\)](#) circuit and a symmetry trimmer to correct unbalance between the two cells.

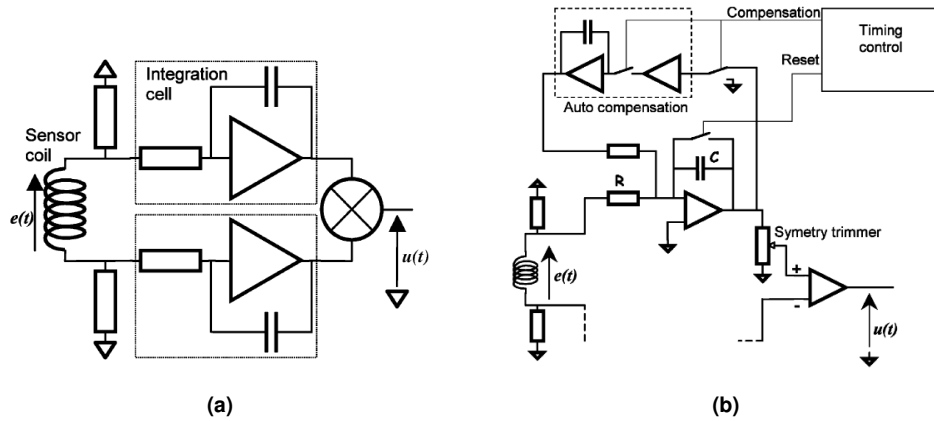


Figure 2.29: Twin cell integrator designed implemented in Tore Supra. The design focus on symmetry with each terminal of the sensor connected to an active integrator (a). Inside each cell, a S/H allows for drift compensation and a trimmer is used to compensate eventual unbalances between the two cells (b). Figure gathered from [111].

Another key innovation in the analogue integrator design was implemented with great success in KSTAR [112]. Unlike the design in Tore Supra, the KSTAR design has only one integration OPAMP being unipolar, with one terminal of the sensor coil grounded. Two important features are introduced. The first is the replacement of the analog S/H circuit by a Digital to Analog Converter (DAC). This allows for digital control of the drift compensation. The second important feature is the imitation in bandwidth through an input filter. Implemented with inductors and capacitors, the passive filter limits high frequency coherent noise that is a major source of drift. With a bandwidth limited to 12 kHz, the integrator showed integration drifts as low as $15 \mu\text{V}\cdot\text{s}$ over 400 s (37.5 nV) [112]. While this design is unipolar, differential amplifiers are used on both ends of the long (100 m) transmission line. This is a common technique to reject noise introduced in the cables. By transmitting both the signal and its inverted polarity dual, noise from external sources, that affects both transmissions is canceled at the receiver.

With the upgrade from Tore Supra to WEST, an evolution of the 2000 design was developed by the same team. The dual-cell concept was dropped in favor of unipolar design like in KSTAR. This method involves a much simpler calibration, not needing to adjust the balance between the cells. The major design change was the introduction of galvanic insulation, which greatly improved the CMRR. During prototyping stage two different methods for drift compensation were tested: with a S/H circuit as in Tore Supra or digital ADC/DAC compensation (see figure 2.30). The prototype tests have shown that the analog drift compensation model was superior, with drift averaging $32 \mu\text{V}\cdot\text{s}$ over 1000 s (32 nV) [113]. This model was chosen for the deployment in WEST [79].

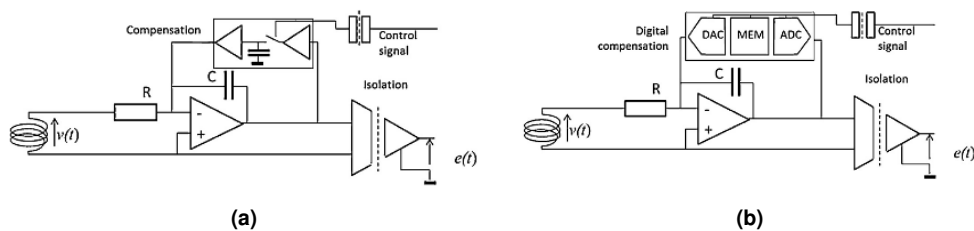


Figure 2.30: The two integrator prototypes developed for qualification for WEST. Both featuring galvanic insulation, one has an analog, S/H based drift compensation mechanism (a), while the other used an ADC/DAC combo. Figure gathered from [113].

Concurrently to the analog integrator, during the early stages of ITER conceptual design, an ‘hybrid’ digital integrator was also developed in DIII-D [114]. This design takes into account that a first order LP filter is a passive integrator (see sections 2.3.1.A and 2.3.2). With this design, the signal beyond its cutoff frequency (f_c) is integrated analogically with the slow part of the signal needing digital integration. In time domain, this is equivalent to saying that the filter will integrate in between the samples (the sampling rate of this system is 10 kSPS). Once the data is sampled, a reconstruction algorithm can recover the integral of the input voltage (V_0) with an integral and proportional dependence

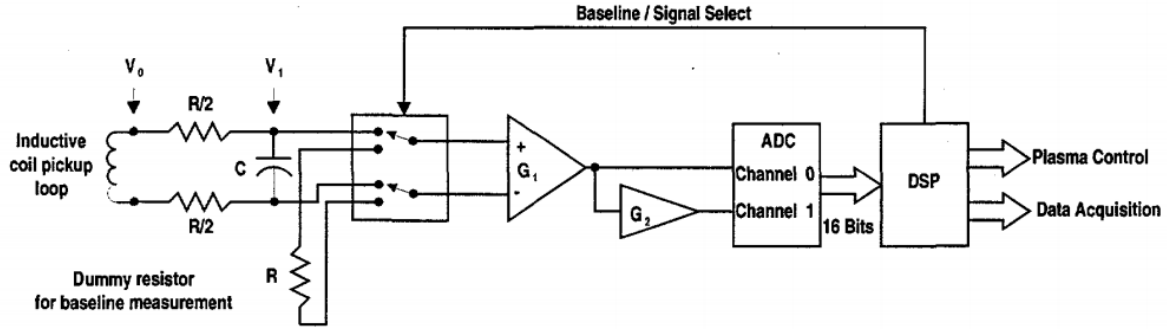


Figure 2.31: Block diagram of the digital-analog integrator. Gathered from [114].

on the voltage after the filter (V_1 , sampled as V_i) [114]:

$$\int V_0 dt = \int V_1 dt + RCV_1 \approx \sum V_i \Delta t + RC V_i. \quad (2.58)$$

This process is essentially a high frequency recovery method as we can observe in the amplitude and phase transfer functions in figure 2.32. In combination with the input filter, the reconstruction technique recovers the transfer function of the ideal integrator.

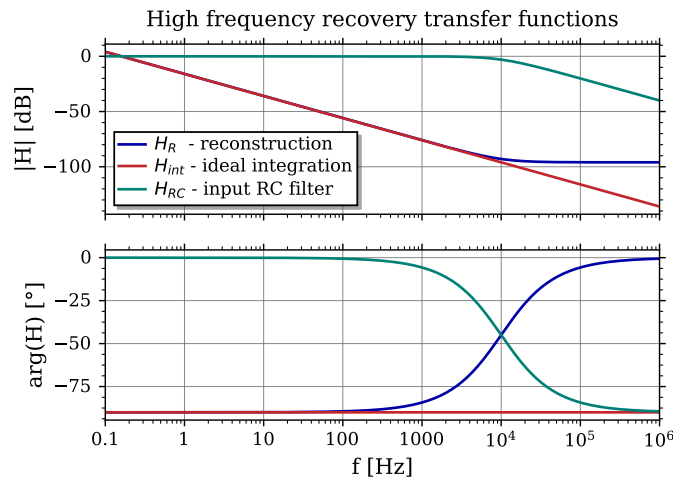


Figure 2.32: Amplitude and phase transfer functions for the ideal integration, a first order low-pass filter ($f_c=10$ kHz) and the reconstruction technique. When combined, these two processes recover the ideal integration (red curve).

A disruptive innovation in integrator design came with the development of a long-pulse digital integrator for W7-X [115]. The challenges and advantages of digital integration are discussed in section 2.3.3. This design achieved good drift rejection results not due to the digital integration itself but rather by the employment of a pulse modulation. This technique and its technical implementation is further discussed in chapter 5. The key underlying logic is that the input signal is periodically inverted by means of a chopper (square modulation) and later demodulated digitally before integration. The accumulated offset appears in the integral as alternating positive and negative slopes, instead of the characteristically monotonous linear drift. That being said, the integral is not free of drift – after all, offsets introduced before the modulation stage are indistinguishable from the signal to the downstream electronics. However, this technique allowed linear drifts as low as 100 nV in its first implementation in WEGA [115].

This concept was later implemented in the [Advanced Telecommunications Computing Architecture \(ATCA\)](#) format in W7-X [116] and ISTTOK [117] with even lower drift values (<70 nV [116]). Simultaneously, a design of integrator for ITER based on this technique started development [118]. ITER has a requirement on drift of 500 $\mu\text{V}\cdot\text{s}$ per hour (139 nV) [118]. And several of the designs presented

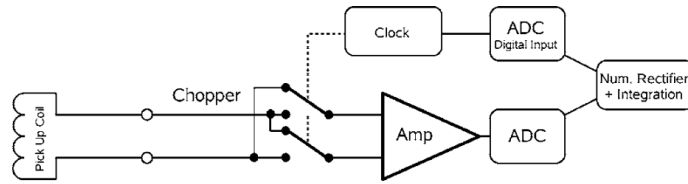


Figure 2.33: Block diagram of the digital integrator with chopper modulation. Figure gathered from [115].

can reach this value, performing consistently under this mark requires a high standard for component choice, PCB design and even temperature control [118, 119]. This led the ITER design to be implemented in a bespoke form factor, with a custom temperature controlled modular encapsulation and integrated in the ITER CODAC, as opposed to an industry standard (VME⁸, ATCA, CAMAC⁹, etc.).

⁸Versa Module Eurocard

⁹Computer Automated Measurement and Control

3

Development of sensors for COMPASS Upgrade

Contents

3.1 COMPASS Upgrade	46
3.2 Challenges and implications to the development of the magnetic diagnostic	48
3.3 Architecture of the magnetic diagnostic	50
3.4 Testbench for calibration of magnetic sensors	52
3.5 Sensor prototyping and development	68

Despite what the name might suggest, COMPASS Upgrade is practically a new device. The majority of the key systems will be developed new, with a relatively low number of components taken over from its predecessor: COMPASS. This is motivated by an ambitious scientific program that sets strict engineering requirements. Among the bespoke systems under development are the vacuum vessel, cryostat, power coils and powerful driving energetics, and most importantly for this work, the magnetic diagnostic system.

This chapter will introduce the COMPASS Upgrade project and detail the research and development efforts in developing a future-proof, state-of-the-art set of magnetic sensors. Some details of this development fall out of scope for this dissertation and are featured as to facilitate the full understanding of the subject of the matter.

3.1 COMPASS Upgrade

COMPASS Upgrade, henceforth COMPASS-U, is a medium-sized tokamak under development in Prague, Czech Republic. It is a major upgrade to the COMPASS (COMpact ASSEMBly) tokamak that was operated in the [Institute of Plasma Physics of the Czech Academy of Sciences \(IPP\)](#) from 2009 to its disassembly in August 2021 [95]. Unlike its predecessor, that was built and operated previously in Culham as COMPASS-D [120], COMPASS-U is conceptualized, designed and built by its operator, IPP [121]. Figure 3.1 gives an idea of the dimensions of the device, with the VV and PFCs visible inside the cryostat.

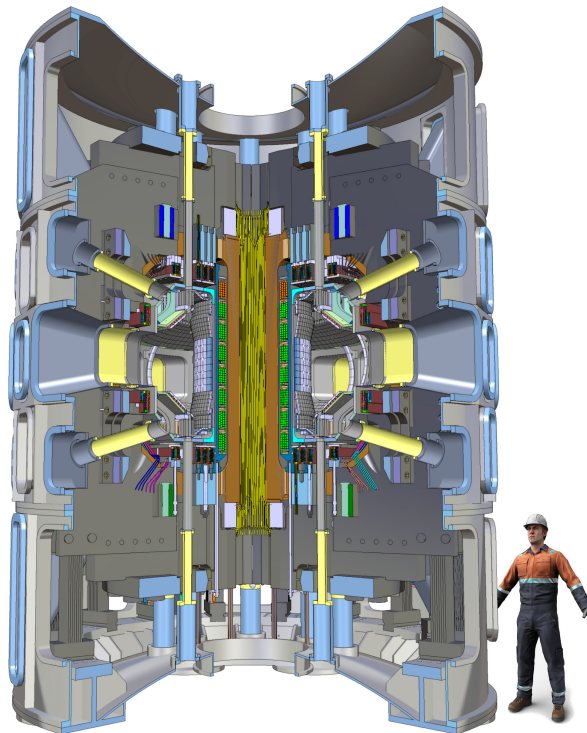


Figure 3.1: Planned 3D view of COMPASS-U. Figure gathered from [122].

COMPASS-U will be a compact and flexible device with a set of unique parameters to support the ITER operation and address the key challenges of the DEMO reactor design [122]. To achieve these goals, the device will be fully metallic, with top and bottom closed and replaceable divertors capable of handling extreme heat fluxes. The main plasma parameters can be found in table 3.1. From these, the high toroidal magnetic field on a relatively small device stands out. This will fill a research void in nuclear fusion created by the decommissioning of Alcator C-Mod ($B_T=8$ T, $R=0.68$ m), and can support the research and development of beyond-ITER devices, auxiliary systems, and diagnostics.

The first wall and poloidal field coils are designed to allow advanced plasma shapes: double null, negative triangularity and snowflake configurations. These are represented in figure 3.2, where it is

Table 3.1: Main plasma parameters of COMPASS-U.

Parameter		Value
Toroidal magnetic field	B_T	≤ 5 T
Plasma current	I_p	≤ 2 MA
Major radius	R	0.9 m
Minor radius	a	0.27 m
Aspect ratio	A	3.3
Triangularity	σ	0.3 – 0.6
Elongation	K	≤ 1.8
Flat top duration		1 – 3 s
Low perf. flat top dur.		11 s
First wall temperature	T_{VV}	300 – 500 °C

also visible the shape of the first wall and disposition of the segmented central solenoid and shaping (poloidal field) coils.

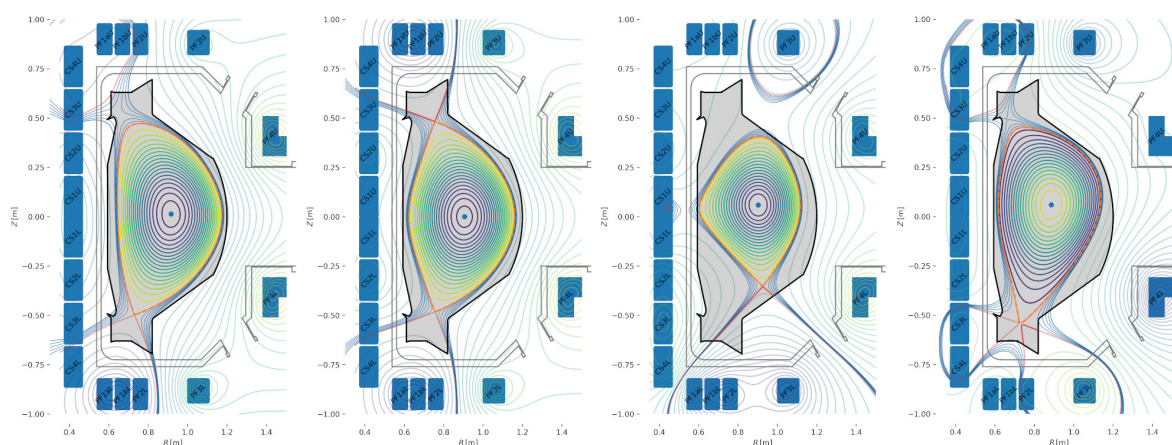


Figure 3.2: Possible plasma scenarios on COMPASS-U. From left to right, lower single null, double null, negative triangularity, snowflake divertor. Figure gathered from [122].

These plasma shapes will be achieved in a staged approach, with an initial phase only featuring lower divertor (single null, negative triangularity at reduced plasma parameters); the top divertor being incorporated at a later stage (double null); and finally the full parameters negative triangularity and snowflake scenarios, as well as new divertor concepts, such those based on liquid metals.

The phasing will also apply to the temperature of the vacuum vessel. Having a high VV temperature is a key distinguishing factor of COMPASS-U. In the first operating stages, the first wall components will be heated up to 300 °C. This temperature will then increase in selected campaigns up to 500 °C. Beyond making the device unique in the fusion community, the high temperature achieves serves the following purposes:

- Reactor relevance – the ultimate goal of tokamak research is to produce cheap energy from abundant raw materials. If ITER should demonstrate robust plasma scenarios, capable of sustaining a plasma that would make this goal possible, DEMO should be the ultimate demonstration of the technology to make it happen and its sustainability. DEMO was initially projected to have a T_{VV} of 200 °C. Since then, the value was lowered to 40 °C for a number of practical concerns [123]. However, the same source concludes that, “A higher VV temperature of 150 °C and above is of benefit for the overall plant efficiency and can contribute ≈ 15 MW (...) to the electrical grid feed-in.” DEMO can ‘take the hit’ in efficiency as it is a demonstration device, however, power plant tokamaks will operate at high first wall temperature, at which it is thermodynamically efficient to extract the heat into cooling water, part of an efficient vapor-turbine cycle. The competitive cost of electricity is the seventh goal of the European fusion project as outlined in the [European Fusion Development Agreement \(EFDA\)](#) roadmap [124], COMPASS-U will be a prime machine research on tokamak operation at very high vessel temperatures, working towards that goal.

- **Liquid Metal Divertor (LMD)** concepts – one of the key issues in tokamak research is the power exhaust problem [124]. Current **PFC** and exhaust systems technology is adequate for ITER. For DEMO, a solution still needs to be found for the heat loads on the divertor. **LMDs** are a proposed disruptive innovation that has shown positive results [125, 126], being able to sustain heat loads up to 20 MW/m² with an increased lifetime when compared with the solid metal counterparts. Of the two main candidates, lithium and tin, the latter was chosen for the European DEMO [127, 128]. It is expected that beyond the need of further testing of **LMD** concepts, by operating the first wall above the melting points of the liquid metals ($T_{\text{melt Li}} = 181 \text{ }^\circ\text{C}$, $T_{\text{melt Sn}} = 232 \text{ }^\circ\text{C}$), the “closed cycle” of the liquid metal can be demonstrated.
- **Wall recycling** – raising the temperature of the wall is one of the more common wall conditioning techniques employed in tokamak operation, including devices with fully metallic first wall. Higher temperatures minimize the amount of deuterium stored or pumped. While it is not known which temperature brings optimal operation, TEXTOR operated at 300 °C [129] and JET (in the ITER-like wall campaigns) operated at 200 °C, with the provision of raising to 325 °C if the fuel retention was found to be significantly higher than expected [130]. Operating at these conditions, fewer issues with break-down were observed gave access to lower density operation at the edge (higher performance). COMPASS-U will be the only machine available for operation at even higher temperatures.

For auxiliary heating systems, on the first phase, 3–4 MW of **Neutral Beam Injector (NBI)** power through two beams is planned. In addition, two 0.5 MW diagnostic beams will be present. In addition, 1 MW of **ECRH** is planned for the first phase. These systems will be upgraded to 8 MW of **NBI** power and up to 10 MW **ECRH**.

3.2 Challenges and implications to the development of the magnetic diagnostic

Some diagnostics for COMPASS-U will be transferred and modified from COMPASS [131]. In particular, for the first stages of operation when the temperature of vessel, and consequently of the diagnostic components will be below 300 °C. This is not the case for the magnetic diagnostic. It was found that all components of the diagnostic needed upgrade: the construction of the sensors is device specific (global sensors) or incompatible with the requirements; the transmission cables are too short; COMPASS integrators are few, nonexpansible (80s design), and incompatible in terms of performance; and even some **DASs** used do not have enough memory to hold the full shot lengths expected.

From the description of the device, we can immediately identify some challenges to the development of magnetic diagnostics. Others are not so obvious and need to be taken into account nonetheless.

- The presence of **ECRH** dictates the need to filter the unwanted high frequency (GHz) noise expected to be introduced by the heating system antennas. As seen in section 2.4.1, this can be achieved by a thin conductive shielding layer applied to the sensors.
- The staged approach of the device operation brings an element of flexibility to the deployment of magnetic sensors. The operational breaks between stages can be used to install new sensors. This way, the first plasma sensors need not be full set of magnetics but a reduced set, with planned expansion, and possible replacement in case of failures.
- The neutronics is not anticipated to be a problem for sensor development. Simulations show a neutron flux of 10^{14} – 10^{15} cm^{-2} per year [121]. This corresponds to $3 \times 10^7 \text{ cm}^{-2}\text{s}^{-1}$, 5 orders of magnitude below the $10^{12} \text{ cm}^{-2}\text{s}^{-1}$ estimation for the ITER sensors [132] and still significantly lower than in devices such as ASDEX Upgrade ($10^{10} \text{ cm}^{-2}\text{s}^{-1}$ [133]) or DIII-D ($2 \times 10^{10} \text{ cm}^{-2}\text{s}^{-1}$ [134]). Sensitive electronics will be installed in a dedicated room, shielded from the experimental hall by 1.5 meter thick boron-doped concrete walls [121].
- As a consequence of the strong magnetic field, disruptions can generate strong forces on the magnetic sensors installed in-vessel. The materials and construction of said sensors should take this into account in order to minimize failures and increase long-term availability.

- Due to having a strong plasma current and high poloidal magnetic field (B_{pol}), COMPASS-U is expected to have a short power decay length (λ_q). This value measures the length at the divertor exposed to the majority of the exhaust power. Empirical scaling laws, calibrated by experimental data from comparable devices, predicts $\lambda_q \sim 1$ mm, comparable to the ITER value (see figure 3.3). While COMPASS-U will not have as extreme heat to the divertor as other devices, most of the power will be deposited in a millimeter-narrow band, which can locally damage structures that are not prepared to withstand them. This sets requirements on the resolution of the equilibrium reconstruction and shape control on the same order. This requirement is propagated to the sensing, installation, and calibration accuracy of the magnetic diagnostic.

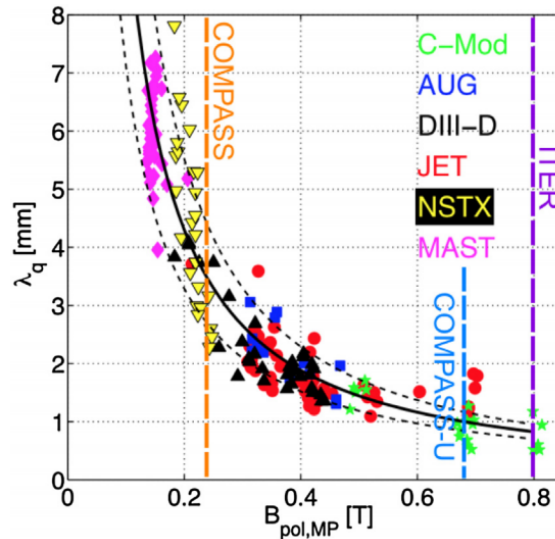


Figure 3.3: Scaling of power decay length (λ_q) at outer midplane across several devices. Predictions for COMPASS-U and ITER superimposed. Figure gathered from [131], adapted from [135].

- The high temperature operation is the most demanding requirement on the development of sensors. Sensors have been developed for devices that have baking at temperatures over 300 °C but the instances of operation at these temperatures are rarer. TEXTOR is the device that comes closer in this aspect. On these devices, the majority of vessel mounted sensors are made of MIC or other high-temperature resistant materials such as molybdenum wires, glass fiber and ceramic insulators. The differential thermal expansion of composite materials is also a sensitive aspect for components that rely on precise alignment.
- The presence of liquid metal in the VV dictates that vaporized metal is possible and expected. The metal can permeate porous insulating materials, such as glass-fibers or ceramics and beyond lowering the insulating properties during operation, droplets can form and irreversibly damage the insulation.
- Regarding data acquisition, the needed integration time is short (10 s reference) but accuracy is important for the previously mentioned factors. The strict accuracy also dictates that despite the short integration time, integrator drift should be mitigated. The high operational temperatures of the sensors can also have a negative impact on the integration performance, specifically by introducing drift.

3.3 Architecture of the magnetic diagnostic

Given the constraints laid out in the previous section, the COMPASS-U magnetic diagnostic architecture will make a key distinction between sensors that are essential to the operation of the device and those which are only needed for the data analysis and plasma research. Figure 3.4 shows the full set of sensors, and highlights this distinction as “Operation” and “Physics”. This categorization is not without a few caveats – it refers to the main usage, in principle all sensors can be used for physics studies, and likewise all can feed advanced control algorithms (i.e. disruption mitigation, [Edge Localized Mode \(ELM\) control](#)).

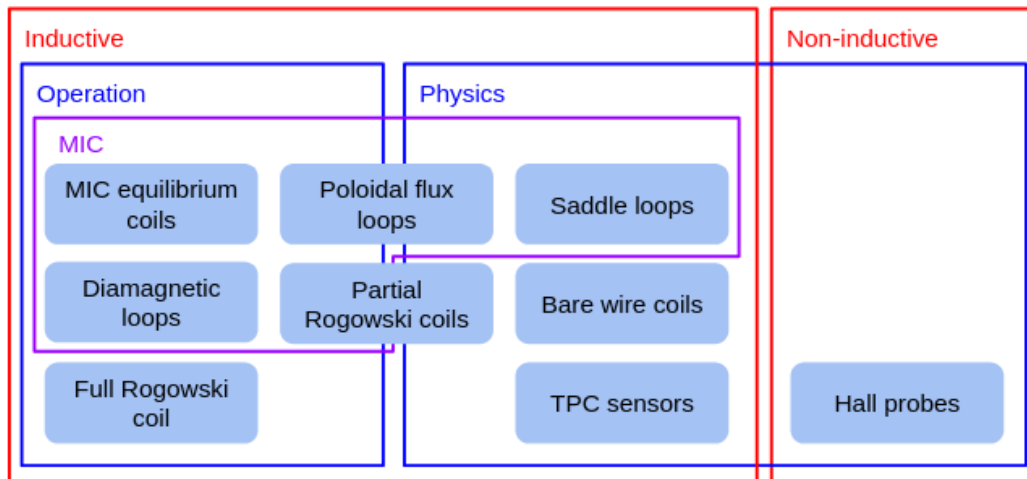


Figure 3.4: Architecture of the magnetic diagnostic system on COMPASS-U. Sub-systems (sensor types) are categorized by physical principle, intended usage, and construction material (MIC).

This classification is connected with the requirement on sensor availability in real-time (with integration) and reliability. The real-time feedback and equilibrium sensors should be installed from day one and highly reliable for the full operation temperature range. Following the state-of-the-art and the lessons learned from other devices, it was decided to manufacture these sensors out of MIC. This construction choice is also highlighted in figure 3.4 with two exceptions standing out. The first is the construction of saddle loops out of MIC. These sensors do not have an immediate need for control or equilibrium reconstruction, nevertheless, as they are mounted ex-vessel no high frequency signal is expected. Being the main disadvantage of the MIC irrelevant, there is no reason not to construct them using this highly reliable material. The second exception is the full Rogowski coil. While the construction of such sensor with MIC is possible, it was decided that the added complexity and space requirements of the design would make it too complicated. In addition, existing designs based on glass fiber exist that have shown compatibility to very high temperatures (300 °C baking [136]). The obvious supplementary sensor is the array of partial Rogowski coils. It is expected that by the time COMPASS-U reaches its highest operation temperatures, the measurement of plasma current by this array is well calibrated and can replace the primary sensor in case of temporary or permanent damage, as was demonstrated in other devices.

Magnetic probes are the sensor type for which the distinction between engineering and physics diagnostic is more relevant. Three types of magnetic probes are classified in figure 3.4: MIC equilibrium coils, Bare wire coils, and TPC sensors.

Of these, the equilibrium coils are made from wound MIC to be used for equilibrium reconstruction and real-time control. It is well known that the shielding of the MIC will prevent the penetration of high frequency magnetic fields. Literature is more scarce on how to design magnetic sensors minimizing this effect on the frequency response, with some investigation having been conducted based on the DIII-D sensors [137]. This is target of investigation in this chapter.

The bare wire coils and TPC sensors are also in-vessel probes, filling in the role of measuring the high frequency oscillations that are not picked up by the (MIC) equilibrium coils. The first is being developed in cooperation with PPPL, in a similar design to the NSTX-U Mirnov coils [78]. These will be the main magnetic sensors for observation and measurement of MHD activity, with toroidal and

poloidal arrays planned. A 1D and 2D prototypes were sent for testing (see figure 3.5) and the results are shown in this chapter.

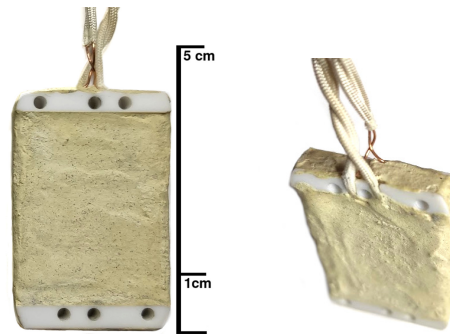


Figure 3.5: 2D prototype of bare wire coil. The copper wire is wound around a ceramic mandrel and protected by a layer of temperature resistant cement. Glass fiber insulated twisted pair visible for both windings on the angled view.

The TPC sensors will be installed as a poloidal array, with poloidal and radial components of the magnetic field being measured at each position. Like the bare wire coils, this sensor is expected to have a higher bandwidth than the MIC equilibrium sensors, adding redundancy with a supplementary measurement of fast plasma dynamics. Moreover, since these sensors are projected to have higher effective area, the poloidal field signals are in a better position to be integrated and provide equilibrium measurements in case of catastrophic failure of the MIC equilibrium coils. This sensor is being developed in collaboration with the Research and Innovation Centre for Electrical engineering (RICE) – R&D centre of the Faculty of Electrical Engineering, University of West Bohemia, that applied the TPC technique [138] to the development magnetic sensors [139]. Early prototypes were provided for testing, see figure 3.6.

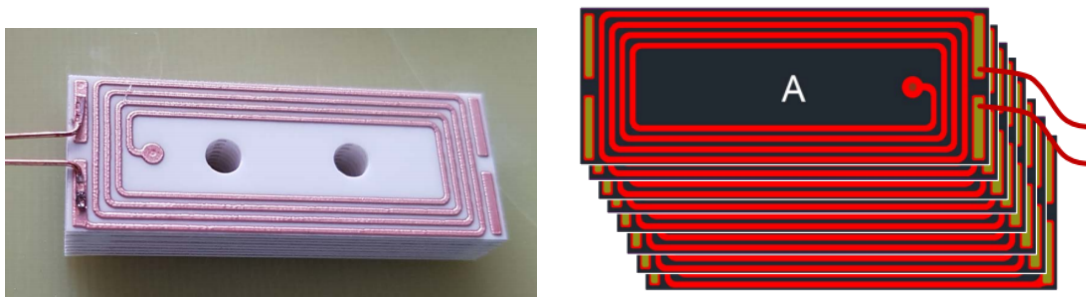


Figure 3.6: Early prototype of the TPC sensor. Photograph showing the connection to the glass fiber insulated twisted pair lead on the left-hand side. On the right-hand side, schematic drawing showing the top of the 8 layer stack. Figure presented in [139].

3.4 Testbench for calibration of magnetic sensors

To research open design problems and support the development of the prototype and final sensors, a testbench for the calibration of the sensors was developed. The key roles of this testbench are to:

- Measure the effective area (S_{eff}) of the prototypes. The construction of the sensors can carry deviations from its expected area by geometrical calculation. In some designs the area might be easy to estimate but difficult to compute to the uncertainty level required.
- Measure the frequency response of the sensors made with **MIC**. In this topic, evaluate the effect of design changes to said frequency response.
- Gain insight on the resonant frequencies of the sensors dedicated to **MHD** perturbations. On these probes (bare wire and **TPC**), the expectation is that the bandwidth will be limited by the resonance between the inductive nature of the sensing coil and the capacity of the long cables.
- Lastly, the setup will also be essential to determine S_{eff} on the final (individual) sensors – the absolute calibration. As well as the bandwidth characterization of the final probe–cable–**DAS** combinations. For this reason effort should be put into automatization and systematization of the procedure, as well as determining (and optimizing) the accuracy and precision of the measurements.

The working principle is to generate magnetic field with a power coil, supplied by a source of harmonic current ($I(t) = I_s \sin \omega t$). A test sensor placed in the magnetic field will measure a voltage

$$V_0 \propto \omega I_s \quad . \quad (3.1)$$

If only a relative frequency response is needed, the proportionality does not need to be resolved, with the transfer function being estimated as

$$g(\omega) = g_{DC} \frac{V_0}{\omega I_s} \quad . \quad (3.2)$$

If g is measured at a sufficiently low frequency, a relative transfer frequency can be determined with minimal error. In practical terms, setting $g(\omega_1) \equiv g_{DC}$ for the lowest frequency measured (ω_1).

If the magnetic flux at the sensing position is known, absolute measurements can be taken. In a point-like approximation, the field at a given point is $B = k_B I_s$ and (3.1) becomes:

$$V_0 = k_B S_{eff} \omega I_s \quad , \quad (3.3)$$

with the DC gain now being determined as:

$$g_{DC} = k_B S_{eff} \quad . \quad (3.4)$$

3.4.1 Preliminary setup

The first attempt at frequency response measurement was done with equipment readily available in the laboratory. Instead of a continuous current source, a manually triggered RC system was connected to a solenoid ($L=32 \mu\text{H}$). The discharge of capacitors in the range $C \in [33 \text{ nF} - 30 \mu\text{F}]$ onto the coil generates damped oscillations with a constant frequency, from 5 to 200 kHz. Recording the waveforms, one can extract the undamped amplitude (V_0) fitting

$$V = V_0 e^{t/\tau} \cos(\omega t + \phi) \quad . \quad (3.5)$$

Figure 3.7 shows an example of the fitting, that is applied to the solenoid (V_s) and test coil (V_c) voltages. The frequency response was obtained as

$$g(\omega) = \frac{V_c}{V_s} \quad . \quad (3.6)$$

Analogous to a transformer, V_s should be proportional to ωI_s . Four cylindrical 22-turn **MIC** coils were wound around a temperature resistant cement former (see figure 3.8). These coils are not prototypes,

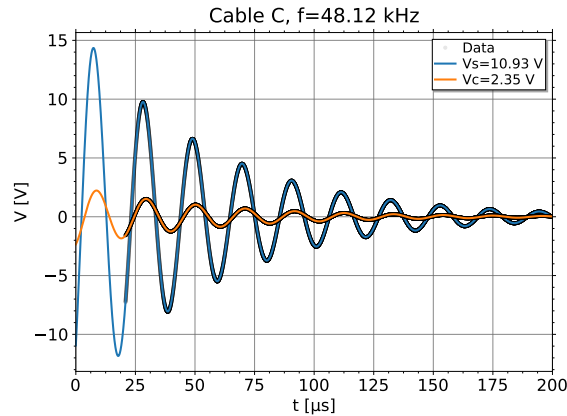


Figure 3.7: Fit of the damped oscillations for the solenoid and test coil voltages, V_s , V_c , respectively.



Figure 3.8: Photo of a tested coil (cable C).

but rather a way of testing the frequency response of the MIC samples purchased. These samples are described in section 3.5.2. Only a subset of these, as identified in table 3.8, was used for the first tests (B,C,D,F).

The frequency response measurement of sensors with the same geometry but made with cables with Outer Diameter (OD) of (B:1.0, C:1.55, D:1.6, F:3.0) mm shows considerably different attenuation, in line with the increased thickness of the shielding. The fit of a first order filter was unsuccessful. However, the fit of a second order filter shows a good agreement (see figure 3.9). The fits also seem to indicate a quality factor around critically-damped ($Q \sim 0.5$) behavior, however with a natural frequency in the limit of the measurable range, making it impossible to see the rollover. This was not expected, or at least not in line with the model proposed in [137] that for sensors of a similar construction predicts a first order attenuation.

This preliminary setup has shown that a MIC construction for probes leads to strong attenuation on the range between 10–100 kHz. This is important for the definition of the final testbench. However, this configuration has shown the following limitations:

- While the fitting of damped oscillations can be very accurate, this technique is not scalable as requires manually changing the capacitors – a time-consuming operation.
- Choice of frequencies is limited by the available high voltage capacitors.
- The lack of proper current measurement is a strong limitation on the accuracy.
- With damped oscillations, measurements are prone to errors due to the triggering definition.

With this in mind, the testbench for frequency response will be based on a Helmholtz coil driven by a harmonic signal of constant amplitude. Absolute measurements have to be based on current measurements and not by proxy, using the power coil voltage.

3.4.2 Frequency response measurements using Helmholtz coil

The Helmholtz coil is one of the most popular devices to generate a highly homogeneous magnetic field in limited area. Physically, the coil is constituted by two circular loops (one or multiple turns) of radius R spaced along the magnetic axis (e_x^z) by R . When connected in series and driven by a current I , the magnetic field of each loop add to a stable plateau of roughly R in length along the axis, see figure 3.10.

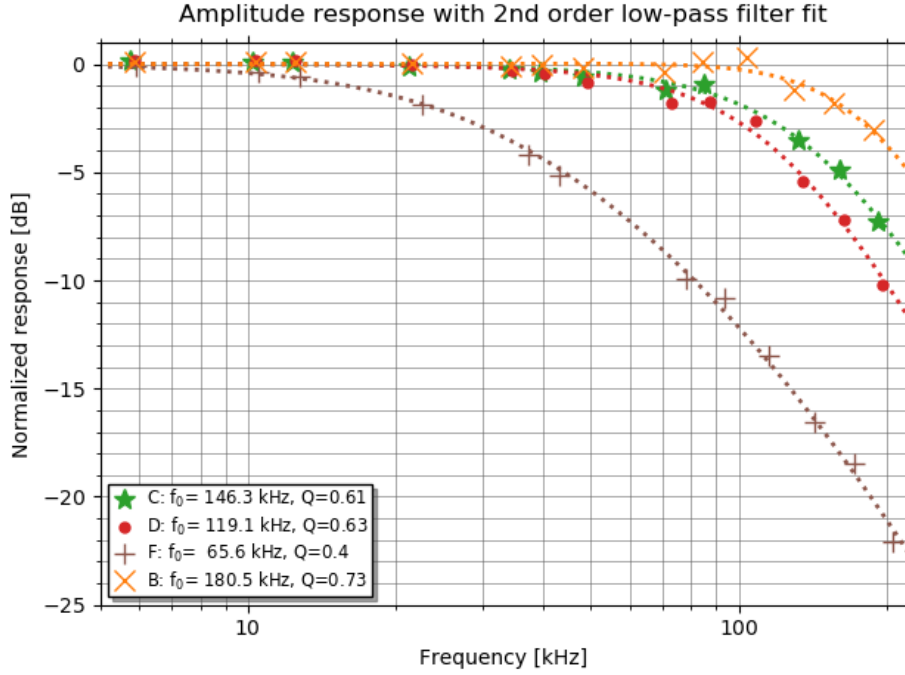


Figure 3.9: Results of the frequency response (amplitude) for the tested MIC coils. Legend for the cable labels can be found in table 3.8. Dotted lines are fits of a second order low-pass filter.

The on-axis magnetic field generated by a wire loop of n turns and radius R can be calculated using the Biot-Savart law as

$$B_1(x) = \frac{\mu_0 n I R^2}{2(R^2 + x^2)^{3/2}} \quad (3.7)$$

The position dependence can be absorbed in the dimensionless term $\xi(x) = [1 + (x/R)^2]^{-3/2}$, simplifying (3.7) to:

$$B_1(x) = \frac{\mu_0 n I}{2R} \xi(x) \quad (3.8)$$

For the Helmholtz coil configuration the field is generated by coils at $x = \pm R/2$:

$$B(x) = B_1(x - R/2) + B_1(x + R/2) = \frac{\mu_0 n I}{2R} [\xi(x - R/2) + \xi(x + R/2)] \quad (3.9)$$

with the field at the center evaluating to

$$B_0 = B(0) = \left(\frac{4}{5}\right)^{3/2} \frac{\mu_0 n I}{R} \equiv \kappa_B I \quad (3.10)$$

Figure 3.10b shows the evaluation of (3.9) as function normalized to B_0 , showing the homogeneity level that can be achieved in this configuration.

These equations imply that the magnetic field inside the coils can be accurately determined, provided the current is known.

3.4.2.A Helmholtz coil construction

The first step in the construction a Helmholtz coil setup adequate to its needs is to identify the key physical and electrical requirements. The construction parameters are only the radius and number of turns. These, however, influence also the inductance and by extension the frequency response. In conjunction with the frequency response of the current source, this means the magnetic field at higher frequencies will suffer attenuation, albeit, the proportionality to the current in the coil stands.

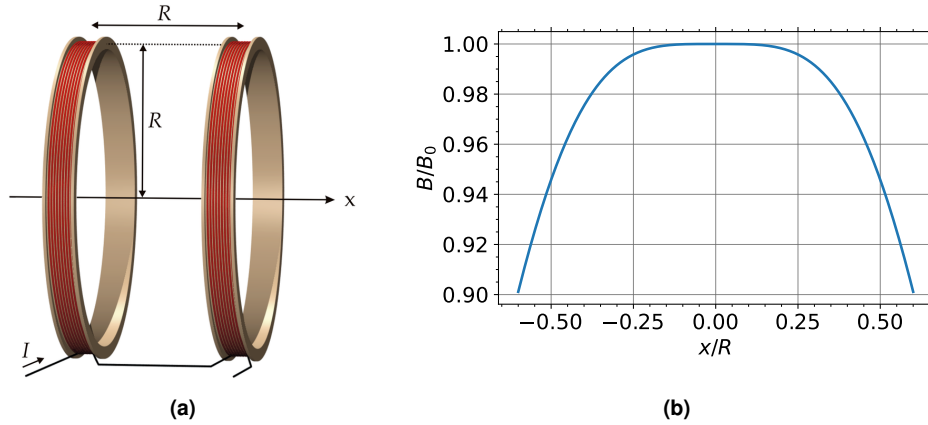


Figure 3.10: a) Schematic representation of a Helmholtz coil [140]. b) Homogeneity of on-axis magnetic field generated by the Helmholtz coil.

For the problem at hand – calibration of magnetic sensors – this effect is mitigated by another effect. If Helmholtz coil is driven by a harmonic signal, $B = |B|e^{j\phi}$ the sensor signal is

$$V = -j\omega S_{eff} B \quad , \quad (3.11)$$

that is, proportional to the frequency.

The physical size of the coil (R) was determined using the criterion that the prototypes should fit in a region with a non-uniformity $<1\%$. It was estimated that the sensor would have a maximum length of 6 cm. The plot in figure 3.11a shows the calculation of $(1 - B_{(3\text{ cm})})/B_0$ as per (3.9), from where $R=10$ cm was chosen, fulfilling the requirement. This dimension roughly yields a cylindrical region of 3.75 cm radius and 6.2 cm length across the magnetic axis where the deviation from the calculated field at the center is below 1 %, as can be seen in figure 3.11b.

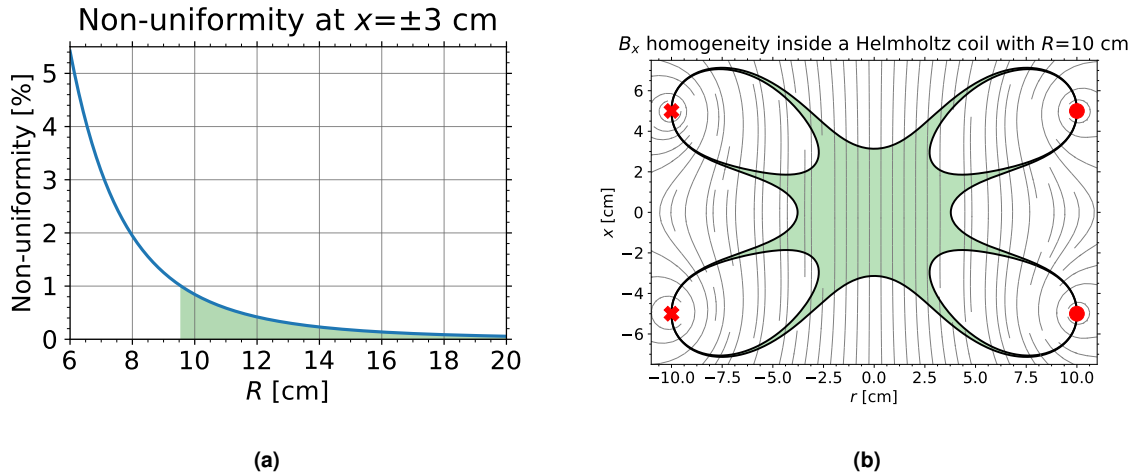


Figure 3.11: a) Non-uniformity $(1 - B(x))/B_0$ at $x=3$ cm as function of R , the radius of Helmholtz coil. $R=10$ cm fulfills the non-uniformity criterion of 1% (shaded region). b) Two-dimensional homogeneity of the field to 1 % for a 10 cm Helmholtz coil construction. Coil current filaments represented in red, magnetic field lines in gray. The shadowed region that satisfies the condition $B_x/B_0 \in [0.99, 1.01]$.

With R fixed, the next step was to determine the appropriate number of turns that ensures a measurable signal with a current that can provided by desktop laboratory signal amplifier on the frequency range of 1 kHz to 1 MHz. The Previous measurements with the preliminary setup have shown that a harmonic signal of 5 mV can be measured reasonably well with the PicoScope 5442D Personal Computer (PC) oscilloscope [141]. To determine the current in the Helmholtz coil, a shunt resistor (R_{shunt}) is typically installed in series. The power rating and inductance of the shunt resistor are additional factors. At the lower end of the frequency range, the high current needed can cause overheating of the resistor, altering its sensitivity as a current sensor. Resistors that are prepared for

high power typically have a wirewound construction that has high parasitic inductance and therefore is not appropriate for high frequencies. The inductance of the coil (L_{Helm}) was calculated according to [142] that provides a precalculated value (α) for the mutual inductance (M) of the coils in Helmholtz configuration:

$$L_{Helm} = 2(L + M) \quad (3.12)$$

$$M = \alpha n^2 R \quad (3.13)$$

$$L = n^2 R \mu_0 \left[\log\left(\frac{8R}{a} - 2\right) \right] , \quad (3.14)$$

where L corresponds to the self-inductance of each of the Helmholtz coil loops and a is the radius of the wire bundle cross-section. The total inductance of the system is thus

$$Z = R_{shunt} + R_{Helm} + j\omega L_{Helm} . \quad (3.15)$$

Being the majority of sources (and amplifiers) voltage driven and not current driven, we can fix a reasonable voltage level (V_s) and estimate the output voltage for the smallest coils we intend to measure, according to (3.11). Those are expected to be the bare wire coils (figure 3.5) whose effective area we estimate at $S_{eff}=60 \text{ cm}^2$. Figure 3.12 shows the result of the simulation for 5 and 10 turns, and with different shunt resistors. For sufficiently high frequencies, the behavior is purely inductive, and

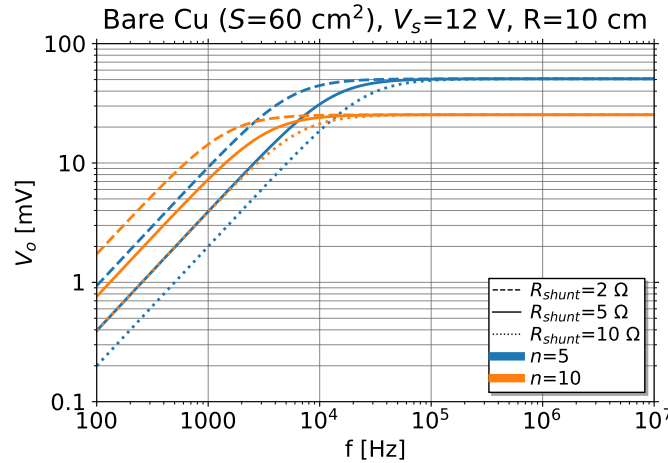


Figure 3.12: Simulation of the expected signal on a 60 cm^3 probe as function of the frequency on a Helmholtz coil with different shunt resistors (line style) and 5 or 10 turns (color). The driving voltage is constant ($V_s=12 \text{ V}$) and the radius is 10 cm.

only the number of turns has influence. The impedance scales with n^2 , reducing the current and field strength. The frequency dependence in (3.11) and (3.15) cancel each other. On the lower end of the frequency range, both parameters (R_{shunt} , n) play a role, with a higher number of turns providing a stronger field and consequently higher signal. In this region the behavior of the system is resistive, dominated by the shunt resistor, given the resistance of the coil itself being on the tenths of Ohm.

The number of turns was chosen as $n = 5$. While the expected signal for the smallest sensor is expected to be small, at higher frequencies the signal strength is adequate. The plot seems to indicate that there is room to double the number of turns and still measure above 20 mV on high frequencies. However, there is one unaccounted behavior – while we can expect a flat frequency response for the bare wire coils, the MIC sensor prototypes we are also interested in measuring will have an unknown attenuation at high frequencies. Precisely one of the measurements this setup is designed for.

An insulated wire of OD=1.5 mm was used, to prevent damage by $\sim 1\text{--}5 \text{ A}$ current expected. The support structure for the windings was 3D printed in plastic (drawing provided as appendix A), taking into account the wire dimensions. Wooden rods keep the separation between the windings.

Table 3.2 summarizes the Helmholtz coil construction parameters. Figure 3.14 shows the measurement of the impedance of the constructed coil.

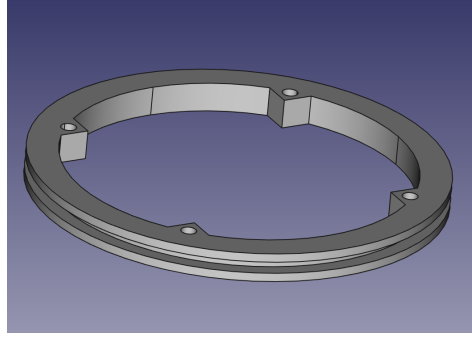


Figure 3.13: Design of the Helmholtz coil structure. The design takes into consideration the wire OD keeping the radius at 10 cm.

Table 3.2: Physical and electrical parameters of the Helmholtz coil

Parameter		Value
Radius	R	10 mm
Turns	n	5
Wire radius	a	0.5 mm
Wire OD	OD	1.5 mm
Inductance	L	$27.4(\pm 0.1)$ μH
DC resistance	R_L	$150(\pm 1)$ $\text{m}\Omega$
Magnetic field	κ	44.96 $\mu\text{T/A}$

3.4.2.B Frequency response measurement

The Helmholtz coil is driven by a Siglent SPA1010 10 W amplifier, with a ~ 1.2 MHz full-power bandwidth. The PC oscilloscope (PicoScope 5442D) provides the 1.2 V input signal that is amplified by a factor of 10.

Current measurement on such a wide bandwidth is not a trivial problem. Three different methods are employed in this setup. All having advantages and disadvantages: (i) shunt voltage drop; (ii) measurement of the current using a Rogowski coil; (iii) comparison to a reference coil.

The problems of the measurement by a shunt were already discussed. In order to try to mitigate them, before carrying out the measurements, the shunt is measured for its resistance and inductance. The current is thus measured as

$$I_{shunt}(\omega) = \frac{V_{shunt}}{Z_{shunt}(\omega)} = \frac{V_{shunt}}{R_{shunt} + j\omega L_{shunt}} \quad , \quad (3.16)$$

and the transfer function of the test coil, according to its measured voltage (V_o) as

$$g_{shunt}(\omega) \cdot S_{eff} = \frac{V_o}{-j\omega\kappa I_{shunt}(\omega)} = \frac{Z_{shunt}(\omega)}{-j\omega\kappa} \frac{V_o}{V_{shunt}} \quad . \quad (3.17)$$

One wants to minimize R_{shunt} as much as possible to increase the magnetic field. However, it was verified that the amplifier requires a load of $\sim 5 \Omega$ not to trigger its internal protection. For this reason, the shunt used is made of two parallel 10Ω high-power resistors (5Ω).

Using a commercial Rogowski coil and integrator¹ a measurement of the current is provided as

$$I_{rog} = \alpha^{-1} V_{rog} \quad . \quad (3.18)$$

with $\alpha = 0.1$ V/A being the constant conversion factor. The transfer function of the test coil can be estimated as

$$g_{rog}(\omega) \cdot S_{eff} = \frac{V_o}{-j\omega\kappa I_{rog}} = \frac{\alpha}{-j\omega\kappa} \frac{V_o}{V_{rog}} \quad . \quad (3.19)$$

The last method is the more direct. By using a second coil with a known frequency response, we can establish a reference for the test coil. If both coils are subject to the same magnetic field,

¹This coil was available in the laboratory and its datasheet or model name is not known.

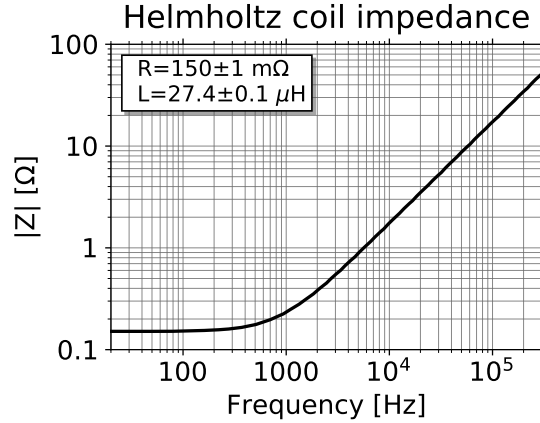


Figure 3.14: Impedance ($|Z|$) of the Helmholtz coil with measurements of the DC resistance and inductance. Measurements taken using four-terminal sensing with a B&K Precision BK891 RLC meter.

the difference in effective area and/or frequency response can be measured. In this case we are interested in the latter. The reference coil was designed with a high frequency response in mind, with only two turns of a thin polyimide insulated cable on a cylindrical former. Having a low effective area of only $S_{ref}=58.6 \text{ cm}^2$, the signal is too low for accurate measurement below 10 kHz. The current can be estimated as

$$I_{ref} = \frac{V_{ref}}{-j\omega\kappa S_{ref}} \quad , \quad (3.20)$$

and the transfer function

$$g_{ref}(\omega) \cdot S_{eff} = \frac{V_o}{-j\omega\kappa I_{ref}} = S_{ref} \frac{V_o}{V_{ref}} \quad , \quad (3.21)$$

where it is assumed that the reference coil is linear throughout the frequency range ($g_{ref} = 1$). Figure 3.15 shows the setup in photograph and schematic representation.

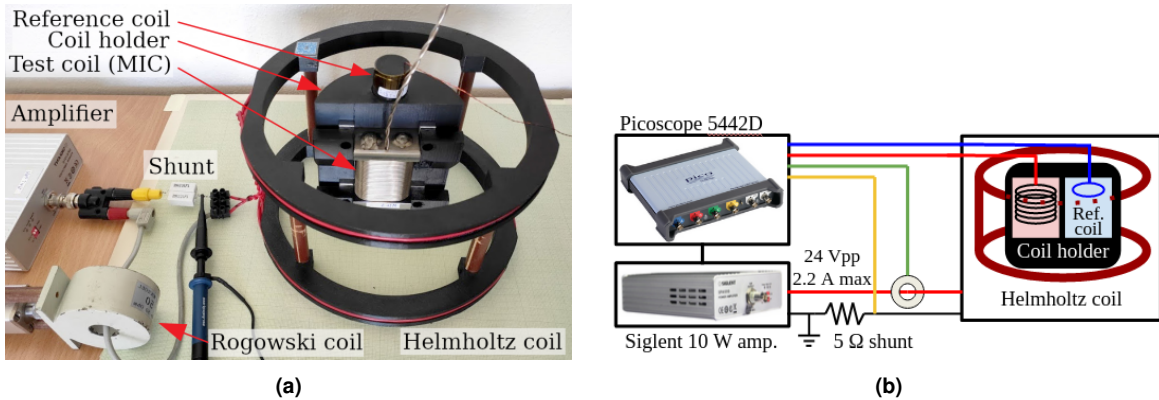


Figure 3.15: a) Labeled picture of the key components of the testbench for frequency measurement. b) Schematic representation of the testbench. Color coded sampled signals are, from top to bottom: reference coil, test coil, Rogowski coil, shunt voltage. Figures published in [31].

Since the accurate measurement of S_{eff} is not to be carried with this setup, one can take only the relative measurements, eliminating all the constant factors ($S_{eff}, \kappa_B, \alpha, S_{ref}$). Figure 3.16 shows the results of the three methods, (3.17), (3.19), (3.21), whereby the voltages are obtained by fitting. In these plots the advantages and disadvantages of each method are evident. The reference coil is not accurate at lower frequencies but provides the best result at higher frequencies. Using the shunt, even with correction for the inductance, there is a substantial error at high frequencies. The Rogowski coil provides the more uncertain result due to the lack of knowledge of the transfer function of the coil and integrator. Furthermore, it shows a resonance at $\sim 5 \text{ MHz}$, particularly evident by the 90° phase shift. Measurements therefore result from the composition of the transfer function obtained with the

shunt up to a merging frequency (f_m) and the reference coil above that frequency:

$$g(\omega) = \begin{cases} g(\omega) = g_{shunt}(\omega) & \text{for } f \leq f_m \\ g(\omega) = g_{ref}(\omega) \frac{g_{shunt}(f_m)}{g_{ref}(f_m)} & \text{for } f > f_m \end{cases} . \quad (3.22)$$

By analysis of the results, $f_m=10$ kHz was found as an appropriate value for the described shunt and reference coil.

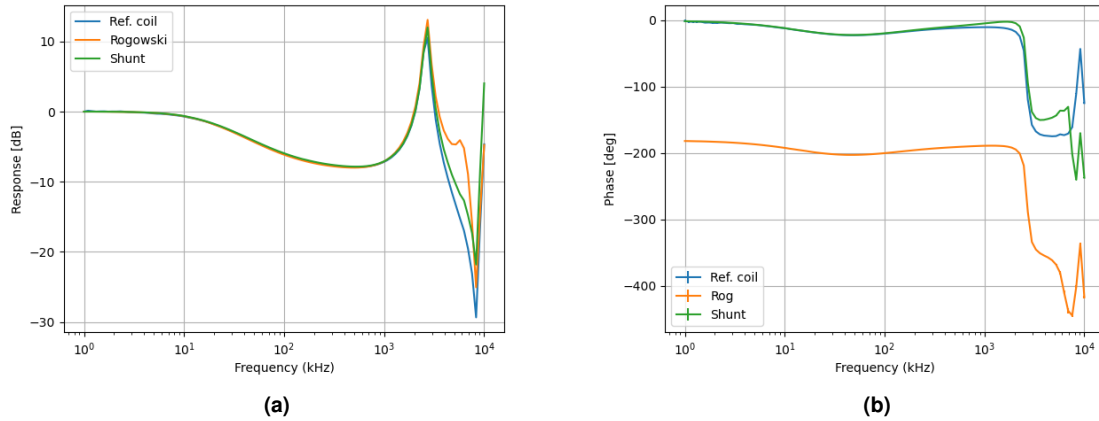


Figure 3.16: The transfer function determined by the three methods: shunt, Rogowski, reference coil. a) magnitude, b) phase. Outputs of the driving/measurement code without processing. Note that the phase for the Rogowski method is shifted by -180° .

3.4.2.C Alignment

The alignment of the test coil inside the Helmholtz coil is achieved through 3D printed parts, designed to ensure sub-mm precision on both calibration setups. The first support (coil holder, figures 3.15a and 3.17a) was designed with a semicircular cross-section that ensures its fit inside the calibration solenoid (section 3.4.3) with the first MIC prototype designed (section 3.5) perfectly aligned in the center. The height of the support centers the prototype in the Helmholtz coil along its axis. Having the precise drawings of all printed parts, the alignment in the other two axes is ensured simply by a printed footprint (figure 3.17b).

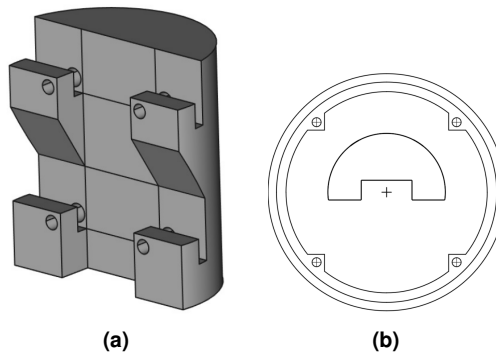


Figure 3.17: a) Coil holder to ensure alignment in both calibration setups. An additional cylindrical hole was drilled to insert the cylindrical reference coil. b) Footprint printed 1:1 to keep the alignment of the holder (and consequently the test coil) in the Helmholtz coil.

For subsequent coil prototypes there was no need to design a new stand-alone holder², but only smaller pieces that ensure the dimensional retro-compatibility to the first prototype, figure 3.18.

²With exception to the normal direction of the 2D MIC coil prototypes, figure 3.18e.

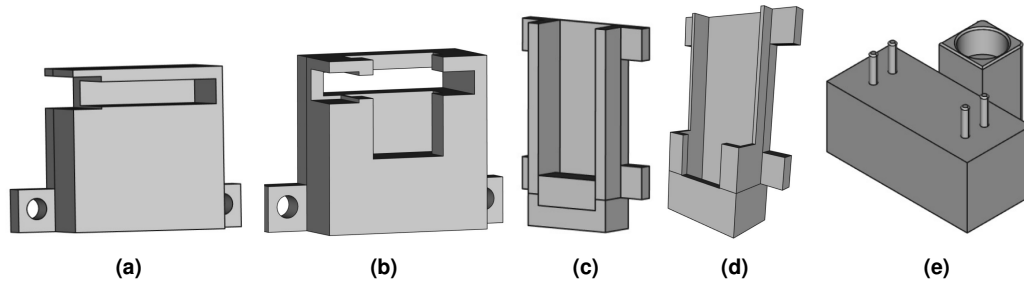


Figure 3.18: Alignment pieces for the sensor prototypes tested: a) TPC sensor; b) bare wire coil (both directions); c) narrow coil designs (MIC{6,7}, EPR1); d) 2D MIC (MIC9) tangential direction; and e) normal direction. See section 3.5 for sensor labels and description. Figures not to scale.

3.4.2.D Automation

The steps described in section 3.4.2.B involve the simultaneous signal generation and signal acquisition by the same equipment, the PicoScope 5442D, a PC oscilloscope with Arbitrary Waveform Generator (AWG). The manufacturer provides a Software Development Kit (SDK) that includes drivers and low-level C Application Programming Interface (API) to control the device [143]. On top of that, a library of python wrappers for the API is also made available by the developers [144].

A python script was developed to automatically drive the Helmholtz coil signal, record the data, analyze it for the determination of $g(\omega)$, and save the data. The key challenge in the automation of this setup is the definition of the oscilloscope ranges (input range) and timescale.

For the timescale, the script computes the minimum acquisition frequency (from the available timebases) that acquires $nPer$ periods of the signal, with $samples$ total samples. These two parameters are configurable by the user. For the input voltages for each signal, the script starts from a pre-configured (typical) set of ranges and performs an acquisition. After acquiring data, and before further manipulation, the algorithm verifies if any of the channels have saturated samples or the signal uses less than 40 % of the input range. If these conditions are not verified, the input ranges on the respective channels are adjusted up or down, accordingly³. If they are, the ‘run’ is deemed valid and the data analyzed.

The number of runs for each frequency is configured by the user and the average values (from the fit results) are saved. In addition, the full time-traces for the last run of each frequency is saved. These can be inspected if there are unexpected results. The algorithm is represented in the flowchart in figure 3.19.

The user-configurable parameters are summarized in the listing 3.1. Beyond those already mentioned, the script also has options to set the amplitude of the signal to be generated, as well as the frequency range, that is exponentially distributed⁴ with $nPoints$ from $fStart$ to $fStop$, including these edges. However, if the *highFreq* flag is parsed, only 20 % of the points are exponentially distributed from *Start* to 100 kHz, with the remaining 80 % providing a high frequency-resolution for high frequencies. This method is particularly useful when there are resonances. These can benefit from a finer resolution, whilst at low frequencies changes are not pronounced. The current, that is resistivity dissipated in the shunt and coil wire, drops exponentially with frequency and therefore, using this method prevents driving high currents ($I_{max} \approx 2$ A) for long periods of time that can damage the coil or shunt ($P_{max, shunt} \approx 10$ W).

³A limit on the number of these iterations is hard-coded. This is above all a safety consideration, as it prevents a particularly noisy signal to lock the algorithm in this loop while high current is being supplied to the coil.

⁴As in equally distributed in a logarithmic scale.

```

usage: DriveHelmholtz_v5.py [-h] [-C configFile] [-f fStart] [-t fStop]
                             [-n nPoints] [-a Amp] [-s samples] [-r runs]
                             [-p nPer] [-P] [-E] [-A] [-R] [-H] [-v]

Drives th Helmholtz coil, aquires and processes the data.

optional arguments:
  -h, --help                show this help message and exit
  -C configFile, --configFile configFile
                           Configuration file, has priority over other flags
  -f fStart, --from fStart
                           Start frequency in kHz
  -t fStop, --to fStop     Stop frequency in kHz
  -n nPoints, --nPoints nPoints
                           Number of frequencies between fStart and fStop
  -a Amp, --amplitude Amp
                           Amplitude of the output signal in mVpp
  -s samples, --samples samples
                           Number of sampling points on each waveform
  -r runs, --runs runs     Number of runs for each frequency
  -p nPer, --periods nPer
                           Approximate number of periods that should be aquired
                           on each run
  -P, --noPlot             Do not plot computed results
  -E, --export             Export the last waveform for each frequency
  -A, --antiPhase         Use if reference coil and test coil are in antifase
  -R, --shunt             Using shunt resistor on ch D.
  -H, --highFreq          Uses only 1/5 of points for f < 100 kHz and the
                           remaining evenly spaced until fStop
  -v, --verbose           Verbosity

```

Listing 3.1: ‘Help’ terminal output of ‘DriveHelmholtz_v5.py’, the script to run a measurement with the Helmholtz coil setup. Usage and possible configuration parameters are deailed.

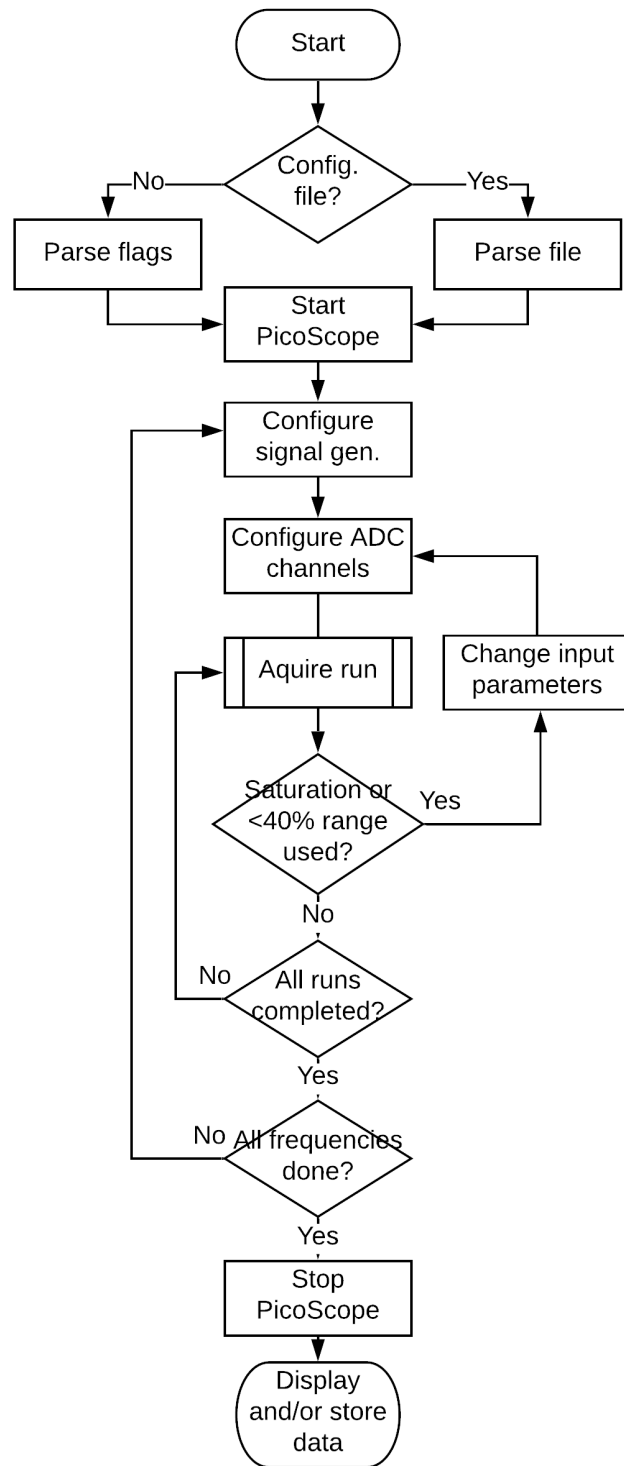


Figure 3.19: Flowchart of the algorithm for 'DriveHelmholtz_v5.py', the script to run a measurement with the Helmholtz coil setup.

3.4.3 Effective area measurements

For the measurement of S_{eff} instead of a Helmholtz coil, a long solenoid is used, see figure 3.21. A harmonic signal is generated by the oscilloscope AWG, amplified by a Kepco 100 V amplifier. Since the frequencies used are up to 1 kHz the current is measured through a shunt – typically, a 2 Ω resistor is used.

The solenoid is constructed with two layers of thick polyimide insulated copper cable, generating $\kappa=637.8 \mu\text{T/A}$ (full parameters in table 3.3 and figure 3.20).

Table 3.3: Physical and electrical parameters of the solenoid

Parameter	Value
Inner diameter ID	52 mm
Length l	73 mm
Inductance L	$847(\pm 1) \mu\text{H}$
DC resistance R_L	$190(\pm 1) \text{m}\Omega$
Magnetic field κ	637.8 $\mu\text{T/A}$

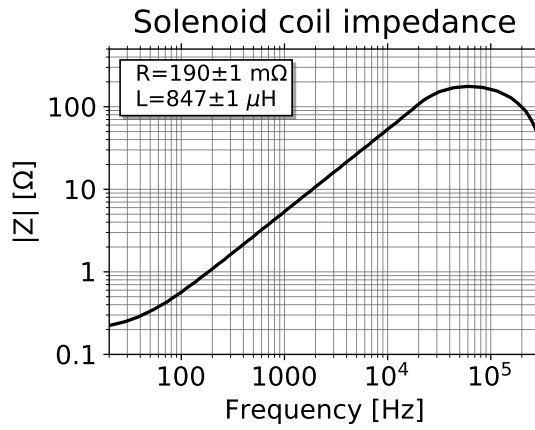


Figure 3.20: Impedance ($|Z|$) of the solenoid with measurements of the DC resistance and inductance. Measurements taken using four-terminal sensing with a B&K Precision BK891 RLC meter.

The amplifier used is limited to 100 V or 4 A and a reasonable frequency response up to the kHz range. The effective area is determined by computing $S_{eff} \cdot g(\omega)$ as in (3.17):

$$g(\omega) \cdot S_{eff} = \frac{V_o}{-j\omega\kappa I_{shunt}(\omega)} = \frac{R_{shunt}}{-j\omega\kappa} \frac{V_o}{V_{shunt}} \quad (3.23)$$

The Rogowski coil for current measurement can be optionally connected, as well as the monitoring of the solenoid voltage, while no reference coil is used. The electrical connection can be seen in figure 3.22a. The driving process is automatized similarly to the Helmholtz configuration. However, the concept of multiple runs is dropped due to the high currents involved.

The script saves all raw data, allowing further processing, as well as the result of $S_{eff} \cdot g(\omega)$. The effective area is obtained fixing that for the lowest frequency $g \equiv 1$. Processing scripts were developed to average sequential runs (improving the accuracy) and to merge the frequency response data ($g(\omega)$) up to (and including) 1 kHz with the measurement with the Helmholtz coil. The process is as described in (3.22) and allows a global frequency response description of the sensor on an even wider frequency band, as exemplified in figure 3.23.

3.4.3.A Accuracy and external calibration

In order verify the accuracy of the calibration testbench, an independent calibration was sought. Two different forms of external calibration were used: (i) independent measurement of S_{eff} for two

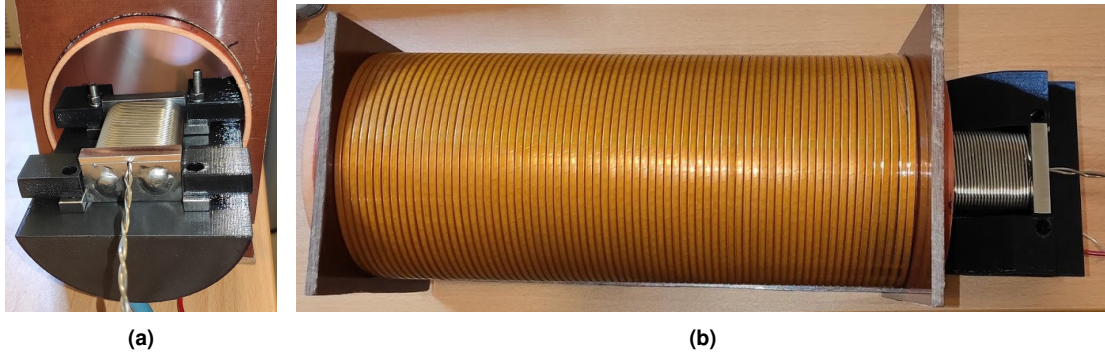


Figure 3.21: Solenoid and test coil insertion. A MIC prototype is centered inside the solenoid through a coil holder. a) Front view, b) top view.

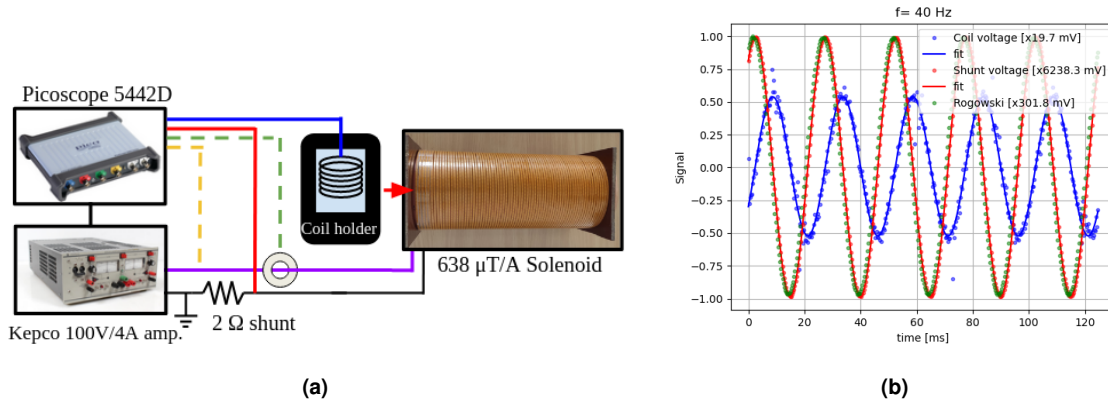


Figure 3.22: Effective area measurement setup in schematic representation: a); and signals and corresponding fits for a 210 cm² test coil at 40 Hz: b). The plot represents 1/10 of the total acquisition time, with 1/10 point density, i.e. 1 % of the total number of points used in the fitting.

coil prototypes; (ii) measurement of the magnetic field coefficient in the solenoid (κ). The calibrations were performed at the [Czech Metrology Institute \(CMI\)](#).

The sensors calibrated at [CMI](#) were a MIC sensor (MIC1) that has strong response derating with frequency; and a bare wire coil (FC1), the prototype with the smallest effective area, and therefore the most problematic to measure. Table 3.4 shows comparison of the measurements of S_{eff} at 40 Hz. The results show that the calibration testbench is accurate to 0.5%, with both measurements being below the those carried out at the [CMI](#), below its uncertainty⁵. The fact that the deviation is much larger for the largest sensor indicates that the physical size plays an important role, as the point-like approximation is less valid.

Regarding the precision of the measurement, we can see in the table that, for measurements at 40 Hz, the very low coil signal on the smallest coil increases the dispersion of the measurement from 0.15 % to 0.17 %, due to the low voltage measurements.

Table 3.4: Calibration of selected prototypes effective area (S_{eff}) at [CMI](#). Measurements at 40 Hz.

Coil	S_{eff} IPP [cm ²]	S_{eff} CMI [cm ²]	Deviation
FC1	39.92 ± 0.07 (0.17 %)	39.969 ± 0.12 %	-0.12 %
MIC1	421.82 ± 0.64 (0.15 %)	423.47 ± 0.12 %	-0.40 %

The measurement of the frequency response in amplitude ($|g(\omega)|$) also has a good agreement with the measurements with the Helmholtz coil. In these, the accuracy *per se* is not as important as the accurate representation of the behavior (stable, attenuation, resonances). This is achieved, as can be seen in figure 3.24

⁵The uncertainty for the CMI values is defined as a confidence interval of 2 standard deviations, for a normal distribution. That is, statistically covers approximately 95% of the probability. This is valid for all CMI measurements presented.

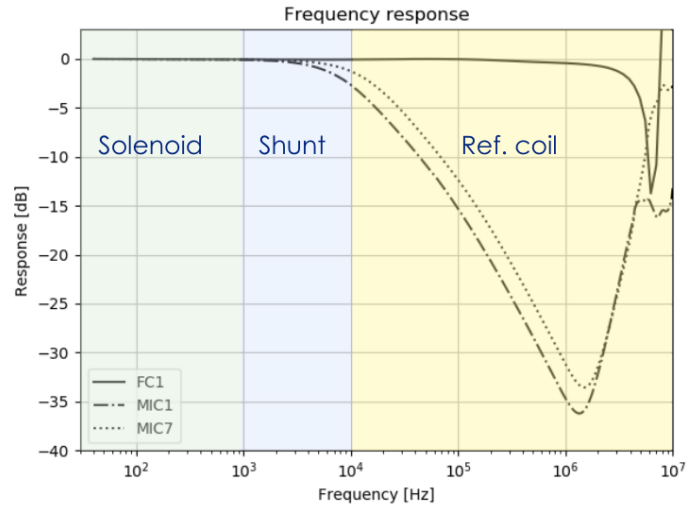


Figure 3.23: Composition of the frequency response ($g(\omega)$) of three different sensor prototypes (see section 3.5). Up to 1 kHz $g(\omega)$ is determined using the effective area calibration setup, while beyond the Helmholtz coil is used. Up to 10 kHz according to the shunt current measurement, and beyond using comparison to a reference coil.

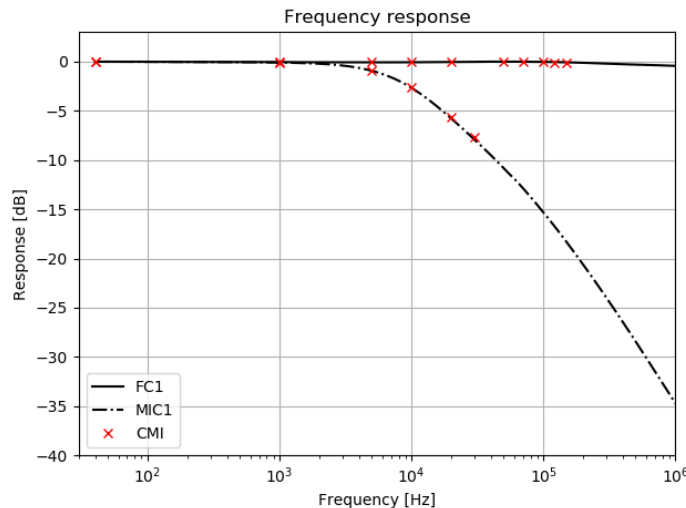


Figure 3.24: Frequency response (amplitude) comparison of the measurements at IPP (black line) and at CMI (red crosses).

Regarding the calibration of the solenoid magnetic field, we can see in table 3.5 that the deviation of the measurements to the originally calculated value for κ is much smaller than its uncertainty. Meaning the computation of κ was accurate. In light of these measurements, the uncertainty in κ is estimated as $\sigma(\kappa) = 0.1\%$ ⁶.

Finally, the homogeneity of the field inside the solenoid was also measured: along its magnetic axis (z) and in the radial direction (r). Despite a systematic deviation of the measurements to the simulated line being noticeable in the plots in figure 3.25, all points fall into the measurement uncertainty. The discrepancy can arise from ‘real-world’ dimensional and electrical factors not accounted on the parallel, infinitely thin filaments used in the simulation. Another important conclusion from this plot is that the setup is not very sensitive to systematic misalignment of the coil holder inside the solenoid. That is, to have an influence of tenths of percent on the measurement (precision scale), the misalignment must be on the order of ~ 1 cm, while with naked eye the coil can be centered to ~ 1 mm accuracy.

When the solenoid was designed, the accuracy goals were not specified to such a high standard. Only with the automation and continuous improvement of the testbench, the precision lowered to

⁶This uncertainty is reflected in all measurements, including those already shown.

Table 3.5: Calibration of the solenoid magnetic field coefficient (κ) at CMI.

Frequency [Hz]	κ [$\mu\text{T/A}$]	Deviation
Calculated	637.82	–
40	638.2 \pm 0.5 %	+0.06 %
1000	638.5 \pm 0.3 %	+0.1 %

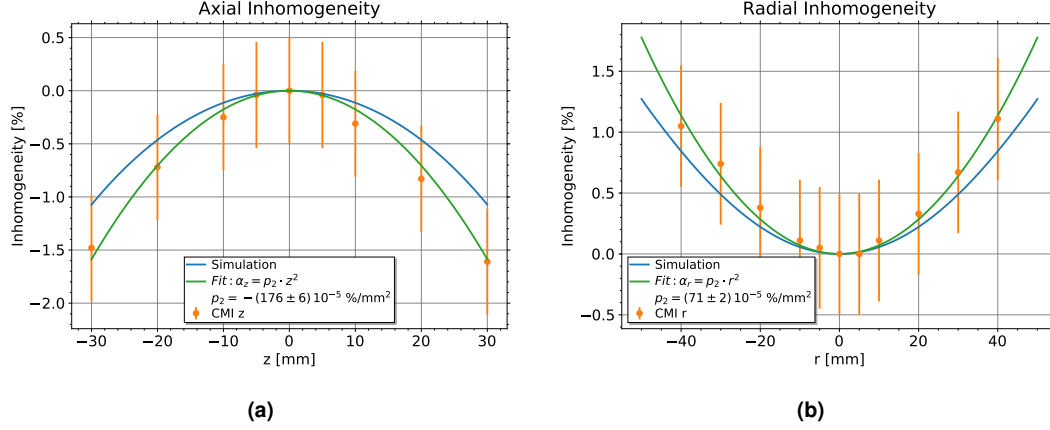


Figure 3.25: Inhomogeneity of the magnetic field inside the solenoid in the axial $-z$, (a) – and radial $-r$, (b) – directions. Inhomogeneity defined as $\alpha_{z,r} = (B(z,r) - B_0)/B_0$. Simulated values (line) agree with the CMI measurements (circles) considering the measurement uncertainty, despite a systematic deviation being noticeable. Parabolic fits by least squares to the measurements also shown.

< 0.2 % and the initial criterion of 1 % inhomogeneity at the edges of the sensor is now too crude. However, this inhomogeneity can be corrected.

Defining the inhomogeneity at each point (α) as the relative deviation to B_0 :

$$\alpha = \frac{B - B_0}{B_0} \quad , \quad (3.24)$$

this value can be integrated along the length of the sensor or the full volume for the length or volume averaged field for each sensor inside the solenoid. The measurements have shown that there is a roughly parabolic dependence of α in the axial and radial directions (see figure 3.25):

$$\alpha_z = p_{2,z} z^2 \quad , \quad (3.25)$$

$$\alpha_r = p_{2,r} r^2 \quad . \quad (3.26)$$

Integrating over the sensor dimensions in z and r , one obtains 1D and 2D correction factors (β_{1D} , β_{2D}) expressed as relative correction like in (3.24) that is equivalent to multiplying the κ in (3.23) by a correction factor $(1 + \beta)$. The 1D and 2D integrations can be computed analytically without introducing numerical integration errors. For the 3D correction, one can get a good estimation by multiplying the 1D and 2D correction factors:

$$(1 + \beta_{3D}) = (1 + \beta_{1D}) \cdot (1 + \beta_{2D}) \quad . \quad (3.27)$$

The calculation of the area integrals for the relevant cross-sections of the prototypes tested (circular, rectangular, racetrack) is provided in appendix B and yields the following coefficients for the sensor prototypes⁷:

Applying these coefficients to the measured values (table 3.4) one obtains a much more accurate result (defining accuracy by the deviation to the independent CMI measurement), see table 3.7. Including this correction, we can establish the setup has an accuracy and precision < 0.2 %. When propagated downstream, this result is also in compliance with the needed accuracy on the equilibrium reconstruction.

⁷The same appendix also shows the full table with coefficients for all the tested prototypes.

Table 3.6: Calculation of correction coefficients due to the inhomogeneity of the magnetic field inside the solenoid.

Coil	Physical parameters [mm]	β_{1D} [%]	β_{2D} [%]	β_{3D} [%]	$(1 + \beta_{3D})$ []
FC1	Rectangular, $l=30, w=24, h=5$	-0.1323	0.0356	-0.0967	0.999033
MIC1	Racetrack, $l=50, a=10.5, R=9.5$	-0.3674	0.0986	-0.2692	0.997308

Table 3.7: Effective area of prototypes corrected for 3D field inhomogeneity ($S_{eff}/(1 + \beta_{3D})$) and comparison with the measurements at CMI. Measurements at 40 Hz.

Coil	S_{eff} IPP corrected [cm ²]	S_{eff} CMI [cm ²]	Deviation
FC1	39.95 ± 0.07 (0.17 %)	39.969 ± 0.12 %	-0.04 %
MIC1	422.96 ± 0.64 (0.15 %)	423.47 ± 0.12 %	-0.12 %

3.4.4 Rogowski coil measurements

The testing procedure for the effective area is adapted also to calibrate the Rogowski coil prototypes. Instead of the solenoid, the high current is driven through a wire loop, encompassed by the Rogowski coil under test. The signal at the test coil terminals is

$$V_o = -\mu_0 n S \frac{\partial I}{\partial t} \equiv -\kappa \frac{\partial I}{\partial t} \quad , \quad (3.28)$$

where n is the turn density and S the area of each turn. Instead of considering the effective area nS , we include also the constant (vacuum) magnetic permeability in the calibrated parameter $\kappa = \mu_0 S_{eff}$. This is convenient as κ is expressed as Vs/A, i.e. directly proportional to the current. With this setup, κ is determined as:

$$\kappa = -\frac{V_o}{\omega I_{shunt}} = -\frac{R_{shunt}}{\omega \kappa} \frac{V_o}{V_{shunt}} \quad . \quad (3.29)$$

Figure 3.26 shows the result of the calibration of a Rogowski coil prototype using this method. The value of $\kappa=34.1$ nVs/A is determined by averaging from 1 kHz to 10 kHz.

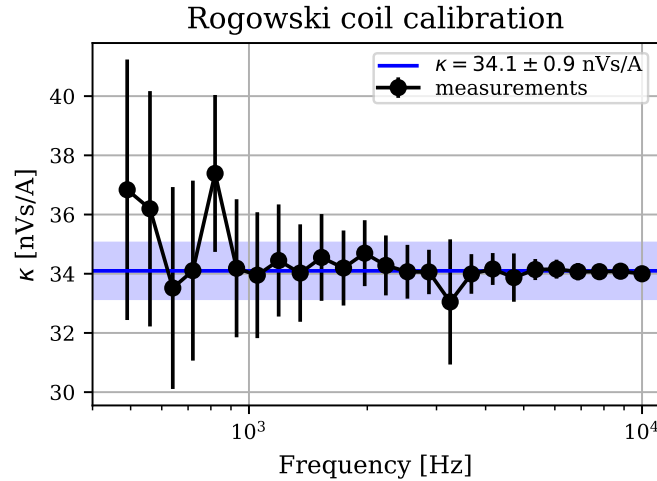


Figure 3.26: Determination of a Rogowski coil prototype constant. Lower frequencies show a large uncertainty due to low signal.

3.5 Sensor prototyping and development

This section details the R&D efforts carried in support of the design of the final COMPASS-U magnetic sensors. The key challenges were the choice of MIC parameters, sensor design for the equilibrium coils and support to the development or to the testing of the sensors developed externally.

In some instances, this work was carried out in parallel to the development of the calibration testbench described in the previous section. For this reason some plots or results are not done to the same accuracy/precision as described, however, this should have no effect on the conclusions, that are mostly qualitative.

3.5.1 Mineral Insulated Cables

Having discussed the advantages and widespread usage of MIC in magnetic diagnostic in section 2.4.1, it is important to discuss the technical parameters that define the cable. There main components and therefore three materials to consider: the conductive core, the insulation, and the sheath.

The conductor will influence directly the resistivity of the sensors. As this type of cables see application in thermocouples, several core materials are commercially available. In general, the higher the conductivity, the better for sensor manufacturing. For this reason copper is a prime candidate. Due to the application of these cables at higher temperatures, it is common to find nickel added to the conductor, either as an alloy or as a coating (nickel-clad copper). The addition of nickel has a small influence on the conductivity but prevents oxidation of the copper and enhances durability and stability at high temperatures.

The insulation layer comes in the form of a compacted ceramic powder. Two materials are the industry standards: MgO, magnesia; and Al₂O₃, alumina. The two have similar electrical proprieties, of which the most significant for this application is the resistivity. The resistivity is hard to compare, as it is extremely dependent on the measurement conditions (test method, purity, compactation level) [145]. While on the same order of magnitude, some sources state a higher resistivity to magnesia, particularly on the interest temperature range [146]. Whilst other sources point that the measuring conditions (physical, electrical) can make the resistivity range orders of magnitude [145].

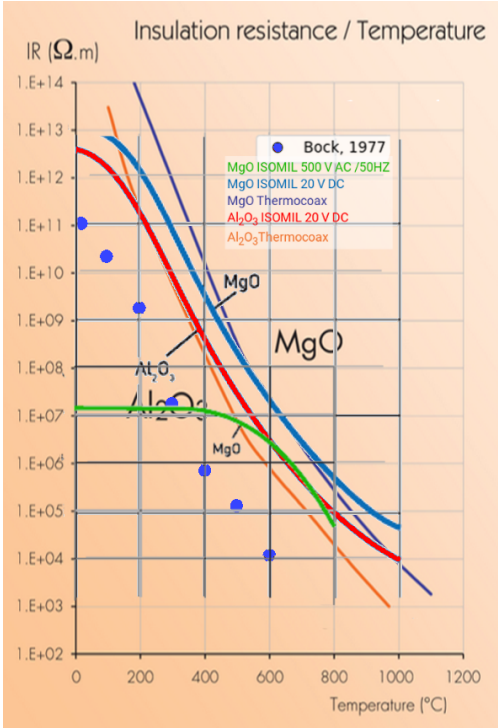


Figure 3.27: Superposition of different plots of MgO and Al₂O₃ MI cables insulation resistance. The majority of the curves is gathered from brochures of two manufacturers (Thermocoax, Isomil) and the series 'Bock 1978' refers to the 1.5 mm OD MgO insulated cable values in [147].

A perhaps more interesting comparison between the materials can be made using commercial products. Figure 3.27 shows this comparison, through the overplotting of different insulation resistance curves on MIC brochures and on literature [147]. From this data we can see that MgO products tend to have higher insulation than its alumina counterparts. It is extremely important to note that the resistivity of both these materials changes by several orders of magnitude with temperature, in the range of COMPASS-U VV temperature range.

The sheath material is typically stainless steel. The vessel mounted sensors will interface with inconel, however this is not a standard material for MIC. From the common stainless steel alloys, ANSI 316L is a good candidate, as it is non-magnetic and is used in other stainless steel in-vessel components.

Besides the materials, the dimensions for these three components are important. Samples of MIC with copper conductor, MgO insulation, and stainless steel sheet from different manufacturers were bought for testing. These are labeled from A to G in table 3.8, sorted by OD.

Table 3.8: Description of the MIC samples and measured electrical proprieties. Originally published in [148].

MIC	Manufacturer	OD [mm]	Core diam. [mm]	Sheath thick. [mm]	$R_{(25\text{ }^{\circ}\text{C})}$ [Ω/m]	α [10^{-3} K^{-1}]	$C_{(25\text{ }^{\circ}\text{C})}$ [nF/m]
A	Thermocoax	0.5	0.20	0.10	0.727	4.0 ± 0.1	0.49
B	Thermocoax	1.0	0.45	0.12	0.231	4.8 ± 1.0	0.42
C	ARi Industries	1.55	0.305	0.152	0.356	3.8 ± 0.2	0.25
D	Sukegawa	1.6	0.53	0.22	0.090	4.2 ± 0.7	0.45
E	Thermocoax	3.0	0.45	0.39*	0.031	2.3 ± 0.4	0.43
F	MICC	3.0	0.45	0.45	0.122	3.4 ± 0.3	0.23
G	Sukegawa	3.2	0.85	0.37	0.044	3.9 ± 1.4	0.45

*estimated

Beyond the cable description, the table also show electrical proprieties measured using 10 m long samples – resistance and capacitance at room temperature, as well as the resistance thermal coefficient, defined as

$$R(T) = R(T_0)(1 + \alpha \cdot \Delta T) \quad (3.30)$$

The values of the resistance are in line with the expectation for copper based cables, when considering the conductor area. This can be observed in figure 3.28. Regarding the capacitance (plot on the right), cables C and F show a much lower capacitance than the remaining. As discussed for the insulation resistance, the insulation depends not only on the thickness but also on the purity and powder quality.

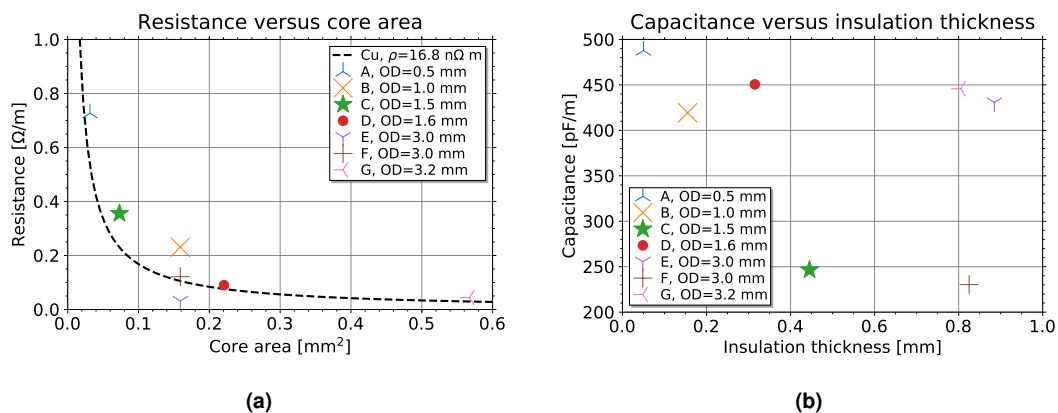


Figure 3.28: (a): Core conductor resistance per unit length versus conductor area. Reference of copper indicated as dashed line. (b): Capacitance between core and sheath per unit length versus insulation thickness.

The temperature dependence on R and C can be seen in figure 3.29. The value for α on table 3.8 was obtained from measurements of resistance $R(T)$ at different temperatures, to which (3.30)

was fitted. The resistance variation with temperature is once again in line with the value for copper ($\alpha_{Cu} = 4.04 \cdot 10^{-3} \text{ K}^{-1}$ [149]), with exception to cable E.

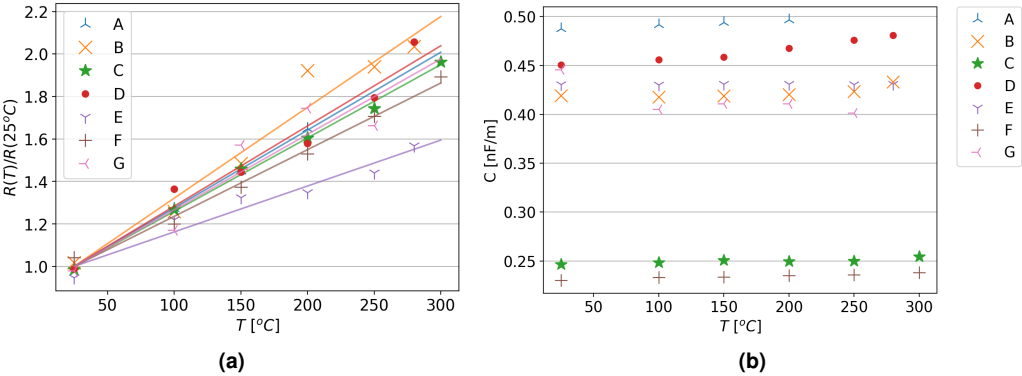


Figure 3.29: (a): Core conductor resistance dependence on temperature for MIC. Linear fit for the thermal coefficient. Resistance values normalized to the resistance at 25 °C, as given by the fitting results. **(b):** Temperature dependence of capacitance between core and sheath per unit length. Both plots originally published in [148].

3.5.2 Flux loop measurements on COMPASS

More important than the resistive and reactive properties of the cable, is the attenuation of the magnetic field that induces the sensor signal. Flux loops are simple enough that can be installed ex-vessel on COMPASS ($R=0.892$ m). The signal source is the toroidal electric field of the tokamak. Plasma oscillations induce signal in a broad spectral band. The loops were insulated from the vessel, each-other and other peripherals installed ex-vessel at midplane. This was done out safety concern, due to the ‘piggyback’ nature of the experiment. In some pulses, the shielding was grounded to the vessel, see figure 3.30. In addition to the MICs B–G (the thinnest was not used), an extra flux loop made out of regular flexible wire of comparable diameter was wound. This loop, having no metallic sheath will serve as reference to the analysis, showing what attenuation we can expect from the shielding.

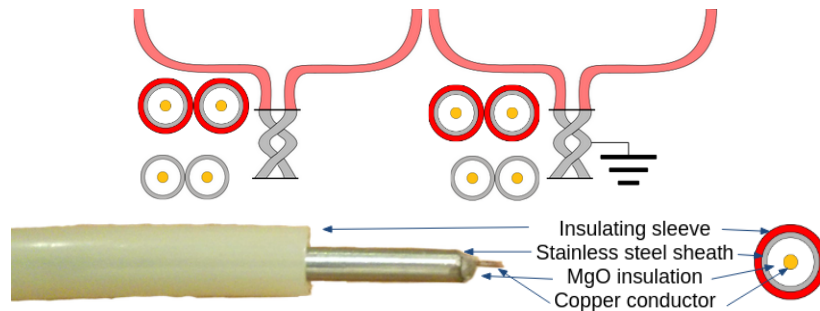


Figure 3.30: On top, the two configurations used on each flux loop. The sheath on the loop itself was insulated from the vessel and peripherals but in electrical contact at the twisted pair. On some pulses the sheet was grounded to the vessel (right). On the bottom, the cross-sections are illustrated and labelled.

At a global (full pulse) first glance, the measurements look identical, which was expected. Once we look at the sub-millisecond timescale the effect of the shielding starts being apparent. Figure 3.31a shows a time trace of the reference loop and one of the MIC loops with the thickest shielding, G. A small attenuation of the fluctuations can be observed. This is particularly noticeable in comparison to the reference signal filtered with a 67 kHz first order low-pass filter. The filter is applied digitally to the reference signal. For this reason the very high frequency noise that is added on the DAS is also attenuated, which is not true for the MIC signal. On the MIC this noise is also present, only the inducted signal is ‘filtered’. The attenuation also manifests itself by a delay of a few samples at the local maxima and minima. By calculating the cross-correlation of the MIC and the digitally filtered signals to the reference, we can quantify this delay or lag to around $1.5 \mu\text{s}$ – see figure 3.31b.

A more systematic comparison can be established using Fourier analysis. The fact that the source of the magnetic signal is not constant in amplitude across frequency or time poses a challenge for the interpretation of the results. Instead of a simple Fast Fourier Transform (FFT) with the full signal, the Welch method [150] provides a more stable estimation of the power spectrum by relying on time-averaging. The last plot in figure 3.31 shows the ratio of the power spectra of the MIC over the reference. Spectra obtained by Welch method of a 10 ms section of the signal, using FFT segments of 8000 points, weighted by a Hann window⁸:

$$\text{Power ratio}(\omega) = 10 \log_{10} \left[\frac{P_{\text{Welch MIC}}(\omega)}{P_{\text{Welch Ref.}}(\omega)} \right] . \quad (3.31)$$

Once again we can observe a general agreement with the transfer function of the filter. The agreement is not perfect, with some bands exhibiting large deviations. This is not unexpected with the limitations of this method already discussed: ratio of numerically low values ($\approx [-10, -60]$ dBV), close to the noise floor of the DAS. An additional issue is noise (non-inductive signal) added at specific frequency bands. Moving forward with the analysis the transfer function of the first order filter was fitted to power ratios, with two frequency bands excluded from the fitting: around 35–50 kHz, constant in spectrograms, even in magnetic silence; and around 100–170 kHz, band with the lowest power and with low agreement with the general behavior (see figure 3.31c).

⁸The caption on the figure reads ‘hanning’. This term is, however, incorrect. The namesake of this popular window function is the meteorologist Julius von Hann, hence Hann window. The term ‘hanning’ appears as a parallel to the also popular (and mathematically similar) Hamming window. However, the namesake of the latter is the mathematician Richard Hamming.

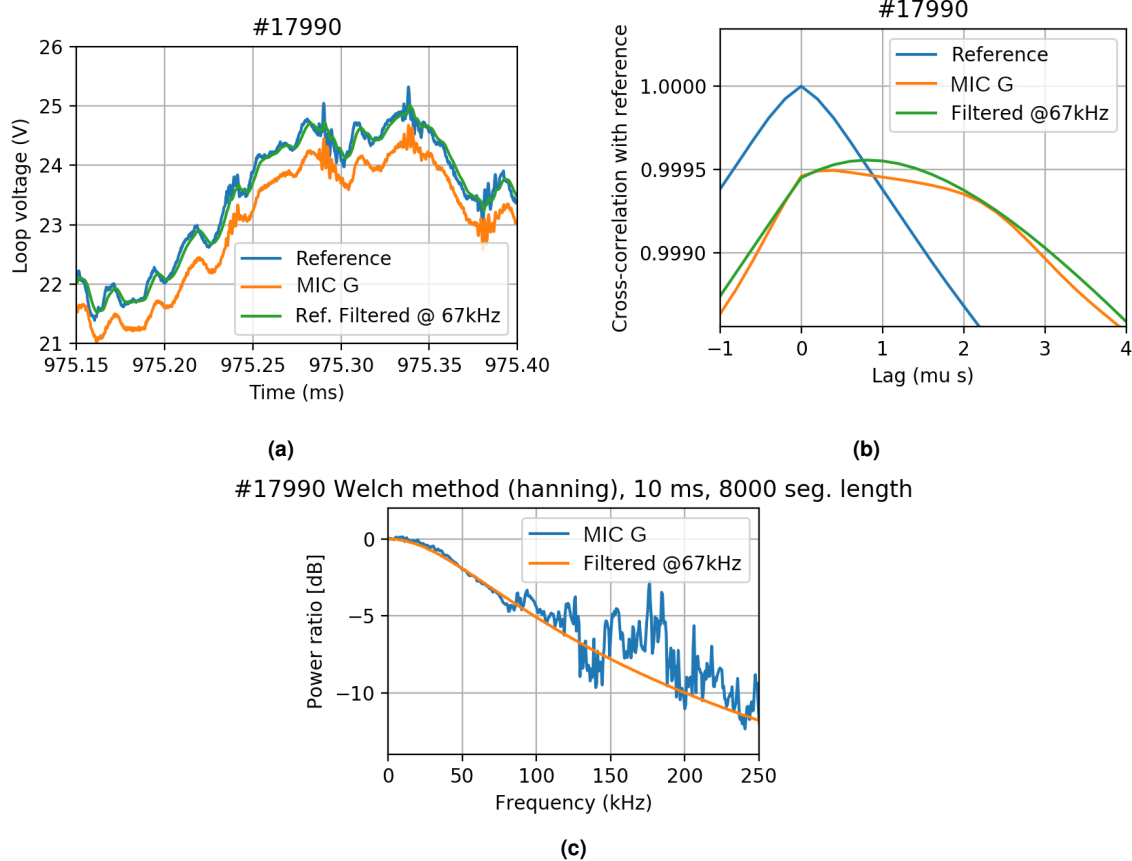


Figure 3.31: (a): Signal of the reference and MIC G flux loops on a sub-millisecond time window. Green line shows the reference flux loop signal filtered with a 67 kHz first order low-pass filter. (b): Cross-correlation of the signals with the reference flux loop signal. (c): Frequency response of the filter and ratio of the power spectra of the MIC and reference flux loops. Spectra obtained by the Welch method, using a 10 ms time window and segments of 8000 points.

Repeating this analysis on different pulses⁹ and different time intervals of ≈ 10 ms. As the analysis involves fitting, it is possible to estimate a fit uncertainty. Table 3.9 shows the estimation cutoff frequency for the tested loops, as an average weighed by the inverse of the uncertainty, i.e. better fits carry more weight, without discarding measurements. The uncertainty value is taken as half the maximum amplitude: $\sigma_X = 1/2(\max(X) - \min(X))$, since the dispersion of the measurements is much larger than the fit uncertainty for each measurement.

Table 3.9: Obtained flux loop cutoff frequencies (F_c) and delay, determined by the maximum of the cross correlations.

MIC	f_c [kHz]	Delay [μ s]	MIC	f_c [kHz]	Delay [μ s]
B	328 ± 56	0.2 ± 0.1	E	92.8 ± 13	1.3 ± 0.1
C	335 ± 50	0.2 ± 0.1	F	64.8 ± 16	1.8 ± 0.1
D	220 ± 7	0.3 ± 0.1	G	69.8 ± 19	1.8 ± 0.1

These results seem to show that the cables with larger diameter have a stronger attenuation of the high frequency components. The plot in figure 3.33 shows the obtained cutoff frequencies against the shielding thickness. With so few, irregularly distributed, data points it is not easy to draw a conclusive model. However, the downwards trend is clear. Roughly, the frequency response, as defined by the half-power point, decreases by 90 kHz for each 0.1 mm of additional shielding thickness.

⁹Not all cables were acquired in every pulse as only 6 data acquisition channels were available, one being used by the reference.

#17986, Welch method power spectra relative to Ref.1050-1085 ms, 5000 points segments

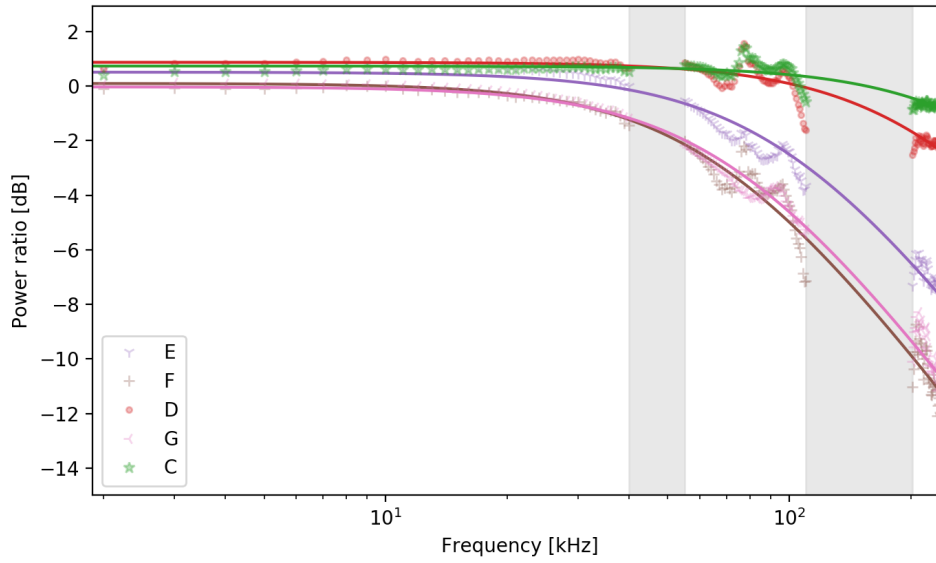


Figure 3.32: Example of the fitting of first order low-pass filters to the power spectra ratios for different MIC cables. Cable legend available in table 3.8. Shaded bands not considered in the fitting. Originally published in [148].

The delay values are also enlightening as there is a clear difference between the thin cables (B–D) and the thick cables (E–G). From a 1.5 mm to a 3 mm cable there is a 9-fold increase in the mean delay. This is an analogue delay, i.e. the attenuated signal will not lag by this amount as it depends on the input signal spectrum. Having used a real tokamak magnetic signal, we gain insight on the effect the usage of MIC has on upstream systems such as real-time control systems.

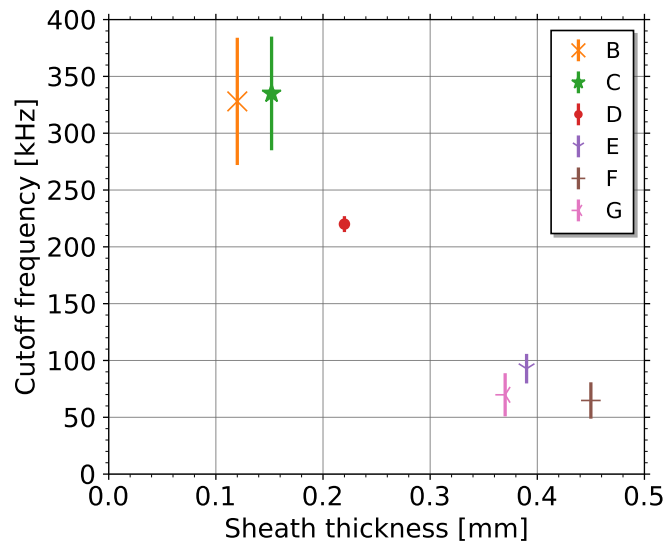


Figure 3.33: Estimated flux loop cutoff frequency versus MIC shield thickness.

3.5.3 MHD probes calibration

One of the most important limiting factors on the operation of ‘fast’ sensors for the detection of MHD activity is the appearance of resonances. From an electricronic point of view, the inductive magnetic sensors are essentially an inductive load. When connected to the long cables that typically connect the sensors to the DAS, the capacitance of the cables will create multiple resonances. More generally, all capacitive components will influence these resonances, shifting its frequency and the exponential growth rates. In fact, even the parasitic capacitance of the sensor itself (C_p) will resonate with the self-inductance (L_p) generating a peak in the frequency response at approximately

$$2\pi f_0 = \frac{1}{\sqrt{L_p C_p}} \quad , \quad (3.32)$$

If only discrete capacitances were considered, these would add in the denominator, hence shifting the frequency. With a long cable, the capacitance is distributed in space, and the propagation of the waves in the medium is relevant. The sensor-cable-DAQ system has to be interpreted in light of the telegraphist equation (see section 2.3.1.D) with the cable terminated by the probe on one end and data acquisition on the other, or by a lumped element modeling using simulation software.

For COMPASS-U, two dedicated sensors are planned for the detection of fast oscillations: Bare wire and TPC sensors (see section 3.3). Both these sensors are being developed externally, with prototypes having been provided for testing. The parameters of these sensors are summarized in table 3.10, where the resistance and inductance measurements are obtained from the fit of a series LR model to the impedance measurements in figure 3.34.

Table 3.10: Measured electrical proprieties of the MHD sensor prototypes.

Parameter		FC1	TPC1
R_p	Ω	0.347 ± 0.004	1.929 ± 0.005
L_p	μH	6.05 ± 0.01	23.191 ± 0.009
S_{eff}	cm^2	39.95 ± 0.07	110.8 ± 0.2

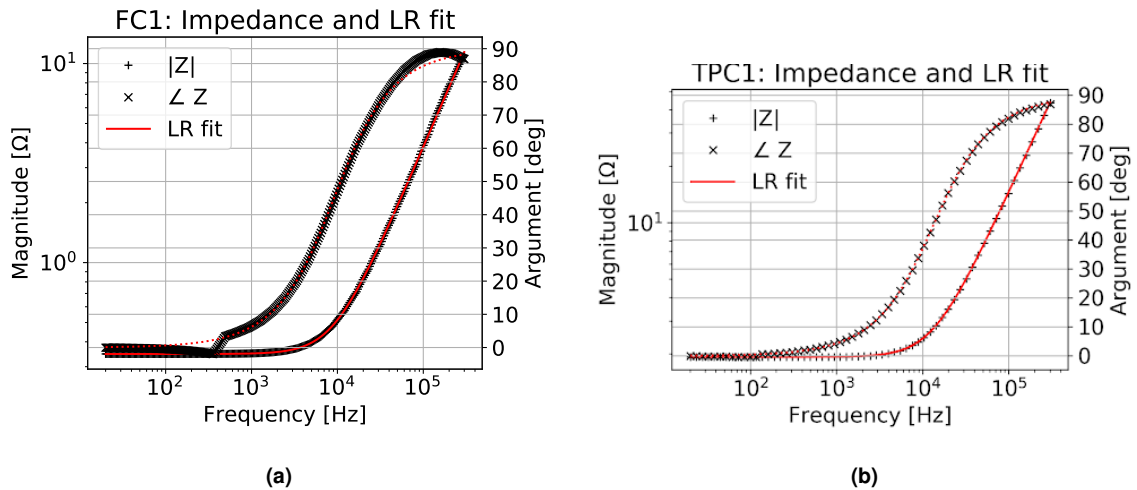


Figure 3.34: Impedance measurements of MDC coil prototypes. (a): FC1, (b): TPC1.

Measuring the frequency response of these sensors, just before the roll-off of LR attenuation, we observe a resonance at a high frequency (>1 MHz). On the frequency response plots, this resonance manifests itself as a peak in the magnitude and a phase drop of 180° . This can be observed in figure 3.35a that shows the frequency response measurement of 5 TPC sensor prototypes, most exhibiting the resonance at 6.05 MHz, 5.8 MHz for prototype TPC4. This frequency is not exactly the self-resonant frequency of the sensor (compromised of the coil and ≈ 15 cm fiberglass-insulated twisted pair lead), f_0 , as the input impedance of the DAS also has a capacitive component, C_x (see

figure 3.36). Modifying (3.32) to include the total resonance:

$$2\pi f_{res} = \frac{1}{\sqrt{L_p(C_p + C_x)}} \quad (3.33)$$

we obtain an estimate of $C_p = 15.8$ pF.

In order to see the effect of the addition of cables, two 15 m coaxial cables were assembled. Figure 3.35b shows the frequency response of one of the prototypes (TPC2) with and without the 15 m cables. We can observe the frequency shifted to a sub-MHz frequency.

Taking a step back, we can ponder the implications for the diagnostic, taking this prototype measurements as example. A sensor is designed with a flat frequency response up to 1 MHz and with its first resonance well above this mark. Upon connecting this sensor to the data acquisition in a different room, the resonance is shifted below 1 MHz. Since the resonance has a finite Q , i.e. it is wide, at 600 kHz the probe system already exhibits a gain of 6 dB (x2). A careless interpretation of the sensor (or sensor arrays) data could induce the user into wrong conclusions, for instance, that a MHD mode is growing in intensity as it chirps up, when in fact the opposite can be happening.

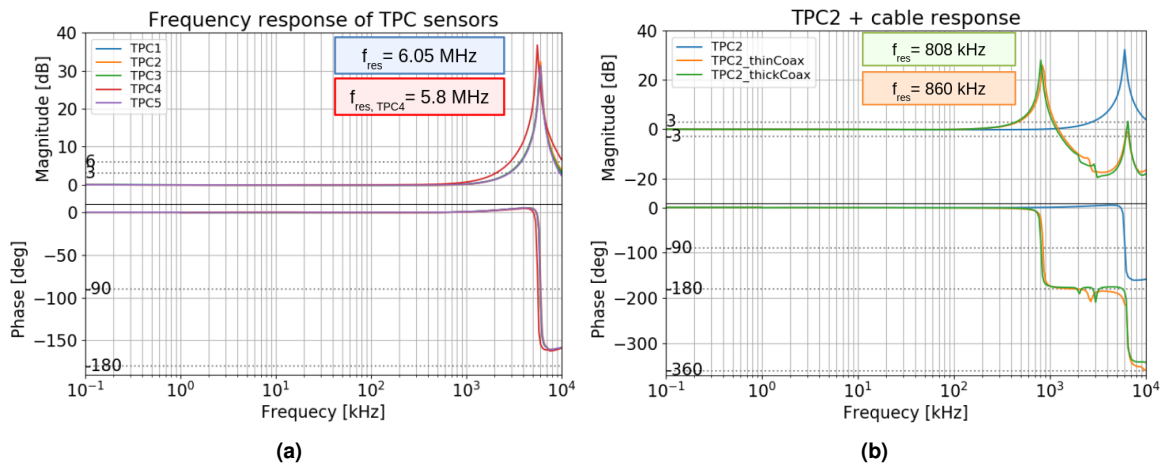


Figure 3.35: Measurement of frequency response of TPC sensors. (a): Without cables, for 5 prototypes. (b): Of prototype TPC2 without and with 2 different coaxial cables connected. Cables labeled as: RG-174/U - 'thinCoax'; RG-58/U - 'thickCoax'.

Both coaxial cables are nominally 50Ω cables, with one being thin (RG-174/U) and the other thick (RG-58/U) in OD. The values for the resistive and reactive proprieties (R_c , L_c , C_c) were measured. With these, we have estimates off the most important parameters for the simple coil model, as seen in figure 3.36.

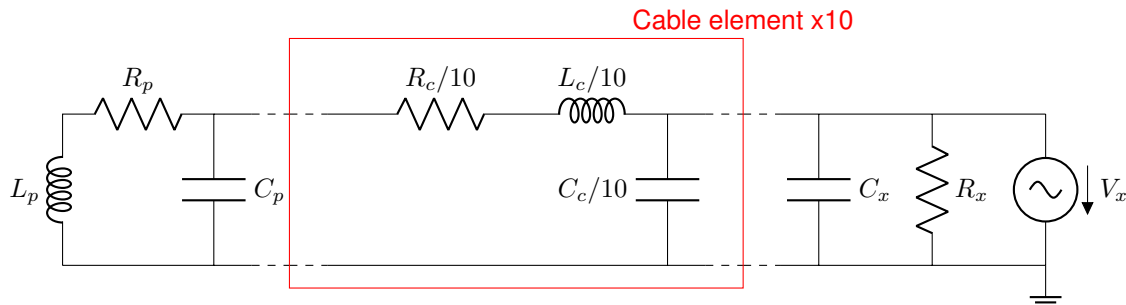


Figure 3.36: Schematic drawing of the sensor-cable-DAS model. Cable element is lumped 10 times. Transfer function obtained by the ration of the current at L_p over the current at the source.

Simulating this model with an open-source SPICE-like¹⁰ circuit simulator [151], we can adjust the model to the frequency response measurements. We can see in figure 3.37 that with this simple

¹⁰Simulation Program with Integrated Circuit Emphasis (SPICE)

model, a good agreement can be reached. It is also visible in the plots that above 1 MHz the agreement is lost, and the data is systematically above than the model curve with a frequency dependency. This discrepancy is assumed to be related to test setup and not the model. As mentioned in section 3.4.2, the setup was developed for a frequency range of 1 kHz to 1 MHz, with the latter being the frequency rating of the amplifier used. The measurement relies on normalization to a reference coil, the frequency response of which can be safely assumed to be flat up to 1 MHz, but it is entirely possible that this is not the case for higher frequencies.

This represents a problem, as we can easily neglect the difference with ‘our eyes’, but ideally we would want to fit the model to the data. Discarding data above 1 MHz would get rid of the resonances, that carry the information on the parameters we want to determine. For this reason, an interactive manual curve fitting routine was developed, allowing the incremental and individual variation of the parameters around the estimated values until a satisfactory convergence with the data is achieved. In this case, the plots in figure 3.37 show that on the first two resonance peak frequencies and growth rates were adjusted well, despite a growing difference to the data points. The measured and fitted values are shown in table 3.11.

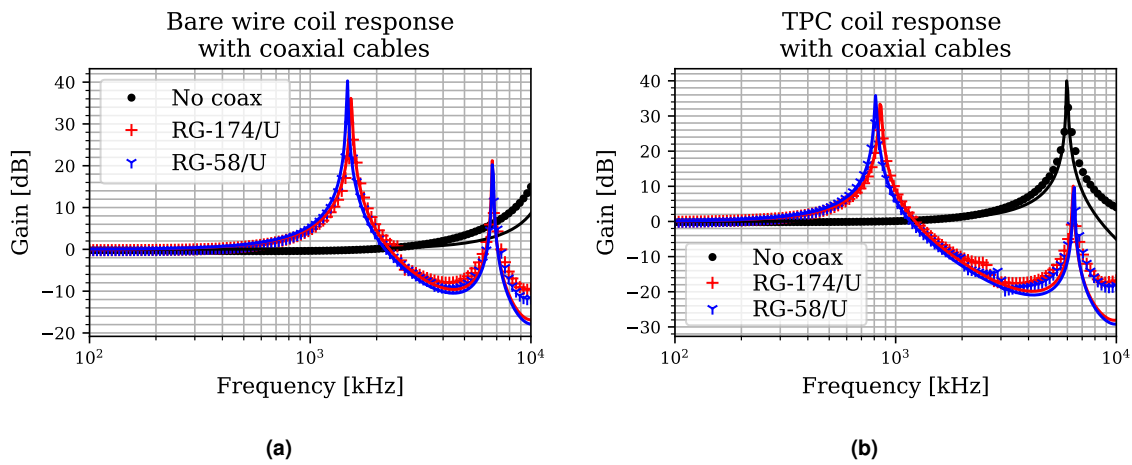


Figure 3.37: Manual adjustment of the simple sensor–cable–DAS model to the experimentally obtained frequency response of the prototypes of (a): bare wire coil; (b): TPC2 sensor.

Table 3.11: Directly measured and fitted parameters of the 15 m coaxial cables.

Parameter		RG-174/U	RG-58/U
Measured			
R_c	Ω	1.990	0.5528
L_c	μH	5.15	4.529
C_c	nF	1.371	1.526
Frequency response fit			
L_c	μH	4.44	3.91
C_c	nF	1.37	1.53

The reactive parameters of the cables can also be expressed as two other quantities: the characteristic impedance

$$Z_0 = \sqrt{\frac{L_c}{C_c}} \quad , \quad (3.34)$$

and the propagation velocity

$$v = \frac{1}{c\sqrt{L'_c C'_c}} = \frac{l}{c\sqrt{L_c C_c}} \quad , \quad (3.35)$$

that can be expressed with the ‘per unit length’ parameters (L'_c , C'_c) or with the cable length (l) explicit. The value is normalized the speed of light in vacuum c and typically expressed as a percentage.

Figure 3.38 shows the impedance and velocity for the measured and fit values, the datasheet value of $Z_0=50\ \Omega$, $v=66\%$. Since the inductance measurements seem to be systematically larger than expected, diamonds represent the measured capacitance with L_c forced for $v=66\%$. We see from this plot that the fitted value is consistent with the cable specifications.

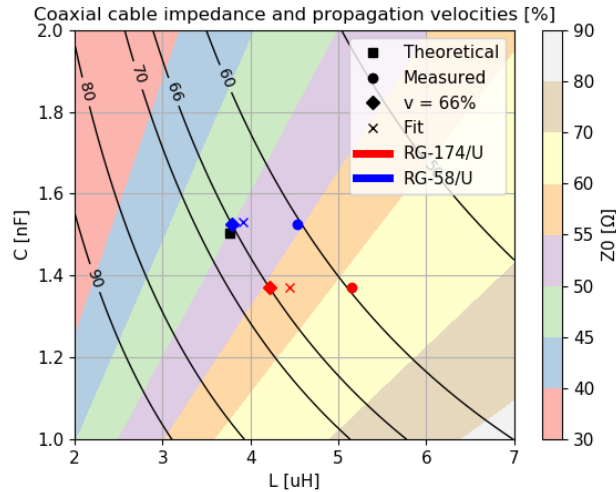


Figure 3.38: Mapping of the reactive properties of the two coaxial cables according to theoretical assumptions and datasheet information, measurement, and fit from frequency response. Characteristic impedance Z_0 represented in color, propagating velocity v as lines.

This fit also provides a better estimate for the probe capacitance, that, as a parasitic component, is difficult to measure directly. The fits allow for an estimation of $C_p=12.7\ \text{pF}$ and $C_p=16.6\ \text{pF}$ for the bare wire coils and TPC sensor, respectively. It is important to note that this value estimation is very sensitive to the assumption of $C_x=14\pm 1\ \text{pF}$ as per the oscilloscope datasheet [141], which is, as we see, comparable.

Having a calibrated set of parameters for the probes (R_p, L_p, C_p), the cable (R_c, L_c, C_c) and the DAS (R_x, C_x), we can use the model to preview the effect of changing one or more of these components. These extrapolations can be seen in figure 3.39, where we can see a projected resonance at 1 MHz for the bare wire coil if the cable length is doubled to 30 m, the expected length needed for COMPASS-U, the effect of a lower input impedance DAS or how the resonant peak can be mitigated at the cost of DC attenuation using an $80\ \Omega$ resistor termination. In this last case, the sensor exhibits a resonance and attenuation free bandwidth up to 1 MHz, with 30 m cables.

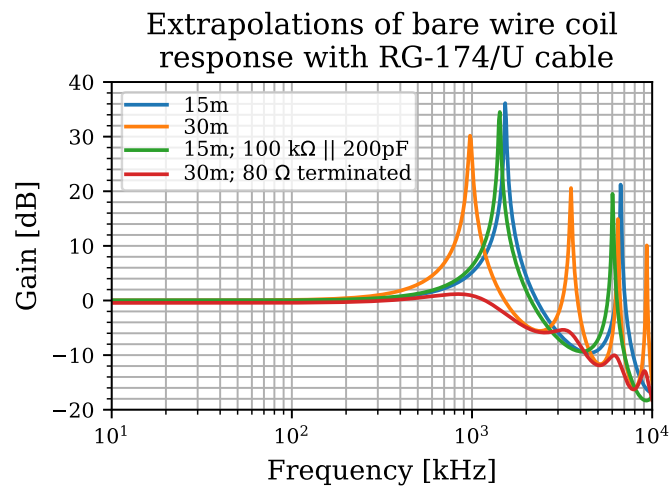


Figure 3.39: Simulation of the fitted model of the bare wire coil for different cable and DAS parameters: original 15 m cable, 30 m cable, 15 m with lower DAS input impedance, and 30 m with 80Ω termination. On the last curve, the DC gain is noticeably lower due to the low input impedance.

3.5.4 Development of MIC probe prototypes

When we consider the frequency response of MIC sensors, the attenuation caused by the enveloping (and enveloped) metallic structures is the dominant effect. When penetrating a conductive material, the magnetic field will create perpendicular eddy currents that will on themselves create an opposing magnetic field. We have seen in the flux loops (section 3.5.2) and the preliminary MIC studies (section 3.4.1) that this effect is unavoidable in MIC wound sensors. In previous studies of this effect, the attenuation was assumed to be that of a first order filter [137]. On the flux loop measurements this behavior was confirmed, albeit the lack of a steady and controllable source of magnetic field does not allow for fully conclusive determination. When the cable was wound into cylindrical coils, however, the frequency response was no longer in agreement with a first order filter. With the improved calibration testbench we can now determine with a high degree of confidence the frequency response of the sensor prototypes.

The harsh environment of COMPASS-U dictates that the MIC sensors design should be robust to withstand strong mechanical forces and differences in thermal expansion when elevated to 500 °C. For this reason, the former structure to hold the coil in place and force a defined constant shape, was built out of Inconel for the first prototype. Essentially, two solid rods with welded stoppers at both ends, around which the cable is wound. The cable is wound in two layers. This design is advantageous when compared to a single layer, as the end of the winding is at the same side as the start, forming right away the twisted pair, and leaving minimal residual area collecting unwanted magnetic field. For a single layer design, the end of the cable must be returned through the inside (or outside) of the coil, like in a Rogowski coil.

As for the cable, the cable C has shown the best results, due to its thin shielding to outer diameter ratio, whilst keeping a good insulation layer with low capacitance. All prototypes, represented schematically in figure 3.40 and summarized in table 3.12, are wound with this cable.

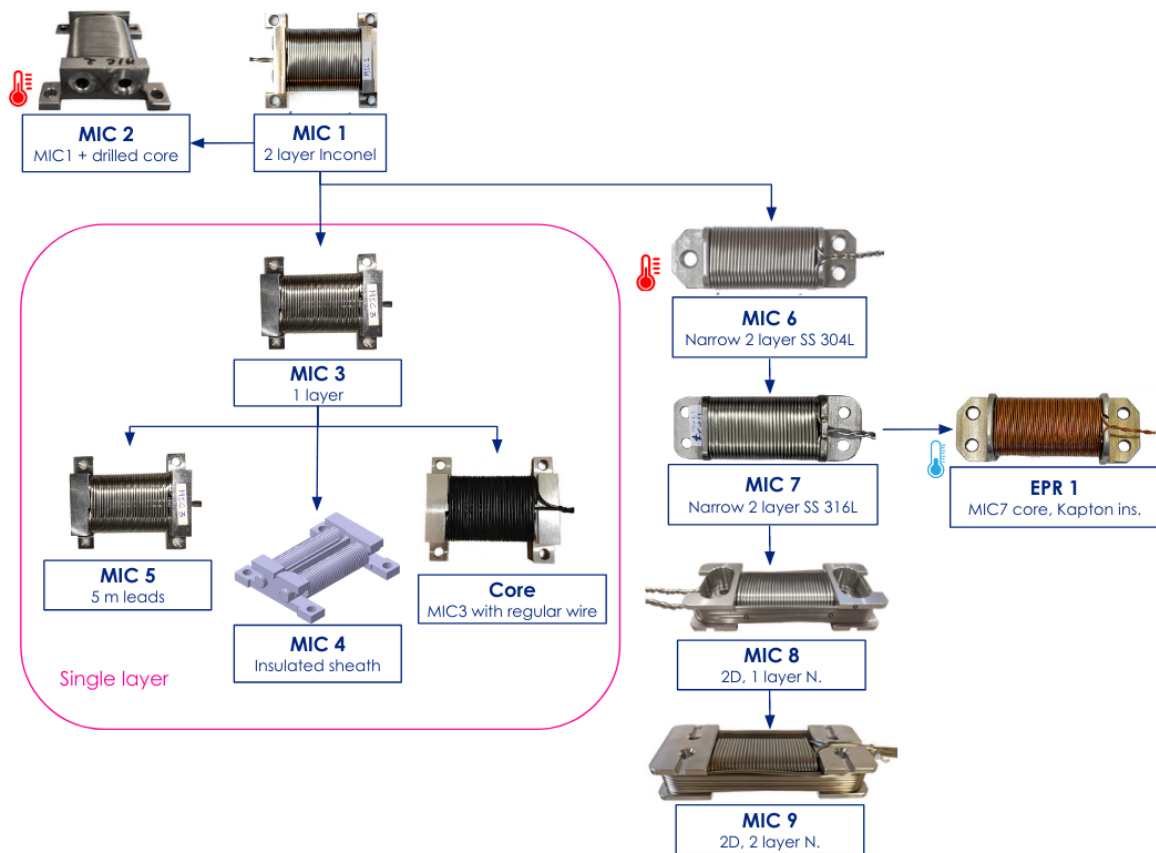


Figure 3.40: Development tree of the sensor prototypes developed at IPP. Each prototype is labeled by an alias and a short description of the most important design change. The red/blue thermometers indicate this prototype was (at some point) submitted to high (500 °C) or cryogenic temperatures, respectively. Photographs or drawings are not to scale.

Table 3.12: Reference of the mineral and polyimide insulated coil prototypes.

Coil	Core material	Layers	Feed length [m]	S_{eff} [cm ²]	f_{-3dB} (± 0.1) [kHz]
MIC1	Inconel 625	2	0.97	422.96 \pm 0.64	11.1
MIC2	Inconel 625	2	0.75	421.62 \pm 0.60	11.4
MIC3	Inconel 625	1	0.90	181.82 \pm 0.74	17.7
MIC4	Inconel 625	1	1.09	187.66 \pm 0.27	18.8
MIC5	Inconel 625	1	5.71	181.53 \pm 0.26	17.5
MIC6	SS 304L	2	0.90	278.59 \pm 0.35	13.2
MIC7	SS 316L	2	0.83	211.12 \pm 0.25	18.1
MIC8	SS 316L	2	0.86	214.23 \pm 0.31	18.2
MIC8N	SS 316L	1	0.86	249.4 \pm 1 *	14.5
MIC9	SS 316L	2	0.79	209.1 \pm 0.25	18.4
MIC9N	SS 316L	2	0.79	457.7 \pm 1 *	13.0
EPR1	SS 316L	2	0.80	319.23 \pm 0.37	32.4

* Estimated from Helmholtz coil at 1 kHz and solenoid measurement of tangential component.

Two similar prototypes were initially developed – MIC1 and MIC2. While exhibiting a high effective area, designed to ~ 400 cm², the frequency response (figure 3.41) starts to derate at low frequencies. As common practice, the -3 dB point, corresponding to half power will be used as reference for the specification of the bandwidth. On this prototype, this would correspond to 11 kHz, roughly. However, one needs to note that the behavior is not that of a first order filter. This can be seen as the roll-off between 30 and 60 kHz is only -4 dB, lowering to -5.2 dB between 100 and 200 kHz, still below the -6 dB per octave predicted. Another indication, visible in the plot, is that the phase response crosses -45° at 17 kHz and not at the -3 dB point.

In an attempt to improve the frequency response, on one of the prototypes (MIC2) the rods were drilled, effectively becoming tubes (see top left corner, figure 3.40). In figure 3.41b we can see that there was indeed a slight improvement by the removal of material from inside the sensing area of the coil. However, in general, the frequency responses are still similar overall as seen in figure 3.41a. The design of the core is therefore important to minimize signal attenuation.

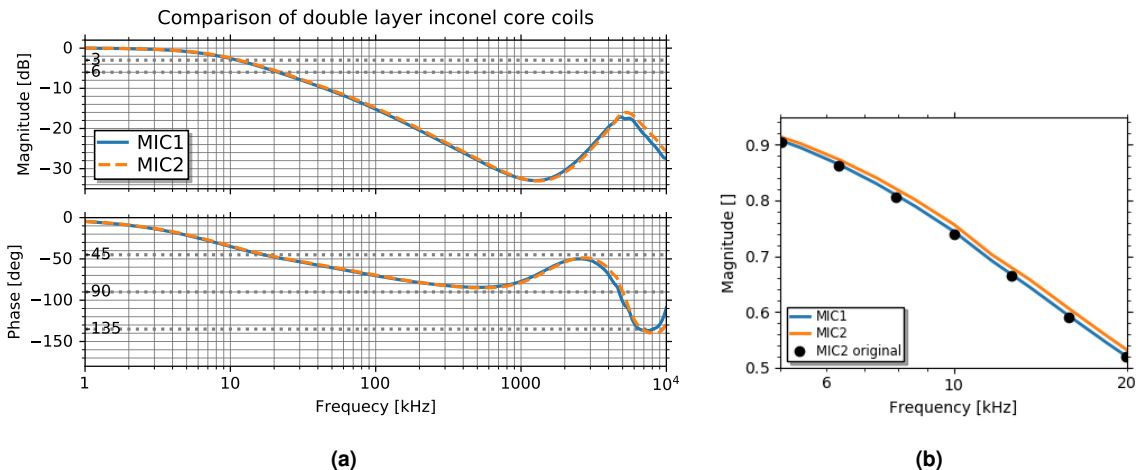


Figure 3.41: Frequency response of two initially identical inconel core double layer coils. The frequency response of MIC2 was measured after the structure rods were drilled. Plot (a) shows that neither that alteration nor the cycling at high temperatures had a significant effect on the frequency response, continuing to exhibit a -3 dB attenuation at circa 11 kHz. Plot (b) compares the frequency response of MIC2 with the measurement before alteration (in linear scale), a small yet systematic improvement is visible.

The development of a one layer coil, without overlay of cable on top of the already wound cable, allowed the study of different configurations. Two identical prototypes were developed with different

feed lengths – MIC3 with ~ 1 m twisted pair as in the rest of the prototypes; and MIC5 with over 5 m, a realistic length for the leading of the signal from the sensor to the vacuum feedthrough at the **VV** port. In line with the effects already described in the previous section, the frequency response of these two prototypes is similar, with the first resonance shifting from 8.5 to 2.5 MHz due to the added length of twisted pair cable (see figure 3.42).

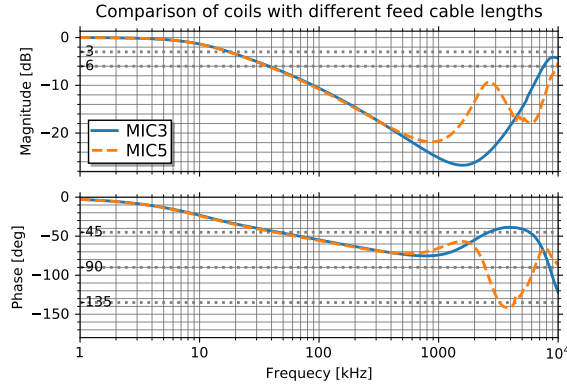


Figure 3.42: Comparison of the frequency response of the same sensor with different feed cable length (MIC twisted pair). The first resonance shifts from 8.5 to 2.5 MHz.

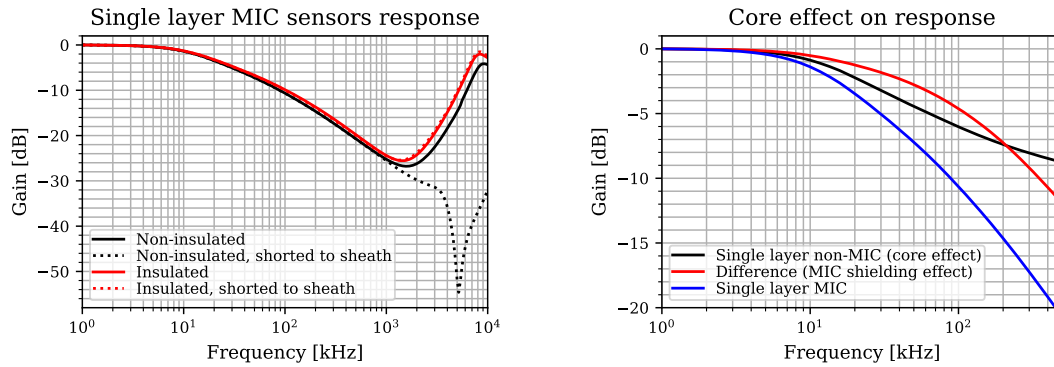
A possible development idea to improve frequency response is to break the electrical contact of the sheath between windings. A core (former) with the same overall dimensions to the MIC3 was manufactured. In order to keep the windings from touching one-another, grooves were made on the core, to fix the winding positions. The core was then spray-coated with a ceramic powder that prevents electrical contact between the sheath and the metallic former of the coil. The sheath is still in electrical contact at the twisted pair, keeping full insulation is unrealistic for tokamak implementation, but at a local level it would be possible that the different conductive paths for eddy-currents would result in a significantly different attenuation. Two points on the 3D geometry might still be in electrical contact but have distinct resistive paths for the currents. As figure 3.43a shows, no significant difference was observed. The two prototypes MIC3 and MIC4 show essentially the same attenuation up to 1 MHz, with no consequent gain in bandwidth on the interest range of 1–50 kHz. There is however a difference when the ‘ground’ conductor is connected to the sheath. On a MIC3, the resonance shifts to a lower frequency, as the capacitance between the ‘live’ conductor and the sheath is now parallel to the capacitance between the conductors, and is much smaller in amplitude, appearing only as a ‘knee’ since eddy currents are drained to ground. With the insulated sheath, this does not happen, the coil always exhibits the behavior of the conductors insulated from the sheath.

Having an extra core available, a coil was wound out of regular wire of a similar OD. This coil is represented as ‘Core’ in figure 3.40 as it aims at providing data that allows the decoupling from the effect of the MIC attenuation from the metallic core attenuation. Assuming the frequency response of the MIC3 coil $g_{MIC3}(\omega)$ is a product of the MIC and core frequency responses:

$$g_{MIC3}(\omega) = g_{MIC}(\omega) \cdot g_{Core}(\omega) \quad , \quad (3.36)$$

by measuring $g_{Core}(\omega)$ sufficiently far away from resonances, we can have a good estimation of the balance of attenuation caused by the metallic core or the sheath. This can be seen in figure 3.43b, showing that up to 200 kHz the core effect is dominant. Considering we are interested in increasing the bandwidth roughly on the 1–20 kHz band, core construction is the dominant problem, not the number of layers of MIC. We can also see that in the absence of core, the expected half power point would fall between 50 and 60 kHz, a value much more in line with published results that do not have metal cores [137].

For the next prototype design, the topology was reverted to double layer and the core was significantly improved. Tubes were used instead of rods for shaper elements, the thickness of the holding structure (top and bottom stoppers) was minimized by using ‘L’ pieces. The material was also changed from inconel to stainless steel. Firstly SS304L was incorrectly used (MIC6). When measured, S_{eff} exceed the geometrical estimation by 48 %. High values of magnetic permeability (μ_r) were measured with a handheld permeability meter [152]. Furthermore, the permeability was not constant across the piece. It is possible that the magnetic properties of the metal were changed



(a) Comparison of the frequency responses of prototypes MIC3 (black) and MIC4 (red) with ceramic insulation covering the core. When the sheath is floating, the frequency response is similar between the prototypes. When the sheath is shorted to one of the terminals (grounded) the insulated prototype keeps the same behavior, while the non-insulated loses the resonance below 10 MHz.

(b) Comparison of single layer coil (MIC3, blue), 'Core' coil made out of non-MIC wire on the same former (black) and the difference between the two curves, representative of the attenuation of the MIC itself.

Figure 3.43: Two studies of variations of single layer coils, based on MIC3.

when the piece was soldered/machined. The piece was submitted to 500 °C and remeasured, being now only 32 % above the expectation, it is possible that local annealing could have occurred, despite the temperatures required for this treatment being usually much higher. The cores of subsequent prototypes were made out of stainless steel to of the standard AISI 316L.

With the correct core, the double layer MIC7 shows a much better frequency response than MIC1. Partly this is due to having roughly half the effective area and lower inductance. However, in parallel simulations, this value was found to still be acceptable for equilibrium reconstruction. In figure 3.44 we can see how the frequency response of the new double layer coil is similar to the single layer coil with the previous core. The half-power point sits above 18 kHz, with the signal response dropping by 10 % above 8 kHz.

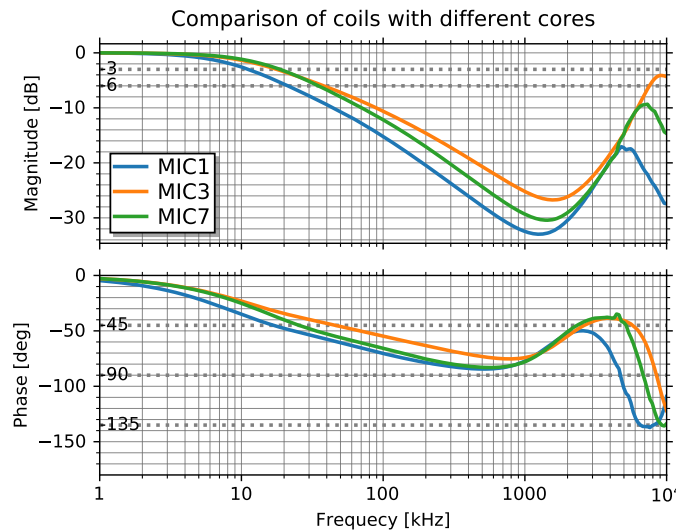


Figure 3.44: Comparison of the frequency responses of prototypes MIC1, MIC3 and MIC7. The first two coils share the same inconel core, with MIC3 only having one winding layer. MIC7 has 2 layers and the optimized stainless steel core, resulting in a similar bandwidth to the single layer coil with the old core.

Being comfortable with the frequency response, the design was iterated to 2D coil with a winding sensing the normal component of the field. On top of a tangential coil similar to MIC7, MIC8 has a one layer normal winding (MIC8N) and MIC9 two layers (MIC9N), for an effective area of more than double that of the tangential component. Figure 3.45 shows the comparison between the coils. We

can see that the addition of the normal coil did not significantly change the frequency response of the tangential coil as the lines are completely overplotted. On the normal components, we can see that in a first stage the response is mostly core dominated, in which both coils behave similarly and worse than the tangential component as they are wound on the outside. From roughly 10 kHz the behavior is mostly dominated by the cable with the single layer outperforming the double layer, that converges to the attenuation level of the tangential (double layer) coils.

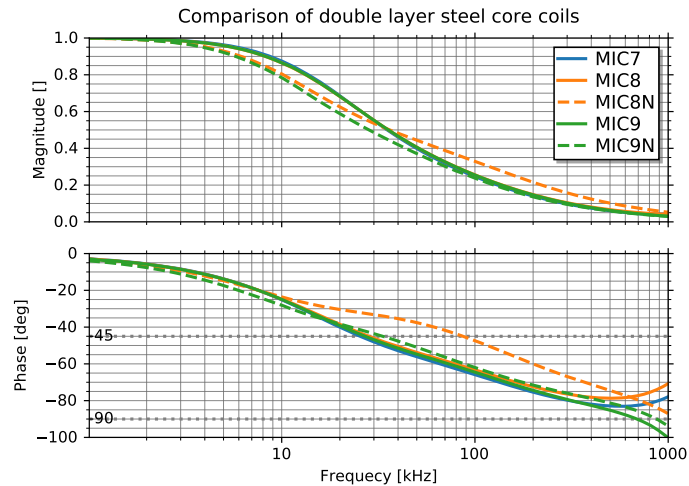


Figure 3.45: Comparison of the frequency responses of prototypes MIC7, MIC8, and MIC9. All have a similar 316L stainless steel cores, with MIC8 and MIC9 having an extra coil wound perpendicularly to measure the normal field (MIC8N single layer, MIC9N double layer). The addition of the normal coil did not alter the frequency response on the tangential coil.

Finally, a prototype for the EPR coil was also developed from the MIC7 core. These coils will be installed ex-vessel in the cryostat, therefore the EPR1 prototype is would from cryogenically compatible polyimide insulated cable. In order to test the survivability at these temperatures, the coil was measured before and after (at room temperature), with no alteration of the behavior recorded. Figure 3.46 shows the comparison of the frequency responses of this non-MIC coil and its MIC equivalent – MIC7.

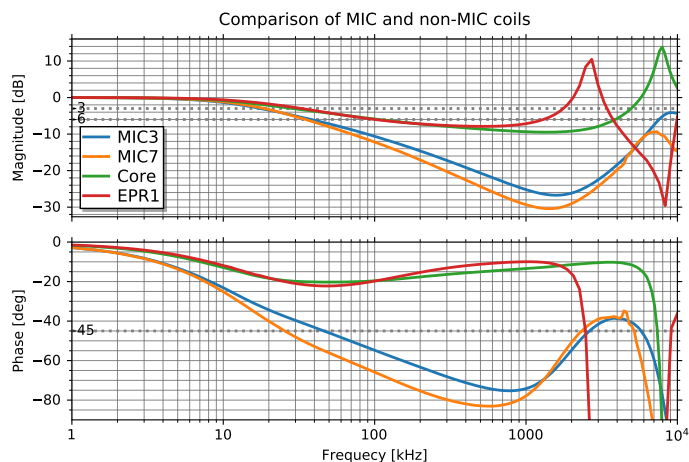


Figure 3.46: Comparison of the frequency responses the non-MIC coils – EPR1 and Core. MIC3 and MIC7 are also represented for comparison.

3.5.4.A Application of MIC probes response to COMPASS data

It is not easy to have an intuitive sense of the effect the frequency response of the sensors has downstream of the magnetics data. If we think of a MHD mode as having a defined frequency and

amplitude, the frequency response plots can be used to ‘lookup’ the attenuation and phase delay the signal would have. Reality is often not as simple, the magnetic signals come in a wide spectrum and amplitude ranges, that are convoluted with the transfer function of the sensor – a process that is hardly intuitive. Furthermore, even MHD activity is often not persistent in time nor stable in amplitude and frequency, the change of which is of importance to physics analysis and controllers alike.

Being confident in the accuracy of the frequency response of the measured sensors, even in the absence of a theoretical model, we can fit a LTI model to the data and then apply this ‘filter’ to existing data through convolution. The COMPASS database has a large amount of magnetic data sampled at 2 MSPS with sensors with a good frequency response and minimal filtering performed. With this analysis we are not creating a complete synthetic diagnostic, ‘replacing’ the hardware used on COMPASS with the prototypes. The effective area would be different, to which the data acquisition input ranges are not optimized and several of assumptions and considerations would have to be made. Rather, we want to study just the effect of the frequency derating. The main consideration to take into account is that the transfer function is applied here to the sampled data, rather than to the magnetic field or coil voltage. The high sampling rate of the signal ($f_{Ny}=1$ MHz) allows us to proceed, keeping in mind that the signal will be unrealistically smooth as the DAQ noise is also being filtered.

The response of two prototypes was fitted: MIC9 the most recent prototype, and MIC1, the first prototype, with worse frequency response. Through trial and error, it was found that a model with a first order polynomial on the numerator and a second order polynomial in the denominator fit the response sufficiently well. The transfer function of the coil $g(\omega)$ is fitted with

$$H(s) = \frac{n_1 s + n_0}{d_2 s^2 + d_1 s + d_0} \quad , \quad (3.37)$$

for the coefficients that are then applied to the data, as a discrete-time system that takes into consideration the sampling frequency,

$$H(z) = \frac{n_1 z + n_0}{d_2 z^2 + d_1 z + d_0} \quad . \quad (3.38)$$

Figure 3.47 shows the fit result in magnitude and phase. No particular care was given to a physical interpretation of the fitted coefficients, shown as reference in table 3.13.

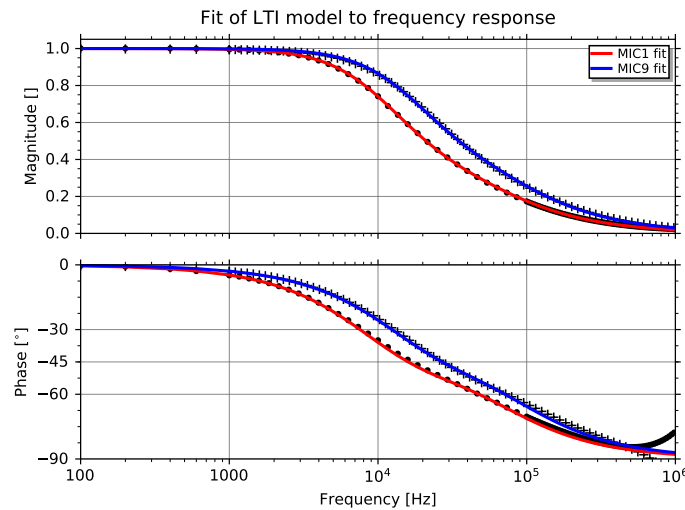


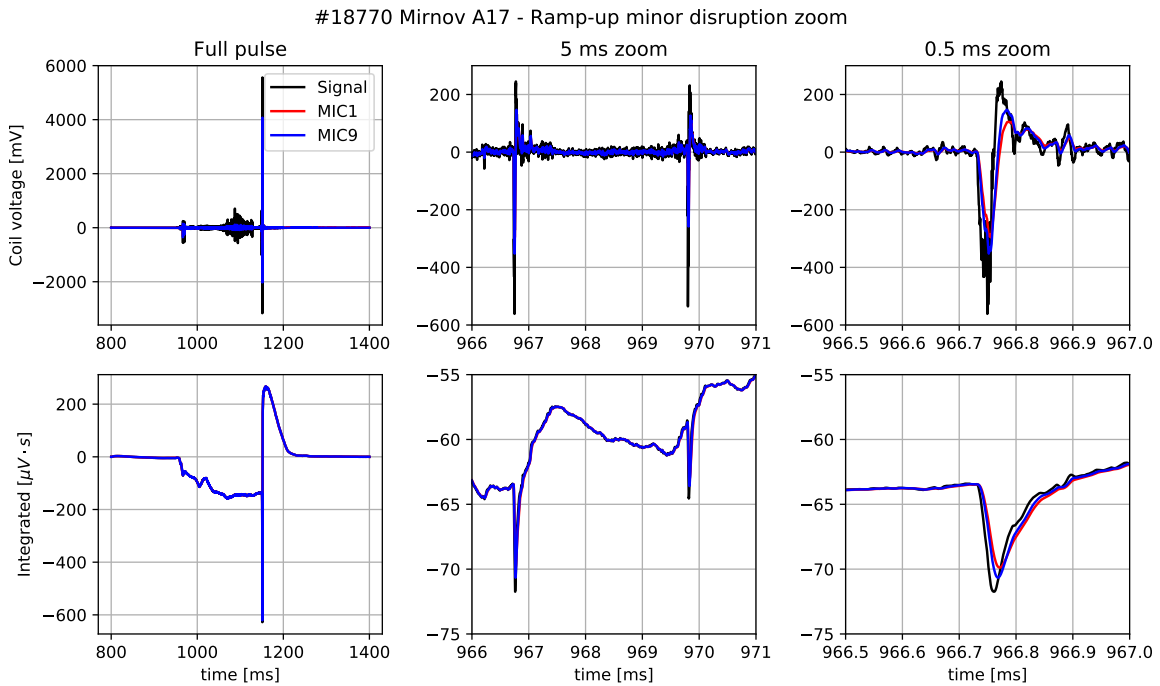
Figure 3.47: Fit of an LTI model to the frequency response of the prototypes MIC1 and MIC9. Fit to the magnitude ($|g(\omega)|$) data, up to 1 MHz with polynomials to the second order.

Table 3.13: Fitted LTI model parameters of the frequency response of prototype coils.

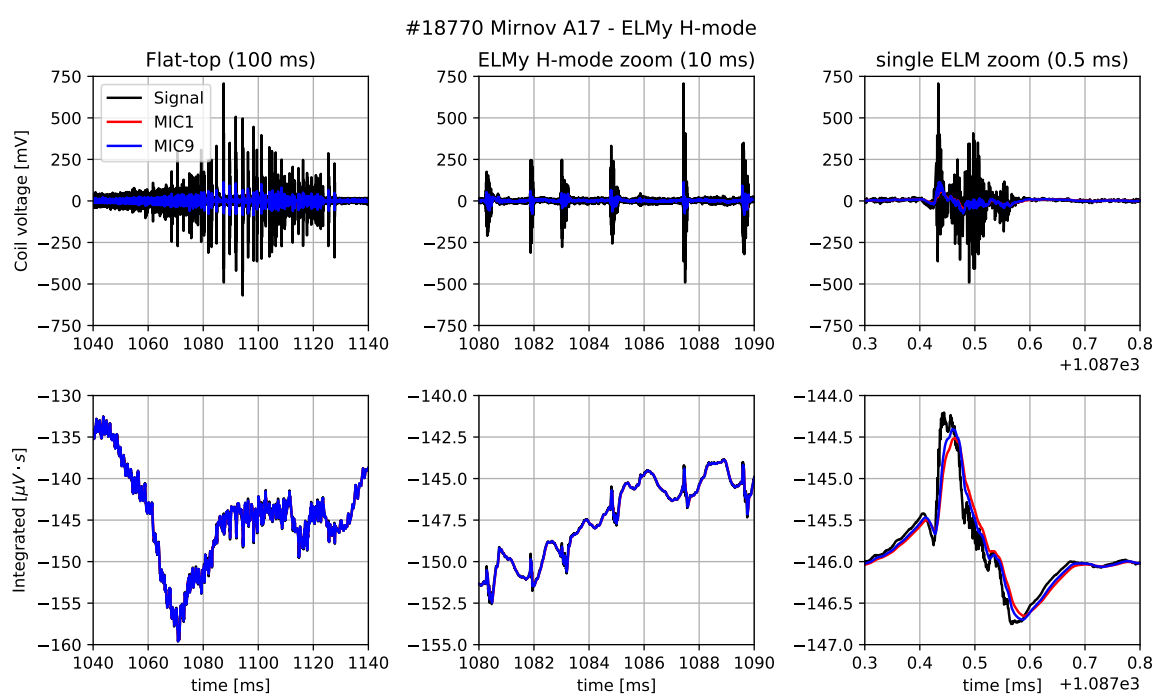
Coil	n_1	n_0	d_2	d_1	d_0
MIC1	$4.15570979 \cdot 10^{10}$	$7.78599961 \cdot 10^{15}$	$3.41071860 \cdot 10^5$	$1.43602404 \cdot 10^{11}$	$7.78680580 \cdot 10^{15}$
MIC9	$9.36841499 \cdot 10^7$	$2.31957522 \cdot 10^{13}$	$4.94591090 \cdot 10^2$	$2.82134482 \cdot 10^8$	$2.31957522 \cdot 10^{13}$

For the demonstration of the MIC effect, a COMPASS pulse with ELMy H-mode and disruption was chosen. Figure 3.48 shows the original signal and 'filtered' signal for a Mirnov coil close to divertor, on HFS. Not only the signal but its numerical integration are shown. The integral is drift corrected, with the drift offset used being the same for all time traces, calculated using the original signal.

In all but the closest zooms, the MIC1 trace is completely overplotted by the MIC9, given that the difference between the coils is not significant above the 0.1 ms scale. In fact, all the features and timescales that are realistically expected to be controlled or of importance to equilibrium reconstruction show no significant degradation, as can be seen for instance in the ELM zoom, where the precursor growth is not significantly affected in the integrated signal. It is however at this scale of events that the differences between the two responses are appreciable. COMPASS-U will feature fast control cycles of 50 μ s, corresponding to one update each half division of the rightmost plots. While the disruption that terminates the pulse is the major event in amplitude, it is not the fastest. Those would be the 'minor disruptions', i.e. sudden losses of plasma current, during ramp-up. In these the difference between the two MIC prototypes is most appreciable, with a drop in peak amplitude and a ~ 10 μ s delay being visible.



(a)



(b)

Figure 3.48: Application of the transfer functions of MIC1 and MIC9 prototypes to a Mirnov coil signal on COM-PASS. (a) shows the full pulse and zooms of 5 and 0.5 ms to fast losses of plasma current during ramp-up, while (b) shows the flat-top, a 10 ms zoom of an ELMy regime and the detail on a single ELM. Top rows show the probe voltage signal, while bottom rows show the numerical integration, corrected for drift using the original signal. The transfer function was applied with unitary gain, only the frequency derating effect is being show.

4

Ex-vessel cabling

Contents

4.1	Signal path from sensor data acquisition system	88
4.2	Ex-vessel cabling options	89
4.3	Testing of externally induced noise	89
4.4	Test of cross-talk	96
4.5	Cable selection	98

The two key aspects of the magnetic diagnostic explored in this thesis are the sensor and the DAS and methods. These two systems are physically separated, in between, we must assure the transmission of the signal with the highest fidelity possible. If in small devices the DAS can be installed in proximity to the device, larger devices such as COMPASS-U require larger separation to ensure easy and independent access to it and prevent electro-magnetic and radiation interference with the electronics.

This chapter details the efforts in qualification and support of the choice of ex-vessel cables for the magnetic diagnostic. Two major sources of noise were evaluated – external (magnetic) noise and cross-talk.

4.1 Signal path from sensor data acquisition system

It is important to define the components of the signal path from transduction to DAQ. In the case of inductive magnetics, the sensors are primarily composed by an inductor, very well-defined in space, inside or outside the VV. For the in-vessel sensors, this means a relatively short bipolar cable must 'lead' the signal from the effective end of the sensing element to the vacuum feedthrough. The simplest and safest way, on wound sensors, is to use the same cable that formed the sensor for the lead cables, in a Twisted Pair (TP) configuration, minimizing the area between the two conductors. This way, vacuum terminations are avoided, which is particularly important for the MIC cables. Terminations are a weak-point for reliability, introduce noise due to thermoelectric voltages, contact resistance, and, in the case of the MIC, can lead to vacuum degradation and insulation losses.

At the feedthrough, the termination is unavoidable. For conventional sensors the issues are not significant, as there is a large amount of Commercial Off-The-Shelf (COTS) solutions with parameters similar to atmospheric connectors. MIC vacuum interfaces are less standard, usually coming in the form of bespoke or adapted solutions, even if developed by industrial partners.

Long signal cables which are the object of this chapter lead from the feedthrough to the DAQ connectors. These should be chosen in a way to minimize signal distortion. Its impedance and electrical properties should be adequate to the signal bandwidth, minimizing attenuation and avoiding resonant behaviors. The cables should also minimize the introduction of noise from external sources, due to external electric and magnetic fields; and cross-talk between signal cables, as these usually form buses of large amounts of signals from the device to the centralized DASs.

One of the ways of increasing the immunity to external noise is by shielding the cable with a conductive layer. This raises the problem of where and how the grounding of this shielding is made. Grounding in a tokamak device is a complex topic that transcends the magnetic diagnostic, however, the grounding reference at the device, where many high-power and high frequency systems are grounded is generally not the same as the one where the DASs are connected to. That is, there is a potential difference.

By connecting both sides of the shielding to the respective ground, we are creating a closed conductive path, allowing currents to run parallel to the signal transmission, which is something to avoid. Since not only one cable (and shielding) is used, this also creates large ground loops, in an environment with abundant stray magnetic fields.

The typical approach is to connect the shielding only on one side. Either at a central tokamak grounding point end or the DAQ end. A path to drain induced currents is established, avoiding ground loops. However, we can see the long metal conductors as unipolar antennas that will 'tune-in' to noise that would otherwise not have been picked up. This connection type can also bring safety concerns, in particular if the device reference is lead to a different physical space. In the event of the failure of a system, the voltage between the two references can be large.

Another option is to use what is sometimes called an 'hybrid' grounding. It consists in grounding both sides. However, whereas on one side the connection is made through a short-circuit, on the other a capacitor is used, see figure 4.1. In this way, the capacitor still enables high-frequency grounding, but blocks low frequency (such as power-line) currents. Typically, a ceramic capacitor between 10 nF to 100 nF is recommended [153, 154].

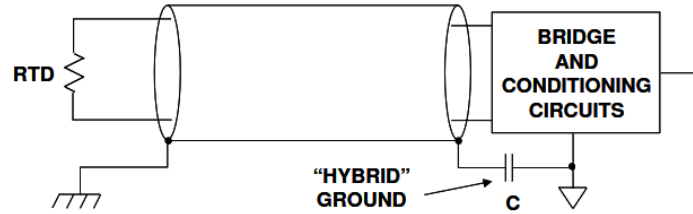


Figure 4.1: Hybrid ground, on a shielded transmission line between a passive sensor (RTD) and the signal conditioning electronics. Figure gathered from [153].

4.2 Ex-vessel cabling options

Three types of cables are considered for leading the magnetic diagnostic signals from the vacuum feedthrough to the data acquisition. These are: coaxial cable, single [Shielded Twisted Pair \(STP\)](#), and Ethernet cables.

The coaxial cables see widespread usage in laboratory data acquisition and instrumentation, however they are indicated for single-ended signals, as the two conductors are different. The core of the cable is a highly conductive wire, typically copper. The conductor is surrounded by an insulation layer (such as PVC or Teflon) and then a braided shielding, typically of a less conductive metal. For single-ended signals, ground is connected to the shielding and the signal is carried in the conductor. This shielding prevents the induction of noise from magnetic sources. Magnetic signals are by nature differential, potential difference between two points. Transmitting either end by different conductors can lead to an imbalance. The shielding effect is also lost, as the shielding is now a conductor.

The typical alternative for differential signals is to use [TPs](#). The conductors are identical – balanced line – and twisted into a helix. The twisting greatly improves the immunity to electromagnetic interference. For additional immunity to external fields, the pair can be shielded – [STP](#). With this added layer, there are now technically three conductors. Two for signal and one for the reference, ground. If only one [TP](#) forms the cable assembly, typically covering the shielding with a polymer, these are considered single [STPs](#). However, a cable assembly can have more than one [TP](#).

Ethernet cables are formed by four [TPs](#). Over time, with increasing need for transmission speed for digital signals, different classes for the links were specified, having corresponding categories (short CAT) of cable and connectors. Relevant for this work is the CAT7 cables¹, this standard is typically only achieved with shielded [TPs](#). Each [TP](#) is wrapped in a foil (FTP) and the bundle of 4 [TPs](#) enveloped by a foil (F/FTP) or, most commonly, a mesh (S/FTP). In some models, a conductive wire is also present, a ‘drain wire’ that ensures good electrical contact with all shielding components, minimizing resistive paths and currents.

A selection of cables was assembled to test immunity to external magnetic fields, crosstalk, as well as studying their electrical properties. Table 4.1 shows the tested cables, of the three types described. The coaxial cable serves as a reference, labeled “cox”. Ethernet cables are labeled as “eth” and single twisted [STP](#), hereby referred only as [STP](#) are labeled “stp”.

4.3 Testing of externally induced noise

The tokamak is an environment with ever-present high non-constant magnetic fields. We want to qualify the cables regarding the immunity to external magnetic fields induced locally on the cable path. In principle, all cables should be immune to constant magnetic fields, however both time changes and gradients of magnetic field can generate spurious voltages and damage the signal integrity.

Simulations of ex-vessel magnetic fields in COMPASS-U at full parameters ($B_T=5$ T, $I_p=2$ MA) show a maximum gradient at midplane of 5 mT/cm. In the worse case scenario, leading the diagnostic cables close to the power coils, would expose them to around 170 mT/cm. Regarding the rate of change, the power engineering department estimates rates of change of 50-100 mT/ms.

¹Used for class F digital links.

Table 4.1: Description and electrical proprieties of the cables tested, as per the respective datasheets. On coaxial cable resistance for the outer conductor between brackets. On Ethernet cables the Near End cross Talk (*NEXT*) value is also displayed.

Cable	Manufacturer	Model	Conductor	Z_0 [Ω]	C [pF/m]	R_{DC} [m Ω /m]	<i>NEXT</i> [dB]
cox1	–	RG 174/U	solid	50 \pm 3	100	134.8 (44.6)	–
eth1	Solarix	27000007	solid	100	–	–	98.22
eth2	DRAKA	UC900 SS23	solid	100 \pm 15	43	82.5	100
eth3	LAPP	DB2170614	solid	100 \pm 5	45	75	105
stp1	Belden	8451	stranded	45	110	47.6	–
stp2	Alpha Wire	6460	stranded	100	77	56	–
stp3	Audio Tech.	IO-A12326	solid	–	50.5	62	–
stp4	Belden	3105A	stranded	120	36	48.2	–

4.3.1 Experimental setup

An existing piece of equipment that can reach fields comparable to the expected stray magnetic fields was available in the laboratory. The system is based on discharging the energy stored in a 100V, 3.2 F capacitor into a coil in a short square(ish) pulse. This setup is not ideal, as there is no continuous source of oscillating magnetic field. However, it should generate two strong current slopes – consequently magnetic field slopes. If the coil is such that the field is spatially localized, high gradients also arise.

A similar experiment was conducted, published in 1988, also for the qualification of ex-vessel diagnostic cables for ASDEX [154]. In that testbench an oscillating 20 mT/cm field was induced continuously, and a motor moved the cable on the field.

Particularly for the TP cables, the symmetry of the design means that only very local effects, on the scale of the twisting length will produce measurable results, hence the importance of moving the cable, as the induced noise will depend greatly on the local disposition of the cable. To try to create the most localized field gradient possible a coil was devised where instead passing on top, the test cable passes through the coil. Figure 4.2 shows a diagram of the geometry, as well as the designed support that was 3D printed to hold the coil windings.

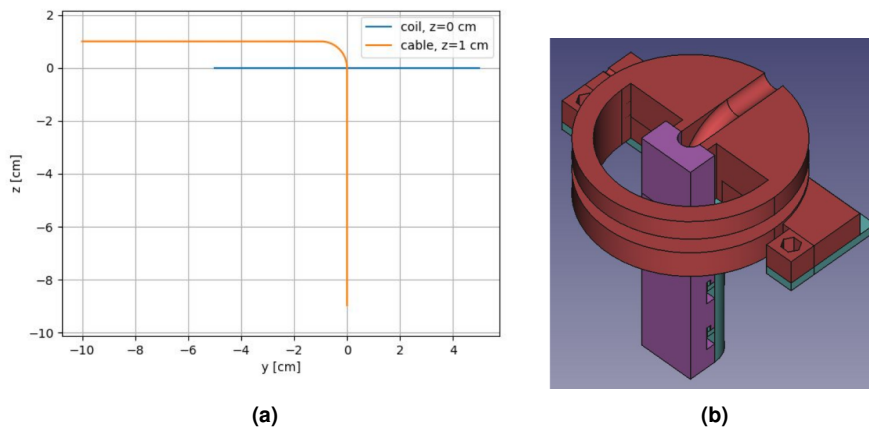


Figure 4.2: (a): Schematic representation of the test cable running through the coil. (b): Three part 3D printed model of the coil and cable structure. This structure is fixed to a table and allows longitudinal movement of the cable, while constraining it to the geometry in the scheme.

The coil used is circular with 8 turns and 10 cm diameter. When high current is run through the coil, high magnetic field gradients appear along the test cable length, see figure 4.3. The lack of symmetry prevents the cancelation of the induced “noise” across the periodic twists of the cables. A worst-case scenario for TP cables. With this test setup, the cables are fixed to a given distance to the active coil, but are free to move along their length.

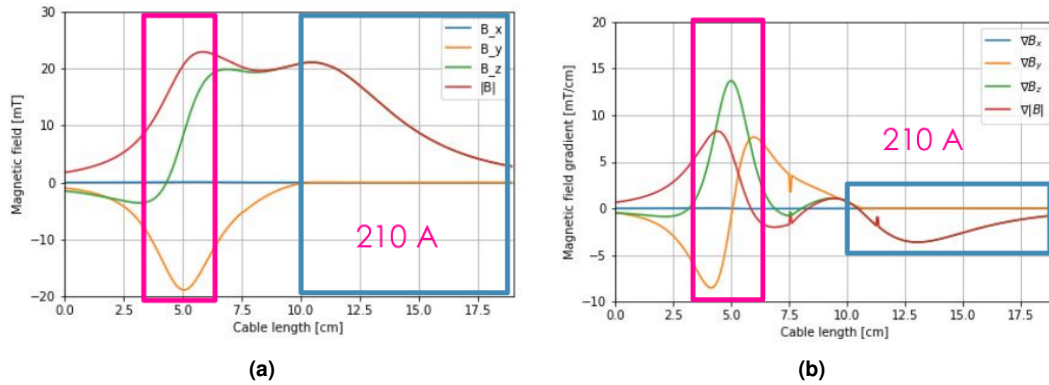


Figure 4.3: Simulation of the components of the magnetic field (a) and field gradient (b) along the length of the cable in the test geometry. Using this configuration the symmetry is broken and distinct, localized, areas of high and low field gradient emerge. These are identified by the magenta and blue boxes, respectively. The simulation uses an input current of 210 A on the coil.

The measured discharge current is shown in the oscilloscope capture in figure 4.4. Both the voltage of the capacitor (proportional to the current) and the pulse time are configurable. For 40 V a current of 210 A is reached.

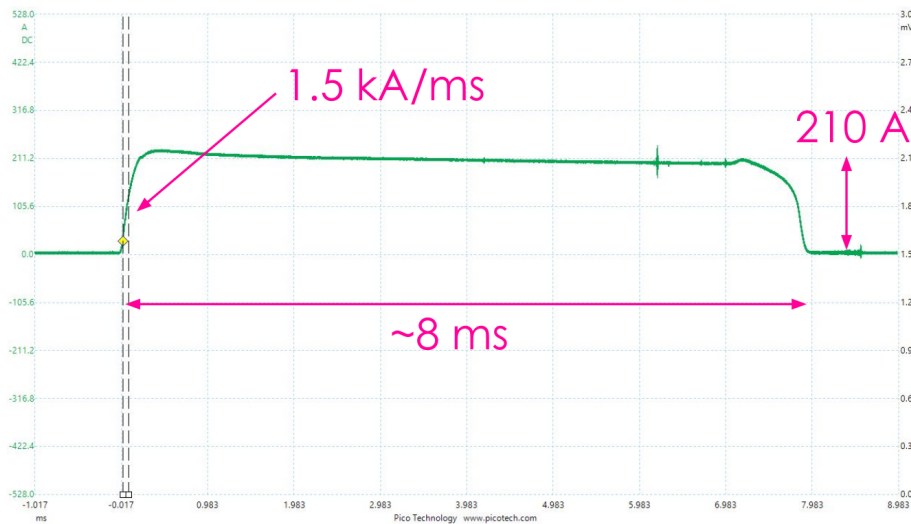


Figure 4.4: Oscilloscope capture showing the coil current measurement. Using a voltage of 40 V, a plateau current of 210 A is reached. The 8 ms pulse has distinct rise and fall rates.

For the testing, 60 V were used, reaching a peak ∇B of 22.5 mT/cm, a value comparable to the COMPASS-U stray magnetic field expectations. Regarding the rate of change, an estimated 140 mT/ms is reached according to the previous plots, comfortably higher than the COMPASS-U predictions.

The data is acquired with a PicoScope 5442D PC oscilloscope [141]. This equipment has a common ground for all the channels. For this reason, the positive and negative wires were connected on different channels, leaving the possibility of connection of the DAS ground to the shielding of the cable. On the other end of the cable, both conductors are shorted.

Given that the shielding of the cables is expected to be one of the key factors in noise minimization, it is important to consider how the shielding is connected to a ground, where the currents can be drained. For this reason the test will be repeated under 6 grounding schemes, see table 4.2. Like the conductors, the shielding has two ends – at DAQ and at the sensor side (free end). The available ground circuits at either end are, in principle different.

With regard to the point along the cable where the field is applied, the tests are repeated at two positions (1 and 2) at 1–2 m from either end of the cable. Since the induced noise will be very dependent on physical aspects such as position or rotation of the cable with regard to the field, the

Table 4.2: Grounding schemes tested. On the free end the cable shielding can be floating or shorted to ground and on the data acquisition end it can be floating or shorted to ground directly or through a capacitor.

gs	Free end	DAS end
0	floating	floating
1	floating	grounded
2	floating	100 nF
3	grounded	floating
4	grounded	grounded
5	grounded	100 nF

analysis is complicated. In order to achieve some degree of reproducibility of the results, and in line with the design of the inductor, we aimed at the worst-case scenario, i.e. the maximum noise we can induce on each cable and position. The data recording process is as follows:

1. The cable is inserted in the coil at the mark of position 1 or 2;
2. a pulse is generated, and the induced peaks are observed in the oscilloscope (see figure 4.5);
3. the cable is moved (against a ruler fixed on the table), and the process is repeated roughly every centimeter for a length of ~ 20 cm;
4. the position where the maximum peak is observed is selected and fine-tuned;
5. the measurements are then recorded (saving oscilloscope data) for all the grounding schemes, without moving the cable.

4.3.2 Results and analysis

The observed results of discharging the pulse on the coil through which the test cable passes are two peaks of opposing sign, corresponding to the rump-up and down of the current. In order to obtain reliable measurements out of these waveforms, the peaks are integrated. Being well above the noise level, this integration is reliable, proportional to the amplitude and more immune to noise than taking the maximum, and not needing any fit. Figure 4.5 shows both peaks and the integration limits. We can see that the first peak is more stable, and hence will be used in the analysis. Five measurements are taken, and their peek integral averaged, for each configuration.

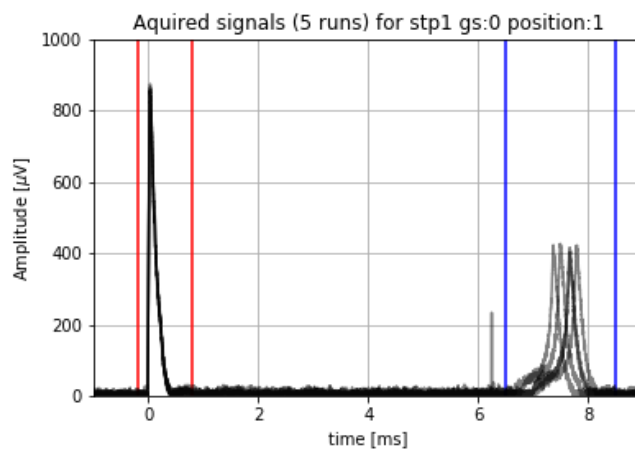


Figure 4.5: Overplot of 5 discharges using for the stp1 cable on the first position with grounding scheme 0. The signal displayed is the absolute value of the cable voltage, the peaks have opposing signals. The blue and red vertical lines represent the limits considered for integration of the peaks.

Figure 4.6 shows the results of the first peak integral for all cables, across the different grounding schemes (horizontal axis), with the plot on the left representing the measurements with induced noise at the DAS end of the cable and on the right at the free end. Comparing the two plots, we see that the order of the cables is not significantly altered. In general, when noise is induced closer to the free end, the noise is higher. However, both these conclusions must be weighted with the experimental difficulties associated with the measurements.

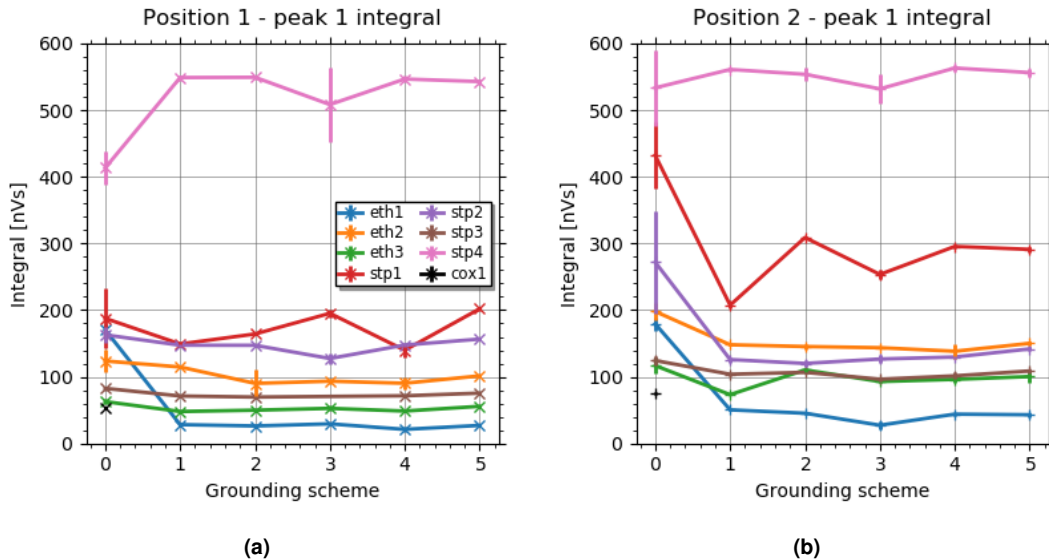


Figure 4.6: Results of the integral of the first peak for the tested cables on the different grounding schemes. **(a)** position 1, close to the data acquisition end; **(b)** position 2, close to the free end. Data points connected with lines to improve readability.

Across the grounding schemes we see no significant change, except for the configuration in which the shielding is completely floating. As long as the currents on the shielding can drain somewhere, the difference between cables is caused by different physical construction rather than grounding type. When analyzing the grounding schemes results, we must be careful in the conclusions. This data does not show which grounding scheme is the best for the real-life scenario. Rather just showing how the grounding of the shielding influences a very particular type of noise (fast, high B transients) that is present. In a tokamak, appropriate grounding is a complex matter. For instance, the grounding scheme 4 creates a large ground loop.

When comparing between the cables (and ignoring the first point) we see that there is no significant difference between *stp* and *eth* cables. This is not unexpected, as topologically, both cables are individually shielded twisted pairs. Furthermore, the best performers have comparable results to the coaxial cable (in black at grounding scheme 0). We can infer that the construction parameters play a key role in the minimization of external magnetic noise.

The test setup was devised to create as localized field as possible. The scale of the magnetic field gradients is the centimeter, comparable with the twisting length of the cables. Figure 4.7 interprets the results of figure 4.6 taking into consideration the length of a twist L , or more concretely, its inverse, the twisting density ($1/L$). Values in table 4.3.

The plot shows that the high twisting density of the Ethernet cables partially explains the good performance. Moreover, this interpretation also explains why the cable *stp4* has such a high sensitivity to magnetic perturbation compared to other cables, as the best performers have roughly 5 times more twists for the same length. This conclusion is shared by the experiment in [154], where some STP cables outperformed the coaxial, while others, with lower twisting density, did not.

Going one step further, another physical parameter that can have an influence is the thickness of the cable insulation. Coupled with the twisting length, a cable with thick insulation will create a larger loop, see figure 4.8. If we plot the same results versus the cross-sectional area of a half-twist S , calculated as function of the twisting length and the height (h) that for a tightly wound TP should correspond to the OD

$$S = \frac{h \cdot L}{\pi} \approx \frac{OD \cdot L}{\pi} , \quad (4.1)$$

Table 4.3: Measured twisting length and density and calculated half-twist normal area.

Cable	L [mm]	$1/L$ [mm ⁻¹]	S [mm ²]
eth1	20.0	50.0	8.47
eth2	20.7	48.4	9.21
eth3	18.0	55.6	7.85
stp1	45.0	22.2	15.79
stp2	50.0	20.0	23.85
stp3	26.5	37.7	13.92
stp4	90.0	11.1	64.46
mic1	31.7	31.6	34.78

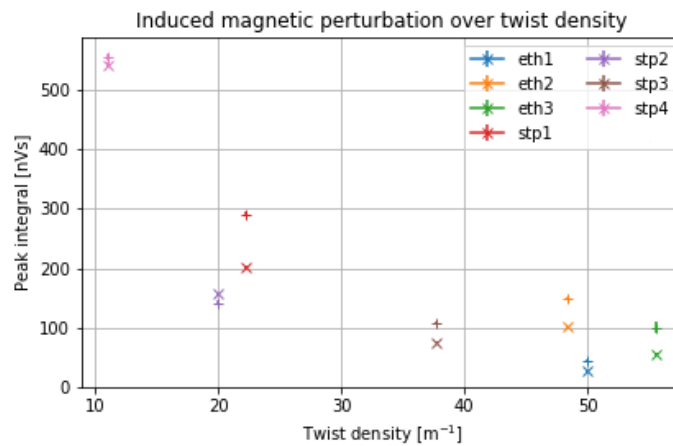


Figure 4.7: Integral of the first peak versus the twisting density for each cable. Measurements with grounding scheme 5, at position 1 represented with “x” and position 2 with “+”.

we obtain figure 4.9. Area values in table 4.3. In this plot an extra point was added for a MIC twisted pair, measured using the MIC5 prototype coil that has a 5 m long lead. The large horizontal error bar reflects the inhomogeneity in the handmade twisting. The correlation of the results to this metric is even more clear.

The results show that a cable with a high twisting density should be chosen for environments with high ∇B and $\frac{\partial B}{\partial t}$. In these scenarios, also the thickness of the insulation of the conductors should be minimized, minding the trade-off with capacitance and breakdown voltage. Perhaps most importantly, this results show that CAT7 Ethernet cables have the same level of rejection of magnetic perturbations as single STPs or coaxial cables, subject to the previous considerations. This is a positive conclusion as the price per meter (per pair) for Ethernet cables is much lower than the other types of cable.

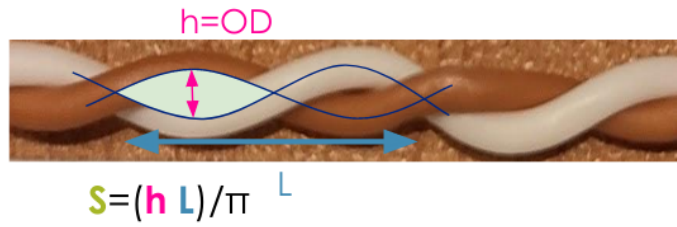


Figure 4.8: Calculation of the normal area of a half twist.

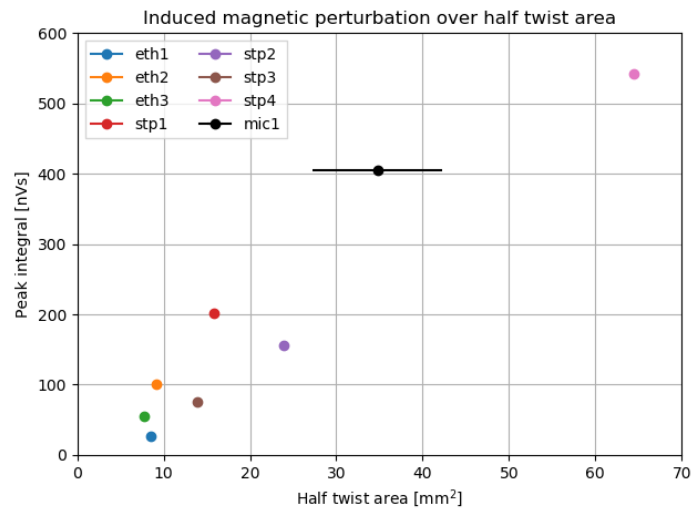


Figure 4.9: Integral of the first peak versus the half-twist area. Only position 1 shown.

4.4 Test of cross-talk

A perhaps more obvious concern when using Ethernet cables for analog signal transmission is that of the cross-talk. On an Ethernet cable, four TP's are in proximity, which raises the possibility of strong signal variations on one pair disturbing the remaining pairs. This can be problematic for magnetic signals, as timing of strong events is a subject of study, and one must ensure the signal is due to a physical phenomenon measured at the sensor position and not influenced by another sensor at a different position.

4.4.1 Experimental setup

The methodology and definition for the study of cross-talk is taken from the realm of digital signal transmission, in which the Ethernet cables are routinely tested and studied. In fact, cross-talk tends to scale with frequency, and digital transmissions are characterized by fast transients (beyond MHz). For magnetic signals we are interested in slower (kHz) yet possibly stronger signals.

Borrowing the nomenclature from digital network analysis, the tests will be based on an “aggressor” and “victim” cable. The aggressor is driven with V_{in} on the near end, which results on V_{out} on the far end. Due to electromagnetic interference, generated by the currents in the aggressor, the victim cable will see [Near End cross Talk \(NEXT\)](#) and [Far End cross Talk \(FEXT\)](#), quantified by V_{NEXT} and V_{FEXT} on the respective ends. Figure 4.10 illustrates these quantities.

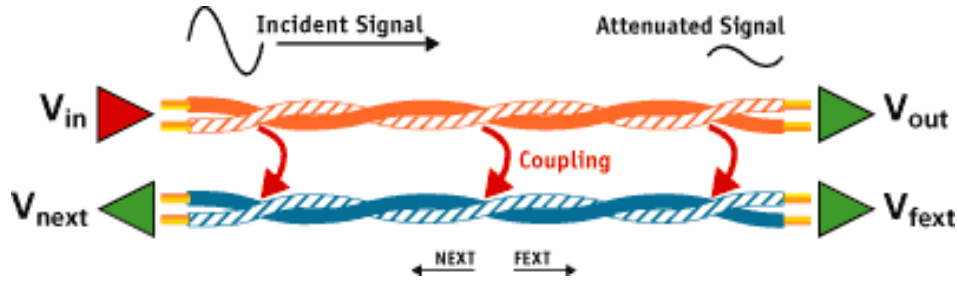


Figure 4.10: Schematic representation of the measured voltages involved in the cross-talk tests.

From these voltages, a few quantities can be extracted. The insertion loss (IL) measures the signal attenuation by losses on the aggressor cable

$$IL = -20 \log_{10} (V_{out}/V_{in}) \quad . \quad (4.2)$$

The cross talk quantities are expressed in terms of the input voltage:

$$NEXT = -20 \log_{10} (V_{NEXT}/V_{in}) \quad , \quad (4.3)$$

$$FEXT = -20 \log_{10} (V_{FEXT}/V_{in}) \quad , \quad (4.4)$$

while for particularly long cables it can be beneficial to define the Equal Level [FEXT](#),

$$ELFEXT = -20 \log_{10} (V_{FEXT}/V_{out}) = FEXT - IL \quad . \quad (4.5)$$

These expressions are expressed in dB with the negative sign being conventional, making the values positive, with an aim of maximizing $FEXT$ or $NEXT$. These values can be interpreted as quantifying the *rejection of* or *immunity to* crosstalk.

To ensure a worst-case scenario, the single [STP](#) aggressors and victims were bound together using electrical tape in a spiral. In order to better manage the 15 m cable assemblies, they were coiled in 2 m perimeter coils, see figure 4.11.

As for the [DAS](#), a NI USB-6218 with insulated analog inputs multiplexed to a 16 bit ADC. The aggregated sampling rate is 250 kSPS. With 7 channels, 35 kSPS sampling was used. This limits the maximum test frequency, which is problematic since the crosstalk effects scale with frequency. The programmable input ranges are ± 0.2 V, ± 1 V, ± 5 V, ± 10 V; and the input impedance is greater than 100 G Ω in parallel with 100 pF. The user manual [155] also specifies crosstalk at 100 kHz in the order of -90 dB, lowering to -75 dB between adjacent channels. The reported [CMRR](#) at 1 kHz is 95 dB.

Table 4.4: Grounding schemes tested. The NE grounding is to the **DAS** while the FE grounding is to the amplifier chassis. (*) In gs 0 the individual shielding of **STP** cables are not connected to each other.

gs	NE	FE
0	floating*	floating*
1	floating	floating
2	grounded	floating
3	grounded	grounded
4	floating	grounded

confirm the increasing crosstalk with frequency. The general behavior of the cables is maintained across the (close) frequencies used.

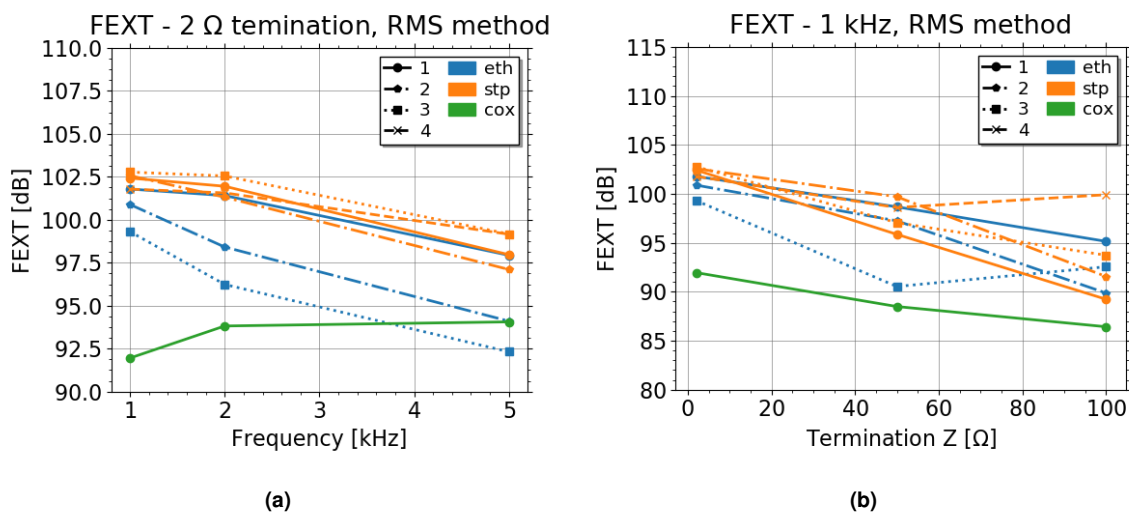


Figure 4.13: FEXT measurements: (a): changing signal frequency; (b): changing victim cable termination impedance.

Fixing the frequency at 1 kHz and ranging the termination impedance of the victim cable, figure 4.13b we see that there is a general trend of increase of crosstalk with the input impedance.

It is not easy to take clear quantitative conclusions from this data. However, it seems fairly clear that the **STP** exhibit the least crosstalk (higher **FEXT** value), then the Ethernet cables follow, with *stp1* having comparable performance to the *stp* cables, while *eth3* tends to have poorer results. Both **TP** cable topologies outperform the coaxial cable.

Finally, instead of leaving the cable shielding floating, we can connect them to ground either at the NE, FE or both. Figure 4.14 shows the **FEXT** results for measurements at 1 kHz with 2Ω termination. First, it is disconcerting that there is a difference between the grounding schemes 0 and 1 as the configurations are the same for *eth* cables. This gives an indication of the uncertainty on the measurements. The only conclusion that can be drawn from this plot is that the crosstalk was greatly minimized when the shielding was connected to the **DAS** reference ground (gs 3 and 4). The change of ~9 dB is much larger than the differences between the cables.

4.5 Cable selection

In addition to the two sources of signal degradation tested in the previous sections, there are other factors that influence the choice of cables. Physical parameters such as rigidity and bending radius, or the actual outer diameter and consequently space occupied in cable fixings or holes through walls. Economical aspects, such as the price is an obvious constraint that can influence the choice, but also the manufacturer and market permanence so that an equivalent cable can be found in years or decades in the future.

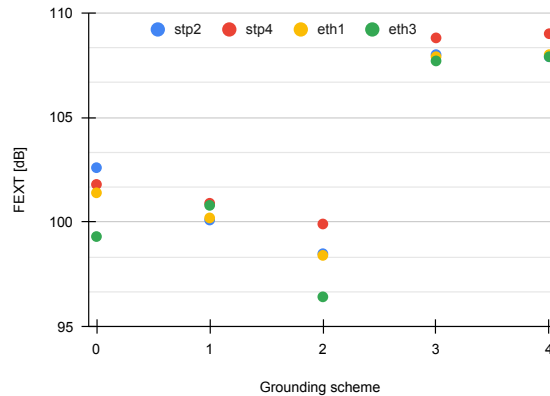


Figure 4.14: Influence of the grounding on FEXT measurements at 1 kHz with 2Ω termination. Reference for grounding schemes provided in table 4.4.

Most importantly, one has to consider the electrical proprieties. In the absence of a harsh radiation environment, the most important ones are the insulation and the reactive parameters. By insulation, we should understand a high resistance between conductors, which is a standard for these types of cable and at these lengths (<100 m); as well as a breakdown voltage adequate for the usage. Some measure of voltage limit is usually provided by the manufacturer, however, the interpretation of the value is not always clear, as it is extremely dependent on the testing conditions. Some provide a value for ‘operating voltage’, of which a typical standard is 300 V. However, unless the cable is marketed for a very specific usage, this value is not thorough – operation at what power and frequency, for how long? For a signal cable application where volt or millivolt signals are the norm, with possible peaks of hundreds of volts, this value is not representative. Sometimes, ‘voltage resistance’ or ‘breakdown voltage’ are provided (in some cases with the testing conditions or standard followed). This value is more relevant and typically higher, with 700 V or 1 kV being typical values. Having a high value for these parameters is recommended. If that is not the case, the cable should pass a test with an expected worse case scenario, for instance 1 kV, 1 ms pulse, mimicking a particularly strong disruption.

In order to evaluate the adequacy of the remaining electrical proprieties of the cables to its application in the magnetic diagnostic, we can repeat the analysis carried out in section 3.5.3. The most affected signal in case of a wrong cable selection would be that of the probes for pickup of high frequency oscillations. We have seen that in these sensor types, the bandwidth is limited by a resonance rather than attenuation. It was also demonstrated how the calibrated probe–cable–DAQ system can be used to simulate the response to magnetic fields with different cable parameters.

For this analysis we start by identifying the RLC proprieties of the cables. These are usually specified in the manufacturer datasheets. When the inductance is not provided, it can be inferred from the impedance (Z_0) or the propagation velocity (velocity factor, v)². These are expressed in the plot in figure 4.15. We see that the cable choices have very different parameters, spanning a wide parameter range, in particular for the STP cables, that are manufactured for distinct or unspecified applications. Conversely, all Ethernet cables appear clustered as they share intended application and requirements.

Using the $(R)LC$ values, we can simulate the response that would be obtained on the Helmholtz testing setup, figure 4.16. In this plot, we can identify a satisfactory agreement with the experimental results, considering the experimental limitations discussed in chapter 3. While some second order behaviors that are not modelled are evident, the first and second resonance frequencies were accurately predicted. Since signals are usually not sampled by oscilloscopes, we can use the same model to implement the full length of cable (30 m) and a more realistic input impedance for the DAS ($200\text{ k}\Omega \parallel 82\text{ pF}$). These results are shown in figure 4.17. The color/marker notation is shared with figure 4.15, and a close interpretation of both figures shows that the frequency of the resonant peaks is mostly dependent on the cable capacitance. The obvious conclusion and ‘rule-of-thumb’ is that for high frequency, low current signals, the minimization of the signal cable capacitance is paramount. Efforts in sensor design optimization might not lead to the expected gains if the wrong cable is se-

²Definitions in section 3.5.3.

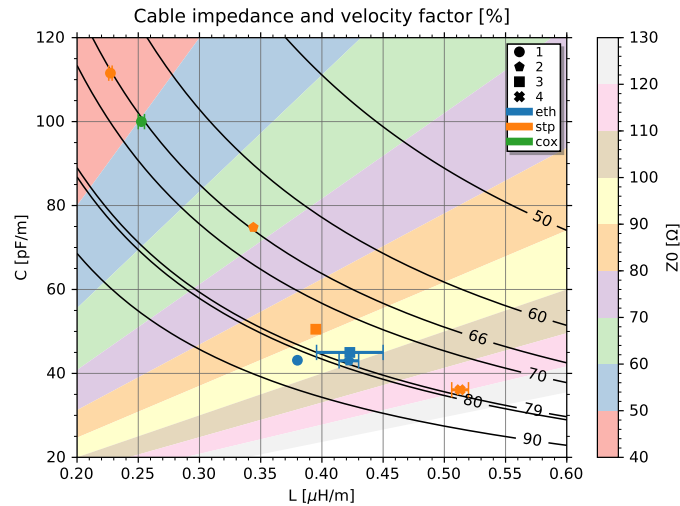


Figure 4.15: Map of the tested cables reactive properties (inductance, capacitance) and derived quantities: impedance (Z_0 , in colors) and velocity factor (black lines, as percentage of c). Parameters taken from datasheet, when available. When L is not provided, it is inferred from C , Z_0 and v , hence the horizontal error bars.

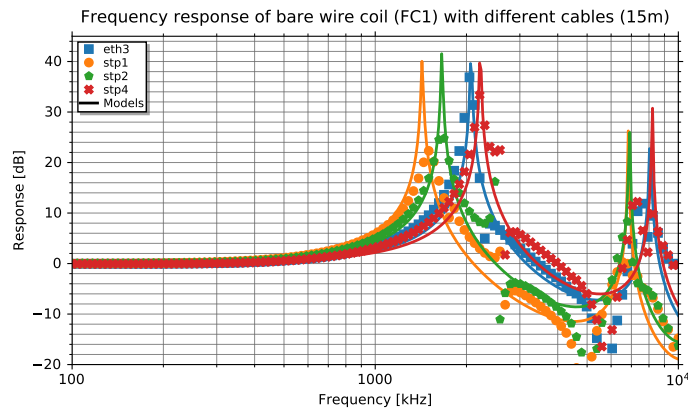


Figure 4.16: Measurements of the frequency response of a bare wire coil (FC1) with different cables. In addition to the measurements (markers), the electrical model for each cable is represented as full line, matching the color.

lected.

Finally, we can reach some conclusions on the cable choice for the COMPASS-U magnetic diagnostic. In section 4.3 it was shown that CAT7 Ethernet cables have better or comparable rejection of external magnetic noise, mostly due to their high twisting density. Despite bundling four TPs in the same assembly, in section 4.4 it was shown that the cross-talk levels are comparable to single-TP cables if bundled tightly. In applications with hundreds of signals, this is often the case, albeit not in such extreme level of contact as in the tests (worse case scenario). Ethernet cables trade a potential 1–3 dB of high frequency cross-talk for savings in price and occupied space. However, a careful choice of the particular cable is important, as the *eth1* cable shows systematically higher FEXT values. Conveniently, this particular cable also has a low capacitance per unit length, being a good choice for high-frequency signals.

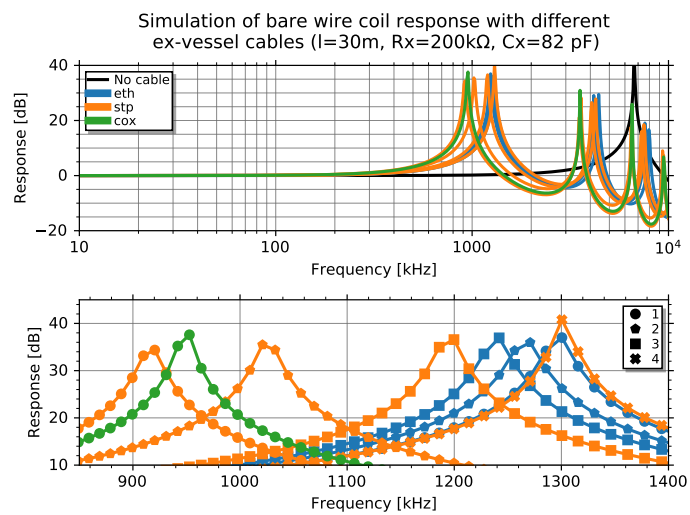


Figure 4.17: Simulation of a bare wire coil (FC1) response with different cables, calculated for a length of 30 m and connected to a DAS characterized by an input resistance of 200 kΩ in parallel with an 82 pF capacitance. Reference with no cable represented as the black line. On the bottom plot, a zoom on the first resonant peaks is provided, on linear scale, with full identification by color and marker.

5

Digital integrator development

Contents

5.1	Conceptual qualification of digital integration as a solution for COMPASS-U . . .	104
5.2	Testing of digital integration on COMPASS	112
5.3	COMPASS-U modular DAS concept	116
5.4	Electronics design and development	118
5.5	Prototype testing and qualification	128
5.6	Implementation for COMPASS-U	146

A ‘digital integrator’, in the context of magnetic diagnostic should be read as data acquisition system that performs real-time numerical integration, using the discretized voltage. Hence, digital, in contrast with the analogue integrators, where the sampled signal is proportional to the integral of the input voltage.

Development of this type of integrators has been ongoing since its first conceptualization for W7-X. Being the state of the art marked by the development of such integrator for ITER, the work on the chapter takes a step back on that evolution and creates a new branch, a digital integrator that uses the current state of the art on a technical level, while aligning its requirements and performance with that of a more conventional research tokamak. The long pulse integration performance is not taken as the ultimate goal, but instead as a solid base for the development of a future-proof, flexible, integration solution for any tokamak in general, and COMPASS-U in particular.

5.1 Conceptual qualification of digital integration as a solution for COMPASS-U

The first step in the development of a new system is the understanding of that system on a conceptual level, and the evaluation of the requirements.

In this section, the phase switched modulation is detailed, key concepts that were not yet introduced are defined, as a groundwork for the technical qualification–design–implementation steps that follow.

The second part of this section examines the requirements on the data acquisition. These were not specified from top-down, but rather constructed over time and with the inputs of others, allowing a conversion between the high-level requirements on plasma parameters, and the low-level technical requirements and/or implications on the electronics.

5.1.1 Architecture of a digital integrator with phase switched modulation

As mentioned in the state of the art (2.4.4), the phase switched modulation made numerical integration of magnetic diagnostic signals feasible. Moreover, beyond feasible, a good solution for long pulses (W7-X, ITER). This mechanism was already covered in previous publications [116, 156], but will be reproduced for clarity. The main idea is to periodically invert the coil signal, before sampling. This is achieved by Complementary Metal-Oxide-Semiconductor (CMOS) switches, that in the ns scale change the polarity of the input of an otherwise standard ADC electronics chain: high input impedance, low output impedance OPAMP as a driver, possibly implementing an anti-aliasing filter, passive settling filter, and the ADC Integrated Circuit (IC) itself. Under the modular ATCA-based architecture used in this thesis, the described steps are physically confined to a galvanically insulated module with the remaining, digital processing in a carrier board with a FPGA at its core (see figure 5.1).

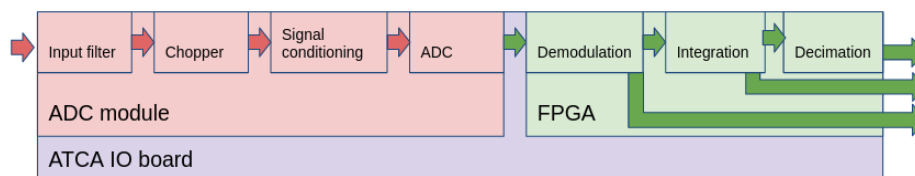


Figure 5.1: Architecture of the implementation of phase switched modulation on the IPFN ATCA-based DAS. The arrows follow the signal path from input to output with red denoting analog signal and green, digital.

The chopper action constitutes a modulation of the signal with a square waveform. On the digital domain, the signal is then (re-)inverted accordingly, that is, demodulated. To see the benefits of the technique, we need to consider the DC or low frequency components added to the signal in the electronics chain. These can arise from the main drift inducing factors identified in 2.3.2 and 2.4.4 – imbalance between the positive and negative paths, component uncertainties, thermoelectric voltages, and above all, OPAMP input offset. Following the notation in [116, 156], we shall categorize all these offsets, between the chopper and the ADC (see figure 5.1) as Electronics Offset (EO). In figure 5.2 we can see the effect of an exaggerated EO added to the signal. Originally sinusoidal,

the signal is modulated by the chopper, with periodic polarity reversal. At this point, the added EO will affect the modulated signal, in this case, raising it. Upon demodulation, already on the digital domain, the initially monotonous offset now appears variable, above and below the original signal. In effect, the demodulation process modulated the EO. The resulting integral is perturbed by this effect, however, on a timescale much larger than the chopper period, the EO can be seen as a noise. Above all, there is no longer a DC component being integrated over time. In the particular example provided, exaggerated for illustration, this offset is 40 % of the signal amplitude, which would completely dominate the integral after a few periods.

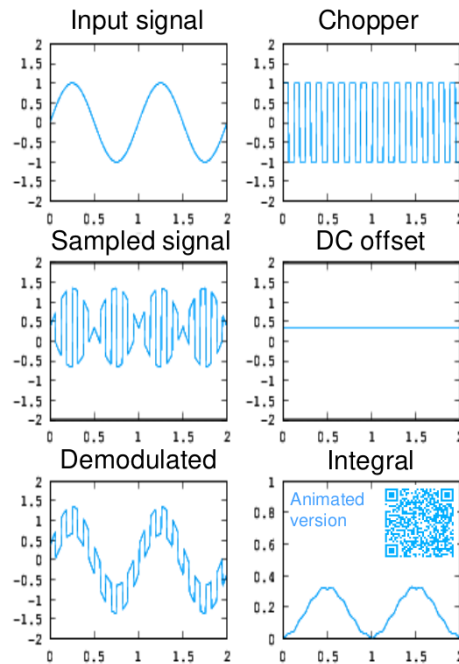


Figure 5.2: Illustration of the modulation effect on an offset of the EO type, inserted after modulation. An animated version, ranging the offset level can be seen in [157], the target of the qr-code on the bottom right plot.

The EO encompasses all noise introduced downstream from the chopper. However, it is not the only offset considered. All DC or low frequency offsets introduced upstream from the chopper – Wiring Offset (WO) – will be indistinguishable from the signal itself at the electronics input. Examples of WO are correlated, low frequency noise picked up by the sensors, thermoelectric or contact resistance voltages introduced upstream, or resulting from unbalance. In the positive and negative signal branches. As in any other integrator design, there is a calibration step, that tries to mitigate the WO. With this architecture, both EO and WO can be calibrated: acquired and removed digitally, in real-time. However, the WO, albeit smaller in magnitude, has stronger time dependence [156], and should be measured in as close conditions to operation as possible, in ‘magnetic silence’ without the interest dB/dt at the sensor. Calibration of the EO can be made in the same conditions or with a short-circuited input, provided that the conditions at the DAS and room are the operational conditions (ambient temperature, elapsed uptime of the system).

While not being strictly necessary, the input filter is a key component of the digital integrator. Its main purpose is to reduce the dynamic range of the signal, that is, it lowers the amplitude of the very high-frequency MHD oscillations or disruptions (stopband) while keeping the low amplitude equilibrium signal unaltered (passband). As a consequence, the sampled signal will look distorted, as the transfer function of the transduction from dB/dt to measured ADC samples is changed. However, the integral – the main objective of the electronics chain – is preserved, on a timescale greater than the characteristic time of the filter. Ignoring minor losses of dissipation on the real-life components, the energy is preserved, stored in the active components and released over a characteristic time τ , minimizing the risk of ADC saturation.

The filter should be placed before the chopper, at the input stage. In this way, it can be implemented together with a DC attenuator, adjusting the signal extremes. Just like the ADC (and OPAMP for that matter), the chopper can also experience saturation, and consequently the same reasoning for dynamic range reduction is valid. Yet another reason for the placement of the filter before

the chopper is that the chopper transition should be as fast as possible, consequently as close to a square waveform as possible. As for the topology of the filter, it is clear that a passive filter should be employed. As any offset introduced before the chopper is **WO**, one should not use **OPAMPs** at this stage. Cascading passive filters also has negative effects as the phase delay will compound.

In summary, the input filter design should be a passive first order **LP** filter, with DC attenuator by resistor divider if needed, with a cut-off as high as possible to minimize phase delay, constrained by the dynamic range reduction needs. The component accuracy (nominal precision and matching) as well as the thermal coefficients are of the utmost importance, as to minimize **WO**. In addition, a careful balance should be reached between DC and frequency attenuation, as to ensure the needed **SNR** and minimize the probability of saturation during the integration time.

5.1.2 Assessment of requirements for COMPASS-U magnetics

In order to establish the requirements on the electronics, one needs to propagate the physics requirements or expected parameters into quantities that are relevant for the design of the data acquisition electronics.

For the magnetic diagnostic, due to the high dynamic range of the signal, the most relevant parameter is the input range. One has to ensure that the data acquisition has enough resolution to prevent signal loss and that the full range of the interest signal is measured.

The resolution constraint will be defined by the equilibrium component of the signal. The maxima, on the other hand, occur during fast events: **MHD** activity and disruptions. The latter can be either total – upon which integration accuracy is not a requirement; or partial – sudden losses of plasma current during ramp-up or ramp-down, upon which the integration must keep running without significant error being committed.

In addition, we can expect integration drift. It is important to evaluate what is the acceptable level, according to the needs of the systems that will use the integrated data in real-time.

5.1.2.A Resolution

While ultimately the resolution is tied to the input voltage by the number of bits of the **ADC** and gain on the electronics chain, these two requirements will be analyzed individually.

Based on the expected equilibrium profiles, as simulated using the Fiesta equilibrium solver [158], the **VV** and **PSP**, and positions and effective areas of the magnetic sensors, the magnetic field and sensor voltages were computed.

The simulation was run for the relevant coils across 99 equilibriums present in the **COMPASS-U Database (CUDb)**¹. Figure 5.3 shows the maxima of the expected voltages.

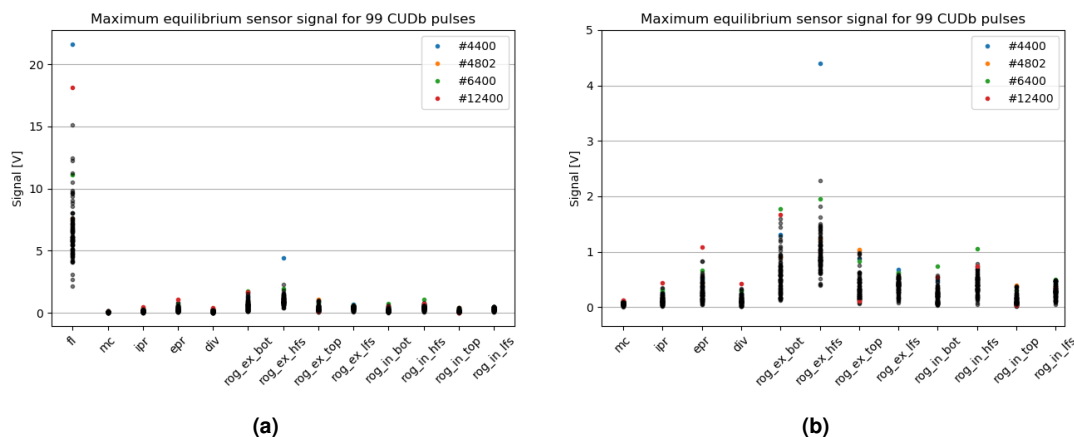


Figure 5.3: Maxima of the voltage signals for magnetic sensors (*x*-axis) across 99 equilibriums (points). For sensor arrays that have more than one voltage, the maximum is taken. Equilibria that have a maximum in at least one sensor type highlighted in color. Plot in **(b)** excludes the flux loops (fl).

¹Not all the equilibriums present in the database are reference or realistic scenarios. Some are parametric ranges for other analysis. However, all were used as we are not only interested in reference plasmas but worse-case scenarios.

While the real maxima will not be defined by the equilibrium signal, one can draw already some conclusions regarding the expected data acquisition input ranges. From the first plot we see that the flux loops are on a class of their own, with more than 20 V being expected. This is in agreement with the observations on COMPASS magnetics. On the second plot, with the flux loops removed, we can further expect the signal of Mirnov Coils (mc) to be one order of magnitude lower than the current measuring segmented Rogowski coil (rog_*).

Expecting only up to ~ 100 mV maxima on the Mirnov coils equilibrium signal, we foresee that the resolution will be the most problematic for these sensors.

In order to evaluate the effect of the resolution, a synthetic discretizer was devised. Starting from the expected sensor voltages, the following processing was applied (see figure 5.4): up-sampling and interpolation of the data to 2 MSPS, addition of white uncorrelated noise, discretization according to a given resolution and integration. The accumulated error was referenced to the integrated signal without the synthetic discretization.

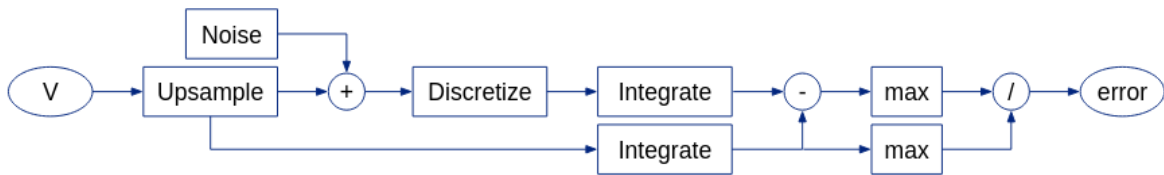


Figure 5.4: Scheme of the discretization error evaluation procedure.

Having a large amount of variables, the simulation analysis was based on plots such as the ones in figure 5.5, with the error displayed as color, across the tested equilibriums in the horizontal, and the resolution in the horizontal. We see that on average, resolutions below $40 \mu\text{V}$ result in negligible

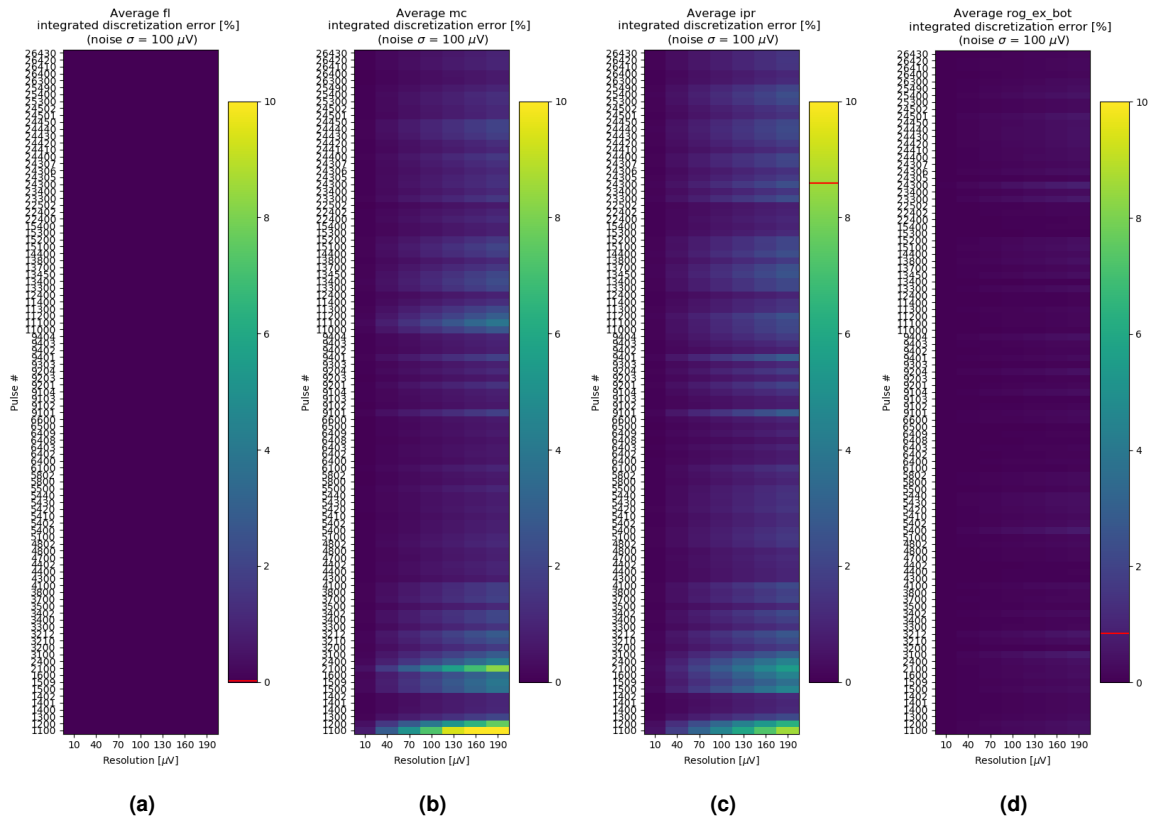


Figure 5.5: Integrated discretization error (color, percent) for different sensor types. The simulation was performed with a synthetic sampling under different resolutions (x -axis), and for multiple equilibriums (y -axis) represented according to their pulse number in the CUDb. Simulations include addition of random noise and the error is averaged across the individual coils of the same type – (a): Flux loops; (b): Mirnov coils; (c): in-vessel partial Rogowski; (d): ex-vessel Rogowski segment (bottom). Data maxima represented in the color bar as a red line.

error. For the sensors with the largest effective areas, resolutions up to 200 μV are reasonable, while for local sensors, with smaller effective areas errors up to 5 % are possible if the resolution is much lower than 100 μV . We can also appreciate the role the plasma scenario plays. In this aspect, the lower plasma current, the lower the equilibrium magnetic signals, as expected.

Being the Mirnov coils the most problematic, particular attention was drawn to its simulation. Figure 5.6 shows the error with and in the absence of added noise for the 30 CUDb entries with the highest error. Given that different coils have widely different voltages, according to their position, for

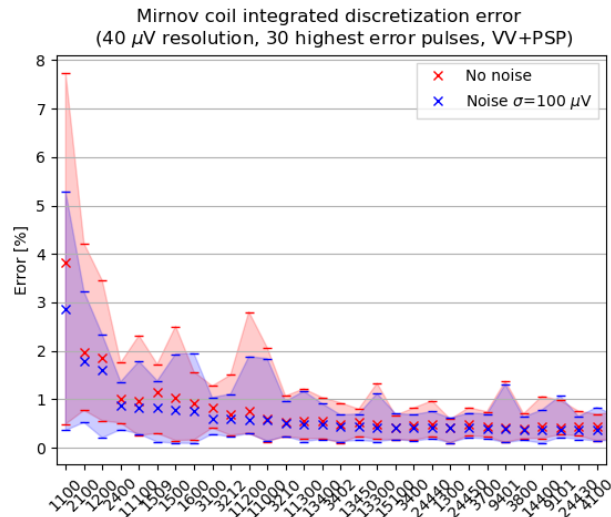


Figure 5.6: Integrated discretization error for Mirnov coils with 40 μV resolution. With added noise (blue) or without (red). For each equilibrium, the minimum, maximum and average values are plotted, sorted by average value.

each 'discharge', the maximum, minimum and average value are represented. We see how the presence of random noise on the oversampled signal helps minimize integration error to a certain degree. We also see that the integrated discretization error amounts to <1 % for the vast majority of scenarios and sensors with a 40 μV resolution (corresponding more or less to $\pm 5\text{ V}$ input range). However, for low current, circular plasma scenarios, where the magnetic signals are lower, this error can represent up to 5 % of the maximum (integrated) signal amplitude. This is an argument for lower input ranges on these channels for the first phase of operation or to extend the dynamic range of the DAS.

5.1.2.B Signal during disruption

Disruptions provide an additional challenge for magnetics. Even if the plasma discharge ends with the disruption, and there is no possibility of actuating on the plasma on this timescale, the strong induced EMF can damage the electronics chain.

In order to analyze its effects on Mirnov coils, a simulation of the strongest, fastest possible disruption – worse case scenario – was requested. These simulations can be performed with the CarMa0NL [159, 160] code. Among other observables, this code can export the magnetic field rate of change at specified points in-vessel.

Figure 5.7 shows the dB_{θ}/dt at selected Mirnov coil positions. The simulation consists of a linear quench of the 2 MA plasma current in 0.6 s (3.3 MA/ms), simultaneous with a VDE towards the top limiter. The maximum was registered for the HFS midplane coil at 25 T/ms.

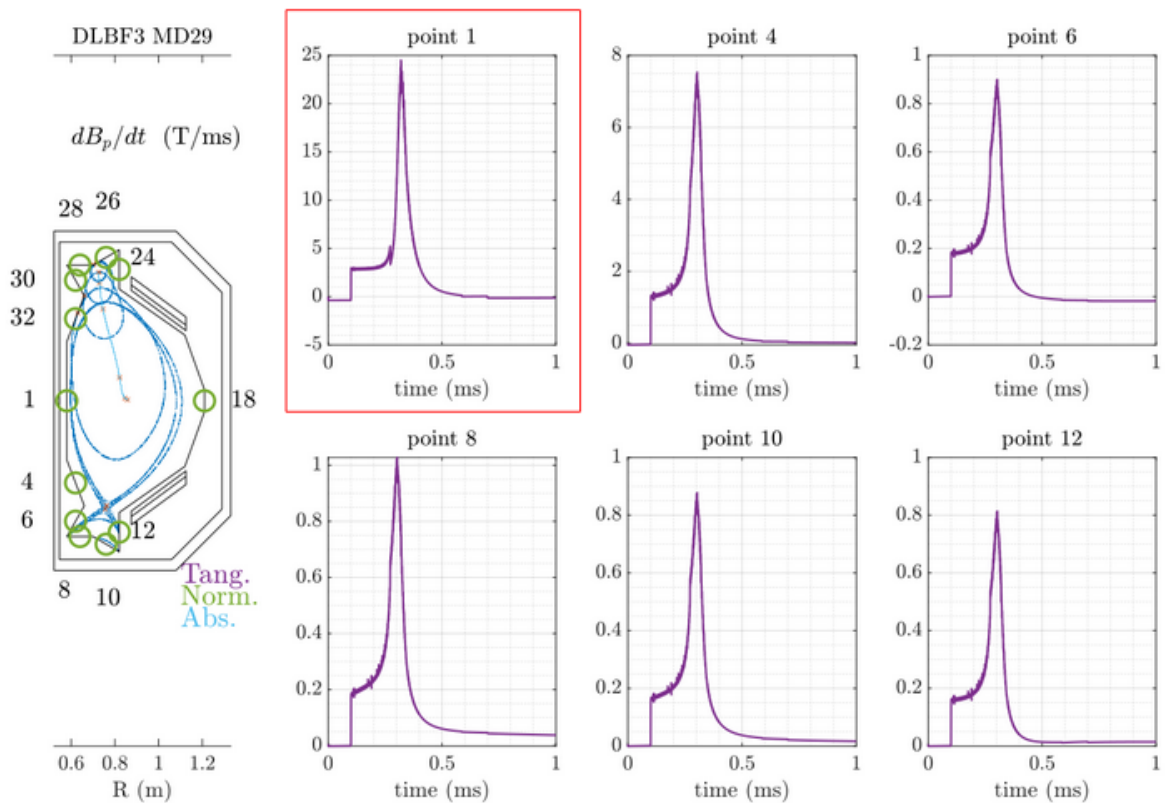


Figure 5.7: Poloidal dB/dt as calculated by CarMa0NL simulation for a 3.3 MA/ms current quench and VDE. Point 1, on HFS, highlighted, exhibits the highest value.

With an effective area of 200 cm² this corresponds to 500 V. To this voltage peak, several attenuation factors have to be added. The simulation takes into account the **VV** and **PSP** eddy currents but not the plasma facing components that will protect the coil and slow down the field penetration at **HFS**. As seen in chapter 3, the **MIC** construction of the sensors will further attenuate the signal. Additionally, the data acquisition system itself includes low-pass filters. Figure 5.8 exemplifies the effect of a first order filter at different cutoff frequencies applied to the disruption signal. The attenuation according to the filter cutoff frequency is expressed in table 5.1. While the ‘correct’ attenuation transfer function is more complex and unknown, these values give an idea that the simulations can be overestimating the actual voltage by a 25–40 % factor.

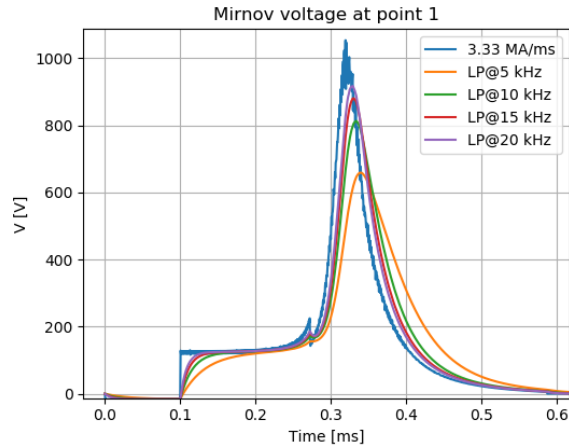


Figure 5.8: Effect of first order low-pass filters on the disruption signal at point 1, using $S_{eff}=430 \text{ cm}^3$.

Table 5.1: Attenuation to the disruption signal provided by different first order low-pass filters.

f_c [kHz]	ratio []	[dB]
5	0.63	-4.1
10	0.77	-2.3
15	0.84	-1.6
20	0.87	-1.2

It makes no sense to try to measure such disruption with the same data acquisition system that controls or reconstructs the equilibrium. After all, even if dedicated disruption studies are carried out, 2 MA disruptions will most likely not be induced, as they generate substantial mechanical loads. However, the fact that 500 V as a sub-ms pulse can appear at the data acquisition input is important knowledge. Even if not intended to measure, the electronics must not be damage by such event.

5.1.2.C Drift requirement

In order to establish a requirement on the maximum integrator drift, EFIT reconstructions were run with and without random integrator drift (normal distribution) added to the magnetic sensor data. This allowed the evaluation of the reconstruction error at key points: including current centroid, clearance to the limiters, and strike point at divertor, see figure 5.9.

Running statistical samples for each drift magnitude, it was determined that a drift below 5 μV prevents reconstruction errors above 1 mm [161]. This value will be taken as a requirement for the integrator drift.

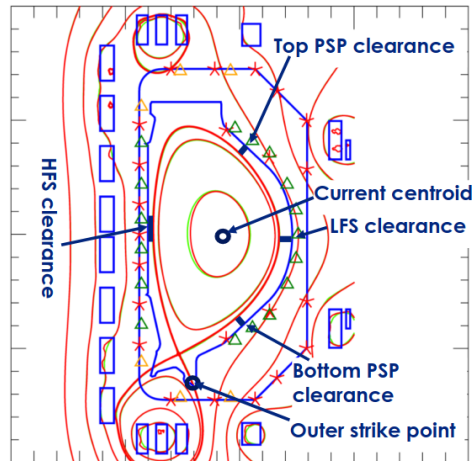


Figure 5.9: Observables used in the analysis of the effect of random and systematic errors in the equilibrium reconstruction. Reference equilibrium in green, EFIT reconstruction in red. Originally presented in [161].

5.2 Testing of digital integration on COMPASS

The performance of the integration with switched modulation was assessed in COMPASS, as a qualification step for implementation on COMPASS-U. These results were published in [162] and are here shown in more detail.

COMPASS DAQ infrastructure includes several ATCA crates with MIMO-ISOL data acquisition boards installed [62, 163]. These boards were developed at IPFN [164] and process inputs through 18-bit, 2 MSPS ADC galvanically isolated modules, in addition to 8 16-bit galvanically isolated DAC channels, hence Multiple Input Multiple Output (MIMO)-ISOLated (ISOL). Over time, compatible modules with integrated ‘chopper’ and similar ADC were developed and operated in ISTTOK and W7-X [116, 117]. It was then possible to test the digital integration on COMPASS, using only a few modules, similar to those used in ISTTOK, and the corresponding software and FPGA firmware.

In addition to the ATCA, a National Instruments PXIe-6368 16-bit DAS is also available. Working at the same sampling rate, this system will be used as a reference, sampling the same signals. The integration of this signal is performed numerically, at data analysis stage.

The ATCA integration modules will not be connected to any real-time system. Instead, the integration is performed in real-time in the FPGA, with the data being streamed asynchronously to the host computer through Direct Memory Access (DMA) blocks with a fixed size.

5.2.1 Integration of COMPASS pulses

The first step in the experiment was to evaluate the adequacy of the electronics chain to the signals to be measured. The experiment was conducted in ‘piggyback’ to a scheduled campaign, hence it should not limit the availability of sensors for the main experiment. Thankfully, COMPASS has a high number of magnetic sensors and this was not problematic. The selected signals are from Mirnov coils in the array ‘C’, out of a total of three such arrays, with 24 probes [21]. These are routinely sampled by a PXIe-6368 DAS with the selected signals being sampled in parallel by the three modules available for testing.

Featuring a configurable input filter², it was important to evaluate if the configuration that is optimized for ISTTOK was adequate for the COMPASS signals. First, the frequency response of the modules was measured with a signal generator, see figure 5.10. We see that the expected frequency response of a first order LP filter is obtained, with a fitted cutoff frequency of $f_c = 8813 \pm 12$ Hz. Similarly, the calibration factor of $1.72071 \cdot 10^{-5}$ V/LSB was measured (1:1.1 gain).

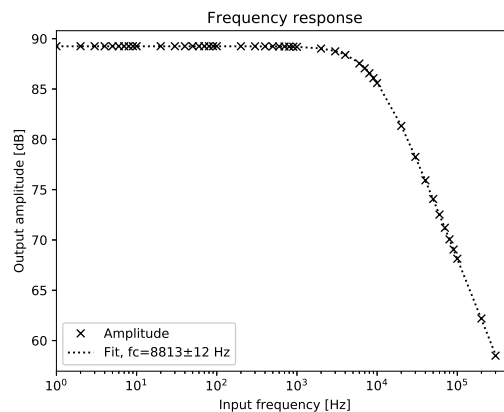


Figure 5.10: Measured amplitudes for a 1 Vpp harmonic input signal, in dB relative to LSB. Fit of the frequency derating with the frequency response of a first order low-pass filter.

Having characterized the input filter, its transfer function can be applied to the signals in the COMPASS database corresponding to the Mirnov array C. From the maxima of these signals, it was possible to conclude that a set of three signals can be chosen with adequate signal strength and minimal probability of saturation (during disruption). Figure 5.11 shows the signal maxima for the past 200 discharges, with the chosen probes (3, 11, 13) and the ADC saturation level highlighted.

²Manually, by replacement of passive components.

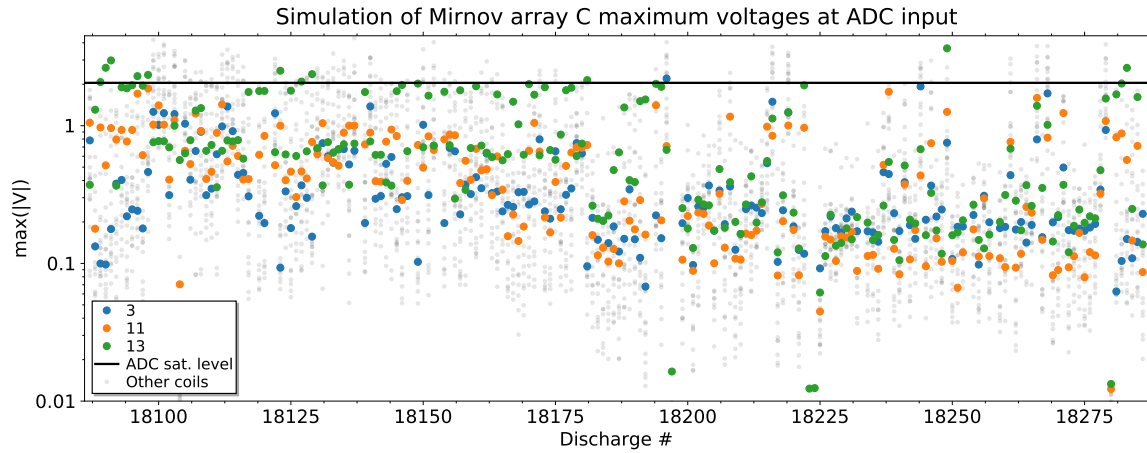


Figure 5.11: Simulation of maximum (bipolar) expected signal for the sensors in Mirnov array C if sampled with the input filter present in the ADC modules. The ADC saturation level is represented by the horizontal line and the three chosen sensors are highlighted in color. The signal maxima depend mostly on the presence or not of disruption (order of magnitude factor) conditioned to the position and time evolution of such event.

Figure 5.12 shows representative results for one signal on a typical discharge without disruption. The figure represents two curves on each plot, the same signal as acquired by the ATCA module and the PXIe card. On the top row the proportional (not integrated) signal is shown, while the bottom row shows the integrated data. From left to right we explore the signals on decreasing timescales. The first column shows the global view of the 500 ms discharge. Here it is noteworthy that despite the ‘raw’ signal envelope being reduced by one order of magnitude, the integral is not affected. This attests the adequacy of the input filter in its role of reducing the dynamic range of the sampled signal.

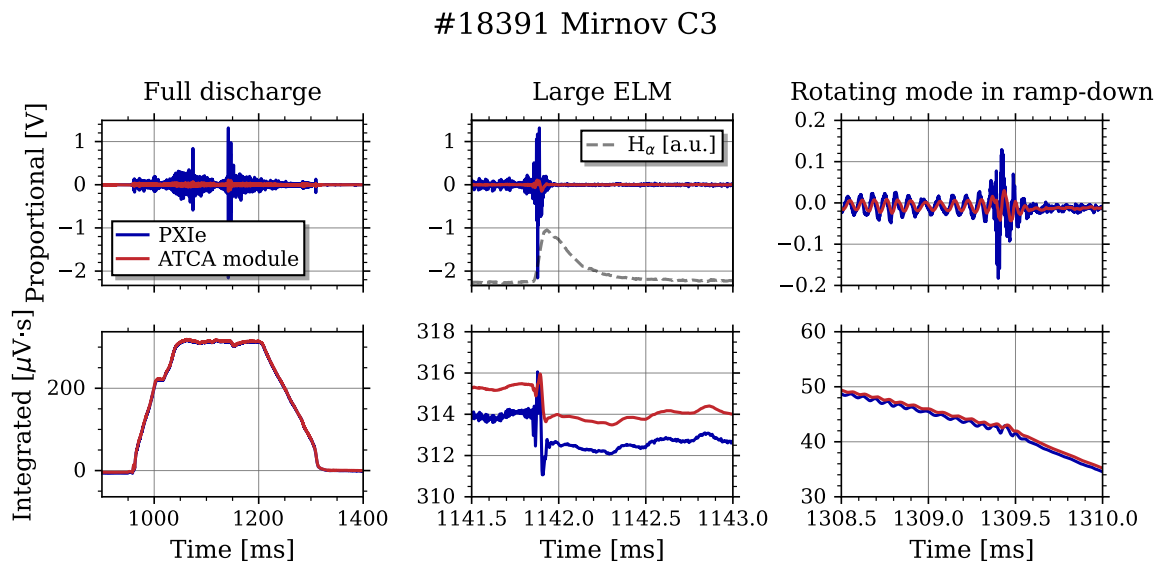


Figure 5.12: Proportional (top) and integrated (bottom) signals of a Mirnov coil for the ATCA modules and NI PXIe for a COMPASS discharge. First column shows the full discharge, middle shows a detail of a strong ELM (H_{α} signal shown for reference) and on the last column, detail of a rotating island observed on the ramp-down. Figure originally published in [162].

The middle column shows a zoom to the event with the largest amplitude – a single ELM during high confinement mode³, as shown by the H-alpha (intensity of atomic hydrogen light) signal. At

³Unfortunately the data was acquired during one of the last days of a (rather successful) campaign that aimed at suppressing ELMs using Resonant Magnetic Perturbations (RMPs). For this reason, no discharge with the usual ‘train’ of ELMs was acquired.

this scale (ms), we better observe the attenuation of the fast even in the sampled signal, resulting in minimal effect on the integrated quantity.

Finally, in the last column we observe the signal produced by a rotating island during ramp-down. As the frequency of this perturbation is roughly 14 kHz we do observe some attenuation ($f_c \approx 9$ kHz). This does not impede its identification and tracking, in part due to the high resolution of the 18 bit ADC. The fine detail (μ s) that is lost, is of no importance for the controllers, as the actuators can not react in this timescale. In fact, one can make the argument that fast transients can ‘trick’ the controllers, for which reason the application of digital filters to reduce the bandwidth of the controller input signal are common.

5.2.2 High frequency recovery

As discussed in 5.1.1, the input filter is a critical component on the integrator design. A careful analysis of the hybrid integrator concept proposed by Strait in [114] and reviewed in chapter 2 (2.4.4) shows that while the key role is different, the same filter is employed. It is therefore possible to apply the same (digital) processing to the COMPASS data, as all ‘raw’ data at the sampling rate was saved. The reconstruction consists in assuming the high frequency components integrated by the filter and integrating digitally only the low frequency part. Using (2.58), with knowledge of the RC constant, the inverse of ω_c , one obtains the results in figure 5.13. In time domain, figure 5.13a adds the reconstruction to the ELM time trace in figure 5.12 and further adds a disruption scenario. On both instances we can see a very good agreement with the reference signal at the μ s scale.

In the frequency domain, the spectrogram in figure 5.13b further reinforces the previous observation, as the major MHD activity features are recovered with the original amplitude.

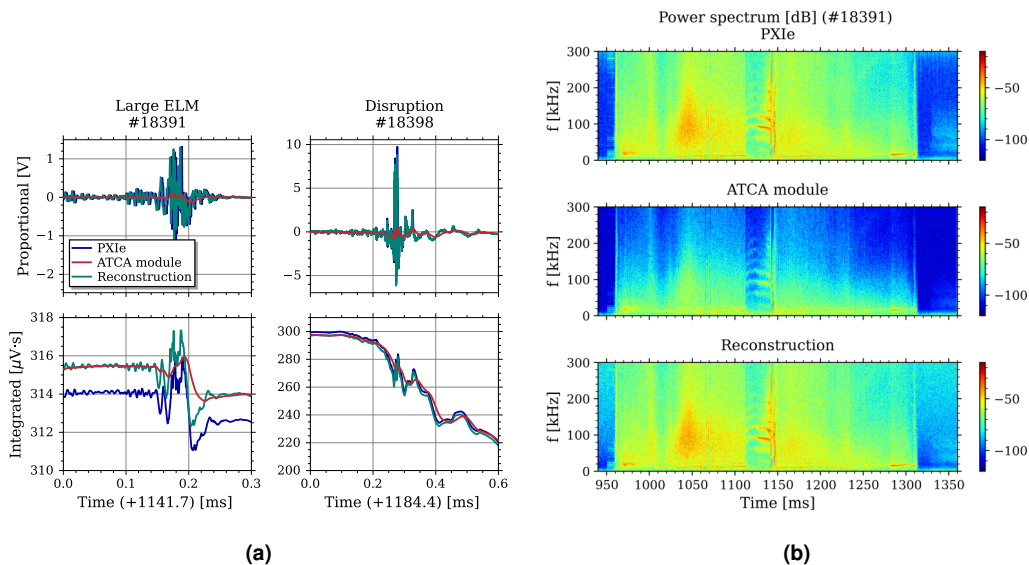


Figure 5.13: Demonstration of the high frequency reconstruction technique in time (a), and frequency (b) domains. In (a) two features with high frequency components are shown: on the left a large ELM and on the right a disruption. In (b), power spectrograms for the reference DAQ (top), the ATCA module, where the analogue filtering is noticeable (middle) and the result of the reconstruction technique (bottom). Figures originally published in [162].

In the spectrogram we can also identify (particularly in the vacuum parts, before and after the plasma) a considerable addition of noise. In fact, high frequency noise that is added to the signal in the electronics chain, after the input filter, is affected by the reconstruction. Unlike the signal itself, it was not affected by the input filter, resulting in a net amplification. This amplification can be seen in the transfer function in figure 2.32, if we consider a (noise) component that is not subject to one of the curves, the perfect integration can not be obtained.

Because of the added noise, this reconstruction technique is not being considered for real-time implementation on COMPASS-U. Real-time applications do not require the measurement of high frequency signals, however, it will be possible to implement the technique offline (systematically or on-demand) since the full non-integrated data will be saved and streamed post-discharge. Another

situation where this technique can be employed is if the high frequency MHD sensors can not be used, due to a high number of failures or complete inoperability during campaigns at elevated temperatures or liquid metals. In such case the technique is a useful backup solution, recovering relevant physics data from the equilibrium coils. As the roadmap of fusion progresses towards devices with more limited diagnostic sets, such techniques (robust and real-time compatible) have an increased relevance.

5.3 COMPASS-U modular DAS concept

The digital integration solution for COMPASS-U will consist of a new instance of the **ATCA** digital integration modular **DAS**. Several factors motivate the development: (i) to take advantage of technological improvements in electronics since previous instances; (ii) due to the incompatibility of the existing COMPASS hardware with COMPASS-U **CODAC** requirements, both quantitatively and qualitatively; (iii) to ensure procurability of the system, for first plasma, and opening the possibility for upscaling in the future; (iv) and to develop the electronics with the COMPASS-U magnetic diagnostic requirements in mind, not focusing on long-pulse performance, whilst benefitting from the consolidated performance and know-how in this aspect.

This task, akin the underlying system, is divided in two: an input processor **ATCA** carrier board; and the **ADC** modules with integrated chopper. Only the latter falls in the scope of this thesis. The development of both systems is decoupled by prototyping the modules in retro-compatibility with an exiting carrier board – the **Input-Output Processor (IOP)**, section 5.3.2. In this way, the modules can be developed and tested ahead, and the new carrier optimized accordingly.

Unlike with the MIMO-ISOL, used in 5.2, each module on the **IOP** has two channels. This feature greatly improves the channel density of the system. With a dual module architecture, other operation modes, in line with the COMPASS-U requirements, can be explored.

5.3.1 Two-channel architecture and operation modes

The **IOP** board has two key advantages over the MIMO-ISOL used in COMPASS and ISTTOK. The first is the disposition of the modules parallel to the forced airflow. Temperature variations are one of the most important drift inducing factors, as changes in the thermoelectric voltages void the calibration carried out at a different temperature [118]. The disposition of the modules parallel to the airflow allows for a more efficient temperature regulation.

Then, the usage of modules with two channels greatly improves the (physical) density of channels in the board. Inside the module, the two channels feature separate power, analog and digital signals. The galvanic insulation is ensured separately for each channel (details in 5.4.2). For this reason the two channels have a good insulation between one-another, a requirement for using the system in ‘individual sampling’, with one module sampling two distinct coils.

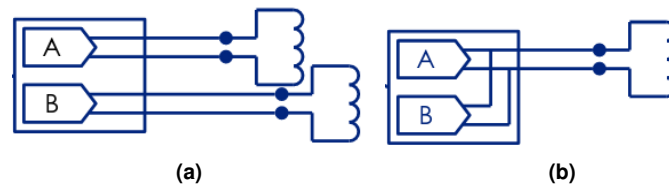


Figure 5.14: Illustration of the coil connections for individual sampling (a), and for parallel and extended dynamic range sampling (b). The two **ADC** channels are labeled ‘A’ and ‘B’.

In spite of the good insulation, having two channels, the modules can also sample the same coil – ‘parallel sampling’. Each channel can have different input ranges and/or filtering at the input. This concept is used in magnetic diagnostic in several devices, such as in COMPASS. Splitting signals from magnetics can be beneficial for integrated (with an analog integrator or numerically) and proportional measurements; a high resolution, filtered signal for control during flat-top and a high input range path for disruption or **MHD** analysis. On this last example, the difference in requirements is particular relevant: if one is interested in studying disruptions, they must adjust the input range as to allow the measurement of an eventual fast, strong disruption ‘landing’ in proximity of the sensor (in the case of probes). This is in obvious contradiction to the requirements of the controllers or equilibrium reconstruction algorithms that privilege the best possible **SNR**, which would result in a saturation of the **ADC** or **OPAMPs**, at a point in time that is meaningless, as there is no plasma in **MHD** equilibrium to control or reconstruct.

In addition, if we consider one channel as the ‘main’ and the other as ‘auxiliary’, with a high input range, the latter can be used to recover the integral lost due to the saturation of the main high-resolution channel. While from an analog signal point of view there is no necessary difference to the parallel sampling, in this manner – ‘extended dynamic range sampling’ – there is only one data stream

and storage, as the digital signal processing can be done in real-time on the [FPGA](#). More details on how this can be implemented are provided in section [5.5.3](#).

5.3.2 Input Output Processor

The [IOP](#) board (figure [5.15](#), [[165](#)]) was developed as part of a prototype [Fast Plant System Controller \(FPSC\)](#) for ITER based on the [ATCA](#) [[166](#)]. While the [FPSC](#) is complex system focusing on interoperability with other ITER systems (hardware, software, networks), the [IOP](#) is capable of standalone operation, being based on a Xilinx Virtex-6 [FPGA](#). The board was designed process up to 24 insulated [ADC](#) or [DAC](#) modules with two independent galvanic isolated analog channels each.



Figure 5.15: Photograph of the [IOP](#) board. The board is fully populated with 24 modules, vertically arranged. The rear transmission module with 3 50-pin D-sub connectors for the analog signals and one 37-pin D-sub connector for digital signals is visible on the bottom. Figure available online [[165](#)].

While the full description of the working of the processor is out of scope for this thesis, it is important to clarify the basic functions it performs. Firstly, the [FPGA](#) generates the digital communication signals for the [ADC](#), the acquisition and data communication signals. The next step is the deserialization of the [ADC](#) data – this data comes from the module as a sequence of pulses in phase with a clock signal and must be ‘read’ and saved, in this case, in the form of a 32-bit integer. More details on these two steps are provided in [5.4.5](#) as these portions of the firmware were re-done for the prototype modules developed. The [ADC](#) data is inserted in a [first In, First Out \(FIFO\)](#) buffer, that is read (dequeued) into fixed-size [DMA](#) blocks. These are transmitted through the [ATCA](#) backplane through a [Peripheral Component Interconnect Express \(PCIe\)](#) bus to the computer installed in the crate. In the computer, a C program that controls and configures the acquisition, assesses this data via a custom driver, optionally processes it, and saves it into binary files.

5.4 Electronics design and development

This section details the most important challenges in the development of a prototype [ADC](#) module with phase switched modulation capability and in retro-compatibility with the [IOP ATCA](#) board. While in the previous section the abstract goals were specified, this section goes one level below in the development and description of the system, documenting the technical implementations.

First and foremost, is the search for new or at the very least procurable (in production) components. This activity is present across all stages but is crucial in section [5.4.1](#).

A technical problem that was identified in previous iterations of the modular [ATCA DASs](#) was a strong noise component at 500 kHz. This noise band is detected in both integration or simple [ADC](#) modules and the source was identified as the switching of the DC-DC transformer, working at 500 kHz. This component powers the analog part of the module, whilst creating the galvanic insulation barrier. There are mechanisms in place to reduce the electric noise of the power rails, in particular the usage of low-noise [Low-Dropout Regulator \(LDO\)](#)s. However, the source of this noise is magnetic, meaning the fast switching in the transformer (of this or adjacent modules), can induce voltages in small conductive loops in the circuitry.

This prototype attempts to shift this noise band from 500 kHz to the Nyquist frequency, 1 MHz. The underlying idea is that, by switching the current in the transformer synchronously with the acquisition, the harmonic components of the noise will appear at the Nyquist frequency (far edge of the measurable spectrum) or as a DC offset. If in general this is catastrophic for integration of the signal, in this particular application the offset is decoupled in [EO](#) and [WO](#) with both being calibrated independently. As this noise impacts mostly on the components in close physical proximity of the transformer, it will mostly manifest itself as [EO](#), that even if not accurately removed, its effect on the integration is strongly mitigated by the modulation technique.

Space constraints are also a common theme across the development of the module. Superficially, this is to keep the retro-compatibility with the [IOP](#) board. Of course one can argue that the prototypes need not fulfill all the constraints as they will not be commissioned as is: modules can theoretically be placed just every other slot, only one board is necessary in the crate, etc. and then adjusted in the future carrier board. However, high channel density is one of the main advantages of the [IOP](#), and it would be shortsighted to reduce or otherwise limit it for minor gains in the module development. Consequently, the development will adhere to strict mechanical retro-compatibility.

5.4.1 Key components market research

At the analog electronics level (module) the only distinction from the digital integrator to a standard digitizer circuit is the chopper. Therefore, the [ADC](#) is the most important component and the remaining components should be chosen accordingly. [Table 5.2](#) show a market probing for 2 MSPS [ADCs](#). All the considered [ICs](#) are either [Successive Approximation Register \(SAR\)](#) or [Sigma-Delta \(\$\Sigma\Delta\$ \)](#). Comparison of the pros and cons between the two types is widely available in literature and is suppressed here, as we are working at a set of parameters at the state of the art. In fact, the 1–5 MSPS is the border region between high-precision [ADCs](#) and high speed [ADCs](#).

Beyond the number of bits and technology, the primary factors considered are whether it can reach higher sampling frequencies (f_s), its noise performance, here expressed by the [SNR](#) and related to the precision, as well as the [Integrated Non-Linearity \(INL\)](#), a measure of the linearity and hence accuracy of the device. For this comparison, the values shown are the nominal values displayed in the respective datasheets. The practical implementation might, of course, dictate different operation conditions, such as different supply voltages and reference voltages or temperature. More practical concerns were also taken into consideration: the lifecycle stage, whereby preference is given to new devices; the size of the footprint, given the narrow 10 mm width for each channel; and the digital communication protocol. Regarding the latter, we need to consider the galvanic insulation. Parallel communication would require too many insulator channels and [FPGA Input/Output \(IO\)](#) pins. Both [Serial Peripheral Interface \(SPI\)](#) and [Low-Voltage Differential Signaling \(LVDS\)](#) are viable options, being the latter a differential standard and the former unipolar. The [FPGA IOs](#) are [LVDS](#) and so is the routing to the modules. Therefore, [SPI](#) communication would require conversion to [LVDS](#), on one or the other side of the insulation barrier. Conversely, [LVDS](#) insulators typically come in larger packages than [SPI](#) equivalents. This is an important factor as the available height on the bottom side of the [PCB](#) is less than 2 mm, for retro-compatibility with [IOP](#).

Table 5.2: Comparison of ADCs available in the market as of March 2020. The device that was chosen is highlighted in **bold**.

ADC	bits	Tech.	f_s [MSPS]	SNR [dB]	INL [LSB]	Lifecycle	Size [mm]	Output
AD4003	18	SAR	2	100.5	0.4	New	3x3	SPI
AD7960	18	SAR	5	99	0.8	New	5x5	SPI
AD7986	18	SAR	2	95.5	1	Prod.	4x4	SPI
AD7641	18	SAR	2	92	2	Prod.	7x7	SPI
LTC2389-18	18	SAR	2.5	99.8	1.25	Prod.	7x7	SPI, LVDS
LTC2385-18	18	SAR	5	95.7	0.6	New	5x5	LVDS
ADS1675	23	$\Sigma\Delta$	4	104	25.2	Prod.	9x9	LVDS
AD7760	24	$\Sigma\Delta$	2.5	100	83.8	Prod.	9x9	Parallel
LTC2380-24*	24	SAR	1.5	100	4.2	New	4x3	SPI

*Without digital filtering. 2MSPS requires 4-sample filter.

Taking these factors in consideration, the AD4003, a brand-new device at the time, was selected, showing an overall good performance in a compact package. The SPI interface allows for the signals to cross the insulation barrier as unipolar and only then be converted to LVDS.

The next step is finding an appropriate OPAMP to drive the ADC. Table 5.3 shows a selection of the candidates, all fully-differential precision amplifiers, developed for ADC driving.

Table 5.3: Comparison of ADC driver OpAmps available in the market as of March 2020. The device that was chosen is highlighted in **bold**.

OpAmp	V Noise [nV/ $\sqrt{\text{Hz}}$]	I Noise [pA/ $\sqrt{\text{Hz}}$]	Slew rate [V/ μs]	Settling time [ns]	CMRR [dB]	Offset [μV]	Drift [$\mu\text{V}/^\circ\text{C}$]	Size [mm]
ADA4945-1	1.8 (100 kHz)	1.0	600	100 (to 18 bit)	-110	15	0.1	3x3
ADA4932-1	3.6 (1 MHz)	1	2800	9 (to 0.1%)	-100	500	3.7	3x3
AD8139ARDZ	2.25 (100 kHz)	2.1	800	45 (to 0.01%)	-80	150	1.25	5x6
LTC6363IMS8-1	2.9 (100 kHz)	0.55	75	330 (to 0.01%)	-94	25	0.45	5x3
THS4551	3.3 (>500 Hz)	0.5	220	50 (to 0.01%)	-110	175	1.8	3x3

The ADA4945-1 was chosen, in spite of the dynamic performance not being the best available, its noise and input characteristics are very good and its output (offset and typical temperature variation), excellent.

5.4.2 Insulated power supply

Improving the power supply was a key objective for the development of this module. Despite the availability of numerous DC-DC converter ICs, it is difficult to find sufficiently miniaturized transformers for the dimensional requirements. That is, as the typical technique for galvanically insulated power supplies is through a transformer, these ICs tend to be large as shielding is present to prevent ElectroMagnetic Interference (EMI). One promising new (2019) IC is the UCC12050. This device has however not ideal: its package is just slightly longer than the available 10 mm (10.3 mm); and it only features a positive voltage output. While the first problem could be solved with some creative PCB placement and routing, generating a negative (isolated) voltage would have to be achieved with a second UCC12050 with reversed outputs; or generating the negative voltage from the insulated (positive) rail using a charge pump inverter. The first solution would require that both modules share the same supply, as four of such ICs can not be acomodated. It was also not a forgone conclusion that it is even possible, as this operation is not mentioned in the materials from the manufacturer and while the 5 V difference between the pins is maintained if the output serves as reference in the design, unknown internal mechanisms can prevent the reversed current direction. Using a charge pump, the application is much more straightforward, however, these devices introduce noise at its operation frequency, that is in the interest band for the magnetic diagnostic (< 300 kHz).

A there is also the possibility of creating a push-pull DC-DC converter with a driver IC and an external transformer. On the insulated side, the switched signals must be rectified and filtered. There are several available transformers with different ratios, however, not all drivers are compatible (or efficient) with all transformers, particularly when there is a requirement on the maximum component height. Apart from the maximum current, the most important criteria in choosing an adequate transformer is its **EMF-Time (ET)** product of the primary winding, that relates the supply voltage V_{CC} and the switching frequency f_{SW} :

$$ET = V_{CC} \times \frac{1}{2 * f_{SW}} \quad . \quad (5.1)$$

For the desired parameters of $V_{CC} = 5 \text{ V}$ and $f_{SW} = 1 \text{ MHz}$, the **ET** parameter of the transformer should be greater than $2.5 \text{ } \mu\text{V}\cdot\text{s}$ to prevent saturation of the magnetic core, that would result in a reduced inductance and consequent current increase.

Figure 5.16 shows a schematic illustration of both DC-DC converter implementations (with the two negative voltages). Two small boards ('power-isol-test', figure 5.17) were manufactured in order to test these three methods in terms of their feasibility and performance.

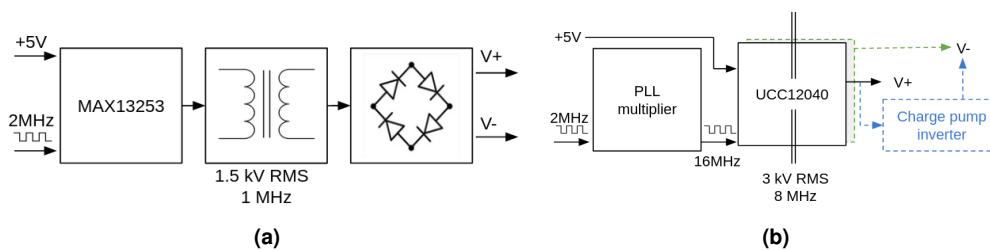


Figure 5.16: Two isolated power supplies considered. In (a) based on the MAX13253 DC-DC converter driver and a transformer; and in (b) using the UCC12040 integrated C-DC converter. In the latter, two different options of generating negative voltage were used: a second IC with the power and ground pins reversed (green) and using a charge pump inverter (blue).

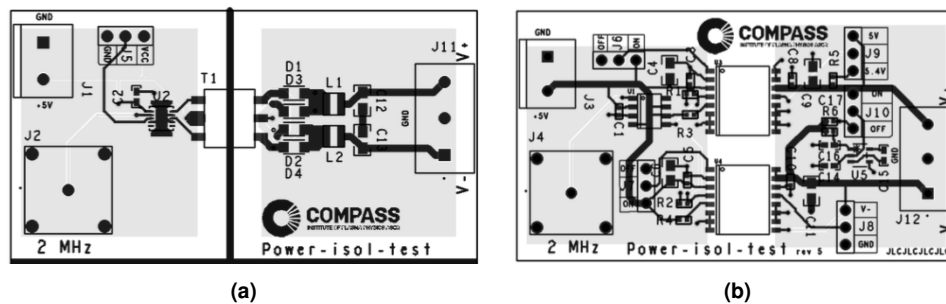


Figure 5.17: Simplified representation of the PCB layout for the 'power-isol-test' board: (a) with the MAX13253 driver and transformer; (b) with the UCC12040. For reference, the dimensions of each board is 65x35 mm.

All three isolated power methods worked as expected and were analyzed. It was confirmed that negative voltages at full power can be achieved with the inverted output UCC12040. While the noise added by the charge pump is minimal and attenuated by the **LP** filter suggested in manufacturer's guidelines, its frequency distribution 'contaminates' the interest band, instead of sharp peaks at multiples of f_{Ny} .

Using the DC-DC converter driver and external transformer one can avoid the practical disadvantages of the large IC. A comparison of the full **PCB** footprints can be appreciated in the layouts in figure 5.17. Beyond being more practical, this method also showed a lower overall noise (-24 %) when compared to the integrated DC-DC converter⁴. A major contributing factor for the low noise is the LC filter after rectification. For this purpose, shielded inductors were used, in order to prevent further **EMI**. Figure 5.18a shows the voltage at the output of the transformer. On top of the 1 MHz switching, we can observe a strong 18 MHz ringing. After rectification and filtering, we observe a

⁴Measured as standard deviation of the output voltage, sampled with an oscilloscope. Full and precise noise density analysis not carried out.

DC signal, with ~ 11.5 mV standard deviation. Figure 5.18b shows the spectrogram for the positive voltage output, with a 75 dB difference to the first noise component.

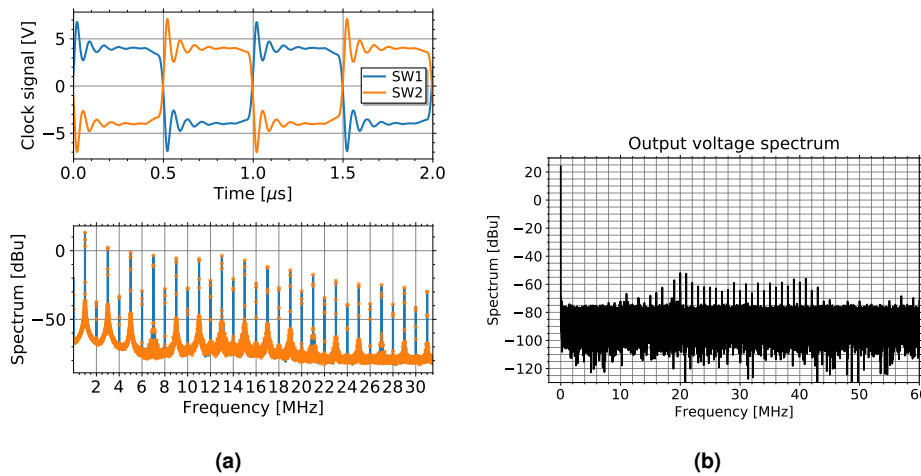


Figure 5.18: Measurements of the MAX13253-based DC-DC converter with a 3:4 transformer. **(a):** Output of the switches (transformer input) with a 4V input voltage. Top plot shows the time trace and the bottom the spectrum. **(b):** Spectrum of the (positive) output voltage, after rectification and filtering. 5V input used on the driver, 470 Ω load.

As the output voltage is unregulated, the added load will lower the voltage, i.e. the calculation given by the transformer ratio of $5 \times (4 : 3) = 6.6$ V is the limit, without load. This voltage will be the input of the LDOs that ensure stable voltage levels. As the highest (regulated) voltage needed is 5 V and each LDO will have a dropout voltage, we need to ensure a margin (typically 0.4 V). The components on each channel have an expected power consumption of <40 mA, according to the breakdown in table 5.4.

Table 5.4: Breakdown of the estimated (isolated) power consumption per channel.

Component	Supply [V]	Current [mA]	Power [mW]	Conditions
Chopper	5	0.002	0.01	Typ.
Buffers	5	12.8	64	Typ.
ADC driver	5	4.2	21	Max.
ADC	2.5	4.4	11	2 MSPS
ADC	1.8	10.6	19.08	2 MSPS
ADC	3.3	0.6	1.98	2 MSPS
LDO	6	0.18 (x3)	3.24	Typ. full load
LDO	-6	0.66	3.9	Typ. full load
Reference	6	0.1	0.6	Max.
Total	–	33.9	125	/channel

The power consumption will also be unbalanced between the positive and negative voltages. There will be a higher voltage drop on the positive rail and one must ensure it does not drop below the level required by the LDOs. This can be tested by ranging the load resistor ($R_+ \in [40, 475] \Omega$) on the positive output of the ‘power-isol-test’ board, while keeping the negative output load constant ($R_- = 470 \Omega$). The plot in figure 5.19 was obtained, showing the sum of the currents and power on the y -axis and the resulting voltage on the positive rail on the x -axis⁵. We can see that with a drain of 40 mA (total, 250 mW) a positive voltage of 5.8 V is maintained, while to reach the 5.4 V limit, 65 mA (360 mW) needs to be drawn. This power supply is therefore sufficient for the expected needs, with some room for optimization.

⁵Strictly speaking, the resistance is the independent variable, of which both current and power depend. As such, these should be represented on the x -axis. However, the representation chosen improves readability.

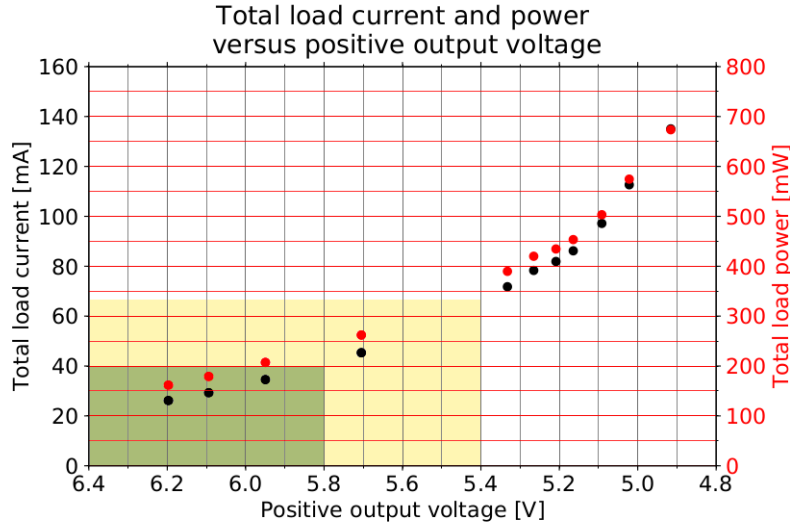


Figure 5.19: Positive output voltage (x -axis, reversed) with variation on its load, under constant on the negative voltage. Both total current (black) and power (red) are shown. Negative voltage not shown, as always higher in absolute value. Shaded regions to be read on the current axis, represent the 40 mA (green) and 5.4 V limits, according to interpolation of the data.

In terms of mitigation of the ringing, snubbers can be added, as described in [167], with a series resistor and capacitor. A resistive snubber will dissipate some energy to attenuate the ringing, hence it is important to conduct the power analysis.

5.4.3 Input Stage

The input stage is simple in the sense that it features exclusively passive components, however it is the most important stage of the analog signal path. As mentioned in 5.1.1, this is the only stage at which unwanted components count as **WO** rather than **EO**, as it sits upstream from the chopper. For this reason, great care must be taken to ensure the components are of high precision and thermal stability: 0.05% tolerance, ≤ 10 ppm/°C resistors, and C0G (class 1) **Multi-Layer Ceramic Capacitors (MLCCs)** with 1% tolerance.

The input stage attenuates the input signal through a resistor divider g_{DC} and a first order **LP** filter with the addition of a capacitor. Figures 5.20a and 5.20b show the equivalent and actual (bipolar) implementation of the filter. It follows from the equivalent scheme that the DC gain ($g_{DC} \equiv \frac{OUT}{IN}$) is given by

$$g_{DC} = \frac{R2}{R1 + R2} \quad (5.2)$$

While the cutoff frequency of the filter can be expressed as

$$f_c = \frac{1}{2\pi} \cdot \frac{R1 + R2}{R1 \cdot R2 \cdot C} \quad (5.3)$$

By replicating the unipolar drawing for a negative signal branch we see that the duplicated capacitors are in series, therefore the equivalent capacitance is $C = 2 \cdot C1$. This capacitor is also in parallel with optional snubber capacitors that aim at improving the switching performance of the chopper. If such resistors are used (as in figure 5.20b) the resulting equivalent capacitance is $C = (2 \cdot C1 + C_{snub})$, and (5.3) simplifies to

$$f_c = [2\pi \cdot g_{DC} \cdot R1 \cdot (2C1 + C_{snub})]^{-1} \quad (5.4)$$

Apart from these equations we must also consider that the input resistors will define the input impedance:

$$R_{in} = 2(R1 + R2) \quad (5.5)$$

that should not be smaller than ~ 100 k Ω as a rule of thumb, although it is not critical and can be adjusted for sensors that have very low resistance, as most magnetics do.

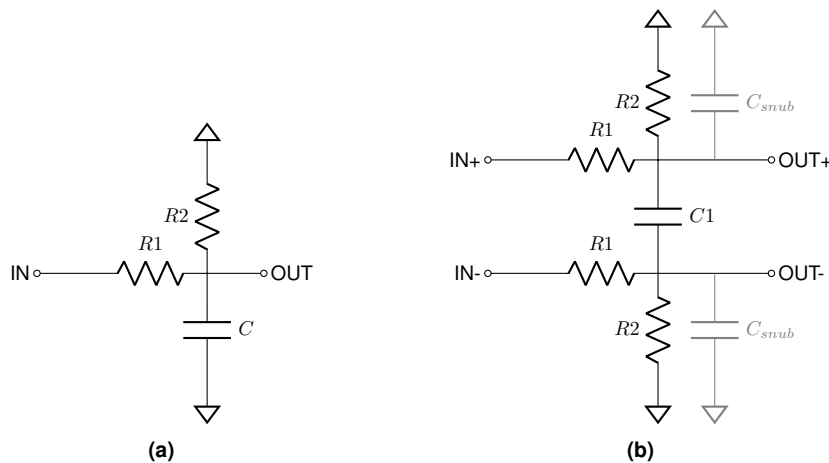


Figure 5.20: Simplified (a) and actual bipolar implementation (b) of the input filter and DC attenuator.

The process to choose the values for the components followed was:

1. Define the desired gain and cutoff frequency;
2. select $R1$ according to available high-voltage precision resistors;
3. check on a map like in figure 5.21 for the corresponding values for C ;
4. using equations (5.2) and (5.4), find appropriate resistors and capacitors for $R2$, $C1$ and C_{snub} .

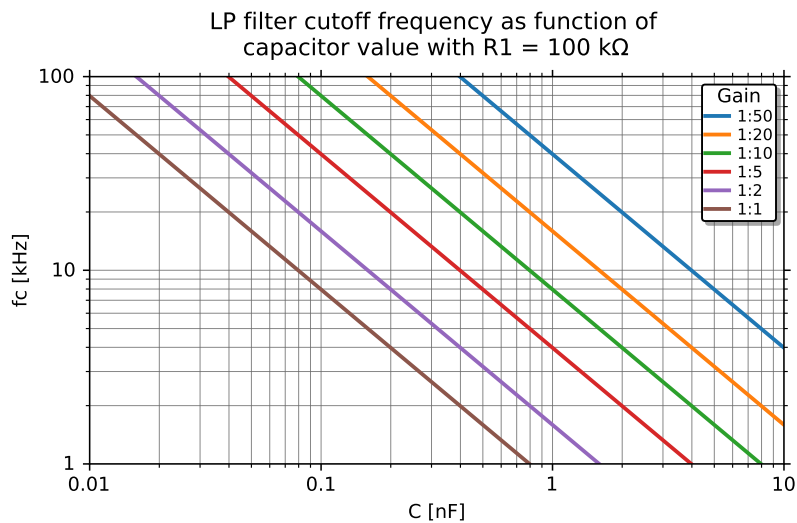


Figure 5.21: Map of required capacitance for a given gain and filter cutoff frequency (f_c) given a fixed $R1$ value.

One function that is typically addressed at the input stage is the protection against strong transients. In this design, this is assured by the chopper, that has internal clamping diodes to protect the downstream electronics. These diodes have a forward current limit of 100 mA for a 1 kHz, 10 % duty cycle pulsed signal. This limit can be assured with a few tens of $k\Omega$ input impedance in the case of a strong (and fast) disruption at the kV level.

5.4.4 Anti-aliasing filtering and ADC driving

The ADC driving stage accomplishes several important tasks, centered around the fully-differential OPAMP. In this case, the ADA4945. First, the amplifier buffers the signal, having a high input impedance and a low output impedance. The amplifier also establishes the common mode voltage,

with or without gain. That is, for an ADC with voltage reference V_{ref} , its differential inputs should be constrained between 0 and V_{ref} for both inputs, being the signals inverted around $V_{ref}/2$. The input of the driver (between pins) is generally a bipolar signal between $\pm V_{ref}$, to which the driver should set the common mode voltage of $V_{ref}/2$. Apart from a DC gain, the driver is also used to apply a filter, in general to reduce the noise at the ADC input, and often as an anti-aliasing filter, limiting the baseband of the signal to f_{Ny} .

Regarding the filter implementation, from the two common topologies, the Sallen-Key is not applicable to fully differential amplifiers, leaving the Multiple FeedBack (MFB) architecture. Figure 5.22 shows the equivalent and fully-differential implementations of the filter. When converting between the two, it is important to note that $C'_1 = C_1/2$.

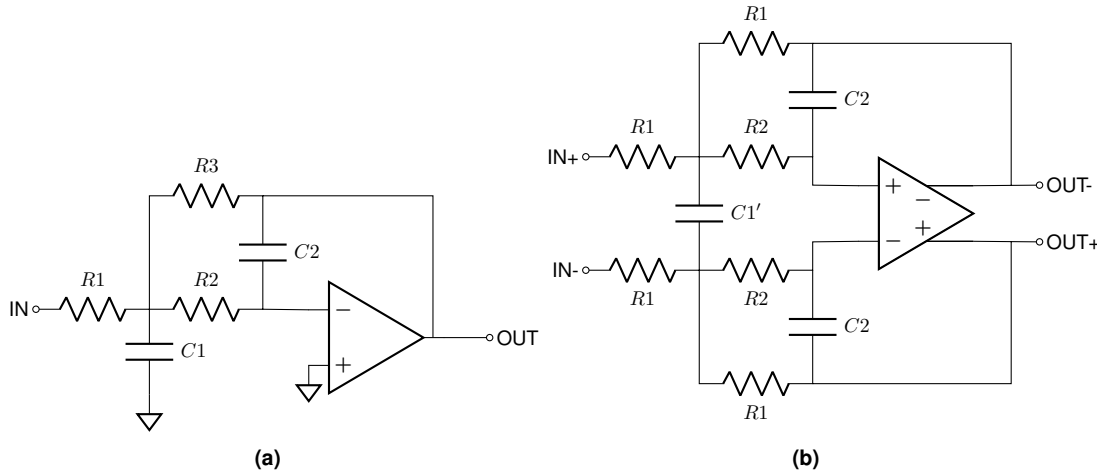


Figure 5.22: Equivalent (a) and actual bipolar implementation (b) of the MFB filter. In (b) gain is set to -1 by setting $R_3 = R_1$.

This filter topology, when implemented as represented in figure 5.22a has the following transfer function:

$$H(s) = \frac{\mathcal{L}V_{OUT}}{\mathcal{L}V_{IN}} = -\frac{1}{C_1 C_2 R_2 R_1} \cdot \frac{1}{s^2 + s \frac{1}{C_1 R_2 R_1} \left(R_1 + R_2 \left(1 + \frac{R_1}{R_3} \right) \right) + \frac{1}{C_1 C_2 R_3 R_2}} \quad (5.6)$$

This equation can obviously be simplified by noting key 'building blocks'. The DC gain can be obtained by setting $s = 0$:

$$g = -\frac{R_3}{R_1} \quad (5.7)$$

In comparison with the equation for a second order LP filter – (2.35) – we obtain expressions for the characteristic frequency:

$$\omega_0 = 2\pi f_c = \sqrt{\frac{1}{R_3 R_2 C_1 C_2}} \quad (5.8)$$

and the quality factor:

$$Q = \frac{\sqrt{\frac{C_1}{C_2}}}{\sqrt{\frac{R_3}{R_2}} + \sqrt{\frac{R_2}{R_3}} + \frac{\sqrt{R_3 R_2}}{R_1}} \quad (5.9)$$

Equation 5.6 thus simplifies to

$$H(s) = \frac{g \omega_0^2}{s^2 + \omega_0/Q s + \omega_0^2} \quad (5.10)$$

It is now easier to optimize the 3 degrees of freedom (g , ω_0 , Q) constrained by this equation, and use equations (5.7)–(5.9) plus two degrees of freedom to choose the values for $(R_1, R_2, R_3, C_1, C_2)$.

Firstly, a unitary gain was set ($g = -1$), setting $R_3 = R_1$. Furthermore, R_1 and C_1 are chosen for the 'free' parameters. The family of the filter was chosen as Butterworth, that ensures the maximum flat-band. This corresponds to $Q = 1/\sqrt{2}$. Figure 5.23 shows the plot of equations (5.8) and (5.9) for $Q = 1/\sqrt{2}$ and a cutoff frequency of 500 kHz. Given combinations of (R_1, C_1) , represented by

color, the appropriate values for R_2 and C_2 can be read at the intersection of the f_c and Q curves. Once suitable components are found in the vicinity of these intersections, the filter can be simulated with equation (5.10) or, as in figure 5.24, with a SPICE circuit simulator which has the advantage of including in the simulation the behavior of the OPAMP, allowing the conduction of other analysis. It is worth mentioning that this is not a canonical anti-aliasing filter, that, as a rule-of-thumb, places the cutoff frequency one decade below from f_{Ny} and not an octave. However, due to the presence of the input filter, anti-aliasing requirements can be relaxed.

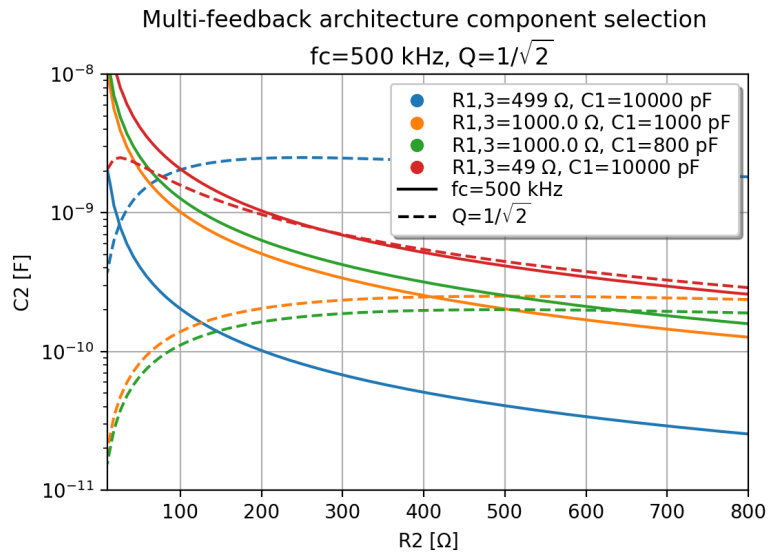


Figure 5.23: Graphical intersection of the f_c and Q curves for a MFB filters with $g = -1$ with R_1 , R_3 and C_1 represented as series, and R_2 , C_2 ranged in the axis. Valid component values for the configuration are read as the intersection of the full and dotted lines, for each color.

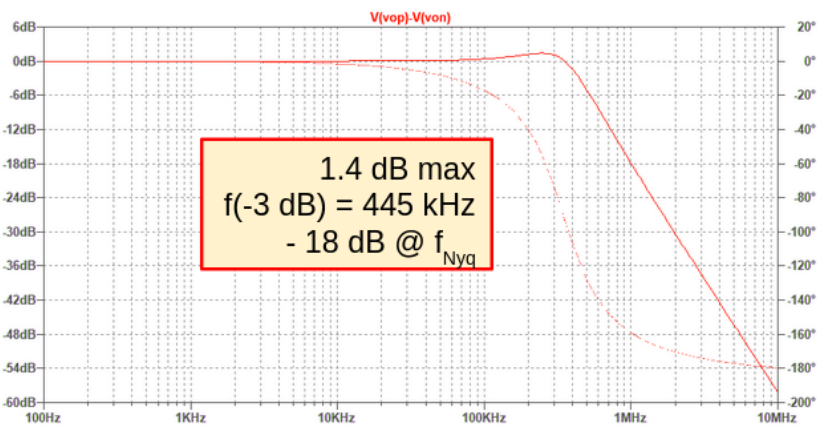


Figure 5.24: SPICE simulation for the MFB filter using selected OpAmp and component values.

One analysis carried out is that of the noise density. Figure 5.25 shows the simulated noise density at the output⁶ for two of the configurations in figure 5.23 (for the same frequency response): ‘old’, $R = 499 \Omega$, $C_1 = 10 \text{ nF}$; ‘new’, $R = 1 \text{ k}\Omega$, $C_1 = 1 \text{ nF}$. We can see that despite the increase in noise density at lower frequencies due to the increase of R_1 , the overall integral of the density is minimized due to the lowering of the resonant peak at the filters natural frequency.

5.4.5 ADC communication and digital signals

The AD4003 has a few characteristics that are uncommon among high-speed, high-performance ADCs. To start with, its physical package has only 10 leads. Whereas other devices rely on config-

⁶Simulation includes the ADC kickback filter, a passive RC filter at high frequencies at the inputs of the ADC.

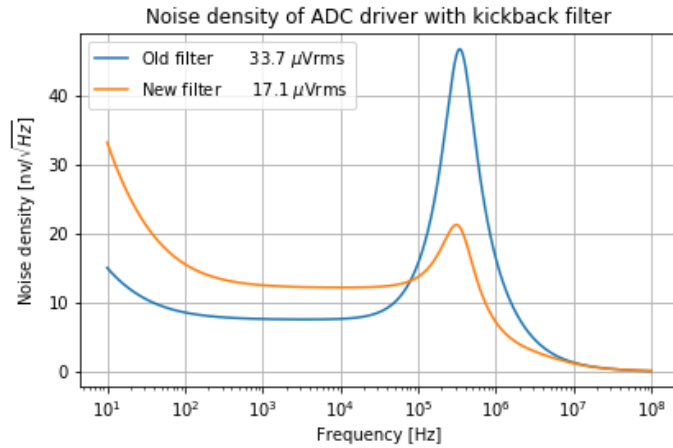


Figure 5.25: Noise simulation in LTSpice of the ADC driver model with kickback filter for two MFB filter implementations with the same parameters. The color of the lines is shared with the configurations in figure 5.23.

uration pins to set the operation modes and timings, this device relies on an internal digital register. Both the configuration of this register and the readout of the data are carried out through SPI on a single ended logic (in this case 3.3 V Low-Voltage Transistor–Transistor Logic (LVTTL)).

In order to achieve the specified 2 MSPS sampling rate, the device must be set to ‘turbo mode’. In this mode the minimum clock frequency for the data streaming is 75 MHz. This is a limitation imposed by the conversion and acquisition times of the ADC, helped by the fact that, in this device, the Most Significant Bit (MSB)s are streamed still on the conversion phase. However, this frequency is problematic for the digital signal insulators, that have a recommended operation up to 140 Mbps, corresponding to a 70 MHz clock.

As the turbo mode is not the default configuration, the register must be written before acquisition can start. The configuration of the ADCs is done according to the state machine in figure 5.26. For the prototype testing, it is important to verify that the devices are correctly configured, therefore, the readout of the register is streamed in the first data acquisition after power-up. Figure 5.26b

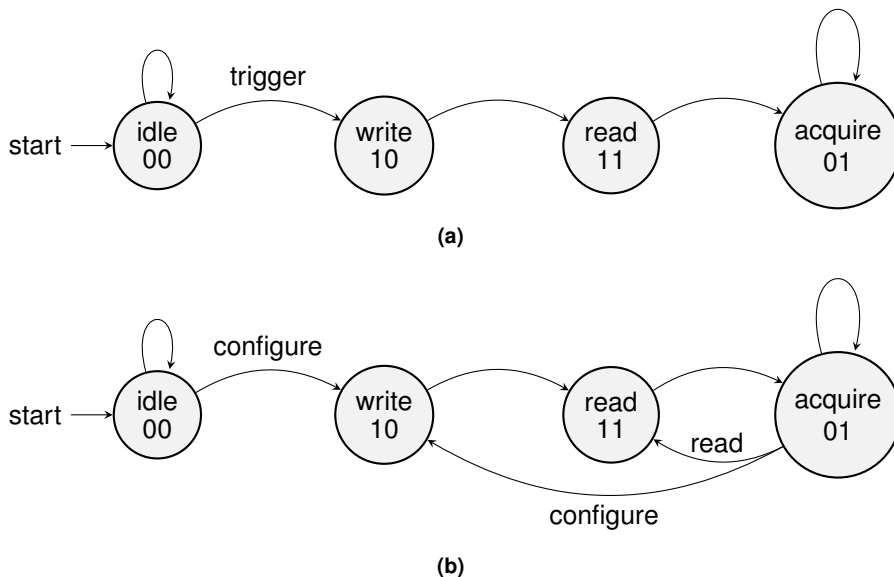


Figure 5.26: State machine for definition of the ADC configuration states. Each state is represented by a 2-bit code and loads a pre-configured 16-bit MOSI signal. (a): Actual implementation for prototype testing, linear and initiated by the main data acquisition trigger. (b): Planned implementation for the production firmware, independent of main trigger and instead controlled by control instructions.

shows a more robust implementation of the state machine to implement on the final firmware, where

reading/writing of the ADC registers is independent from acquisition.

The main piece of firmware that was developed is the deserializer for this ADC. The main challenge for its development (which would otherwise require a standard SPI host) concerns the digital insulation of the signals. The distance of the tracks from the FPGA to the modules, the conversion from LVDS to LVTTTL, and the optical insulators all add propagation delay. Some ADCs provide an output of the data clock signal that helps in the reading of the data, as this clock is delayed with respect to clock on the FPGA (its original source).

Figure 5.27 shows a behavioral simulation of the deserializer⁷, zoomed to the register read cycle (mode b11). The signals synchronous with the main 100 MHz (10 ns) clock are shown in magenta

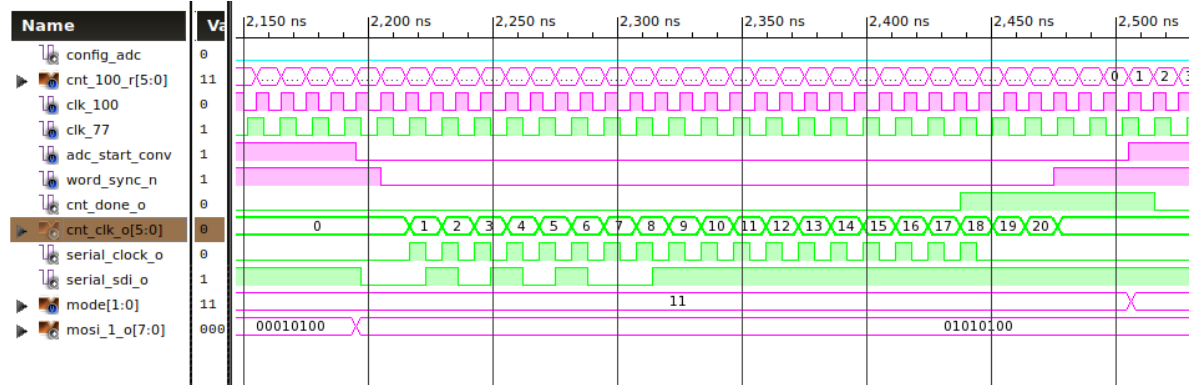


Figure 5.27: Simulation of the deserializer algorithm using an HDL simulator. Zoom to the ADC register ‘read’ state (mode=11). Colors represent whether the signal is synchronous with the 10 ns clock (magenta) or the 13 ns clock (green). The blue trace is asynchronous.

while those synchronous with the SPI clock at ~77 MHz (13 ns) are shown in green. The SPI clock signal clocks out 18 periods ‘serial_clock_o’, for the 18 bits, however, the counter ‘cnt_clk_o’ counts two more cycles. This is because the deserializer reads the Master Input Slave Output (MISO) signal on the falling edge of this clock with a two cycle offset, i.e. the last bit is read $2.5 \times 13 = 32.5$ ns after the rising edge of the clock output. The algorithm was adjusted experimentally, by reading the signals with an oscilloscope. However, this delay is in agreement with the expected propagation delay according to the datasheets of the converter and insulator: $\tau \approx 30$ ns. Further adjustments can be introduced using delays on the FPGA IO modules.

⁷Simulation carried out in ISim, integrated in Xilinx ISE.

5.5 Prototype testing and qualification

Three identical prototypes were manufactured for testing. Figure 5.28 shows one of them in one-to-one scale. A few elements can be identified immediately: the symmetry of the design with two identical channels; the analog signal input on the left-hand side and the digital on the right-hand side; the galvanic insulation point with the large transformers on top and the array of optical digital signal insulators on the bottom; all signal path components are placed on the top, with the bottom reserved for the LDOs and digital signal insulators.

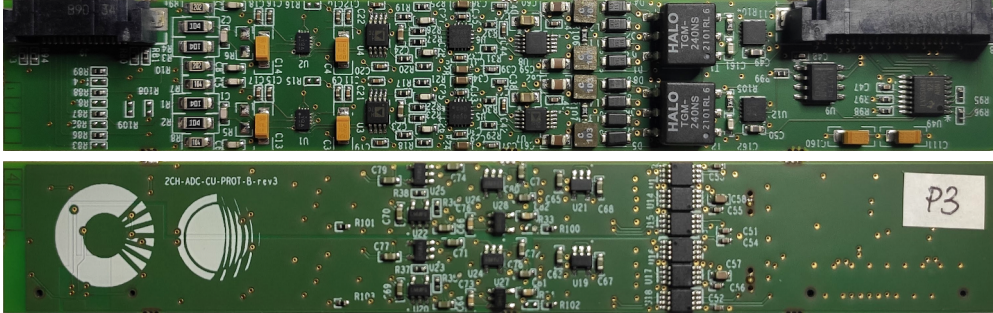


Figure 5.28: Photograph of a module prototype (2CH-ADC-CU-PROT-B-rev3) viewed from top and bottom, respectively. Reproduced in 1:1 scale.

Throughout this section, the signals will be labeled as M_xCH_y , with $x \in \{1, 2, 3\}$ the module number and $y \in \{A, B\}$ the channel, of which B generally has higher input range, while A being a more sensible configuration for the expected magnetic signals. Table 5.5 shows the initial configurations. These values should be assumed if not explicitly stated otherwise.

Table 5.5: Initial configuration of the module prototypes.

CH	Input range	Resolution (LSB)	Input filter (f_c)	MFB (f_0)
A	± 5 V	~ 38 μ V	19.4 kHz	347 kHz
B	± 127.5 V	~ 973 μ V	495 kHz	347 kHz

The logic behind this configuration was for a representative channel A with around 20 kHz bandwidth and a channel B with a high input range and high bandwidth, allowing the test of the configurations enabled by the two-channel architecture, as described in 5.3.1.

Unless stated otherwise, the chopping frequency used is 1 kHz. This frequency has previously shown to be adequate (ISTTOK, COMPASS test). Thinking in time domain, an argument can be made to lower this frequency to minimize chopper transitions to the minimum and avoiding possible loss of signal integrity in the samples after transition. On the other hand, thinking in the frequency domain, it makes sense to shift this frequency (and their odd harmonics) to a higher value, beyond the signal baseband. This minimizes the demodulation artifact described in [119] whereby a signal of twice the chopping frequency is interpreted as a DC component. Previous testing with a similar system has shown that ranging the chopper frequency has limited influence on the drift performance of the integrator [156] and for this reason the chopper frequency is kept at 1 kHz unless specifically tested.

5.5.1 Testing software

The experimental control software needs for a prototype testing and development stage are different from that of the final implementation upon commissioning of the system. If for the latter a great deal of importance is given to performance, consistence and interface with higher level systems (experimental control software or data archiving and distribution architectures), on a development and testing phase, priority is given to a simple system that gives access to the data at all steps of processing, and flexible enough to analyze the data in light of changes made to the electronic components and digital processing alike. In this particular case, the four digital processing steps – offset removal, demodulation, integration, conversion to Volt or Volt-second – are to be carried out in the **FPGA**, in real time. Instead, all the analysis carried for thesis was carried out in an external (host) computer, based on the ‘raw’ **ADC** data. This brings flexibility, as all steps can be analyzed and diagnosed independently and avoids constant firmware changes or the development of a robust and configurable firmware just for testing purposes. The implementation in the **FPGA** and integration with real-time software is known and proven, as demonstrated in [116] and [117].

The data is transmitted in 512 kB **DMA**s, containing 16384 sequential 32 B packets. These contain the data from 3 modules (6 **ADC**s) in 4 B integers, a counter and the chopper phase, both as 4 B unsigned integers. This means each **DMA** packs 8.192 ms of data.

A C code, adapted from a previous implementation, awaits the **Interrupt ReQuest (IRQ)** configured in the device driver and copies the **DMA** to the **Random-Access Memory (RAM)** in a loop for the desired number of **DMA**s and, finally, from the **RAM** to a file. This code: ‘**DMAirq_32B.c**’, also carries out basic control functions of the **IOP**: sending a software trigger (in alternative to the hardware trigger) and enabling or disabling the chopper.

For convenience, a simple experiment management system and set of wrappers were built for this code. The most important function being correctly saving the data. A sequential ‘shot’ number is saved locally in a text file – ‘**data/lastShot**’. Figure 5.29 shows the algorithm for a simple Bash wrapper to acquire and save (copy) the data according to the incrementing shot number. On top of this routine, other scripts were written to loop this process with a given time interval or re-arm the acquisition for consecutive hardware triggers.

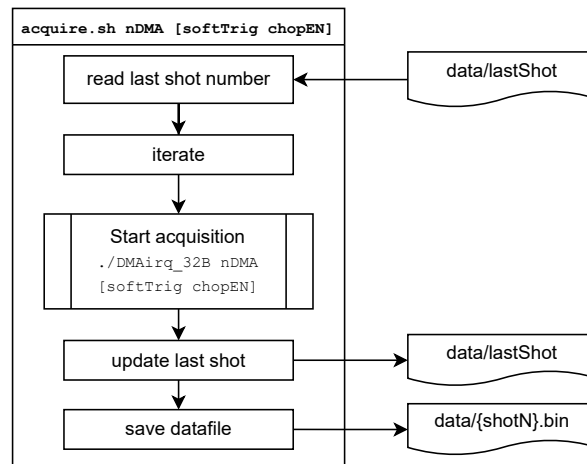


Figure 5.29: Schematic representation of the algorithm to perform a data acquisition ‘shot’, implemented as a Bash script.

As previously mentioned, the data is not processed nor archived in the **ATCA** but rather in a host computer. The synchronization of the two machines is achieved by the algorithm described in figure 5.30. This constitutes a ‘pull’ logic, independent of the measurement routines.

With the data files available and a shot archiving system in place, a set of Python routines and scripts were developed for the basic processing: compute the **EO** and **WO** offsets, demodulate, integrate, convert to natural units according to the component modifications change log; to debug problems with the data integrity, such as quick inspection of the hexadecimal and binary composition of the data; and for more advanced processing tasks, such as drift analysis and representation, spectral analysis, etc.

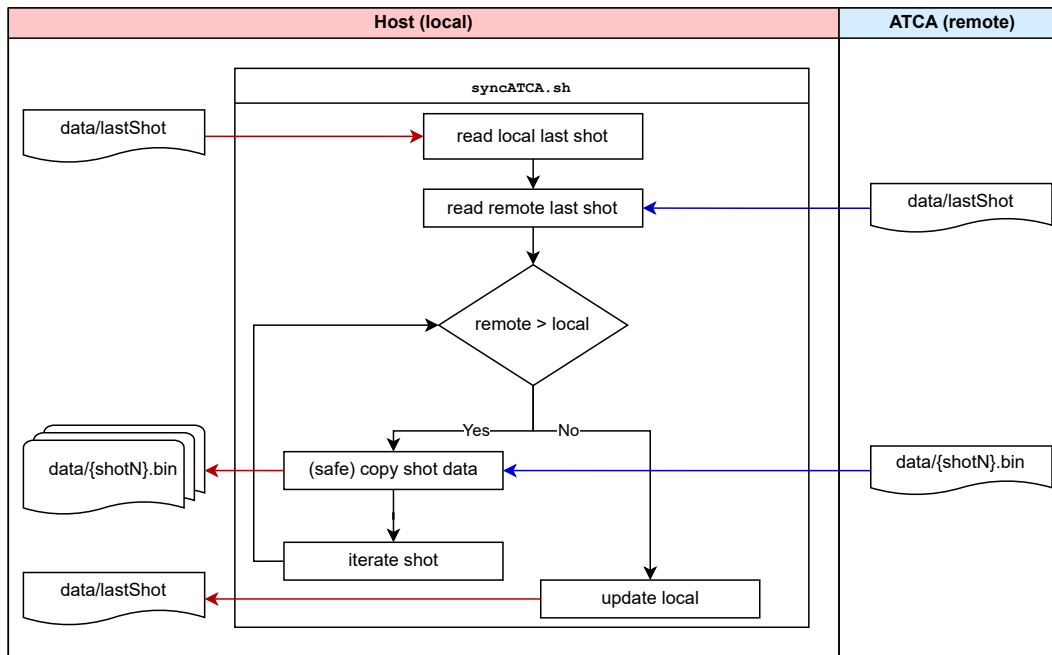


Figure 5.30: Schematic representation of the algorithm to sync the ATCA computer with the host computer that archives and processes the data. Red horizontal arrows represent file read/write operations on the host and blue ones across machines.

5.5.2 Benchtop tests

Upon ensuring the correct data acquisition and transmission, the noise characteristics of the signal were measured by recording acquisitions with short-circuited inputs. Figure 5.31a shows a 2 LSB standard deviation for both channels, with and without chopper (after demodulation). This value is

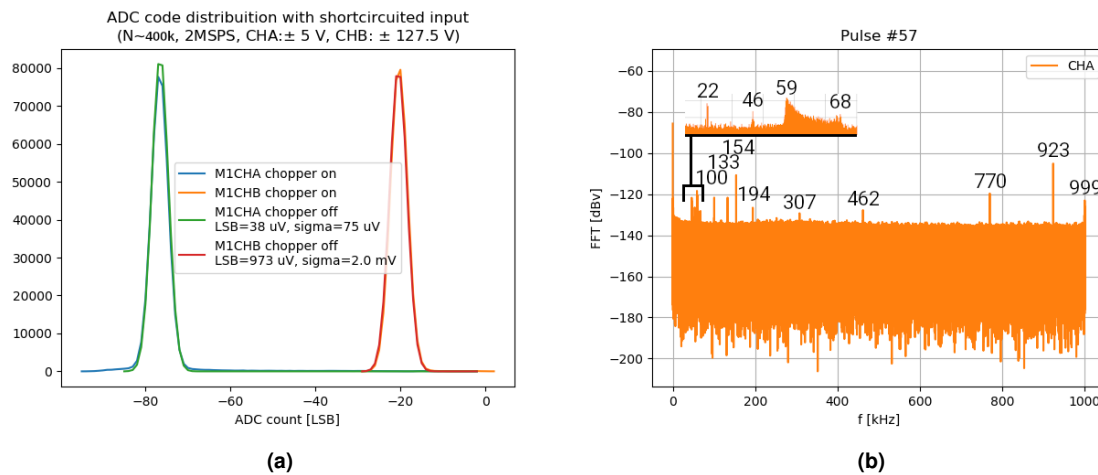


Figure 5.31: Noise measurements with short-circuited input. **(a):** As a histogram representing counts on each ADC bin. **(b):** As a spectrogram (linear frequency scale) with the key peaks frequencies highlighted. Chopper disabled.

18 % higher than the 1.7 LSB transition noise specified in the ADC datasheet. It is possible that the overall noise can be further reduced by using a higher reference voltage. In general, it is possible to keep the same input range by increasing the reference voltage and lowering the input attenuation, which would increase the SNR.

Looking at the spectrum of the noise (figure 5.31b) we can observe some discrete frequencies surging above the noise floor. Some of these appear to be related: $923/2 \approx 462$, $/3 \approx 307$, $/6 \approx 154$. However, it is not easy to identify the source of this noise.

Regarding the drift performance of the integrator, the first results are compliant with the requirements set even for the ± 125 V channels. Instead of very long acquisitions, a strategy of measuring integration lengths comparable to COMPASS-U pulses (≤ 10 s) was chosen. This way we obtain more time-traces of with increased relevance, which is important when dealing with random effects. With this method, we obtain plots such as the one in figure 5.32. In this plot we can pinpoint individual pulses of 8.2 s that stand out, with a much higher drift. If instead a one-hour acquisition would be used, these would manifest simply as ‘humps’ or ‘valleys’ that might be compensated. The drift will be further investigated in section 5.5.6.

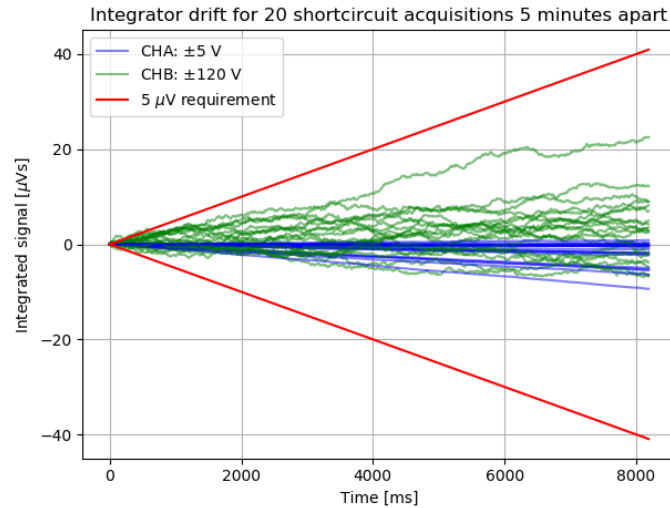


Figure 5.32: Results of the integrated output for 20 8.2 s acquisitions taken roughly 5 minutes apart. The established drift requirement is represented in red.

When considering the two-channel architecture, and furthermore considering the high density of components on the PCB, a reasonable concern is cross-talk between channels. Figure 5.33 shows the results of a 19 Vpp, 100 Hz signal applied to either channel with the other short-circuited. We observe no deviation from the noise floor at the signal frequency. The risk of cross-talk is higher for higher frequencies, however, this system will be mostly measuring mV–V signals in a limited band.

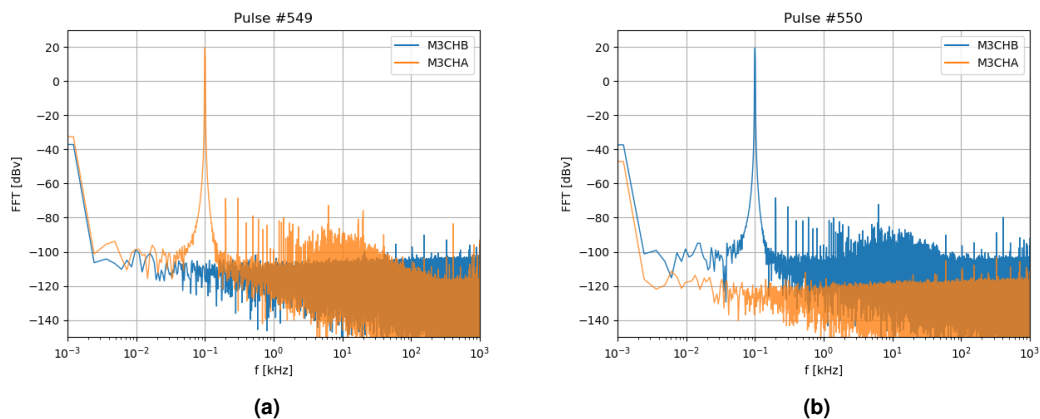


Figure 5.33: Signal spectra for measurement of crosstalk at 100 Hz with 19 Vpp input on (a) channel A, or (b) channel B with the input of the other channel short-circuited. Configuration no. 1, details in appendix C.

5.5.3 Implementation of extended dynamic range

As mentioned in section 5.3.1, the extended dynamic range sampling subordinates the high input range (auxiliary) to the high resolution (main) channel. The goal is to use the auxiliary data to keep track of the integral lost during saturation of the main channel, in real time. When considering a possible implementation one problem appears: the mismatch between the bandwidths of the two channels. This mismatch can be involuntary, as the capacitors and resistors that form the input filter have limited available nominal values, making it hard to control gain and bandwidth independently; or it can exist by design, i.e. having an auxiliary channel with higher bandwidth and higher attenuation to prevent saturation or lower bandwidth to further prevent saturation in spite of the already higher input range.

Furthermore, due to the nature of magnetic signals, we know that eventual saturations will occur as peaks. These can range from a single to hundreds of samples, sometimes in bursts of opposing polarity, triggered by MHD activity or disruption events, but always as peaks. The fine detail of these peaks is less important than its amplitude. With this knowledge we can consider two distinct algorithms for the switch between one source channel to the other. These are more easily understood graphically, in figure 5.34. The first algorithm is the ‘direct’ combination, in blue. Simply, when satura-

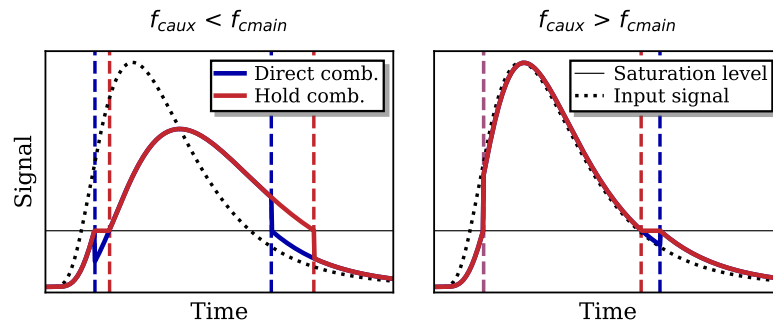


Figure 5.34: Demonstration of the two extended dynamic range algorithms. Originally published in [162].

tion is detected on the main channel, the value from the auxiliary is used instead. This will invariably lead to ‘vertical jumps’ as the phase delay of the filters dictates that one is slower than the other. The second method is the ‘hold’ combination, in red. We see that instead of one of the jumps (on saturation or desaturation, depending on the cutoff frequencies), the algorithm ‘holds’ the saturated main channel until (or if) the auxiliary channel reaches the threshold of (de)saturation of the main channel.

The two combination methods were applied as a synthetic diagnostic to COMPASS magnetics data, by simulating the sampling (with filtering) by two channels. The main with a fixed input range (5 V) and input filter cutoff frequency ($f_c^{main} = 20$ kHz). If both channels have the same f_c no error is committed after integration of the signal; for any other f_c on the auxiliary channel there will be an error upon saturation, that one aims at minimizing. In figure 5.35 f_c^{aux} is ranged, and the error introduced is compared. On the flux loop simulation (5.35b) there are two distinct saturation events, however, other than magnitude, the conclusions are the same: for unintentional mismatch in f_c both methods introduce a similar small error; the hold combination method is only advantageous if the auxiliary channel is ‘slower’ than the main ($f_c^{aux} < f_c^{main}$); and that if the auxiliary channel is fast enough ($f_c^{aux} \sim 400$ kHz), a very small error is introduced by direct combination. It is noteworthy that on both counts (Mirnov coil, flux loop), the error introduced by integrating the saturated samples with no compensation is much higher: 79 and 2012 $\mu\text{V}\cdot\text{s}$, respectively.

The next step is the implementation of the extended dynamic range with the actual module prototypes. The direct combination is straight forward, but the hold method requires additional logic. Due to the demodulation and EO removal, the saturation occurs at four thresholds, correspond to different voltage levels. However, the algorithm is simple enough to be implemented as a state machine on the FPGA, depending only on real-time available information (chopper phase, ADC saturation) and precomputed parameters (saturation levels converted to bins of the auxiliary ADC, EO). Figure 5.36 shows the implementation of the hold method in post-processing (not on the FPGA) for a regular signal from a signal generator and a transformer⁸. While at this zoom level, the recovered signal appears

⁸The simulations show that with this module configuration, direct combination would be more advantageous. However, the implementation with the modules’ data actually predates the simulations, and that fact was not clear at the time.

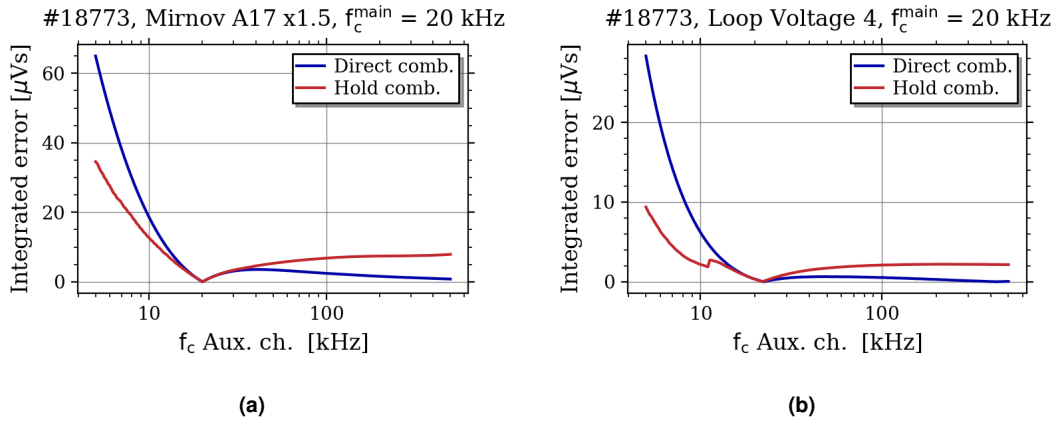


Figure 5.35: Simulation of the two extended dynamic range algorithms on a COMPASS magnetic signals: **(a)** Mirnov coil scaled by a 1.5 factor; **(b)** a flux loop signal. Plot in **(a)** originally published in [162].

to follow the auxiliary channel (CHB), however, in the range of $[-5, 5]$ V the resolution is much higher, as the main channel (CHA) is used.

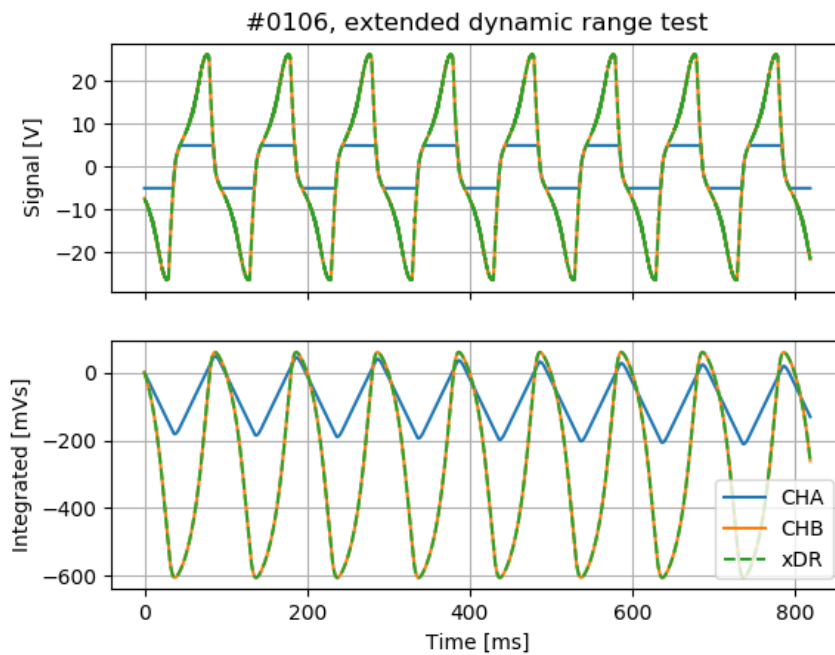


Figure 5.36: Implementation of the 'hold' extended dynamic range (xDR) algorithm on the prototype modules data with enabled chopper. The xDR signal appears to follow the CHB (auxiliary) channel, however in the range of $[-5, 5]$ V the resolution is much higher (CHA, main). Configuration no. 0, details in appendix C.

5.5.4 Acquisition of ISTTOK discharges

The integrators were also tested with real magnetic signals at ISTTOK. The available magnetic sensors consist of a poloidal array of 12 Mirnov coils, of which the first 6 were sampled with the available channels. Figure 5.37 shows the arrangement of the probes in the poloidal cross-section. The sampled coils are positioned in the bottom, arranged from LFS to HFS, according to the distribution in table 5.6.

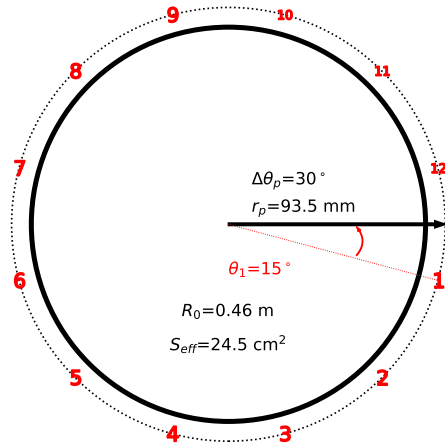


Table 5.6: Initial configuration of the module prototypes.

Module	M1	M2	M3
Channel	A B	A B	A B
Probe	2 1	4 3	6 5

Figure 5.37: Positions and details of the ISTTOK Mirnov coil array.

The magnetic signal from the probes is also needed for real-time plasma position control [117]. The controller is executed in the **Multithreaded Application Real-Time executor (MARTe)** [168] and sampled by a MIMO-ISOL board (see section 5.2.1). The probes are sampled in parallel by both systems, hereby labeled as ‘MARTe’ and ‘IOP’. While the IOP data was acquired correctly for all channels, some of the MARTe data acquisition channels were not successful, due to an undiagnosed problem, possibly connected to the loading with the input impedance of the IOP modules. For this reason there was no active position control and the plasma was short-lived. Figure 5.38a shows the plasma current for one of these discharges with low current ($I_p < 2$ kA) and only a few cycles. Instead of a long flat-top, ISTTOK operates AC discharges with alternating positive and negative plasma current [169], allowing for fast current variations during switching. From MARTe only decimated (integrated) data is available. On the remaining plots in figure 5.38 the acquired (integrated) data is shown, in comparison with the MARTe data, if possible. There is a good agreement between the two signals, to the $\sim 0.1 \mu\text{V}\cdot\text{s}$ level. The modules input range was not adapted to the ISTTOK magnetics range beforehand. Therefore, the inadequacy of the CHB signals in particular is not strange, as the maximum voltage recorded was 80 mV, less than 0.1 % of the ADC range! No performance conclusions will be drawn from the analysis of these channels.

With a 25 ms pulse one can hardly comment on the integrator drift. However, one can sample the full discharge procedure, starting from the toroidal field ramping trigger. Figure 5.39 shows the sampling of a discharge in such conditions. Theoretically, a poloidal probe should not be sensitive to toroidal field, however, due to the fact that toroidal field is generated by coils at discrete positions, and that there are installation uncertainties and/or errors, the coils will nevertheless pick up a fraction of this field. Given the difference in magnitude between the toroidal field and the poloidal field generated by the plasma current, this component is much larger than the plasma signal. Regarding the polarity of the signals, all should be positive. Some signals are sampled with inverse polarity, due to their connection. While in other plots this is corrected, in this plot in particular, the correction was not applied as to facilitate its reading.

It is noteworthy that for relevant lengths (5 s) and amplitudes ($200 \mu\text{V}\cdot\text{s} = 0.49 \mu\text{T}$) the integration was generally successful. While for the reasons presented before, the signal M3CHB is not particularly relevant due to its configuration, it illustrates the consequence of $2.59 \mu\text{V}$ drift, highlighted in figure 5.39b.

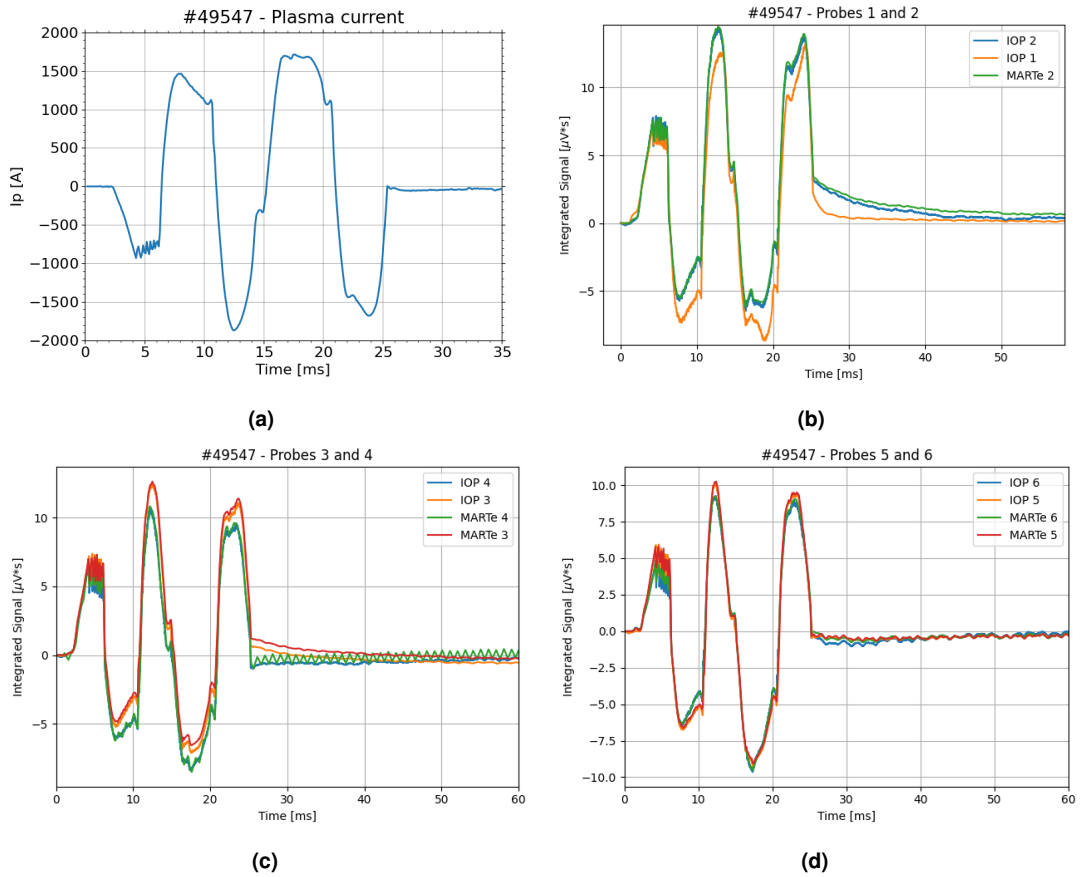


Figure 5.38: Low current, 25 ms discharge on ISTTOK. (a): Plasma current, (b)–(d): Integrated magnetic signals, sampled by the IOP and MARTe, two by two.

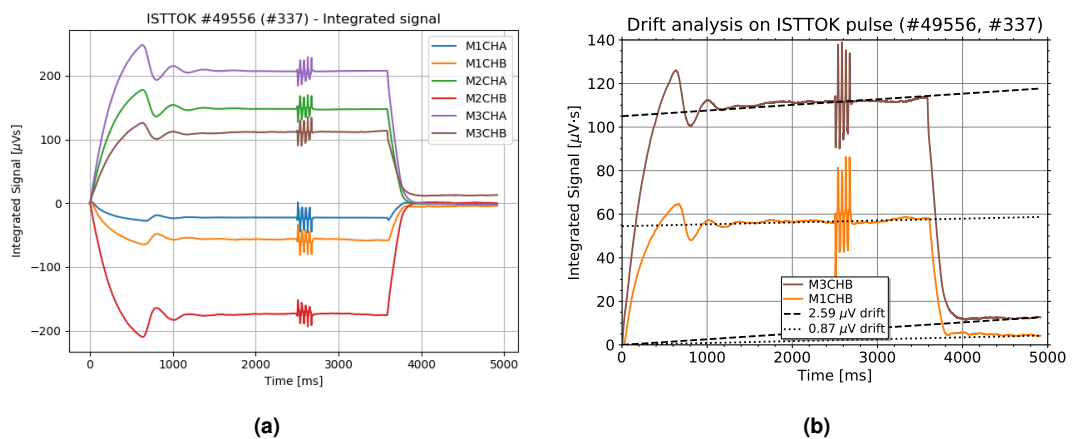


Figure 5.39: Plasma discharge on ISTTOK with toroidal field ramp-up and ramp-down. The acquisition uses the same trigger as the power supplies for the toroidal field coils, hence we observe the plasma component only starting from 2500 ms. (a): All channels, see configuration 0 in appendix C for details. (b): Integrator drift analysis for the two channels with the largest error.

5.5.5 Demodulation error minimization

The demodulation step essentially consists in multiplying the **ADC** value, subtracted of its **EO** by the chopper phase ($ph_{chopper} \in \{1, -1\}$):

$$demod[n] = (ADC[n] - eo) \cdot ph_{chopper}[n] \quad , \quad (5.11)$$

this process can be done in integer format. The next step is the removal of the **WO**, hereby corrected (*corr*):

$$corr[n] = demod[n] - wo = (ADC[n] - eo) \cdot ph_{chopper}[n] - wo \quad . \quad (5.12)$$

Because of the low value of the **WO** in **LSB**, this operation usually requires floating point arithmetic. The integration is a standard numerical integration. For the Riemann sum method (using the right-rule), this corresponds to the multiplication of the cumulative sum by the sampling period ($T_s = 1/f_s$):

$$integrated[n] = \sum^n corr[n] \cdot T_s = \sum^n (ADC[n] - eo) \cdot ph_{chopper}[n] \cdot T_s - wo \cdot nT_s \quad . \quad (5.13)$$

The conversion to volt second, can be made at any of the previous steps. This operation is simply the multiplication by a constant coefficient (k_{LSB}), that is in principle given by the input filter gain (g) and the **ADC** reference voltage (Ref_{ADC}) and number of bits (n):

$$k_{LSB} = \frac{Ref_{ADC}}{g \cdot 2^{n-1}} \quad . \quad (5.14)$$

This value can be alternatively measured/calibrated, using an accurate voltage source.

A known problem of this method a peak appearing due to the demodulation. This was immediately observed on the module prototypes, as shown in figure 5.40a. The consequences for the integral are

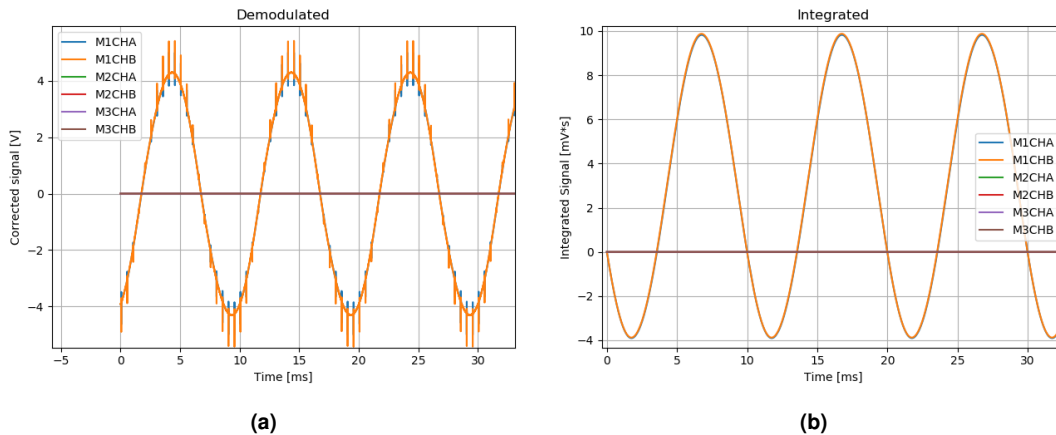


Figure 5.40: Sinusoidal signal of 4.5 V amplitude. **(a):** Demodulated signal; **(b):** integrated. The demodulation errors are clearly seen on the demodulated signal but not on the integrated signal. See configuration 0 in appendix C for details.

minimal (figure 5.40b) for two reasons: (i) this phenomenon has the duration of a few samples (μs scale); it is proportional to the signal amplitude itself, which for magnetic signals tend to be very low, for the majority of time. As reported in [116], a simple solution is to hold the value of the last sample before the chopper transition for a few samples.

A question arises of how many samples to hold. This was empirically studied, first by observing the effect the holding length has on sinusoidal signal with chopper transitions (figure 5.41a); and then by integrating the deviation to the fit of the signal (figure 5.41b). From the analysis of both plots, holding two samples seems to be a reasonable approach.

Another possibility for correction of this error is to try to remove it as a calibration or correction. Using DC signals of different ranges, it was observed that the demodulation artifact depends almost exclusively on the voltage at the transition. This value is known (last sample before chopper transition). Figure 5.42 shows the demodulation error for transitions at constant input voltage, normalized to the value of the last sample before transition. Using the average of these coefficients a table can be constructed and used on the demodulation process. This 'table' method is real-time and **FPGA**

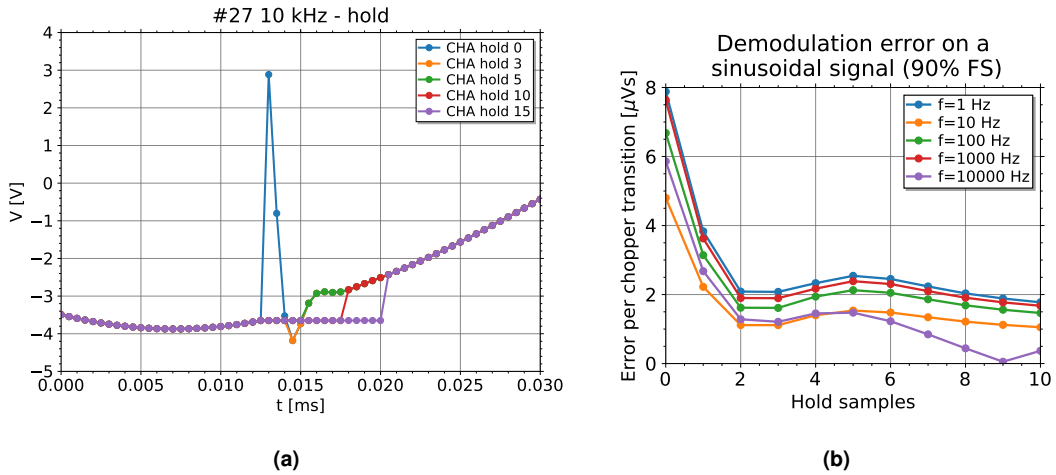


Figure 5.41: Study of holding technique with sinusoidal signals. **(a):** Detail of a chopper transition on a 10 kHz signal holding none or up to 15 samples. **(b):** Integrated error as function of the number of samples for sinusoidal signals with amplitude of 90% of the full scale (FS) for different frequencies. All signals sampled as CHA, configuration 0. See appendix C for details.

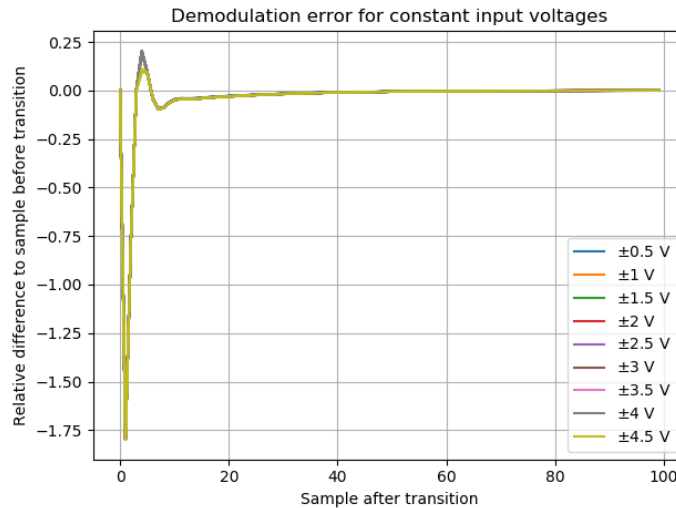


Figure 5.42: Chopper transition error normalized to the last sample before transition. All signals sampled as CHA, configuration 0. See appendix C for details.

compatible and produces good results, when compared to the 'hold' method. However, two caveats must be considered. First, saturation must be properly for accounted. As we see on the last line in the plot in figure 5.42 shows: $1.12 \cdot 4.5 \text{ V} > 5 \text{ V}$. In the implementation algorithm, the correction was not applied if the sample was saturated. Of course, it can be evaluated if the saturation occurs due to the demodulation, in which case subtract only the difference, at the cost of adding additional complexity to the algorithm. The second important point is that this method requires calibration (to fill the table) for each unique configuration. Strictly speaking, due to component variations, each channel can be considered a different configuration. We see that this can lower the robustness of the DAS as a whole, requiring extra calibration steps and another feature that can be tweaked, on a system that one want as simple to the end-user as possible. It is therefore not clear that in practical terms this method is advantageous when compared to the 'hold' method.

5.5.5.A Systematic approach for demodulation error minimization

In order to try to prevent the demodulation error, instead of mitigating its consequences, a more thorough analysis is required. In figure 5.43, the demodulated signal shows the peak we have already seen, however, the raw (ADC) signal, on the left-hand side, is much more clear on the origin of the

phenomenon. The signal arriving at the ADC is not fast enough to traverse the full scale in less than

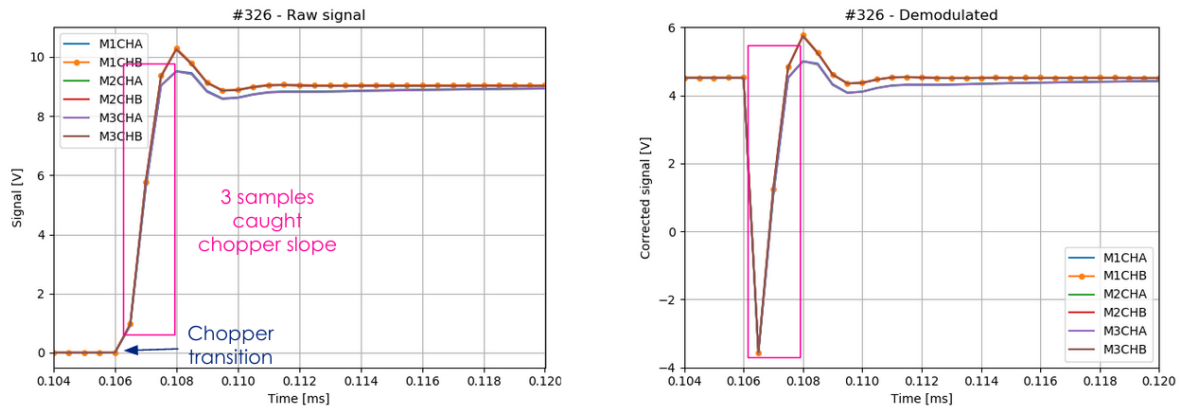


Figure 5.43: Acquisition with a 4.5 V DC signal zoomed on a chopper transition. Raw (ADC) signal on the left-hand side with 0 set as the pre-transition value. On the right-hand side, the demodulated signal. The samples during the chopper transition are highlighted in magenta. All signals sampled as configuration 0. See appendix C for details.

a sample (T_s). As a consequence if demodulated according to (5.11), three samples are incorrectly demodulated as the chopper phase is assumed a perfect square, with no values between -1 and 1. These originate the peak seen in the demodulated signal.

This plot also allows us to decouple the problem in two: the peak and the exponential. We observe that during the signal rise (the first few samples after transition), both channels A and B have similar behavior. However, the slow (tens of samples) exponential recovery of the DC value is different – slower for the channels with $f_c=20$ kHz (A) than for the channels B, with higher bandwidth.

5.5.5.B MFB filter adjustments

The peak behavior of the peak is the same for both channels as it is related to the [Anti-Aliasing \(AA\) MFB filter](#), with the same parameters. The first plot in figure 5.43 closely resembles the step function of the filter. Simply put, the filter is not fast enough, which leads to the question of how fast is ‘fast enough’ – i.e. what are the optimal filter parameters to eliminate the demodulation peak without compromising the drift performance?

The first step was to remove the AA filter. In the plots in figure 5.44, the filter on module 1 was modified to $f_0 = 2.17$ MHz, $Q = 0.99$, whilst on the other two modules was completely removed. On the former, the peak was much reduced, from close to 200 % to less than 20 % of the input signal voltage. On the modules with no filter, the peak was completely removed (only the exponential effect slightly distorts the signal).

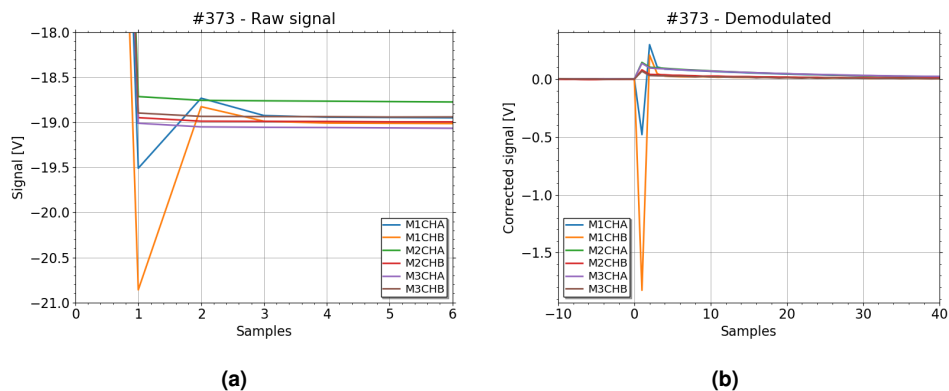


Figure 5.44: Acquisition with a 9.75 V DC signal zoomed on a chopper transition. **a:** Raw (ADC) signal; **b:** demodulated signal. On both plots, 0 is set as the pre-transition value. Module 1 signal sampled as configuration 2. See appendix C for details. The first sample after chopper transition is saturated for M1CHA. The AA filter was removed on modules 2 and 3.

The next step was to simulate the circuit using a **SPICE** simulator (see figure 5.45). A 70 ns

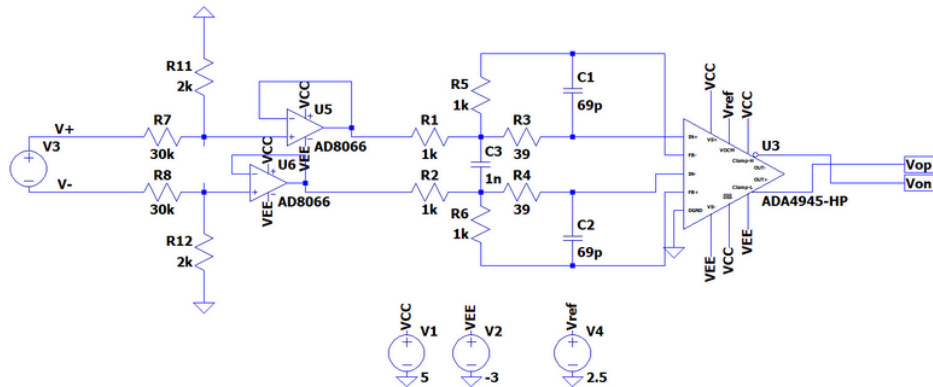


Figure 5.45: Electrical simulation using LTSpice of the input attenuation (chopper, through a pulsed input voltage), buffers and AA filter.

rise time for the voltage source 'V3' was assumed in the simulation, as it is the maximum transition time specified in the chopper IC datasheet. The results of these simulations are the dotted lines in figure 5.46. Adjusting the delay from the sample '0' to the chopper transition, the lines in blue are

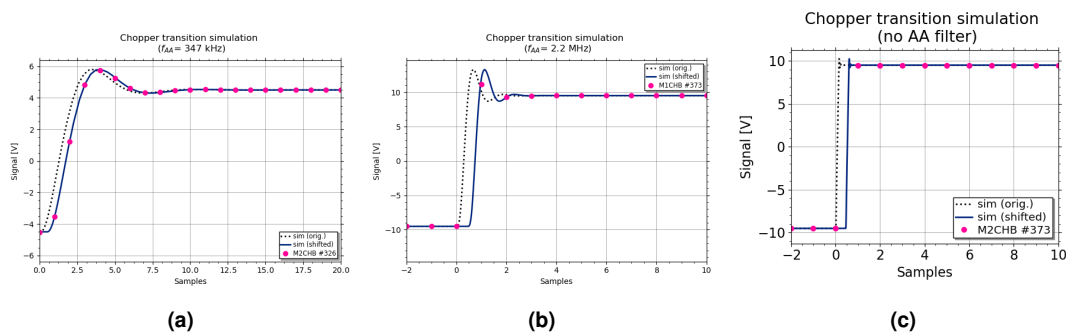


Figure 5.46: Comparison of the chopper transition response simulation (lines) with the ADC data (points) for the three AA filters tested: **(a):** $f_0 = 347$ kHz, $Q = 0.95$; **(b):** $f_0 = 2.17$ MHz, $Q = 0.99$; **(c):** no AA filter (capacitors removed). The blue line is obtained by delaying by the original simulation (dotted line) by 217 ns.

obtained. We can see that there is a reasonable agreement to the data points from the acquisitions for the three scenarios presented so far: original filter ($f_0 = 347$ kHz), $f_0 = 2.2$ MHz, and no filter. Note that the channels with the highest input filter bandwidth were used, as to mitigate the impact of the 'exponential' part.

The delay between the chopper transitions and the sampling can in principle be reduced by firmware. The chopper signal was not synchronous with the conversion 2 MHz acquisition clock in order to prevent chopper transition during the conversion phase. This was achieved by a 190 ns. This time was progressively reduced, as the plot in figure 5.47 shows, up to -150 ns (67 ns delay applied to the simulation). The agreement with the data is not perfect, as beyond the delay the chopper transition model is simplified. However, it is clear that reducing the delay has the expected effect, giving more time for the signal to traverse the ADC input range in between samples.

Having the simulation relatively well benchmarked, the next logical step is to try to find the optimal filter parameters of the filter. The adequacy is evaluated by the integral of the first 5 samples after the transition. The two independent variables are the f_0 and Q that define the second order filter. Using the equations in section 5.4.4, these values are converted to component values that are input to the (automatized) SPICE simulation. The result is the map in figure 5.48a. The white areas represent the lowest error under the established criterion, with the 0 contour lines represented in black. A selection of points on these lines is identified on the map and the resulting simulations shown in figure 5.48b.

Not all these solutions are relevant. Labeling them from 1 to 8 as they appear in the legend, we see that solutions 7 and 8 are artifacts from the optimization criterion chosen – the error of the first 5 samples is high but cancels out numerically. The three best solutions identified are:

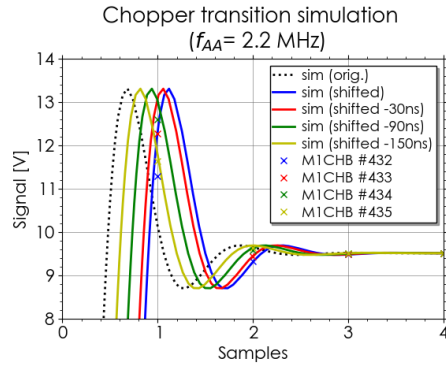


Figure 5.47: Simulated and measured data for the $f_0 = 2.17$ MHz, $Q = 0.99$ configuration changing the chopper delay introduced by firmware.

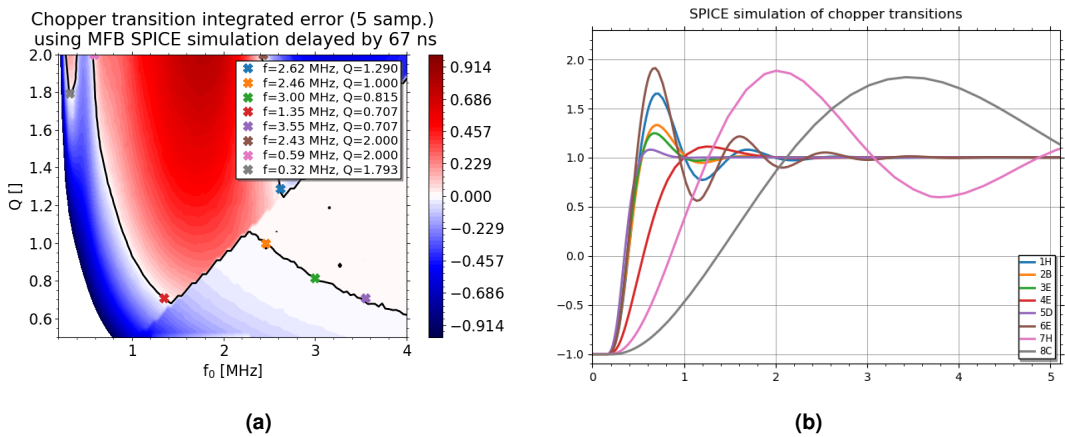


Figure 5.48: (a): Integrated error after chopper transition according to the AA filter parameters f_0 and Q . Contour corresponding to 0 error highlighted as the black lines. Selected combinations highlighted on the map and represented individually in (b), using the same color and order.

- 2, orange – keep f_0 around 2.5 MHz and allow an overshoot (high Q) to speed up the rise;
- 4, red – relax f_0 , catching the first sample on the rise, at the set-point voltage;
- 5, lavender – Increase f_0 beyond 3 MHz and use the flattest passband possible ($Q = 1/\sqrt{2}$).

The component values for the filter were found according to the method described in section 5.4.4, see appendix D for details. The results were mixed, as shown in the first row of figure 5.49. Solution 5, the safest of the three, showed very good results, with no peak visible on the demodulated signal. Solution 2 with the highest Q was the worse, with a large overshoot. Potentially more rewarding, due to the lower frequency, solution 4 showed a ~ 1 V (10 %) peak⁹. In light of the simulations, a further decreasing the chopper delay on the FPGA can correct this error.

The second row in figure 5.49 shows the same two modules now with 20 ns less delay. Solution 2 (M1, orange) had no substantial improvement, but, as expected, solution 4 improved greatly, exhibiting but a minor ripple.

⁹Channel B data unavailable due to hardware problem.

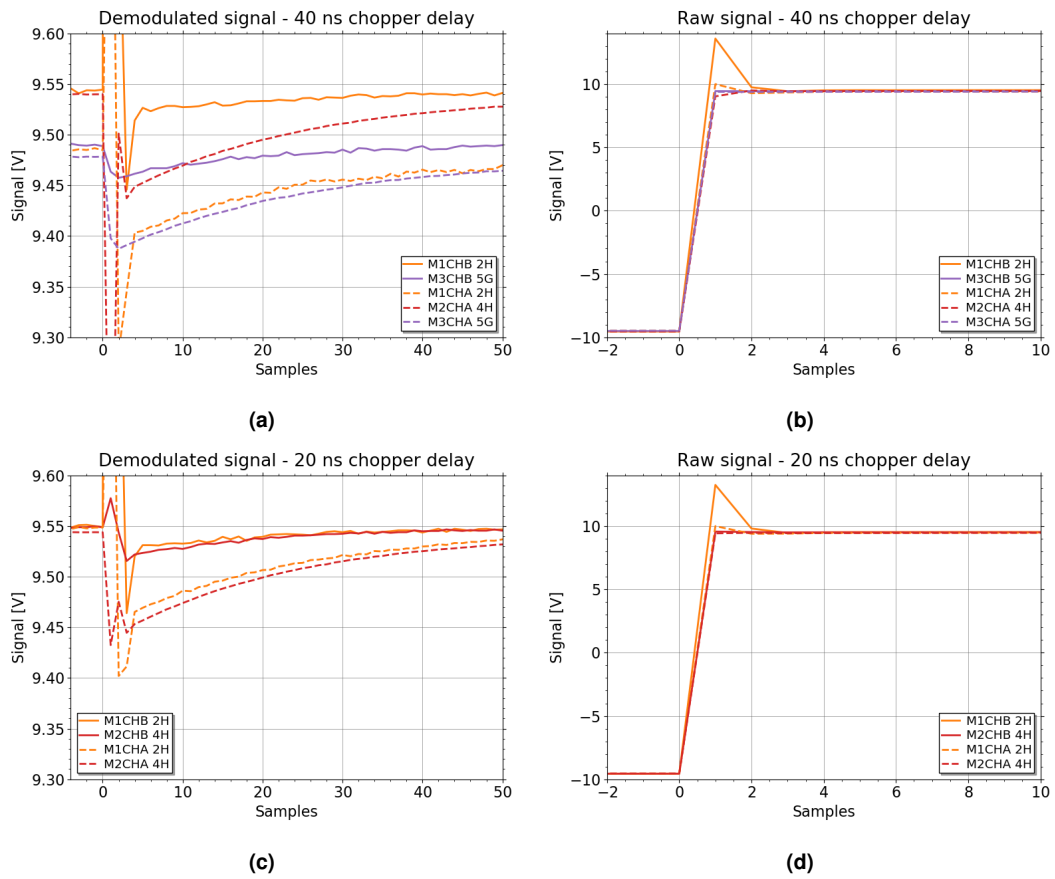


Figure 5.49: Implementation of the optimized filter coefficients M1:2, M2:4, M3:5. Top plots with a chopper delay of 40 ns, bottom 20 ns. Demodulated signal on the left-hand side, raw signal on the right-hand plots.

5.5.5.C Input filter contribution

In order to confirm and study the relation between the input filter and the exponential effect upon chopper transition, the time constant τ of this transition was measured, by fitting the equation

$$y(t) = y_0 e^{(-t/\tau)} \quad (5.15)$$

For these experiments, the modules were fitted with input filters between 12 – 18 kHz. The curve fits (figure 5.50) indeed confirms that the measured τ is that of the input filter, with deviation of up to 2 % to the calculated value.

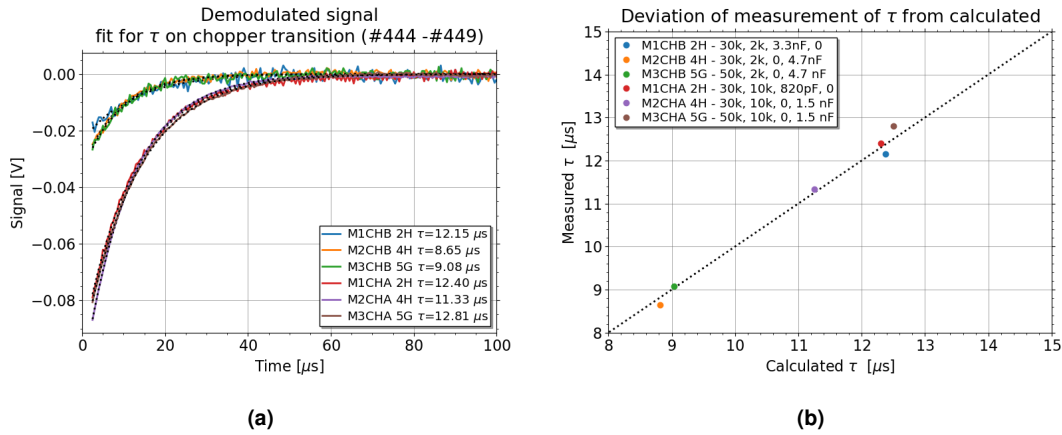


Figure 5.50: (a): Fit (dotted) of exponential function to the chopper transition. First 5 samples ignored in fit. (b): Comparison of the fitted τ with the input filter time constant, calculated with the nominal component values. Dotted line represents the 1:1 relation.

While not surprising, this confirmation is important due to its implication – the exponential part of the demodulation error is directly tied to the input filter, that is crucial to the working of the integrator concept.

The input stage consists of four essential components: as labeled in figure 5.20 R_1 , R_2 , C_1 , C_{snub} . The values for the components are expressed in the plot legends in this order. The same f_c can be achieved by adjusting the balance between R ($R_1 \parallel R_2$) and C ($2C_1 + C_{snub}$). While R is constrained by the desired input range, the two capacitors influence only the filter. However, the different connection to ground could help drain charge injected from the chopper switches differently. Modules M1 and M2 were configured with identical R and similar f_c but using only C_1 or C_{snub} , respectively. The third module features the same capacitors as M2 but higher input resistance $R_1 = 50 \Omega$.

Having evaluated the dynamic part of the exponential (τ) we can analyze the static part (y_0), its magnitude, that we aim at minimizing. For this, the area under the fitted curve will be used:

$$\int_{t=0}^{\infty} y = y_0 \tau \quad (5.16)$$

representing the error committed in the integrated data. As the modules have different input ranges, the ‘jump’ on chopper transition at the ADC will be widely different. The plot in figure 5.51a shows the integral as function of the ‘jump’ in the ADC full scale, represented as a percentage. From this plot we can observe no substantial difference between M1 and M2 (either channel), i.e. between distributing the capacitance in C_1 or C_{snub} .

In figure 5.51b, the difference in input range is removed by normalizing the integral to the voltage at the ADC. On the x-axis, C is represented. We observe no substantial change with C but rather with the input resistance, R_1 , with the M3, with higher input resistance showing a larger error. Once again the conclusion is clear but not encouraging: higher demodulation errors are observed for higher input ranges. This represents a trade-off between demodulated signal fidelity and input range. At the same time, a positive outlook is that, while a generic DAS should have a very high input impedance, the relatively low output impedance of the magnetic diagnostics allows for a relaxation of this parameter, that nonetheless should be three orders of magnitude higher than the output resistance of the sensors.

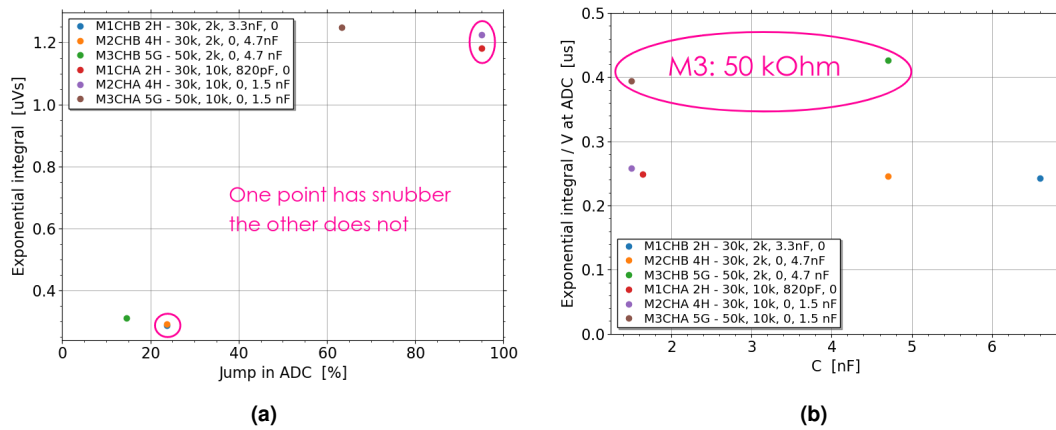


Figure 5.51: (a): Integral of the exponential (error) as function of the percentage of the ADC full scale covered by the transition. Two pairs of channels that differ on the capacitor used to form the input filter. (b): Error normalized to the transition voltage jump at the ADC input over the capacitance of the input filter.

5.5.6 Drift and temperature dependence

The integrator drifts displayed in figure 5.32 seem to suggest a pattern in the individual drift measurements rather than a random distribution. These acquisitions were taken sequentially, so a time pattern can be investigated. Figure 5.52a shows the time evolution of the drift measurements, as measured by the final integrated value over the integration time. For the less noisy channel (± 5 V)

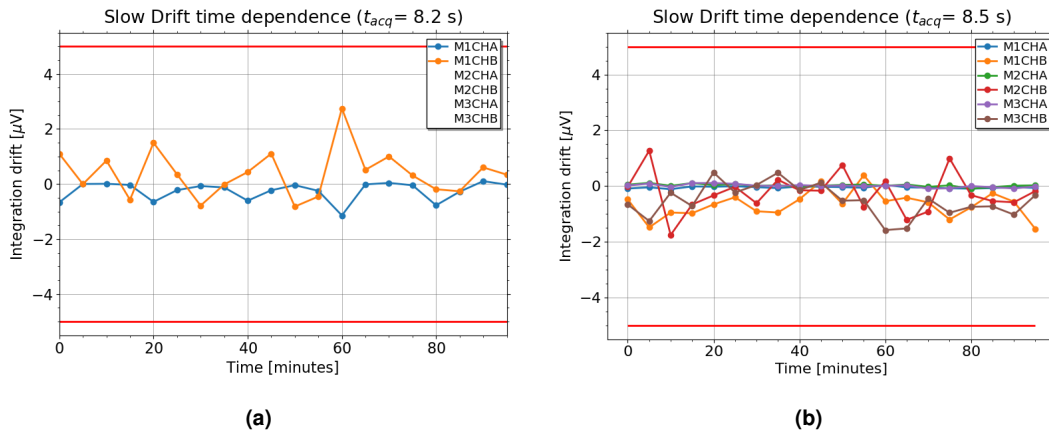


Figure 5.52: Comparison of drift measurements at IPP (a) and IST (b) for the modules under the initial configuration (0), see appendix C for details.

a clear pattern emerges, verified by other such acquisition with different integration times and time resolution. It was hypothesized that this behavior can have two causes: either thermal regulation problems, such as an air conditioning cycle; or a sub-Hertz noise component, possible arising from aliasing of the insulated power supply working at the Nyquist frequency. Figure 5.52b shows a similar acquisition, in the same module configuration, carried out at ISTTOK. The results are clear, no such time pattern emerges, and the second hypothesis can be discarded.

In order to investigate the first, back at IPP, it was verified that the room temperature is stable up to ± 0.2 °C. Then the cubicle air temperature above the ATCA chassis was measured simultaneously with drift acquisitions. Figure 5.53 shows the results. Above, 10 s drift acquisitions, where a roughly 35-minute pattern is visible. Below, the cabinet temperature, confirming this periodicity.

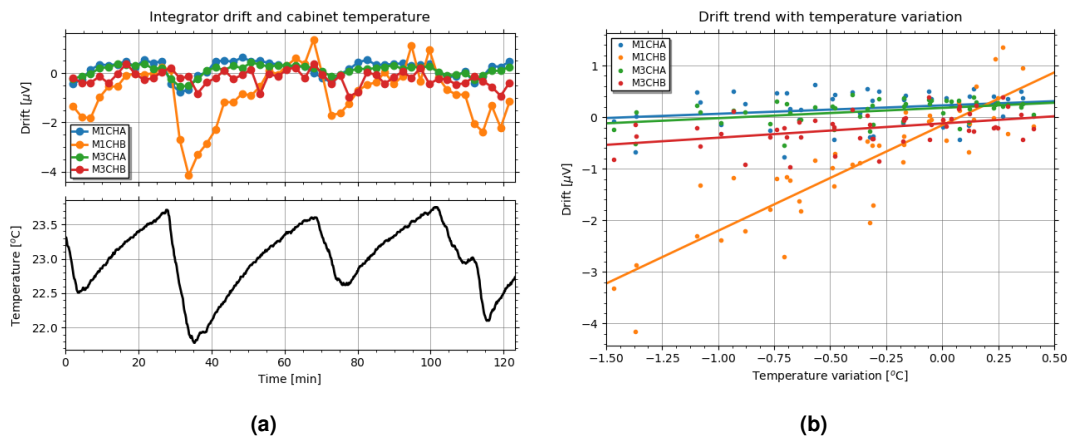


Figure 5.53: Influence of cabinet temperature on integrator drift (10 s acquisitions). (a): Drift and temperature in the cabinet. (b): Measured drift as function of the temperature variation since calibration. Linear fits. Module configurations 1 and 3, see appendix C for details.

Figure 5.53b shows the same points (drift measurements) not in time but according to the temperature difference since the calibration acquisition. Even through the large spread and uncertainty on temperature and time, the linear fits show a systematic trend. The fitted drift temperature dependence (k_T) is different between the modules but above one standard deviation, see results in table 5.7. This correlation would be much stronger if the temperature was measured at the ATCA board (or module)

itself.

Table 5.7: Fits of integrator drift temperature dependence. Input Range (IR) for reference. Full module configuration in appendix C.

Channel	k_T (fit) [$\mu\text{V}/^\circ\text{C}$]	k_T/σ	IR [V]	Config.
M1CHA	0.16 ± 0.10	1.6	± 10	3
M1CHB	2.05 ± 0.15	13.7	± 40	
M3CHA	0.20 ± 0.06	3.3	± 15	1
M3CHB	0.28 ± 0.08	3.5	± 65	

The cause of this temperature excursions, that were not observed at ISTTOK is the disabled [ATCA](#) shelf manager, that is responsible for the management of fan speed. The temperature and air-flow control on the crate is therefore not optimized. The correct configuration of this element or the usage of a different crate should fix this issue. Regarding the reason why the M1CHB has a one order of magnitude higher thermal dependence, this can be attributed to the components used. In order to expedite the testing, lower quality components, from inexpensive resistor and capacitor kits were used, violating the design rules established in section [5.4](#).

Regarding the actual drift measurements, due to the problem mentioned above, the measurements carried out in IST are the most representative. These were made with the original configuration and a typical drift of under 50 nV was observed for the most representative input range (± 5 V). Under these conditions and with a statistical sample, the maximum observed was 116 nV (2.7 times higher), still safely below the 5000 nV requirement for COMPASS-U. The full set of drift measurements is shown in table [5.8](#).

Table 5.8: Drift measurements, performed with statistical samples of acquisitions (N) on a COMPASS-U relevant timescale (t_{acq}). Average and maximum values for each configuration. Full module configuration in appendix C.

Config.	Linear drift [nV]		t_{acq} [s]	N	Lab.
	avg.	max.			
0A	266	1144	8.2	19	IPP
0B	698	2748	8.2	19	IPP
0A	46	116	8.5	20x3	IST
0B	646	1738	8.5	20x3	IST
3A	337	765	10	50	IPP
3B	1024	4148	10	50	IPP
1A	222	546	10	50	IPP
1B	291	957	10	50	IPP
3A	170	328	10	20	IPP
3B	587	1081	10	20	IPP
1A	310	710	10	20	IPP

Once again, the results taken at IPP need to be read with the caveat of the temperature correlation, in particular for the high sensitivity channels. The configuration 0A appears to exhibit 6 times higher drift at IPP. However, when we look at the visual representation of this dataset – figure [5.52a](#) in blue – we see that without the temperature variations the drifts are systematically lower. A ‘cherry-picked’ dataset indeed confirms the results at IST, the average dropping to 106 nV with $N = 14$ and to 50 nV with $N = 10$.

As elaborated in the next section, we are confident that these values can be further reduced on the final system upon commissioning.

5.6 Implementation for COMPASS-U

Having identified no major problems with the prototypes, the final production modules will feature only minor changes:

- replacement of the analog and digital connectors, as the ones present in the IOP are obsolete;
- a reduction in the dimensions (to 130x20 mm) due to the smaller connectors;
- improvements on the PCB layout aiming at noise minimization.

Regarding the aspects that are configurable by component replacement, the following conclusions follow from the analysis of the prototype results:

- The ADC voltage reference, was initially chosen as 2.5 V as a conservative approach due to the very low equilibrium signals expected on Mirnov coils (section 5.1.2.A). This choice incurs a considerable trade-off with noise at the ADC. As discussed in section 5.5.2, an increase of the reference voltage can increase the SNR, possibly leading to lower integrator drift. The reference voltages of 3, 3.3 and 4.096 V are available on the same IC model. Both the equilibrium simulations (partially in section 5.1.2.C) and the testing on ISTTOK (section 5.5.4), with surprisingly successful integration with significantly unadjusted input ranges for signals of the expected amplitude of the COMPASS-U Mirnov coils, suggests that one does not need to be that conservative on the resolution.
- On the input filter and attenuator, the demodulation error analysis (section 5.5.5.C) has shown that there is a significant advantage in reducing the value of the input resistors. A resultant input impedance of $Z_{in}=30\text{--}50\text{ k}\Omega$ should be plenty, considering the low resistance of the magnetic sensors.
- On the AA filter, three valid options were presented in section 5.5.5.B: If the signal integrity of the demodulated signal is very important, a filter with ($f_0=3.55$, $Q=0.707$) in conjugation with a low input impedance ensures the minimum demodulation artifacts, at the cost of possible aliases and increased noise. On the other end, if only the integration performance is important, a more canonical filter with ($f_0 \in [350, 500]$ kHz, $Q=0.707$) ensures the lowest noise and drift. As a compromise solution, it was shown through optimization that with a ($f_0=1.35$, $Q=0.707$) filter can greatly minimize the demodulation artifacts with a large increase of the stopband.

It is hard to predict the best configuration without having real magnetics data. The flexibility of the design and the emphasis on the description of methods in this chapter will make it easier to adjust the electronics during operation of the machine. In this sense, the advantages of the different operation modes was also shown. The need for parallel or extended dynamic range sampling is not obvious in extent (which sensors) nor if for all campaigns or operation stages, depending on the needs for these magnetic measurements, other than the critical roles of control and equilibrium reconstruction. However, it has shown how these sampling modes can be implemented. Even if not implemented, the two module architecture under individual sampling has shown how a very high channel density can be achieved, without crosstalk problems for the signal voltage and frequency ranges expected.

6

Conclusions and Future Work

Contents

6.1 Summary and achievements	148
6.2 Outlook and future work	151

The work carried out in this thesis led to the publication of three peer-reviewed articles in journals relevant to the field. The majority of chapter 3 is covered by “*Mineral insulated cable assessment for inductive magnetic diagnostic sensors of a hot-wall tokamak*” [148] and “*Testbench for calibration of magnetic field sensor prototypes for COMPASS-U tokamak*” [31], while the article “*Data acquisition with real-time numerical integration for COMPASS-U magnetic diagnostics*” [162] covers qualification part of chapter 5.

In this chapter, the main conclusions and achievements are summarized, and the implications of the work, particularly regarding the commissioning of the magnetic diagnostic system are discussed.

6.1 Summary and achievements

The first important results came from the comprehensive study of the MIC as a material for magnetic sensors. In this regard, the key qualitative finding was that the internal composition of the cable is important for this application. This might appear as a foregone conclusion, however once one contemplates the diagnostic development the qualitative and quantitative results become important as: (i) these cables are often just referred to and compared by their OD, that closely relates to the spatial requirements; (ii) sensor development is not the main application for this type of cable, hence they are optimized for signal transmission in fire-resistant circuits or industrial applications, where electrical performance for high bandwidth signals is not important; (iii) these are expensive cables, not often compared. For these reasons, even if intuitive, the conclusions and the quantitative data is relevant for the design of future diagnostic systems. In particular, it was verified that the ideal cable for this purpose has a thin metallic sheath and a low capacitance to the core. For the capacitance, the data shows the insulation thickness is not a good indicator by itself. This is possibly due to differences in purity and how compactness level of the ceramic powder. Furthermore, the measurement proved stable with temperature, a good outlook for COMPASS-U high-temperature sensors. Regarding the attenuation of high frequency components, by using a real COMPASS magnetic signal (flux loop), referenced to a non-MIC sensor, it was confirmed that the metallic sheath indeed behaves like a first order filter to magnetic induction. Moreover, a clear trend with sheath thickness was observed. Opting for a thin (sheath) cable can make the delays negligible (sub- μ s), while a thick MIC will greatly reduce the bandwidth five-fold. This qualitative conclusions are (only) valid for toroidal loop voltage measurements. However, these are the most important measurements for state-of-the-art vertical stabilization controllers (on fast control loops). These results had real implications for the commissioning of sensors, providing core rationales for the establishment of parameter-space in the tendering of MIC for construction of magnetic sensors and as in-vessel signal transmission for other diagnostics.

In order to aid the development and calibrate the local sensors (magnetic probes) a two part testbench was developed. Gradually developed over time, this setup allowed the measurement of frequency responses to magnetic fields and the effective area of the sensors with increasing levels of confidence and accuracy. This setup achieves an accuracy and uncertainty on the effective area measurement of under 0.2 %. The accuracy was determined by comparison with independent measurements at the CMI, enabled by a geometrical correction based on the field distribution inside the solenoid. The uncertainty is expressed as one standard deviation ($\sigma/\mu < 0.2$ %). A few noteworthy aspects about this setup are: (i) its low cost, taking full advantage of a desktop PC oscilloscope, 3D printed parts and coils developed in-house. (ii) The automation process allows for a high repetition rate (higher statistical samples) and a higher degree of uniformity between measurements. (iii) The detailed algorithmic and construction details provided in this thesis can be a valuable tool for future devices to reproduce the calibration procedure on a low budget without compromising on the accuracy. (iv) High frequency resolution and availability – it is hard to draw conclusions towards sensor design from frequency response plots, with small variability between models. With only a few data points one can verify the response, have a rough idea of the bandwidth of the sensor. For a detailed analysis in prototyping stage and/or usage in modeling, the high resolution (in f), high degree of confidence on the data, and availability (as opposed to outsourcing the analysis) is required.

One of the most important outcomes of the calibration setup, the Helmholtz coil in particular, was the modeling of the frequency response of the sensors. For the MHD perturbation sensors – bare copper and TPC – an electrical model was calibrated. With this model, it was possible to predict the frequency response under different DAQ input impedances, ex-vessel and in-vessel (leads) cable lengths. In this, it was shown how impedance matching can help mitigate resonances, allowing a flatter baseband, at the cost of signal strength across the full bandwidth. Months later, the model was

further validated when it successfully reproduced the frequency response of the sensor with different ex-vessel cables (in section 4.5). The frequency response of the MIC sensors was never successfully modeled in the same way (parametrically). The attenuation introduced by the MIC itself was shown to be possible to model (both in literature [137] and by the COMPASS flux loops results), but the contribution from the metallic mandrel is complex and in principle needs to be either modelled by Finite Element Method (FEM)s or measured. This possibility is discussed in the ‘future work’ section. However, this is not needed as both methods depend on an already defined or existing model, nullifying the ‘predictive’ goal of the model. The other (and more important) goal is the determination of the frequency dependent attenuation and delay for control and equilibrium reconstruction usages. This is achieved by the LTI model fitted to the data, which allowed us to have an idea of the effect of MIC sensor attenuation on real tokamak (COMPASS) data. While this is not directly translated to the expected signals on COMPASS-U, it provides a better (perhaps reassuring) intuition on the attenuation expected, something that is sometimes not easy to obtain just by interpretation of logarithmic frequency response plots. Furthermore, this five-parameter model can be introduced, for instance, in the simulation of control algorithms, in a form familiar to any control engineer.

Chapter 3 shows the qualification of data cables for the diagnostic, according to signal integrity. These tests of ex-vessel were performed in difficult experimental conditions, i.e. the crosstalk tests were carried out on the limit of the data acquisition capabilities and for the external noise, only a pulsed source was available. However, a few conclusions can be drawn towards the cable choice for commissioning. Depending on the individual cable, Ethernet cables have shown similar crosstalk rejection as individual shielded twisted pair cables. It is true that these cables were tested for the worst-case scenario where two adjacent cables are in constant contact. However, in the real implementation the cables would be bundled together in sets of cables carrying identical signals (in terms of general magnitude and bandwidth), creating comparable cross-talk exposition. It was also shown how proper grounding can be more important than cross-talk effects. Both effects can manifest themselves in the same way when analyzing output signals leading to the incorrect attribution to cross-talk. A general recommendation is made to use a hybrid ground, with one end of the cable shielding grounded directly and the other through a capacitor. The capacitor prevents low-frequency ground loops through the cable shielding whilst also preventing the pick-up of high frequency electrical fields.

Regarding the externally induced noise, no substantial difference can be attributed to the topology of the cable assembly. In general Ethernet cables have shown better noise rejection, however, this was attributed to the fact that Ethernet cables have higher twisting density and thinner insulation around the conductor, both factors contributing to smaller infinitesimal loops sensitive to magnetic field variations. The smaller these loops are, the higher the spatial gradients of magnetic field can be for the twisting pair approach to provide effective cancellation of the induced voltages. Another conclusion from the analysis of the reactive properties of the tested cables is that minimization of the capacitance between the conductors is important for the high frequency MHD perturbation sensors. It was shown how, with 30 m distance to the tokamak, the choice of cable can influence the perceived mode amplitude in the >500 kHz band and the presence or not of a resonance, that can show as a horizontal line in spectrograms.

In summary, this study points to a recommendation for the usage of CAT7 Ethernet cables outside the tokamak, choosing a model with high twisting density, and low capacitance between conductors. This brings savings in space (particularly in the holes in the thick radiation shield walls) and money, as the Ethernet cables have similar price per meter to comparable (individual) twisted pair cables, whilst featuring four twisted pairs. These experiments and conclusions were carried out with the requirements of the magnetic diagnostic in mind, however, they are general enough to be valuable to other diagnostics and auxiliary systems in COMPASS-U as well as in other devices.

For the data acquisition and signal integration, in chapter 5 a qualification of digital integration is presented. This includes an estimation of the needed resolution and maximum amplitudes expected during disruption. While it is hard to provide an exact evaluation before operation of the device, no significant impediments were found. The key problem with numerical integration of magnetic signals is the high dynamic range. The analysis carried out showed that for COMPASS-U equilibrium signals, the required resolution (and dynamic range) is achievable with the current concept and technology. Furthermore, the testing of the ‘integrator’ modules of ISTTOK on COMPASS was successful. Despite being tested only at a small scale, on top of negligible drift, the integrated signals have shown good fidelity, with the prerequisite filtering of the input signal effectively lowering the input range of the signals from the coils without compromising the integration at the sub-ms scale. Furthermore, it was demonstrated how the attenuated high frequency components can be recovered in real-time. The

benefits and shortcomings of the robust algorithm were discussed, and its implementation, not considered necessary for first-plasma, will be considered for more advanced MHD perturbation control algorithms.

It was shown how a two-channel architecture with separated and isolated paths can provide the user with the following options: *individual sampling* with a higher channel density (more coils sampled); *parallel sampling* providing two distinct static or dynamic input configurations; and *extended dynamic range sampling* where the output signal is generated from the composition of two channels with different input ranges. For the latter, the problem of different dynamic characteristics (bandwidth) was simulated. It was concluded that the signal composition introduces minimal error for small deviations of the bandwidth of the channels. A new causal (real-time compatible) method for merging the channels was also proposed and implemented on real data. The simulations with real saturation-inducing (COMPASS) magnetic signals have shown that this method is only advantageous for the scenario where the auxiliary channel has a lower bandwidth in addition to higher input range. This configuration is not the most likely however, as it is only useful in a scenario of strong disruptions in which the magnetic signal amplitude needs to be recorded, either for operational or disruption studies.

A new two-channel data acquisition module was developed in retro-compatibility with the IPFN IOP carrier board. Beyond more up-to-date procurable components, one of the innovations in this design is the isolated power supply switching at the Nyquist frequency. This feature required testing of non-standard solutions which was carried out in a dedicated PCB. Having chosen an adequate solution, the module prototyping resumed. Indeed, the noise spectrum reveals no frequency with major noise contribution from the power-supply, as it was characteristic in previous IPFN designs (at 500 kHz). Another noteworthy aspect of the electronics development detailed in the thesis is the filter calculation process. A 'physicist' approach was followed, whereby the process was detailed and documented, accompanied by the respective implementations in code (omitted in the present document). This is relevant because the flexibility of the design is a praised factor, and it is, in general, one of the advantages of bespoke hardware over COTS. The end-user, through this document (and the accompanied code repository), is provided with the conceptual tools to modify the design, as well as the rationales followed. Additionally, in the prototype testing phase, the simulation tools developed for filter design proved useful in the optimization of the design and understanding of its problems. Despite the technical problems faced in the testing of the prototypes in real plasma scenario (ISTTOK), positive conclusions can be drawn. In the qualification stage, the low signals were a vulnerability identified, directly related to the ADC resolution. By having only low plasma currents on a small device (that would otherwise produce stronger signals) worst-case scenario coil voltages were obtained (order of 10–100 mV). The non-optimized default configuration with ± 5 V input range was capable of integrating the signal without errors, as evaluated both by comparison to the existing ISTTOK integrators¹ and by the integral zeroing after the discharge. Lasting only 30 ms, the discharges recorded on ISTTOK can hardly be used to evaluate drift at the scale relevant for the 5 s typical COMPASS-U discharges. This was overcome by recording the full discharge sequence including the magnetization of the TF coils. In this experiment the worse results are shown (referring to figure 5.39, where one channel exhibits a much larger drift). In other discharges recorded, the drift exhibited by that particular channel is lower, however this particularly unlucky acquisition (in the statistical sense) motivates a discussion of the effect of 2.6 μ V on a signal that is relevant in amplitude and time to COMPASS-U. This drift is roughly half the limit established based on equilibrium reconstruction, therefore, it is not expected it would have operational consequences on COMPASS-U. This is because the reconstruction algorithm is based on the input of multiple coils, more than those needed, for the sake of accuracy and redundancy. When analyzing this extreme drift, it was concluded that the reason can be traced to the calibration. To prevent such cases, a revision of the calibration procedures is suggested in the future work section.

One advantage of a digital integration system is that non-integrated data can also be provided to the real-time controllers. As more advanced control systems are developed apart from the current, position and shape controllers, in particular for fast or oscillatory phenomena that can lead to disruptions, the availability of dynamic (dB/dt) data is increasingly useful, in complement to field measurements. For this reason it is important to minimize the known demodulation error associated with the chopper modulation. In this work, this effect was comprehensively studied and solutions to its mitigation proposed: either digitally by compensation with holding the last sample value or through a look-up table; or analogically, by optimization of the AA filter and the delay on the chopper switching signal. As result of the study of the former, three perfectly valid configurations are proposed, exploring the

¹Used in the real-time control system and qualified in COMPASS.

trade-off between aliasing mitigation (and drift performance) and fidelity of the non-integrated signal.

Regarding drift, the laboratory measurements confirm an adequacy to the requirement for COMPASS-U. Even the channels tested with a high input range (± 127.5 V) and no input filtering are compliant. The study of drift performance was hindered by a belatedly detected problem in the testing hardware. In spite of that, the level of thermal sensitivity of drift was discussed, and proper measurements were nevertheless acquired for the configuration optimized for drift mitigation. The overall average drift measurements of 46 nV obtained is definitely among the state-of-the-art results and furthermore, constitutes an improvement over the predecessor upon which the digital integrator was based, as it was set as a goal for the development. A note must be made on the measurement of the drift. The typical procedure is to measure the drift on a long acquisition, to which a linear approximation between zero and the error at the end is taken. As the end goal of the integrator is its employment on COMPASS-U, the acquisition times used were relevant to this role (8.5 or 10 s). To increase the meaningfulness of the results, instead of integrating continuously for e.g. one hour, 10 s measurements were taken every 5 minutes. This configuration is much closer to the expected usage during tokamak operation, where 5–10 s acquisitions will be performed hours after calibration.

Finally, a mention to the title of this thesis is in order. The thesis provides description, methodical and cutting edge work on key aspects of the diagnostic system development organized with a conductive line towards its commissioning. However, it falls short from the full *commissioning* of the system. This would have been an impossibility because the necessary technical work transcends that of a PhD candidate, and because delays on the whole project (COMPASS-U) propagate downstream to individual systems. The last factor is particularly relevant due to the challenging times that the work on the thesis spanned.

6.2 Outlook and future work

The current work leaves a few open questions that in some cases can be improved and in others are needed before commissioning of the diagnostic system.

The magnetic probe calibration setup produced good results and is in a position that can be used as-is for the commissioning of the system. Specifically, to calibrate the final sensors before installation in or on the VV. In spite of that, improvements are possible. The measurement of current by voltage drop in the shunt resistor is the main contributor to the uncertainty of the measurement of the effective area. In order to improve this, its replacement with a low nominal value power resistor is recommended. On the Helmholtz coil setup, the same comment can be made, however, in this case a high resistance is needed because of the 5Ω output impedance of the amplifier. A more powerful wide bandwidth amplifier with lower output impedance would allow a stronger signal, that would in turn allow reaching lower frequencies. Finally, while the correction of the field non-uniformity inside the solenoid produces accurate results, a larger solenoid would provide a more uniform central region, eliminating the need for this correction. In both the choice of amplifier and solenoid design, we are looking at a *victim of its own success* situation, as the requirements (sub-percent accuracy, high frequency resolution) evolved as the operation of the test bench provided ever more positive results.

Still on the magnetic sensors, despite previous attempts, an electrical model of the MIC prototypes was never successfully calibrated. This is attributed to two factors: the attenuation contribution of the core, that does not relate to the measurable electrical proprieties of the coil; and the double layer configuration, whereby the modeling of the MIC shielding as the secondary of transformer might need a more complicated modeling. By starting with single-layer coils and decoupling and measuring separately the core transfer function ($g_{core}(\omega)$) as specified in section 3.5.4 it should be possible to obtain a model for the contribution of the coil itself (g_{MIC}). The advantage of having this model would not be designing new sensors, but simulating the frequency response at high temperatures, as we currently have no high-temperature frequency response measurements, but have high temperature impedance measurements ($Z(\omega, T)$) for some prototypes.

On the data acquisition modules testing, it was concluded that the calibration procedure is crucial for the overall results. From the experience in this regard, the calibration procedure should be revised according to the following points: (i) avoid system restarts – the system takes time to thermalize and reach the optimal operation conditions. In the prototyping stage this was not prioritized, with the procedure often being, booting the ATCA board and immediately acquiring a calibration run to be used throughout the experiments, while thermalization effects can be in the order of tens of minutes to an hour. For operation of the system on the tokamak, automatic ‘warm-up’ acquisitions should be

considered, before calibration; (ii) Longer acquisition times – the calibration acquisition times used were short (~ 10 s), this should be increased, in combination with (iii) a more robust algorithm for offset calculation. The algorithm used essentially the same as the drift measurement described in the previous section and is a valid approximation for systems with large (linear) integrator drift. What we observe at this performance level is that a large random or Brownian component is similar in magnitude to the linear part. A more robust algorithm, such as a linear fit, would be more immune to a random effect at the last seconds of the recorded integration. (iv) Redundancy and confirmation – on top of ‘warm-up’ runs, more than one acquisition should be made during calibration (while there is ‘magnetic silence’). This can be as a confirmation – *is the drift acceptable?* – or as redundancy – have 2 calibrations. Both these procedures can be easily automated with reports or alerts for the operator generated.

There is also the envisioned possibility of improving upon the drift measurements. This was not a particularly strong motivation since it complies well with the requirements established, but given the good results obtained, it can be further optimized, in light of possible application on devices with long pulses and tighter drift requirements. Another important factor is that these are bench-top, short-circuited input measurements. Adding cables, sensors and picked-up noise during device operation will increase the drift (WO). For this reason, drift minimization is not a futile effort, even for short pulses. At the electronics, this minimization could be achieved by: (i) better thermal regulation; (ii) increasing the ADC reference voltage, reducing the attenuation needed at the input stage; (iii) limiting the bandwidth of the input according to the minimum requirements by real-time control; and (iv) using better components than those used in the testing phase.

A next necessary step is the integration in the new processor board. This was already initiated, designing the new modules with different analog and digital connectors. Now that the design of the full diagnostic system has progressed to final design stage. Fully integrated measurements with the final probe prototypes is also envisioned. These include measurements with the probe–cable–integrator at room temperature under Helmholtz coil magnetic fields and drift measurements with the probe at high temperatures and using the prototype vacuum feedthroughs under development/procurement.

Moreover, this work lays a solid basis for future work, both directly on the data acquisition and magnetic diagnostic but also for the downstream interfacing systems, such as real-time control, equilibrium reconstruction, scientific exploitation based on the magnetic data. It is impossible to predict exactly the full extent of applications of the magnetic diagnostic data or even its exact configuration at first plasma or after years of operation. However, this work was developed aiming at a robust system, in which future engineers and physicists know with the best fidelity possible what they are measuring.

Bibliography

- [1] B. Pillot, M. Muselli, P. Poggi, and J. B. Dias, "On the impact of the global energy policy framework on the development and sustainability of renewable power systems in sub-saharan africa: the case of solar pv," 2017.
- [2] H. Ritchie and P. Rosado, "Energy: Key charts," *Our World in Data*, 2021, <https://ourworldindata.org/energy-key-charts>.
- [3] T. Stocker, D. Qin, G.-K. Plattner, M. Tignor, S. Allen, J. Boschung, A. Nauels, Y. Xia, V. Bex, and P. Midgley, "Ipcc, 2013: Climate change 2013: The physical science basis. contribution of working group i to the fifth assessment report of the intergovernmental panel on climate change," Cambridge University Press, Cambridge, United Kingdom and New York, NY, US, 2013.
- [4] U. of Wisconsin Madison, "Fusion reaction crosssections," accessed January, 2023. [Online]. Available: <http://iec.neep.wisc.edu/images/crossSections.jpg>
- [5] ITER, "Fuelling the fusion reaction," [Online; accessed 2023-06-09]. [Online]. Available: <https://www.iter.org/sci/fusionfuels>
- [6] J. P. H. Goedbloed and S. Poedts, *Introduction*. Cambridge University Press, 2004, p. 3–33.
- [7] V. D. Shafranov, "The initial period in the history of nuclear fusion research at the kurchatov institute," *Physics-Uspekhi*, vol. 44, no. 8, p. 835, aug 2001. [Online]. Available: <https://dx.doi.org/10.1070/PU2001v044n08ABEH001068>
- [8] A. J. H. Donné, "The european roadmap towards fusion electricity," *Philosophical Transactions of the Royal Society A: Mathematical, Physical and Engineering Sciences*, vol. 377, no. 2141, p. 20170432, 2019. [Online]. Available: <https://royalsocietypublishing.org/doi/abs/10.1098/rsta.2017.0432>
- [9] EUROfusion, "The road to fusion energy," 2018. [Online]. Available: <https://euro-fusion.org/eurofusion/roadmap/#>
- [10] L. Artsimovich, "Tokamak devices," *Nuclear Fusion*, vol. 12, no. 2, pp. 215–252, mar 1972. [Online]. Available: <https://doi.org/10.1088/0029-5515/12/2/012>
- [11] Equipe TFR, "Tokamak plasma diagnostics," *Nuclear Fusion*, vol. 18, no. 5, pp. 647–731, may 1978. [Online]. Available: <https://doi.org/10.1088/0029-5515/18/5/004>
- [12] E. J. Strait, E. D. Fredrickson, J.-M. Moret, and M. Takechi, "Chapter 2: Magnetic diagnostics," *Fusion Science and Technology*, vol. 53, no. 2, pp. 304–334, 2008. [Online]. Available: <https://doi.org/10.13182/FST08-A1674>
- [13] J. Wesson, *Tokamaks; 4th ed.*, ser. International series of monographs on physics. Oxford: Oxford Univ. Press, 2011.
- [14] D. Gates, J. Menard, and R. Marsala, "Vessel eddy current measurement for the national spherical torus experiment," *Review of Scientific Instruments - REV SCI INSTR*, vol. 75, pp. 5090–5093, 12 2004.
- [15] J.-M. Moret, F. Buhlmann, D. Fasel, F. Hofmann, and G. Tonetti, "Magnetic measurements on the tcv tokamak," *Review of Scientific Instruments*, vol. 69, no. 6, pp. 2333–2348, 1998. [Online]. Available: <https://doi.org/10.1063/1.1148940>

- [16] V. D. Shafranov, "Determination of the parameters β_t and l_i in a tokamak for arbitrary shape of plasma pinch cross-section," *Plasma Physics*, vol. 13, no. 9, pp. 757–762, sep 1971. [Online]. Available: <https://doi.org/10.1088/0032-1028/13/9/006>
- [17] L. Giannone, R. Fischer, A. Kappatou, G. Tardini, M. Weiland, C. Angioni, E. Fable, M. Griener, R. McDermott, B. Sieglin, A. J. van Vuuren, R. Bilato, M. Dunne, A. Gude, A. Kallenbach, J. Kurz, M. Maraschek, D. Rittich, F. Ryter, P. Schneider, K. Schuhbeck, U. Stroth, H. Zohm, and the ASDEX Upgrade Team, "Measurements and modelling of diamagnetic flux in ASDEX upgrade," *Nuclear Fusion*, vol. 61, no. 6, p. 066021, may 2021. [Online]. Available: <https://doi.org/10.1088/1741-4326/abea56>
- [18] O. Barana, E. Joffrin, A. Murari, and F. Sartori, "Real-time determination of confinement parameters in jet," *Fusion Engineering and Design*, vol. 66-68, pp. 697–701, 2003, 22nd Symposium on Fusion Technology. [Online]. Available: <https://www.sciencedirect.com/science/article/pii/S0920379603003314>
- [19] L. Lao, H. S. John, R. Stambaugh, and W. Pfeiffer, "Separation of β_p and l_i in tokamaks of non-circular cross-section," *Nuclear Fusion*, vol. 25, no. 10, pp. 1421–1436, oct 1985. [Online]. Available: <https://doi.org/10.1088/0029-5515/25/10/004>
- [20] W. A. Cooper and A. J. Wootton, " β_p analysis for tokamak plasma with anisotropic pressure and mass flow," *Plasma Physics*, vol. 24, no. 9, pp. 1183–1185, sep 1982. [Online]. Available: <https://doi.org/10.1088/0032-1028/24/9/014>
- [21] E. Matveeva, J. Havlicek, A. Havranek, V. Yanovskiy, S. Gerasimov, V. Pustovitov, O. Hronova, and V. Weinzettl, "Toroidal and poloidal vessel currents during asymmetrical disruptions on compass," *46th EPS Conference on Plasma Physics, EPS 2019*, 2019. [Online]. Available: <https://www.scopus.com/inward/record.uri?eid=2-s2.0-85084022477&partnerID=40&md5=4a3b5eb91f925c66dacf484ed34b55fb>
- [22] G. Tonetti, J. P. Christiansen, and L. de Kock, "Measurement of the energy content of the jet tokamak plasma with a diamagnetic loop," *Review of Scientific Instruments*, vol. 57, no. 8, pp. 2087–2089, 1986. [Online]. Available: <https://doi.org/10.1063/1.1138747>
- [23] J. Gernhardt and F. Schneider, "Design and electronic compensation of a diamagnetic loop and its applications in the asdex tokamak," Max-Planck-Institut für Plasmaphysik, Tech. Rep., 1986.
- [24] B. Shen, B. Wan, and X. Zhang, "Diamagnetic measurement on ht-7 superconducting tokamak," *Fusion Engineering and Design*, vol. 70, no. 4, pp. 311–318, 2004. [Online]. Available: <https://www.sciencedirect.com/science/article/pii/S0920379604001218>
- [25] J.-M. Moret, F. Buhlmann, and G. Tonetti, "Fast single loop diamagnetic measurements on the tcv tokamak," *Review of Scientific Instruments*, vol. 74, no. 11, pp. 4634–4643, 2003. [Online]. Available: <https://doi.org/10.1063/1.1614856>
- [26] J. G. Bak, S. G. Lee, and E. M. Ka, "Diamagnetic loop for the first plasma in the kstar machine," *Review of Scientific Instruments*, vol. 79, no. 10, p. 10F118, 2008. [Online]. Available: <https://doi.org/10.1063/1.2956963>
- [27] L. A. Kojovic, R. Beresh *et al.*, "Practical aspects of rogowski coil applications to relaying," *IEEE PSRC special report*, vol. 9, 2010.
- [28] S. V. Mirnov, "A probe method for measuring the displacement of the current channel in cylindrical and toroidal discharge vessels," *Journal of Nuclear Energy. Part C, Plasma Physics, Accelerators, Thermonuclear Research*, vol. 7, no. 3, pp. 325–328, jan 1965. [Online]. Available: <https://doi.org/10.1088/0368-3281/7/3/112>
- [29] D. Testa, A. Corne, C. Jacq, T. Maeder, M. Toussaint, S. Antonioni, R. Chavan, S. Couturier, F. Dolizy, P. Lavanchy, J. Lister, X. Llobet, B. Marletaz, P. Marmillod, C. Moura, U. Siravo, M. Stoeck, L. Blondel, B. Ellenrieder, G. Farine, Y. Fournier, M. Garcin, A. Iantchenko, L. Perrone, L. Stipani, A. Tolio, and P. Windischhofer, "LTCC magnetic sensors at EPFL and TCV: Lessons learnt for ITER," *Fusion Engineering and Design*, vol. 146, pp. 1553–1558, 2019. [Online]. Available: <https://www.sciencedirect.com/science/article/pii/S0920379619303096>

- [30] D. Testa, "Manufacturing, installation, commissioning, and first results with the 3D low-temperature co-fired ceramic high-frequency magnetic sensors on the Tokamak à Configuration Variable," *Review of Scientific Instruments*, vol. 91, no. 8, p. 081401, 2020. [Online]. Available: <https://doi.org/10.1063/1.5115004>
- [31] A. Torres, K. Kovarik, T. Markovic, J. Adamek, I. Duran, R. Ellis, M. Jerab, J. Reboun, P. Turjanica, V. Weinzettl, and H. Fernandes, "Test bench for calibration of magnetic field sensor prototypes for COMPASS-U tokamak," *Fusion Engineering and Design*, vol. 168, p. 112467, 7 2021.
- [32] Y. Ding, N. Wang, B. Rao, X. Jin, Z. Chen, Q. Hu, H. Jin, W. Jin, J. Li, S. Xie, B. Yi, G. Zhuang, and Y. Pan, "Analytical compensation of axisymmetric equilibrium fluxes picked up by locked mode detectors in tokamaks," *Review of Scientific Instruments*, vol. 85, pp. 043502–043502, 04 2014.
- [33] T. Bolzonella, M. Cavinato, E. Gaio, L. Grando, A. Luchetta, G. Manduchi, G. Marchiori, L. Marrelli, R. Paccagnella, A. Soppelsa, and P. Zanca, "Feedback control of resistive wall modes by saddle coils in RFX-mod," *Fusion Engineering and Design*, vol. 82, no. 5, pp. 1064–1072, 2007, proceedings of the 24th Symposium on Fusion Technology. [Online]. Available: <https://www.sciencedirect.com/science/article/pii/S0920379607002414>
- [34] I. Duran, S. Entler, M. Kočan, M. Kohout, L. Viererbl, R. Mušálek, T. Chraska, and G. Vayakis, "Development of bismuth hall sensors for iter steady state magnetic diagnostics," *Fusion Engineering and Design*, vol. 123, 06 2017.
- [35] I. Ďuran, J. Stöckel, G. Mank, K. H. Finken, G. Fuchs, and G. V. Oost, "Measurements of magnetic field fluctuations using an array of Hall detectors on the TEXTOR tokamak," *Review of Scientific Instruments*, vol. 73, no. 10, pp. 3482–3489, 2002. [Online]. Available: <https://doi.org/10.1063/1.1502018>
- [36] S. Itoh, K. Sato, K. Nakamura, H. Zushi, M. Sakamoto, K. Hanada, E. Jotaki, K. Makino, S. Kawasaki, H. Nakashima, and N. Yoshida, "Recent progress on high performance steady state plasmas in the superconducting tokamak TRIAM-1m," *Nuclear Fusion*, vol. 39, no. 9Y, pp. 1257–1270, sep 1999. [Online]. Available: <https://doi.org/10.1088/0029-5515/39/9y/304>
- [37] M. Xue, B. Shen, D. Chen, Y. Wang, T. Shi, H. Wang, Y. Sun, J. Qian, H. Xiao, and B. Xiao, "Fiber-optic current sensor for plasma current on experimental advanced superconducting tokamak," *Fusion Engineering and Design*, vol. 140, pp. 11–15, 2019. [Online]. Available: <https://www.sciencedirect.com/science/article/pii/S092037961930078X>
- [38] M. Aerssens, A. Gusarov, B. Brichard, V. Massaut, P. Mégret, and M. Wuilpart, "Faraday effect based optical fiber current sensor for tokamaks," in *2011 2nd International Conference on Advancements in Nuclear Instrumentation, Measurement Methods and their Applications*, 2011, pp. 1–6.
- [39] Wuilpart, Marc, Leysen, Willem, Gusarov, Andrei, Moreau, Philippe, and Mégret, Patrice, "Measurement of plasma current in tokamaks using an optical fibre reflectometry technique," *EPJ Web Conf.*, vol. 170, p. 02009, 2018. [Online]. Available: <https://doi.org/10.1051/epjconf/201817002009>
- [40] F. M. Levinton, "The motional Stark effect: Overview and future development (invited)," *Review of Scientific Instruments*, vol. 70, no. 1, pp. 810–814, 01 1999. [Online]. Available: <https://doi.org/10.1063/1.1149316>
- [41] F. M. Levinton, R. J. Fonck, G. M. Gammel, R. Kaita, H. W. Kugel, E. T. Powell, and D. W. Roberts, "Magnetic field pitch-angle measurements in the PBX-M tokamak using the motional Stark effect," *Phys. Rev. Lett.*, vol. 63, pp. 2060–2063, Nov 1989. [Online]. Available: <https://link.aps.org/doi/10.1103/PhysRevLett.63.2060>
- [42] S. Gerasimov, P. Abreu, M. Baruzzo, V. Drozdov, A. Dvornova, J. Havlicek, T. Hender, O. Hronova, U. Kruezi, X. Li, T. Markovič, R. Pánek, G. Rubinacci, M. Tsalas, S. Ventre, F. Villone, and L. Zakharov, "JET and COMPASS asymmetrical disruptions," *Nuclear Fusion*, vol. 55, p. 113006, 9 2015. [Online]. Available: <https://iopscience.iop.org/article/10.1088/0029-5515/55/11/113006>

- [43] V. Riccardo, S. Walker, and P. Noll, "Parametric analysis of asymmetric vertical displacement events at jet," *Plasma Physics and Controlled Fusion*, vol. 42, pp. 29–40, 1 2000. [Online]. Available: <https://iopscience.iop.org/article/10.1088/0741-3335/42/1/304>
- [44] V. Riccardo, G. Arnoux, P. Beaumont, S. Hacquin, J. Hobirk, D. Howell, A. Huber, E. Joffrin, R. Koslowski, N. Lam, H. Leggate, E. Rachlew, G. Sergienko, A. Stephen, T. Todd, M. Zerbini, R. Delogu, L. Grando, D. Marcuzzi, S. Peruzzo, N. Pomaro, and P. Sonato, "Progress in understanding halo current at JET," *Nuclear Fusion*, vol. 49, p. 055012, 5 2009. [Online]. Available: <https://iopscience.iop.org/article/10.1088/0029-5515/49/5/055012>
- [45] J. Kates-Harbeck, A. Svyatkovskiy, and W. Tang, "Predicting disruptive instabilities in controlled fusion plasmas through deep learning," *Nature 2019 568:7753*, vol. 568, pp. 526–531, 4 2019. [Online]. Available: <https://www.nature.com/articles/s41586-019-1116-4>
- [46] B. H. Guo, D. L. Chen, B. Shen, C. Rea, R. S. Granetz, L. Zeng, W. H. Hu, J. P. Qian, Y. W. Sun, and B. J. Xiao, "Disruption prediction on EAST tokamak using a deep learning algorithm," *Plasma Physics and Controlled Fusion*, vol. 63, p. 115007, 11 2021. [Online]. Available: <https://iopscience.iop.org/article/10.1088/1361-6587/ac228b>
- [47] J. Vega, A. Murari, S. Dormido-Canto, G. A. Rattá, M. Gelfusa, and J. Mailloux, "Disruption prediction with artificial intelligence techniques in tokamak plasmas," *Nature Physics 2022 18:7*, vol. 18, pp. 741–750, 6 2022. [Online]. Available: <https://www.nature.com/articles/s41567-022-01602-2>
- [48] S. Sabbagh, J. Berkery, Y. Park, J. Ahn, Y. Jiang, J. Riquezes, J. Butt, J. BIALEK, J. Bak, M. CHOI *et al.*, "Tokamak disruption event characterization and forecasting research and expansion to real-time application," in *Proc. IAEA Fusion Energy Conf*, 2020.
- [49] V. Pustovitov, "General approach to the problem of disruption forces in tokamaks," *Nuclear Fusion*, vol. 55, p. 113032, 9 2015. [Online]. Available: <https://iopscience.iop.org/article/10.1088/0029-5515/55/11/113032>
- [50] J. P. Freidberg, *Plasma Physics and Fusion Energy*. Cambridge University Press, 2007.
- [51] L. Lao, H. S. John, R. Stambaugh, A. Kellman, and W. Pfeiffer, "Reconstruction of current profile parameters and plasma shapes in tokamaks," *Nuclear Fusion*, vol. 25, no. 11, pp. 1611–1622, nov 1985. [Online]. Available: <https://doi.org/10.1088/0029-5515/25/11/007>
- [52] J. Ferron, M. Walker, L. Lao, H. S. John, D. Humphreys, and J. Leuer, "Real time equilibrium reconstruction for tokamak discharge control," *Nuclear Fusion*, vol. 38, pp. 1055–1066, 7 1998. [Online]. Available: <https://iopscience.iop.org/article/10.1088/0029-5515/38/7/308>
- [53] Y. Jiang, S. Sabbagh, Y. Park, al, X. N. Yue, B. J. Xiao, Z. P. Luo, Y. Huang, A. Mele, Z. Luo, M. Mattei, A. Pironti, B. Xiao, and Q. Yuan, "Implementation of a kalman filter-based eddy current estimator for the p-efit magnetic equilibrium reconstruction code," *Nuclear Fusion*, vol. 62, p. 086010, 6 2022. [Online]. Available: <https://iopscience.iop.org/article/10.1088/1741-4326/ac6ef2https://iopscience.iop.org/article/10.1088/1741-4326/ac6ef2/meta>
- [54] B. Faugeras, "An overview of the numerical methods for tokamak plasma equilibrium computation implemented in the nice code," *Fusion Engineering and Design*, vol. 160, p. 112020, 2020. [Online]. Available: <https://www.sciencedirect.com/science/article/pii/S0920379620305688>
- [55] J.-M. Moret, B. Duval, H. Le, S. Coda, F. Felici, and H. Reimerdes, "Tokamak equilibrium reconstruction code liuqe and its real time implementation," *Fusion Engineering and Design*, vol. 91, pp. 1–15, 2015. [Online]. Available: <https://www.sciencedirect.com/science/article/pii/S0920379614005973>
- [56] L. C. Appel and I. Lupelli, "Equilibrium reconstruction in an iron core tokamak using a deterministic magnetisation model," *Computer Physics Communications*, vol. 223, pp. 1–17, 2 2018.

- [57] W. Treutterer, K. Behler, L. Giannone, N. Hicks, A. Manini, M. Maraschek, G. Raupp, M. Reich, A. Sips, J. Stober, and W. Suttrop, "Real-time diagnostics at asdex upgrade—integration with mhd feedback control," *Fusion Engineering and Design*, vol. 83, no. 2, pp. 300–303, 2008, proceedings of the 6th IAEA Technical Meeting on Control, Data Acquisition, and Remote Participation for Fusion Research. [Online]. Available: <https://www.sciencedirect.com/science/article/pii/S0920379607004401>
- [58] L. Lao, J. Ferron, R. Groebner, W. Howl, H. S. John, E. Strait, and T. Taylor, "Equilibrium analysis of current profiles in tokamaks," *Nuclear Fusion*, vol. 30, pp. 1035–1049, 6 1990. [Online]. Available: <https://iopscience.iop.org/article/10.1088/0029-5515/30/6/006>
- [59] J. Christiansen, J. Callen, J. Ellis, and R. Granetz, "Determination of current distribution in JET from soft x-ray measurements," *Nuclear Fusion*, vol. 29, no. 5, pp. 703–711, may 1989. [Online]. Available: <https://doi.org/10.1088/0029-5515/29/5/001>
- [60] V. Mukhovatov and V. Shafranov, "Plasma equilibrium in a tokamak," *Nuclear Fusion*, vol. 11, no. 6, p. 605, dec 1971. [Online]. Available: <https://dx.doi.org/10.1088/0029-5515/11/6/005>
- [61] J. Lister, Y. Martin, T. Fukuda, R. Yoshino, and V. Mertens, "The control of modern tokamaks," in *Proceedings of the International Conference on Accelerator and Large Experimental Physics Control Systems, Trieste, Italy*, 1999.
- [62] D. F. Valcárcel, A. Neto, I. S. Carvalho, B. B. Carvalho, H. Fernandes, J. Sousa, F. Janky, J. Havlicek, R. Beno, J. Horacek, M. Hron, and R. Pánek, "The compass tokamak plasma control software performance," *IEEE Transactions on Nuclear Science*, 2011.
- [63] G. D. Tommasi, "Plasma magnetic control in tokamak devices," *Journal of Fusion Energy*, vol. 38, pp. 406–436, 8 2019. [Online]. Available: <https://link.springer.com/article/10.1007/s10894-018-0162-5>
- [64] T. Hender, J. Wesley, J. Bialek, A. Bondeson, A. Boozer, R. Buttery, A. Garofalo, T. Goodman, R. Granetz, Y. Gribov, O. Gruber, M. Gryaznevich, G. Giruzzi, S. Günter, N. Hayashi, P. Helander, C. Hegna, D. Howell, D. Humphreys, G. Huysmans, A. Hyatt, A. Isayama, S. Jardin, Y. Kawano, A. Kellman, C. Kessel, H. Koslowski, R. L. Haye, E. Lazzaro, Y. Liu, V. Lukash, J. Manickam, S. Medvedev, V. Mertens, S. Mirnov, Y. Nakamura, G. Navratil, M. Okabayashi, T. Ozeki, R. Paccagnella, G. Pautasso, F. Porcelli, V. Pustovitov, V. Riccardo, M. Sato, O. Sauter, M. Schaffer, M. Shimada, P. Sonato, E. Strait, M. Sugihara, M. Takechi, A. Turnbull, E. Westerhof, D. Whyte, R. Yoshino, H. Zohm, D. the ITPA MHD, and M. Group, "Chapter 3: Mhd stability, operational limits and disruptions," *Nuclear Fusion*, vol. 47, pp. S128–S202, 6 2007. [Online]. Available: <https://iopscience.iop.org/article/10.1088/0029-5515/47/6/S03>
- [65] A. Fasoli, D. Testa, S. Sharapov, H. L. Berk, B. Breizman, A. Gondhalekar, R. F. Heeter, M. Mantsinen, and contributors to the EFDA-JET Workprogramme, "MHD spectroscopy," *Plasma Physics and Controlled Fusion*, vol. 44, pp. B159–B172, 12 2002. [Online]. Available: <https://iopscience.iop.org/article/10.1088/0741-3335/44/12B/312>
- [66] S. Sharapov, B. Alper, H. Berk, D. Borba, B. Breizman, C. Challis, I. Classen, E. Edlund, J. Eriksson, A. Fasoli, E. Fredrickson, G. Fu, M. Garcia-Munoz, T. Gassner, K. Ghantous, V. Goloborodko, N. Gorelenkov, M. Gryaznevich, S. Hacquin, W. Heidbrink, C. Hellesen, V. Kiptily, G. Kramer, P. Lauber, M. Lilley, M. Lisak, F. Nabais, R. Nazikian, R. Nyqvist, M. Osakabe, C. P. von Thun, S. Pinches, M. Podesta, M. Porkolab, K. Shinohara, K. Schoepf, Y. Todo, K. Toi, M. V. Zeeland, I. Voitsekhovich, R. White, and V. Yavorskij, "Energetic particle instabilities in fusion plasmas," *Nuclear Fusion*, vol. 53, p. 104022, 10 2013. [Online]. Available: <https://iopscience.iop.org/article/10.1088/0029-5515/53/10/104022>
- [67] M. F. F. Nave, D. Borba, R. Galvão, S. Hacquin, B. Alper, C. Challis, S. Gerasimov, N. Hawkes, J. Mailloux, S. Sharapov, C. Boswell, M. Brix, E. Joffrin, E. de la Luna, and P. Smeulders, "On the use of MHD mode analysis as a technique for determination of q-profiles in JET plasmas," *Review of Scientific Instruments*, vol. 75, pp. 4274–4277, 10 2004. [Online]. Available: <http://aip.scitation.org/doi/10.1063/1.1791333>

- [68] T. Hender, D. Howell, R. Buttery, O. Sauter, F. Sartori, R. L. Haye, A. Hyatt, C. Petty, J. E. contributors, and the DIII-D team, "Comparison of $m = 2$, $n = 1$ neo-classical tearing mode limits in JET and DIII-D," *Nuclear Fusion*, vol. 44, pp. 788–794, 7 2004. [Online]. Available: <https://iopscience.iop.org/article/10.1088/0029-5515/44/7/010>
- [69] M. J. Hole and L. C. Appel, "Fourier decomposition of magnetic perturbations in toroidal plasmas using singular value decomposition," *Plasma Physics and Controlled Fusion*, vol. 49, pp. 1971–1988, 12 2007. [Online]. Available: <https://iopscience.iop.org/article/10.1088/0741-3335/49/12/002>
- [70] S. Santoso, E. J. Powers, R. D. Bengtson, and A. Ouroua, "Time-series analysis of nonstationary plasma fluctuations using wavelet transforms," *Review of Scientific Instruments*, vol. 68, pp. 898–901, 1 1997. [Online]. Available: <http://aip.scitation.org/doi/10.1063/1.1147715>
- [71] F. Taylor and A. Williams, *Electronic Filter Design Handbook, Fourth Edition*. McGraw-Hill Education, 2006. [Online]. Available: <https://books.google.cz/books?id=2CBGAQAIAAJ>
- [72] F. Taylor, *Digital Filters: Principles and Applications with MATLAB*, ser. IEEE Series on Digital & Mobile Communication. Wiley, 2011. [Online]. Available: https://books.google.cz/books?id=GBkE_W3eOxIC
- [73] S. Butterworth, "On the theory of filter amplifiers," *Experimental Wireless and the Wireless Engineer*, vol. 7, pp. 536–541, 1939.
- [74] C. Shannon, "Communication in the presence of noise," *Proceedings of the IRE*, vol. 37, no. 1, pp. 10–21, 1949.
- [75] E. T. Whittaker, "Xviii.—on the functions which are represented by the expansions of the interpolation-theory," *Proceedings of the Royal Society of Edinburgh*, vol. 35, p. 181–194, 1915.
- [76] Omegatron, via Wikimedia Commons, 2017, cC BY-SA 3.0. [Online]. Available: <https://commons.wikimedia.org/w/index.php?curid=1943024>
- [77] —, via Wikimedia Commons, 2017, cC BY-SA 3.0. [Online]. Available: <https://commons.wikimedia.org/w/index.php?curid=1960030>
- [78] S. P. Gerhardt, K. Erickson, R. Kaita, J. Lawson, R. Mozulay, D. Mueller, W. Que, N. Rahman, H. Schneider, G. Smalley, and K. Tresemer, "Magnetic diagnostics for equilibrium reconstruction and realtime plasma control in NSTX-Upgrade)," *Review of Scientific Instruments*, vol. 85, p. 11E807, 7 2014. [Online]. Available: <https://aip.scitation.org/doi/abs/10.1063/1.4889781>
- [79] P. Moreau, A. Le-Luyer, P. Spuig, P. Malard, F. Saint-Laurent, J. F. Artaud, J. Morales, B. Faugeras, H. Heumann, B. Cantone, M. Moreau, C. Brun, R. Nouailletas, E. Nardon, B. Santraine, A. Berne, P. Kumari, and S. Belsare, "The new magnetic diagnostics in the west tokamak," *Review of Scientific Instruments*, vol. 89, p. 10J109, 7 2018. [Online]. Available: <https://aip.scitation.org/doi/abs/10.1063/1.5036537>
- [80] J. G. Bak, H. S. Kim, S. H. Hahn, J. H. Kim, and J. W. Lee, "Evaluation of plasma current quench time using a discrete rogowski coil in the kstar tokamak," *Fusion Engineering and Design*, vol. 185, p. 113324, 12 2022. [Online]. Available: <https://linkinghub.elsevier.com/retrieve/pii/S0920379622003155>
- [81] S. G. Lee and J. G. Bak, "Fabrication details, calibrations, and installation activities of magnetic diagnostics for korea superconducting tokamak advanced research," *Review of Scientific Instruments*, vol. 77, p. 10E306, 9 2006. [Online]. Available: <https://aip.scitation.org/doi/abs/10.1063/1.2227437>
- [82] P. Moreau, A. Le-Luyer, P. Malard, P. Pastor, F. Saint-Laurent, P. Spuig, J. Lister, M. Tous-saint, P. Marmillod, D. Testa, S. Peruzzo, J. Knaster, G. Vayakis, S. Hughes, and K. M. Patel, "Prototyping and testing of the continuous external rogowski ITER magnetic sensor," *Fusion Engineering and Design*, vol. 88, pp. 1165–1169, 10 2013.

- [83] P. Moreau, P. Spuig, A. Le-Luyer, P. Malard, B. Cantone, P. Pastor, F. Saint-Laurent, G. Vayakis, D. Delhom, S. Arshad, J. Lister, M. Toussaint, P. Marmillod, D. Testa, C. Schlatter, and S. Peruzzo, "Development of the ITER continuous external rogowski: From conceptual design to final design," *Fusion Engineering and Design*, vol. 96-97, pp. 878–881, 10 2015.
- [84] E. J. Strait, "Magnetic diagnostic system of the DIII-D tokamak," *Review of Scientific Instruments*, vol. 77, no. 2, p. 023502, 2006. [Online]. Available: <https://doi.org/10.1063/1.2166493>
- [85] G. Vayakis and C. Walker, "Magnetic diagnostics for ITER/BPX plasmas (invited)," *Review of Scientific Instruments*, vol. 74, no. 4, pp. 2409–2417, 2003. [Online]. Available: <https://doi.org/10.1063/1.1534388>
- [86] H. Takahashi, S. Sakakibara, Y. Kubota, and H. Yamada, "Magnetic probe construction using thick-film technology," *Review of Scientific Instruments*, vol. 72, no. 8, pp. 3249–3259, 2001. [Online]. Available: <https://doi.org/10.1063/1.1384431>
- [87] M. Adaikkan, Y. Ma, U. Walach, M. Bochard, F. Bechtold, G. Vayakis, M. Walsh, M. P. C. Lino, and G. Counsell, "Producing high quality Itcc sensors for iter in-vessel magnetic diagnostics," *Fusion Engineering and Design*, vol. 184, p. 113316, 2022. [Online]. Available: <https://www.sciencedirect.com/science/article/pii/S0920379622003088>
- [88] Y. Jeon, Y. Nam, S. W. Yoon, and J. Bak, "Equilibrium reconstruction of KSTAR plasmas with large uncertainty on magnetics," in *FEC 2010: 23. IAEA Fusion Energy Conference*, 2010.
- [89] L. Giannone, M. Reich, M. Maraschek, E. Poli, C. Rapson, L. Barrera, R. McDermott, A. Mlynek, Q. Ruan, W. Treutterer, L. Wenzel, A. Bock, G. Conway, R. Fischer, J. Fuchs, K. Lackner, P. McCarthy, R. Preuss, M. Rampp, K. Schuhbeck, J. Stober, and H. Zohm, "A data acquisition system for real-time magnetic equilibrium reconstruction on asdex upgrade and its application to ntm stabilization experiments," *Fusion Engineering and Design*, vol. 88, no. 12, pp. 3299–3311, 2013. [Online]. Available: <https://www.sciencedirect.com/science/article/pii/S0920379613006844>
- [90] P. J. M. Carthy, "Identification of edge-localized moments of the current density profile in a tokamak equilibrium from external magnetic measurements," *Plasma Physics and Controlled Fusion*, vol. 54, p. 015010, 1 2012. [Online]. Available: <https://iopscience.iop.org/article/10.1088/0741-3335/54/1/015010>
- [91] J. Blum, C. Boulbe, and B. Faugeras, "Reconstruction of the equilibrium of the plasma in a tokamak and identification of the current density profile in real time," *Journal of Computational Physics*, vol. 231, pp. 960–980, 2 2012.
- [92] J. W. Berkery, S. A. Sabbagh, L. Kogan, D. Ryan, J. M. Bialek, Y. Jiang, D. J. Battaglia, S. Gibson, and C. Ham, "Kinetic equilibrium reconstructions of plasmas in the MAST database and preparation for reconstruction of the first plasmas in MAST upgrade," *Plasma Physics and Controlled Fusion*, vol. 63, p. 055014, 5 2021. [Online]. Available: <https://iopscience.iop.org/article/10.1088/1361-6587/abf230>
- [93] M. Boyer, D. Battaglia, D. Mueller, N. Eidietis, K. Erickson, J. Ferron, D. Gates, S. Gerhardt, R. Johnson, E. Kolemen, J. Menard, C. Myers, S. Sabbagh, F. Scotti, and P. Vail, "Plasma boundary shape control and real-time equilibrium reconstruction on NSTX-U," *Nuclear Fusion*, vol. 58, p. 036016, 3 2018. [Online]. Available: <https://iopscience.iop.org/article/10.1088/1741-4326/aaa4d0>
- [94] M. Ferrara, I. Hutchinson, and S. Wolfe, "Plasma inductance and stability metrics on Alcator C-Mod," *Nuclear Fusion*, vol. 48, p. 065002, 6 2008. [Online]. Available: <https://iopscience.iop.org/article/10.1088/0029-5515/48/6/065002>
- [95] M. Hron, J. Adánek, J. Cavalier, R. Dejarnac, O. Ficker, O. Grover, J. Horáček, M. Komm, E. Macušová, E. Matveeva, R. Pánek, M. Peterka, J. Seidl, D. Tskhakaya, V. Yanovskiy, F. Artola, S. Atikukke, P. Bartoň, A. Bencze, M. Berta, P. Bílková, W. Bin, K. Bogár, O. Bogár, P. Böhm, I. Borodkina, S. Brezinsek, F. Brochard, P. Buratti, J. Čaloud, A. Casolari, C. Castaldo, J. Čečrdle, J. Čeřovský, D. Cipciar, A. Devitre, M. Dimitrova, I. Đuran, S. Entler, M. Farník,

- H. Fernandes, D. Fridrich, S. Fuková, E. Gauthier, J. Gerardin, M. Gobbin, G. Grenfell, Y. Gribov, M. Grof, J. Gunn, P. Háček, J. Havlíček, A. Havránek, C. Hidalgo, K. Hromasová, O. Hronova, M. Iafrazi, M. Imříšek, N. Iernia, F. Jaulmes, M. Jeřáb, M. Jirsa, P. Junek, A. Kallenbach, O. Kovanda, K. Kovařík, J. Krbec, L. Kripner, L. Krlín, P. Kulhánek, M. Lehnen, N. Lemoine, X. Litaudon, Y. Liu, N. Logan, T. Loarer, A. Loarte, P. Lourenco, S. Lukes, P. Mácha, M. Rabinski, A. M. Roldan, T. Markovič, J. Matějček, G. Mazzitelli, J. Mlynář, I. Mysiura, F. Napoli, D. Naydenkova, J.-K. Park, N. Patel, P. Pavlo, R. Pitts, A. Podolník, M. Poradzinski, J. Preinhaelter, A. Prishvitsin, D. Refy, R. Roccella, D. Šesták, O. Shyshkin, V. Škvára, M. Šos, M. Spolaore, J. Stöckel, J. Svoboda, M. Tomeš, A. Torres, P. Turjanica, G. Tynan, M. Valovič, G. V. Oost, M. Varavin, J. Varju, P. Veis, M. Vilemova, F. Villone, P. Vondráček, V. Weinzettl, F. Žáček, G. Zadviitskiy, J. Zajac, D. Zaloga, J. Zebrowski, and S. Zoletnik, “Overview of the compass results,” *Nuclear Fusion*, vol. 62, p. 042021, 4 2022. [Online]. Available: <https://iopscience.iop.org/article/10.1088/1741-4326/ac301f>
- [96] D. Terranova, L. Marrelli, J. Hanson, S. Hirshman, M. Cianciosa, and P. Franz, “Helical equilibrium reconstruction with V3FIT in the RFX-mod reversed field pinch,” *Nuclear Fusion*, vol. 53, p. 113014, 11 2013. [Online]. Available: <https://iopscience.iop.org/article/10.1088/0029-5515/53/11/113014>
- [97] R. Santos, R. Coelho, P. Rodrigues, B. Faugas, H. Fernandes, B. B. Carvalho, D. Corona, H. Figueiredo, and H. Alves, “Plasma boundary reconstruction in ISTTOK using magnetic diagnostic data,” *Journal of Instrumentation*, vol. 14, no. 09, pp. C09019–C09019, sep 2019. [Online]. Available: <https://doi.org/10.1088/1748-0221/14/09/c09019>
- [98] O. Meneghini and L. Lao, “Integrated modeling of tokamak experiments with OMFIT,” *Plasma and Fusion Research*, vol. 8, pp. 2 403 009–2 403 009, 2013.
- [99] O. Meneghini, S. Smith, L. Lao, O. Izacard, Q. Ren, J. Park, J. Candy, Z. Wang, C. Luna, V. Izzo, B. Grierson, P. Snyder, C. Holland, J. Penna, G. Lu, P. Raum, A. McCubbin, D. Orlov, E. Belli, N. Ferraro, R. Prater, T. Osborne, A. Turnbull, and G. Staebler, “Integrated modeling applications for tokamak experiments with OMFIT,” *Nuclear Fusion*, vol. 55, p. 083008, 8 2015. [Online]. Available: <https://iopscience.iop.org/article/10.1088/0029-5515/55/8/083008>
- [100] B. Faugas, J. Blum, and C. Boulbe, “First equilibrium reconstruction for ITER with the code NICE,” *Journal of Instrumentation*, vol. 17, p. C02024, 2 2022. [Online]. Available: <https://iopscience.iop.org/article/10.1088/1748-0221/17/02/C02024>
- [101] J. Blum, C. Boulbe, and B. Faugas, “Equilibrium reconstruction for iter,” in *International Conference on Fusion Reactor Diagnostics - ICFRD2021*, 11 2021.
- [102] L. Lao, K. Burrell, N. Ferraro, B. Grierson, Y. Huang, J. Kinsey, K. Li, O. Meneghini, G. Trevisan, and B. Xiao, “Recent advances in equilibrium reconstruction for fusion data analysis and plasma control and prospect for iter applications,” in *3rd IAEA Technical Meeting on Fusion Data Processing, Validation and Analysis*, 2019.
- [103] A. Piccione, J. W. Berkery, S. A. Sabbagh, and Y. Andreopoulos, “Physics-guided machine learning approaches to predict the ideal stability properties of fusion plasmas,” *Nuclear Fusion*, vol. 60, 2020.
- [104] R. Albanese, R. Ambrosino, G. Calabr’o, A. Castaldo, F. Crisanti, G. D. Tommasi, L. Liu, Z. P. Luo, A. Mele, A. Pironti, B. J. Xiao, and Q. P. Yuan, “A MIMO architecture for integrated control of plasma shape and flux expansion for the EAST tokamak,” *2016 IEEE Conference on Control Applications, CCA 2016*, pp. 611–616, 10 2016.
- [105] G. De Tommasi, S. Galeani, S. Jachmich, E. Joffrin, M. Lennholm, P. Lomas, A. Neto, F. Maviglia, P. McCullen, A. Pironti, F. Rimini, A. Sips, G. Varano, R. Vitelli, and L. Zaccarian, “First experimental results with the current limit avoidance system at the jet tokamak,” *Fusion Engineering and Design*, vol. 88, no. 5, pp. 400–407, 2013. [Online]. Available: <https://www.sciencedirect.com/science/article/pii/S0920379613003980>
- [106] R. Albanese, R. Ambrosino, A. Castaldo, G. D. Tommasi, Z. Luo, A. Mele, A. Pironti, B. Xiao, and Q. Yuan, “ITER-like vertical stabilization system for the east tokamak,” *Nuclear Fusion*,

- vol. 57, p. 086039, 8 2017. [Online]. Available: <https://iopscience.iop.org/article/10.1088/1741-4326/aa7a78>
- [107] Y. H. Wang, Y. Huang, Q. P. Yuan, Z. P. Luo, and B. J. Xiao, "First implementation of plasma shape GAP control method in EAST," *Fusion Engineering and Design*, vol. 142, pp. 1–5, 5 2019.
- [108] D. Corona, N. Cruz, G. D. Tommasi, H. Fernandes, E. Joffrin, M. Mattei, A. Mele, Y. Miyata, A. Pironti, T. Suzuki, H. Urano, and F. Villone, "Plasma shape control assessment for JT-60SA using the CREATE tools," *Fusion Engineering and Design*, vol. 146, pp. 1773–1777, 9 2019.
- [109] S. Inoue, Y. Miyata, H. Urano, and T. Suzuki, "Development of jt-60sa equilibrium controller with an advanced iso-flux control scheme in the presence of large eddy currents and voltage saturation of power supplies," *Nuclear Fusion*, vol. 61, p. 096009, 9 2021. [Online]. Available: <https://iopscience.iop.org/article/10.1088/1741-4326/ac1260>
- [110] J. Degrave, F. Felici, J. Buchli, M. Neunert, B. Tracey, F. Carpanese, T. Ewalds, R. Hafner, A. Abdolmaleki, D. Casas, C. Donner, L. Fritz, C. Galperti, A. Huber, J. Keeling, M. Tsimpoukelli, J. Kay, A. Merle, J.-M. Moret, and M. Riedmiller, "Magnetic control of tokamak plasmas through deep reinforcement learning," *Nature*, vol. 602, pp. 414–419, 02 2022.
- [111] P. Spuig, P. Defrasne, G. Martin, M. Moreau, P. Moreau, and F. Saint-Laurent, "An analog integrator for thousand second long pulses in tore supra," *Fusion Engineering and Design*, vol. 66–68, pp. 953–957, 2003, 22nd Symposium on Fusion Technology. [Online]. Available: <http://www.sciencedirect.com/science/article/pii/S092037960300382X>
- [112] J. G. Bak, S. G. Lee, D. Son, and E. M. Ga, "Analog integrator for the korea superconducting tokamak advanced research magnetic diagnostics," *Review of Scientific Instruments*, vol. 78, p. 043504, 2007. [Online]. Available: <http://scitation.aip.org/content/aip/journal/rsi/78/4/10.1063/1.2721405>
- [113] P. Spuig, P. Kumari, M. Moreau, P. Moreau, A. Le-luyer, and P. Malard, "Enhanced integrators for WEST magnetic diagnostics," *Fusion Engineering and Design*, vol. 96–97, pp. 966–969, 10 2015. [Online]. Available: <https://www.sciencedirect.com/science/article/pii/S0920379615300788>
- [114] E. J. Strait, J. D. Broesch, R. T. Snider, and M. L. Walker, "A hybrid digital–analog long pulse integrator," *Review of Scientific Instruments*, vol. 68, pp. 381–384, 1997. [Online]. Available: <http://dx.doi.org/10.1063/1.1147835>
- [115] A. Werner, "W7-x magnetic diagnostics: Performance of the digital integrator," *Review of Scientific Instruments*, vol. 77, p. 10E307, 2006. [Online]. Available: <http://dx.doi.org/10.1063/1.2220073>
- [116] B. B. Carvalho, A. Batista, M. Zilker, K. Rahbarnia, A. Werner, C. Team, and E. Association, "Design, implementation and commissioning of atca based high-speed multichannel data acquisition systems for magnetic diagnostics in w7-x," in *11th IAEA Technical Meeting on Control, Data Acquisition and Remote Participation for Fusion Research, Greifswald, Germany, 2017*.
- [117] D. Corona, N. Cruz, J. J. E. Herrera, H. Figueiredo, B. B. Carvalho, I. S. Carvalho, H. Alves, and H. Fernandes, "Design and simulation of isttok real-time magnetic multiple-input multiple-output control," *IEEE Transactions on Plasma Science*, vol. 46, pp. 2362–2369, 2018.
- [118] A. J. Batista, L. Capella, A. Neto, S. Hall, G. Naylor, A. Stephen, J. Sousa, B. Carvalho, F. Sartori, R. Campagnolo, I. Bas, B. Goncalves, S. Arshad, G. Vayakis, S. Simrock, and L. Zabeo, "F4e prototype of a chopper digital integrator for the iter magnetics," *Fusion Engineering and Design*, vol. 123, pp. 1025–1028, 2017, proceedings of the 29th Symposium on Fusion Technology (SOFT-29) Prague, Czech Republic, September 5-9, 2016. [Online]. Available: <https://www.sciencedirect.com/science/article/pii/S0920379617301072>
- [119] A. J. Batista, G. Naylor, L. Capellà, A. Neto, A. Stephen, N. Petrella, S. Hall, J. Sousa, B. Carvalho, F. Sartori, R. Campagnolo, I. Bas, B. Gonçalves, S. Arshad, G. Vayakis, S. Simrock, and L. Zabeo, "Testing results of chopper based integrator prototypes for the iter

- magnetics," *Fusion Engineering and Design*, vol. 128, pp. 193–197, 2018. [Online]. Available: <https://www.sciencedirect.com/science/article/pii/S0920379618300905>
- [120] R. Panek, O. Bilyková, V. Fuchs, M. Hron, P. Chraska, P. Pavlo, J. Stockel, J. Urban, V. Weinzettl, J. Zajac, and F. Žáček, "Reinstallation of the compass-d tokamak in ipp ascr," *Czechoslovak Journal of Physics*, vol. 56, pp. B125–B137, 10 2006.
- [121] P. Vondracek, R. Panek, M. Hron, J. Havlicek, V. Weinzettl, T. Todd, D. Tskhakaya, G. Cunningham, P. Hacek, J. Hromadka, P. Junek, J. Krbec, N. Patel, D. Sestak, J. Varju, J. Adamek, M. Balazsova, V. Balner, P. Barton, J. Bielecki, P. Bilkova, J. Błocki, D. Bocian, K. Bogar, O. Bogar, P. Boocz, I. Borodkina, A. Brooks, P. Bohm, J. Burant, A. Casolari, J. Cavalier, P. Chappuis, R. Dejarnac, M. Dimitrova, M. Dudak, I. Duran, R. Ellis, S. Entler, J. Fang, M. Farnik, O. Ficker, D. Fridrich, S. Fukova, J. Gerardin, I. Hanak, A. Havranek, A. Herrmann, J. Horacek, O. Hronova, M. Imrisek, N. Isernia, F. Jaulmes, M. Jerab, V. Kindl, M. Komm, K. Kovarik, M. Kral, L. Kripner, E. Macusova, T. Majer, T. Markovic, E. Matveeva, K. Mikszuta-Michalik, M. Mohelnik, I. Mysiura, D. Naydenkova, I. Nemeec, R. Ortwein, K. Patocka, M. Peterka, A. Podolnik, F. Prochazka, J. Prevratil, J. Reboun, V. Scalera, M. Scholz, J. Svoboda, J. Swierblewski, M. Sos, M. Tadros, P. Titus, M. Tomes, A. Torres, G. Tracz, P. Turjanica, M. Varavin, V. Veselovsky, F. Villone, P. Wąchal, V. Yanovskiy, G. Zaditskiy, J. Zajac, A. Zak, D. Zaloga, J. Zeld, and H. Zhang, "Preliminary design of the compass upgrade tokamak," *Fusion Engineering and Design*, vol. 169, p. 112490, 2021. [Online]. Available: <https://www.sciencedirect.com/science/article/pii/S0920379621002660>
- [122] IPP, "Compass upgrade," Official webpage, Jan. 2023. [Online]. Available: https://www.ipp.cas.cz/vedecka_struktura_ufp/tokamak/compass_u/
- [123] T. Haertl, C. Bachmann, E. Diegele, and G. Federici, "Rationale for the selection of the operating temperature of the DEMO vacuum vessel," *Fusion Engineering and Design*, vol. 146, pp. 1096–1099, 2019, sl:SOFT-30. [Online]. Available: <https://www.sciencedirect.com/science/article/pii/S0920379619301863>
- [124] F. Romanelli, P. Barabaschi, D. Borba, G. Federici, L. Horton, R. Neu, D. Stork, and H. Zohm, *Fusion Electricity: A roadmap to the realization of fusion energy*. Efd, 2012.
- [125] G. Mazzitelli, M. Apicella, D. Frigione, G. Maddaluno, M. Marinucci, C. Mazzotta, V. P. Ridolfini, M. Romanelli, G. Szepesi, and O. Tudisco, "Ftu results with a liquid lithium limiter," *Nuclear Fusion*, vol. 51, p. 073006, 7 2011. [Online]. Available: <https://iopscience.iop.org/article/10.1088/0029-5515/51/7/073006>
- [126] R. Dejarnac, J. Horacek, M. Hron, M. Jerab, J. Adamek, S. Atikukke, P. Barton, J. Cavalier, J. Cecrdle, M. Dimitrova, E. Gauthier, M. Iafrati, M. Imrisek, A. M. Roldan, G. Mazzitelli, D. Naydenkova, A. Prishvitsyn, M. Tomes, D. Tskhakaya, G. V. Oost, J. Varju, P. Veis, A. Vertkov, P. Vondracek, and V. Weinzettl, "Overview of power exhaust experiments in the compass divertor with liquid metals," *Nuclear Materials and Energy*, vol. 25, p. 100801, 12 2020.
- [127] S. Roccella, G. Dose, R. D. Luca, M. Iafrati, A. Mancini, and G. Mazzitelli, "Cps based liquid metal divertor target for eu-demo," *Journal of Fusion Energy*, vol. 39, 2020. [Online]. Available: <https://doi.org/10.1007/s10894-020-00263-4>
- [128] P. Rindt, J. L. van den Eijnden, T. W. Morgan, and N. J. L. Cardozo, "Conceptual design of a liquid-metal divertor for the European DEMO," *Fusion Engineering and Design*, vol. 173, p. 112812, 12 2021.
- [129] F. Waelbroeck and Textor Team, "Behaviour of plasma discharges in TEXTOR with warm surrounding walls and preliminary observations made after a carburization of the surface," *Journal of Nuclear Materials*, vol. 121, pp. 378–384, 5 1984.
- [130] G. F. Matthews, M. Beurskens, S. Brezinsek, M. Groth, E. Joffrin, A. Loving, M. Kear, M.-L. Mayoral, R. Neu, P. Prior, V. Riccardo, F. Rimini, M. Rubel, G. Sips, E. Villedieu, P. de Vries, and M. L. Watkins, "Jet iter-like wall—overview and experimental programme," *Physica Scripta*, vol. T145, p. 014001, 12 2011. [Online]. Available: <https://iopscience.iop.org/article/10.1088/0031-8949/2011/T145/014001>

- [131] R. Panek and et al., “Conceptual design of the COMPASS upgrade tokamak,” *Fusion Eng. Des.*, vol. 123, pp. 11 – 16, 2017, proceedings of the 29th Symposium on Fusion Technology (SOFT-29) Prague, Czech Republic, September 5-9, 2016.
- [132] R. Barnsley, “Radiation hardness in ITER diagnostics,” in *1st EIROforum School on Instrumentation*, 2009.
- [133] M. Garcia-Munoz, H.-U. Fahrback, and H. Zohm, “Scintillator based detector for fast-ion losses induced by magnetohydrodynamic instabilities in the ASDEX upgrade tokamak,” *Review of Scientific Instruments*, vol. 80, no. 5, p. 053503, 2009. [Online]. Available: <https://doi.org/10.1063/1.3121543>
- [134] H. Hendel and D. Jassby, “The tokamak as a neutron source,” Princeton Univ., Tech. Rep., 1989.
- [135] T. Eich, A. Leonard, R. Pitts, W. Fundamenski, R. Goldston, T. Gray, A. Herrmann, A. Kirk, A. Kallenbach, O. Kardaun, A. Kukushkin, B. LaBombard, R. Maingi, M. Makowski, A. Scarabosio, B. Sieglin, J. Terry, A. Thornton, A. U. Team, and J. E. Contributors, “Scaling of the tokamak near the scrape-off layer h-mode power width and implications for iter,” *Nuclear Fusion*, vol. 53, no. 9, p. 093031, aug 2013. [Online]. Available: <https://dx.doi.org/10.1088/0029-5515/53/9/093031>
- [136] S. Gerhardt, “NSTX-U system requirements document plasma facing components,” National Spherical Torus Experiment-Upgrade, Tech. Rep., 2017.
- [137] E. J. Strait, “Frequency response of metal-clad inductive magnetic field probes,” *Review of Scientific Instruments*, vol. 67, pp. 2538–2540, 1996.
- [138] J. Reboun, J. Hlina, R. Soukup, and J. Johan, “Printed thick copper films for power applications,” in *2018 7th Electronic System-Integration Technology Conference (ESTC)*. IEEE, 2018, pp. 1–5.
- [139] I. Duran, S. Entler, K. Kovarik, A. Torres, P. Turjanica, J. Reboun, L. Viererbl, D. Najman, M. Kocan, G. Vayakis *et al.*, “New approaches for magnetic diagnostic of future fusion devices,” in *31st Symposium on Fusion Technology (SOFT 2020)*, 2020.
- [140] A. Hellwig, via Wikimedia Commons, 2005, cC BY-SA 2.0 DE. [Online]. Available: https://commons.wikimedia.org/wiki/File:Helmholtz_coils.png
- [141] Pico Technology, *PicoScope @ 5000D Series*, accessed October, 2020. [Online]. Available: <https://www.picotech.com/download/datasheets/picoscope-5000d-series-data-sheet.pdf>
- [142] E. Javor and T. Anderson, “Design of a helmholtz coil for low frequency magnetic field susceptibility testing,” in *1998 IEEE International Symposium on Electromagnetic Compatibility*, 09 1998, pp. 912 – 917 vol.2.
- [143] Pico Technology Ltd, *PicoScope 5000 Series (A API) Programmer’s Guide*, 2018. [Online]. Available: <https://www.picotech.com/download/manuals/picoscope-5000-series-a-api-programmers-guide.pdf>
- [144] —, “picosdk-python-wrappers – a set of python bindings and examples for PicoScope® oscilloscope and PicoLog® data logger products,” Git repository, Jan. accessed January, 2023. [Online]. Available: <https://github.com/picotech/picosdk-python-wrappers>
- [145] L. E. Plambeck, “Microstructure and electrical resistivity of calcined magnesite,” Master’s thesis, University of Wollongong University of Wollongon, 1990.
- [146] Y. Liu and D. Smith, “Ceramic electrical insulators for liquid metal blankets,” *Journal of Nuclear Materials*, vol. 141-143, pp. 38–43, 1986. [Online]. Available: <https://www.sciencedirect.com/science/article/pii/S0022311586800071>
- [147] H. Böck and M. Suleiman, “Investigations of mineral insulated cables exposed to high temperature and intense gamma radiation,” *Nuclear Instruments and Methods*, vol. 148, no. 1, pp. 43–50, 1978. [Online]. Available: <https://www.sciencedirect.com/science/article/pii/0029554X78903336>

- [148] A. Torres, K. Kovarik, T. Markovic, J. Adamek, V. Weinzettl, B. Carvalho, H. Fernandes, M. Hron, and R. Panek, "Mineral insulated cable assessment for inductive magnetic diagnostic sensors of a hot-wall tokamak," *J. Instrum.*, vol. 14, no. 09, pp. C09 043–C09 043, sep 2019.
- [149] R. A. Matula, "Electrical resistivity of copper, gold, palladium, and silver," *Journal of Physical and Chemical Reference Data*, vol. 8, no. 4, pp. 1147–1298, 1979. [Online]. Available: <https://doi.org/10.1063/1.555614>
- [150] P. Welch, "The use of fast fourier transform for the estimation of power spectra: A method based on time averaging over short, modified periodograms," *IEEE Transactions on Audio and Electroacoustics*, vol. 15, no. 2, pp. 70–73, 1967.
- [151] G. Venturini *et al.*, "ahkab: Open source electronic circuit simulation in Python," 2006, [Online; accessed 2023-02-22]. [Online]. Available: <http://ahkab.github.io/ahkab/>
- [152] List-Magnetik, "Magnet permeability meter Ferromaster," [Online; accessed 2023-03-07]. [Online]. Available: [#https://www.list-magnetik.com/en/permeability/magnet-permeability-meter-ferromaster#](https://www.list-magnetik.com/en/permeability/magnet-permeability-meter-ferromaster#)
- [153] Analog Devices, *MT-095 TUTORIAL – EMI, RFI, and Shielding Concepts*, rev. 0 ed., 01 2009. [Online]. Available: <https://www.analog.com/media/en/training-seminars/tutorials/MT-095.pdf>
- [154] J. Gernhardt, *Low-noise cable for diagnostics, control and Instrumentation of the ASDEX tokamak fusion experiment*, Institut fur Plasmaphysic, 1988.
- [155] National Instruments, *DAQ M Series – NI USB-621x User Manual*, 2009.
- [156] A. G. Torres, "Preliminary design of the ITER magnetic diagnostic integrators," Master's thesis, Instituto Superior Tecnico, 2017.
- [157] A. Torres, "Modulation," 2020. [Online]. Available: <http://web.tecnico.ulisboa.pt/andregtorres/PhDEvent2020/modulation.html>
- [158] G. Cunningham, "High performance plasma vertical position control system for upgraded MAST," *Fusion Engineering and Design*, vol. 88, no. 12, pp. 3238–3247, 2013. [Online]. Available: <https://www.sciencedirect.com/science/article/pii/S0920379613006753>
- [159] V. Yanovskiy, N. Isernia, V. Pustovitov, V. Scalera, F. Villone, J. Hromadka, M. Imrisek, J. Havlicek, M. Hron, and R. Panek, "Global forces on the compass-u wall during plasma disruptions," *Nuclear Fusion*, vol. 61, no. 9, p. 096016, aug 2021. [Online]. Available: <https://dx.doi.org/10.1088/1741-4326/ac1545>
- [160] F. Villone, L. Barbato, S. Mastrostefano, and S. Ventre, "Coupling of nonlinear axisymmetric plasma evolution with three-dimensional volumetric conductors," *Plasma Physics and Controlled Fusion*, vol. 55, no. 9, p. 095008, 2013.
- [161] T. Markovic, A. Torres, D. Fridrich, M. Imrisek, F. Jaulmes, and V. Balner, "Plasma position reconstruction using the COMPASS-U magnetic diagnostics," in *WDS 2022 - Week of Doctoral Students 2022*. CHARLES UNIVERSITY , FACULTY OF MATHEMATICS AND PHYSICS, 06 2022.
- [162] A. Torres, B. Carvalho, T. Markovic, A. Batista, A. Havranek, V. Weinzettl, and H. Fernandes, "Data acquisition with real-time numerical integration for COMPASS-U magnetic diagnostics," *Fusion Engineering and Design*, vol. 191, p. 113580, 2023. [Online]. Available: <https://www.sciencedirect.com/science/article/pii/S0920379623001643>
- [163] D. F. Valcárcel, A. Neto, J. Sousa, B. B. Carvalho, H. Fernandes, J. C. Fortunato, A. S. Gouveia, A. J. Batista, A. G. Fernandes, M. Correia, T. Pereira, I. S. Carvalho, A. S. Duarte, C. A. Varandas, M. Hron, F. Janky, and J. Písačka, "An atca embedded data acquisition and control system for the compass tokamak," *Fusion Engineering and Design*, 2009.
- [164] A. J. N. Batista, A. Neto, M. Correia, A. M. Fernandes, B. B. Carvalho, J. C. Fortunato, J. Sousa, C. A. F. Varandas, F. Sartori, and M. Jennison, "ATCA control system hardware for the plasma vertical stabilization in the JET tokamak," *IEEE Transactions on Nuclear Science*, vol. 57, no. 2, pp. 583–588, 2010.

- [165] IPFN, "ATCA-IO-PROCESSOR," 2015, [Online; accessed 2023-04-21]. [Online]. Available: http://metis.ipfn.tecnico.ulisboa.pt/CODAC/IPFN_Instrumentation/Boards/ATCA/ATCA-IO-PROCESSOR
- [166] B. Gonçalves, J. Sousa, B. Carvalho, A. Batista, A. Neto, B. Santos, A. Duarte, D. Valcarcel, D. Alves, M. Correia, A. Rodrigues, P. Carvalho, J. Fortunato, P. Carvalho, M. Ruiz, J. Vega, R. Castro, J. M. Lopez Navarro, N. Utzel, and P. Mota, "Iter prototype fast plant system controller based on atca platform," in *2011 IEEE Nuclear Science Symposium Conference Record*, vol. 87. IEEE, 10 2012, pp. 171–178.
- [167] D. Huang, "How to design an isolated, high frequency, push-pull DC/DC converter," *LT Journal of Analog Innovation*, vol. V25, no. 1, Apr. 2015. [Online]. Available: <https://www.analog.com/en/technical-articles/high-frequency-push-pull-dc-dc-converter.html>
- [168] A. C. Neto, F. Sartori, F. Piccolo, R. Vitelli, G. De Tommasi, L. Zabeo, A. Barbalace, H. Fernandes, D. F. Valcarcel, and A. J. N. Batista, "MARTE: A multiplatform real-time framework," *IEEE Transactions on Nuclear Science*, vol. 57, no. 2, pp. 479–486, 2010.
- [169] H. Fernandes, H. Figueiredo, J. Sousa, C. Freitas, J. Cabral, and C. Varandas, "Operation of the tokamak ISTTOK in an alternating current regime," in *Fusion Technology 1996*, C. VARANDAS and F. SERRA, Eds. Oxford: Elsevier, 1997, pp. 977–980. [Online]. Available: <https://www.sciencedirect.com/science/article/pii/B9780444827623502135>



Helmholtz coil structure technical drawing

H G F E D C B A

4

4

7.46 mm

6.00 mm

4.50 mm

15.00 mm

3

3

15.02 mm

45.00°

R105.00 mm

R97.54 mm

R89.26 mm

2

2

1

1

AUTHOR NAME: Andre Torres		Helmholtz Coil Structure Base and top		I	_____
DATE: 31/7/2019				H	_____
SUPERVISOR NAME:		COMPANY: IPP AVCR		G	_____
DATE:		VERSION: v3		F	_____
FORMAT: A3	WEIGHT (kg):		SHEET: 1/1	E	_____
SCALE: 1:1	VERSION: v3			D	_____
				C	_____
				B	_____
				A	_____

H G F E D C B A

B

Calculation of the field homogeneity integrals

B.1 1D

The magnetic field inside the solenoid is not homogeneous. In its center the magnetic field B_0 and the corresponding field per unit current (κ) can be precisely calculated. Likewise, the field in any point can also be computed, but precise measurements have shown a deviation from the simulated field. It is easier to think in terms of inhomogeneity, α expressed as the relative deviation to B_0 :

$$\alpha = \frac{B - B_0}{B_0} \quad . \quad (\text{B.1})$$

The measurements have shown that there is a roughly parabolic dependence of α in the axial and radial directions (see figure 3.25):

$$\alpha_z = p_{2,z} z^2 \quad , \quad (\text{B.2})$$

$$\alpha_r = p_{2,r} r^2 \quad . \quad (\text{B.3})$$

On the axial direction is easy to see that a long sensor will measure a non-homogeneous field, the degree of which can be obtained by integrating α_z over the length ($2l$) of the sensor for a correcting factor β_{1D} :

$$\begin{aligned} \beta_{1D} &= \frac{1}{l} \int_{z_1}^{z_2} \alpha_z dz = \frac{1}{l} \int_{-l/2}^{l/2} p_{2,z} z^2 dz \\ &= \frac{p_{2,z}}{l} \left[\frac{1}{3} z^3 \right]_{-l/2}^{l/2} = \frac{p_{2,z}}{l} \frac{1}{12} l^3 \\ &= \frac{p_{2,z} l^2}{12} \quad . \end{aligned} \quad (\text{B.4})$$

B.2 2D

On the radial component, the integration is 2-dimensional and is dependent on the shape of the sensor profile and not only on the length. The sensors used fall into three categories, according to the profile: circular, rectangular and racetrack.

B.2.1 Circular

If the cross-section of the sensor is circular with radius R , total area $A = \pi R^2$, the correcting factor is:

$$\begin{aligned} \beta_{2D} &= \frac{1}{A} \int_0^R \int_0^{2\pi} \alpha_r r d\theta dr = \frac{2\pi}{A} \int_0^R p_{2,r} r^3 dz \\ &= \frac{2\pi p_{2,r}}{\pi R^2} \left[\frac{1}{4} r^4 \right]_0^R \\ &= \frac{p_{2,r} R^2}{2} \quad . \end{aligned} \quad (\text{B.5})$$

B.2.2 Rectangular

If the cross-section of the sensor is rectangular with width w along x and height h along y , total area $A = wh$, one can take advantage of the quadrant symmetry and compute the integral for only

the first quadrant.

$$\begin{aligned}
 \beta_{2D} &= \frac{4}{A} \int_0^{w/2} \int_0^{h/2} p_{2,r} \left(\sqrt{x^2 + y^2} \right)^2 dy dx \\
 &= \frac{4p_{2,r}}{wh} \left[\frac{h}{2} \int_0^{w/2} x^2 dx + \frac{w}{2} \int_0^{h/2} y^2 dy \right] \\
 &= \frac{2p_{2,r}}{wh} \left(\frac{h}{3} [x^3]_0^{w/2} + \frac{w}{3} [y^3]_0^{h/2} \right) \\
 &= \frac{2p_{2,r}}{3wh} \left[\frac{w^3}{8} + \frac{h^3}{8} \right] \\
 &= \frac{p_{2,r}}{12} \frac{w^3 + h^3}{wh} .
 \end{aligned} \tag{B.6}$$

B.2.3 Racetrack

When the coil has a racetrack profile, as if the figure, the integral and area must be divided in two sections. The first, a centered rectangular section where the area and the integral (A_1, I_1) are computed like in the previous case, however, now considering the first and fourth quadrant (positive x).

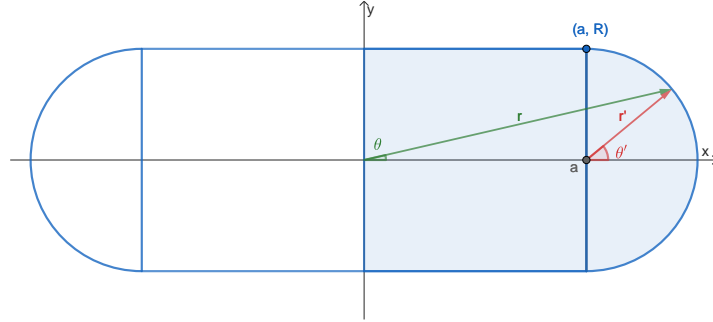


Figure B.1: Geometry of the racetrack profile, with free parameters a and R . Identification of the coordinate systems used and integration area shaded.

$$A_1 = 2aR \quad , \tag{B.7}$$

$$I_1 = \frac{2}{3} (ra^3 + ar^3) \quad , \tag{B.8}$$

the next step is computing the integral of α_r for the semicircular section that is not centered, but with radius R around $(a,0)$. Starting by using polar coordinates:

$$I_2 = \int \int r^2 r dr d\theta \quad , \tag{B.9}$$

one needs to define r and θ in terms of r' and θ' :

$$r = \sqrt{r'^2 + a^2 + 2ar'\cos(\theta')} \equiv \sqrt{\gamma} \quad , \tag{B.10}$$

$$\theta = \arctan \left(\frac{r'\sin(\theta')}{r'\cos(\theta') + a} \right) \quad . \tag{B.11}$$

The Jacobian determinant for the coordinate transformation can be simplified to:

$$\det(\mathbf{J}) = \frac{r'}{\sqrt{\gamma}} \quad , \tag{B.12}$$

therefore the integral in (r', θ') is:

$$\begin{aligned}
I_2 &= \int_{-\pi/2}^{\pi/2} \int_0^R \gamma \sqrt{\gamma} \frac{r'}{\sqrt{\gamma}} dr' d\theta' \\
&\int_{-\pi/2}^{\pi/2} \int_0^R r'^3 + 2r'^2 a \cos(\theta') + a^2 r' dr' d\theta' \\
&\frac{\pi R^4}{4} + \frac{\pi a^2 R^2}{2} + 2a \int_{-\pi/2}^{\pi/2} \int_0^R r'^2 \cos(\theta') dr' d\theta' \\
&\frac{\pi R^4}{4} + \frac{\pi a^2 R^2}{2} + \frac{4aR^3}{3} \\
&\frac{\pi R^2}{2} \left[\frac{1}{2} R^2 + a^2 \right] + \frac{4aR^3}{3} .
\end{aligned} \tag{B.13}$$

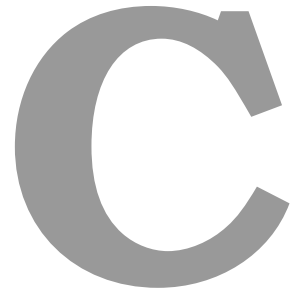
The area is that of the semicircle $A_2 = \frac{\pi R^2}{2}$ and the integrated coefficient is then:

$$\beta_{2D} = \frac{p_{2,r}}{A_1 + A_2} (I_1 + I_2) \tag{B.14}$$

B.3 Computed corrections

Table B.1: Calculation of correction coefficients due to the inhomogeneity of the magnetic field inside the solenoid.

Coil	Physical parameters [mm]	β_{1D} [%]	β_{2D} [%]	β_{3D} [%]	$(1 + \beta_{3D})$ []
FC{1,2}	Rectangular, $l=30, w=24, h=5$	-0.1323	0.0356	-0.0967	0.999033
TPC{1-5}	Rectangular, $l=8, w=40, h=15$	-0.0094	0.1081	-0.0987	1.000987
MIC{1,2}	Racetrack, $l=50, a=10.5, R=9.5$	-0.3674	0.0986	-0.2692	0.997308
MIC{3-5}	Racetrack, $l=53, a=10, R=8.5$	-0.4128	0.0837	-0.3295	0.996705
MIC{6-9}, EPR1	Racetrack, $l=50, a=7.5, R=6.5$	-0.3674	0.0481	-0.3160	0.996805



Module configurations

Table C.1: Initial configuration of the module prototypes.

Config.	Channel	Input range	Input Stage		MFB filter	
			Gain	f_c [kHz]	f_0	Q
0	M*CHA	± 5 V	1:2	19.4	347 kHz	0.95
	M*CHB	± 127.5 V	1:51	495	347 kHz	0.95
1	M3CHA	± 15 V	1:6	12.7	3.55 MHz	0.707
	M3CHB	± 65 V	1:26	17.6	3.55 MHz	0.707
2	M1CHA	± 10 V	1:4	12.9	2.17 MHz	0.99
	M1CHB	± 40 V	1:16	12.9	2.17 MHz	0.99
3	M1CHA	± 10 V	1:4	12.9	2.46 MHz	1
	M1CHB	± 40 V	1:16	12.9	2.46 MHz	1
4	M2CHA	± 10 V	1:4	14.1	1.35 MHz	0.707
	M2CHB	± 40 V	1:16	18.1	1.35 MHz	0.707

D

Determination of MFB filter components

The determination of a filter with a given f_0 and Q will invariably result in values for the components that can not be exactly materialized because components are manufactured in discrete (and in a finite number of) values.

The procedure described in section 5.4.4 was once again repeated, and extended. Instead of representing the curves for f_0 and Q , only their intersections are now represented. In this way, we can lock a larger number of $R1, C1$ values (table D.1) without crowding the plot too much.

Table D.1: Combinations of $R1$ and $C1$. For implementation on the differential configuration the central capacitor should have capacitance $C1' = C1/2$.

		$C1$ [nF]		
		0.2	2	20
$R1$ [Ω]	200	A	B	C
	499	D	E	F
	1 k	G	H	I

Figure D.1 shows the resulting map of the component values, under the fixed $R1, C1$ values represented by letters, and the strategies identified in section 5.5.5.B, represented by colors.

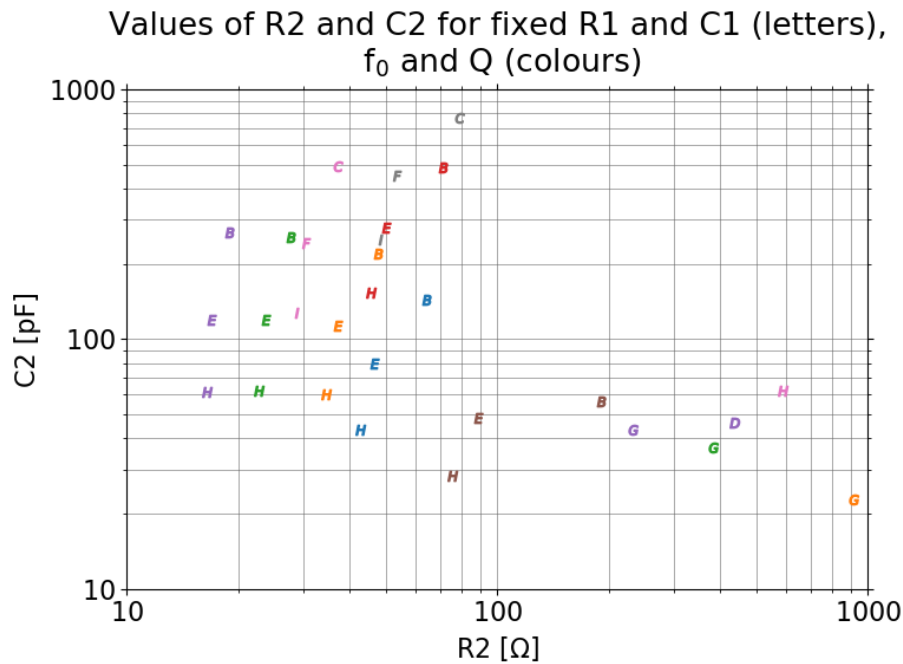


Figure D.1: Map of required $R2$ and $C2$ values for fixed $(R1, C1)$ represented by letters and (f_0, Q) , represented by colors.

The end result is a much faster determination of adequate values for the filter implementation from the pool of available (either in stock or procurable) components. Whilst minimizing trial and error and without compromising the accuracy of the implemented filter properties.